Bio-inspired Synthesis of Co_3O_4 and NiO Nanoparticles for Electrocatalytic H_2O_2 Generation and Sensing

Thesis
Submitted in Partial
Fulfillment of the Requirements for the Degree of

Doctor of Philosophy

by

RAJ KUMAR DAS
(126107036)

Department of Chemical Engineering
Indian Institute of Technology Guwahati
June 2018

Dedication

To Golder Sir & my Family

Indian Institute of Technology Guwahati

Department of Chemical Engineering

Statement

*I, hereby declare that the content embodied in this thesis entitled "**Bio-inspired Synthesis of Co_3O_4 and NiO Nanoparticles for Electrocatalytic H_2O_2 Generation and Sensing**" is the result of investigations carried out by me at the Department of Chemical Engineering, Indian Institute of Technology Guwahati, Guwahati, India, under the supervision of **Associate Professor Dr. Animes K Golder**.*

In keeping with the general practice of reporting scientific observations, due acknowledgements have been made wherever the work described is based on the findings of other investigators.

Guwahati,
June, 2018

Raj Kumar Das

Indian Institute of Technology Guwahati

Department of Chemical Engineering

CERTIFICATE

*This is to certify that the thesis entitled "**Bio-inspired Synthesis of Co_3O_4 and NiO Nanoparticles for Electrocatalytic H_2O_2 Generation and Sensing**", being submitted by **Mr. Raj Kumar Das**, to the Indian Institute of Technology Guwahati, India, for the award of Doctor of Philosophy, is a record of bonafide research work carried out by him under my guidance and supervision. The work embodied in this thesis has not been submitted for any other degree or diploma. In my opinion, the thesis is up to the standard of fulfilling the requirements of the doctoral degree as prescribed by the regulations of this Institute.*

Date:

Dr. Animes K Golder
(Thesis Supervsior)
Associate Professor
Department of Chemical Engineering
Indian Institute of Technology Guwahati

Acknowledgment

Firstly, I would like to express my sincere gratitude to my supervisor ***Dr. Animes Kumar Golder*** for giving a great opportunity to do research work under his pretty guidance. He demonstrated honestly any hard doubts about research work despite of his busy work schedules. He also rectified consistently any kind of mistakes with insightful discussions during research work and carried me in the right the direction as my guardian whenever needed. I am also gratefully indebted to him for his endless support, his patience, motivation, and immense knowledge on Ph.D. study and related research. I could not have imagined having a better advisor and mentor for my Ph.D. study instead of him. This thesis would not have been possible in time without his remarkable guidance.

Besides my advisor, I would like to thank my thesis committee: ***Prof. Mihir K Purkait***, ***Dr. V. V. Goud***, and ***Dr. Subhendu Sekhar Bag***, for their insightful comments and encouragement, but also for the hard question which assisted me to extend my research from various perspectives. I am really thankful to ***Dr. Chandan Das, Prof. Bishnupada Mandal Prof. Tamal Banerjee, Prof. Subrata K Majumder, Dr. Tapas K Mandal and Dr. Pankaj Biswas*** for helping me from any kind of troubles. A special thanks go to ***Dr. Vimal Katiyar and Dr. Dipankar Bandyopadhyay*** for providing a slot in emergency time.

In addition, a thank you to ***Prof. Chiranjib Bhattachariya, Prof. Ranjana Chowdhury, Prof. Pinaki Bhattachariya and Prof. Tapas Kumar Dutta*** for enlightening me the first import of research and also encouraging with precious support.

In particular, a profound gratitude must be expressed to ***Mr. Indrajit Das, Rakhee Das, Rima Biswas, Mr. Subhrajit Sarkar and Piyali Ghosh*** for liberating me from any kind of bad circumstance. I am also grateful to ***Amit Baran Das, Rahul Saha, Pallab Das, Chitrita Kundu, Gorachand Barman, Subrata Mondol, Mitali Sahu, Soumi Sarkar and Arunabha Banerjee*** *who* cared about my every step on my journey.

Special thanks goes to my labmates ***Dr A.S. Giri, Dr. Sujoy Bose, Mr. C.V. Rao, Mr. Vinay Kulkarni, Mr. Anirban Chowdhuri, Mr. Smruti R. Dash, Ms. Paulomi Bose, Mr. Suman Saha, Mr. Abhradeep Pal, Mr. A. Sukla, Mr. Santosh K Yedla, Ms. Devipriya Gogoi, Mr. M Alam, Mr. Bharath Velaga and Mr. Shravan Kumar*** for giving simulating discussions when we were working together before deadlines, and for all the fun we have had in the last four years. Also big credits go to my friends ***Mood Mohan, Kuldeep Roy, Piyal Mondal, Debashis Kundu, Supriyo Kumar Mondal, Soumen Mondal, Atanu Kumar Paul,***

Pradip Das, Prodyut Dhar, Fahad M K for assisting me project related works in any situation.

My sincere thanks go to official and lab technical stuff who gave access to the laboratory and research facilities. A sincere thanks go out to the ***Science & Engineering Research Board, Department of Science and Technology, India***, for providing the research grant (reference no. SERC/ET-0343/2012) to carry out this work. A big thanks to ***Central Instrument Facilities*** for providing the necessary research facilities.

In end of letter, no words are set for my best philosopher in my life, ***Mrs. Anindita Das*** and ***Mr. Jagannath Das***. They all-time provided me with unfailing support and continuous encouragement mentally and spiritually throughout my years of study and completing this thesis. I would like also to acknowledge my parents, ***Binod Das*** and ***Kalpana Das*** for their great patience and love all time. It would not be possible to conduct this research without their precious support.

Indian Institute of Guwahati *Raj Kumar Das*

Guwahati

June, 2018

Abstract

Hydrogen peroxide (H_2O_2) has wide applications in chemical synthesis, food, clinical, biological, and environmental processes. One of the common applications of H_2O_2 is its use as a precursor for the formation of hydroxyl radicals ($^{\bullet}OH$) in the advanced oxidation processes (AOPs) for the treatment of wastewater. The end products of H_2O_2 decomposition reaction are water and oxygen. Therefore, H_2O_2 is considered as an environment friendly reagent. H_2O_2 electrogeneration is usually carried out through the reduction of dissolved O_2 (DO) in an acidic solution at a low cathodic potential. It could reduce the cost and the hazards involved during its transportation and handling of concentrated H_2O_2. The present study comprises of three parts.

The first part of this work is undertaken to investigate on H_2O_2 decomposition over a broad range of its concentration (60-600 mg/L) which is typically employed in water treatment. pH and reaction temperature were varied from 2 to 12 and 30 to 70 °C for a reaction period of 10 h. The experimental data shows that H_2O_2 decomposition was increased dramatically at pH> 8, and it was more than 10 % irrespective of the initial concentration and temperature. The effects of common mono- and bi-valent cations such as Na^+, Ca^{2+}, Ni^{2+}, Co^{2+}, Cu^{2+}, etc. on H_2O_2 stability are investigated at lower concentrations (≤ 10 mg/L). H_2O_2 became essentially unstable at a higher pH in the presence of these trace metal ions except Co^{2+} and Ni^{2+} due to low catalytic effect. This work also focused on the role of common supporting electrolytes (SEs) in the electro-chemical inertness of Ti-based materials employed for the anodic (direct) oxidation coupled with H_2O_2 electrogeneration at the graphite cathode for the concurrent decomposition of organic contaminants. The use of ClO_4^- is encouraged in the electro-Fenton process as it does not form complexes with Fe^{2+}/Fe^{3+}; however, it was found that ClO_4^- corroded TiO_2 coated Ti (TiO_2–Ti) anode very fast (>60 min), and Ti^{4+} ions formed a yellow color complex (λ_{max} = 380 nm) with H_2O_2. The influence of Cl^-, NO_3^-, and SO_4^{2-} was insignificant on the stability of TiO_2–Ti. The cell current efficiency of H_2O_2 formation dropped sharply with ClO_4^- in the case of TiO_2–Ti anode. The TiO_2–Ti corrosion also reduced the mass transfer co-efficient of DO transport from bulk to the cathode surface because of Ti^{4+} adsorption on graphite cathode.

In the second part, the NiO and Co_3O_4 NPs were successfully synthesized by a green synthesis pathway using the analytes extracted from *Sechium edule*, the fruit of a perennial climber, for electrocatalytic applications of these NPs in H_2O_2 generation and sensing. The

proposed synthesis process is inexpensive and simple. The reducing analytes such as ascorbic acid (AA) are rich in this fruit extract. It was found that Ni(II)-AA complex was formed in an aqueous solution near the neutral pH. At a higher pH, $Ni(OH)_2$ could be formed by the ligand exchange between AA^- and OH^-. At pH>10, AA^- is converted to 2,3-diketogulonic acid (2,3-DKG). Similarly, AA mediated CoOOH transformation to $Co(OH)_2$, and CoOOH was abundant with Co_3O_4 NPs synthesized in the control condition without the use of the bio-extract.

The NiO and Co_3O_4 NPs were characterized by X-ray diffraction (XRD), Fourier transform infrared spectroscopy (FTIR), Atomic force microscopy (AFM), Field emission scanning electron microscopy (Fe-SEM), Transmission electron microscopy (TEM) and Vibrating sample magnetometer (VSM). The pure microporous NiO (75 % pores within 1.52 to 2 nm) and Co_3O_4 (90 % pores within 0.6 to 2 nm) NPs exhibited weak ferromagnetic properties. TEM micrographs showed that the NiO and Co_3O_4 NPs had an average diameter of 14.48 and 31.79 nm, respectively.

The synthesized NiO NPs were immobilized on the graphite surface and tested for its electrocatalytic activity for the production of H_2O_2 in an acidic pH ($1.5 \leq pH \leq 4.5$, 0.5 M Na_2SO_4 and O_2 flow rate 1.0 LPM). From the cyclic voltammetric (CV) tests (vs. Ag/AgCl), it was found that O_2 reduction took place at a low overpotential which was independent on the solution pH, but the cell current was diminishing beyond the optimal pH of 2.5. There was a remarkable increase in the cell current (3.5 times) and current efficiency (61 % higher) of H_2O_2 formation with graphite/NiO NPs cathode than the bare graphite, and the current efficiency didn't decrease (5-7 %) much during electrolysis. It was even higher with the graphite/Co_3O_4 NPs electrode. The limiting current density (1.42 A/m^2) was independent on the surface area of graphite/NiO NPs cathodes, and the mass transfer coefficient (k_m) and thickness (δ) of O_2 diffusion layer were 0.955×10^{-5} m/s and 209 µm, respectively. But, marginally higher mass transfer coefficient and thickness of the diffusion layer were found as $1.1.3\times10^{-5}$ m/s and 177 µm, respectively, due to higher limiting current density (1.60 A/m^2) in the case of graphite/Co_3O_4 NPs electrode.

The degradation of CIP was quite impressive (71-78 %) in the electro-Fenton process (EFP) where H_2O_2 generation was catalyzed by NiO and Co_3O_4 NPs. However, the mineralization efficiency was notably lower due to the formation of the refractory intermediates attached to the quinolone structure. The degradation of the CIP molecule mainly took place through three different pathways such as piperazine moiety breaking, cyclopropyl group cleavage, and decarboxylation reaction. The proposed mechanisms were

well supported by the fragments appeared in the mass spectra, and most of the fragments were originated from the cleavage of piperazine ring moiety. The pseudo 1st order kinetic model well fitted the experimental data of CIP cleavage.

In the last part of the work for the electrocatalytic H_2O_2 sensing, the Co_3O_4 and NiO NPs were tailored on a graphite electrode with an average concentration of 5.92×10^{-13} and 5.19×10^{-13} mol/cm^2 in a deaerated phosphate buffer media (pH 7.2). The CV at -E_{cat}= 0.5 to −0.5 V vs. Ag/AgCl showed a low H_2O_2 reduction peak at –0.117 V vs. Ag/AgCl for the graphite/Co_3O_4 NPs and at −0.129 V vs. Ag/AgCl for the graphite/NiO NPs electrode with a quasi-reversible electrochemical system. The modified electrode was exhibited a quick amperometric response (< 5 s), a low limit of detection (LOD) of H_2O_2 of 0.0217 µM, and a high electrode sensitivity of 65.32 nA/µM/cm^2 compared to the graphite/NiO NPs electrode (LOD of 0.0271 µM with electrode sensitivity of 62 nA/µM/cm^2). No alteration of the amperometric responses was noted in the presence of common interferents.

Keywords: H_2O_2 decomposition; Trace metal ions; Catalytic H_2O_2 decomposition; Electrode stability; H_2O_2 electro-generation; O_2 reduction; Graphite cathode; Graphite working electrode; TiO_2-Ti anode; Catalytic H_2O_2 generation; Catalytic H_2O_2 sensing; Microporous Co_3O_4 NPs; Microporous NiO NPs; Ferromagnetic NPs; Plant based analytes; NPs green synthesis; Cyclic voltammetry; Steady current efficiency; Limiting current density; quasi-reversible electrochemical system; Electrode sensitivity; Limit of detection; Interfering analytes

TABLE OF CONTENTS

LIST OF FIGURE CAPTIONS

List of Tables captions

Chapter–1

Background of the Work and Research Objectives

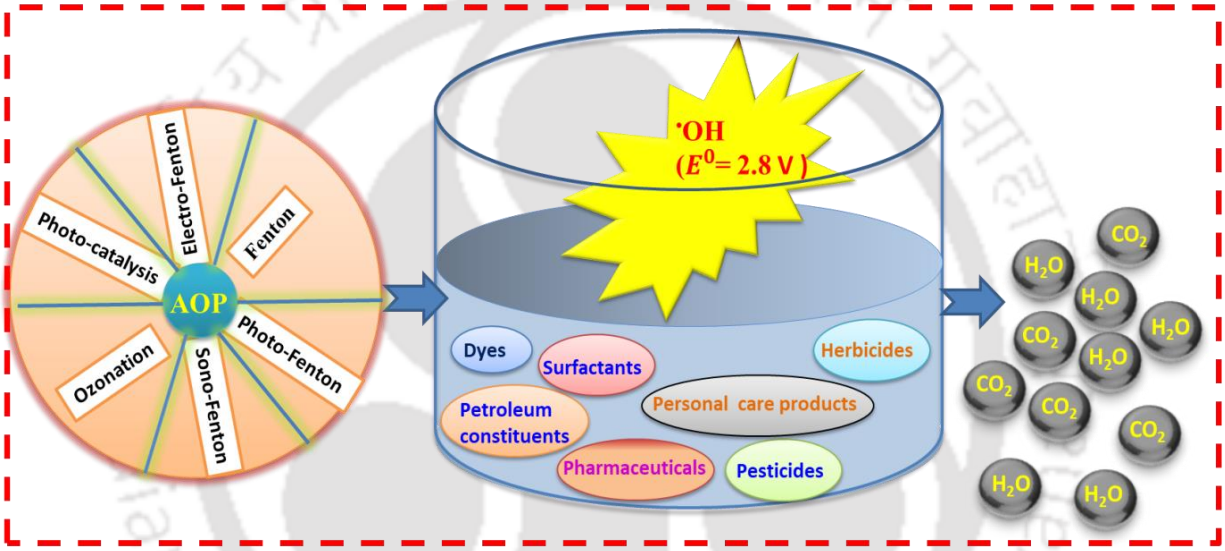

Chapter1 introduces the research problem, includes the literature survey and outlines the research objectives. At the beginning, an introduction of the significance of the H_2O_2 utilization for the treatment of wastewater is provided. Different processes for the use, formation, and determination of H_2O_2 are discussed in the following sections. The state-of-the-art literature review is covered in details to find out the knowledge gap and to define the research objectives of the present work.

1.1 Wastewater treatment and significance of H_2O_2

Water is an essential compound for living beings on the Earth. The Earth is composed of nearly by 70% water. The freshwater content is only 2.5%. This is the reason that water is considered as a limited resource (Estrada, 2012). Moreover, freshwater pollution is one of the severe environmental concerns of the 21st century.

The anthropogenic activities of water pollution include inappropriate water management policies, unregulated discharges of wastewater from petroleum, textile, agriculture, medicine, and chemical industries. Non-biodegradable organic pollutants such as petroleum constituents, surfactants, pesticides & herbicides, dyes, phenolic compounds, and pharmaceuticals & personal care products (PPCPs) are released every day in the form of different kinds of wastewater. Such compounds cannot be degraded easily by the conventional biological treatment due to their resistance to microbial attack (Brillas et al., 2009). They are detected at a very low concentration even as low as nanograms per liter in drinking water, rivers, lakes, and oceans (Estrada, 2012). The carcinogenic, mutagenic, and bactericidal effects of most of the persistent organic pollutants (POPs) are still unknown (Martınez-Huitle and Brillas, 2009).

It is well-known that conventional treatments like physical, chemical, and biological are generally applied for the removal of organic pollutants. But, they are unable to cause an effective degradation of POPs. Plenty of reagents are required in chemical treatment to degrade and mineralize the contaminants. A long residence time should be provided for biological treatment. Moreover, the micro-pollutants are very difficult to be removed completely from water by traditional methods namely, primary, secondary, and tertiary treatments.

The primary methods practiced for the treatment of industrial wastewater are summarized in Figure 1.1. Among these techniques, advanced oxidation processes (AOPs) are highly efficient due to their ability to cause deep changes in chemical structure of any organic pollutants. AOPs refer to a set of chemical-oxidative treatments designed to remove organic and inorganic materials present in wastewater. AOPs primarily involve two steps of oxidation. First is the formation of strong oxidants such as hydroxyl radical ($^{\bullet}OH$). Second is the reaction of $^{\bullet}OH$ with contaminants to form stable inorganic compounds such as water and CO_2. Inorganic ions such as NH^{+}, NO_3^{-}, SO_4^{2-}, Cl^{-} etc. are also originated.

The most typical AOPs for the production of $^{\bullet}OH$ radicals are Fenton reagent-based and TiO_2-based catalytic oxidation processes (Daughton and Ternes, 1999). Some

combinations of ozone, H_2O_2, and UV-irradiation are also commonly employed. Table 1.2 shows the common reagents and pH for oxidative decomposition of organic pollutants in different AOPs processes. It can be seen that $^{\bullet}OH$ radical is the 2nd strongest oxidizing agent after fluorine with a standard reduction potential of 2.8 V vs. SHE (standard hydrogen electrode).

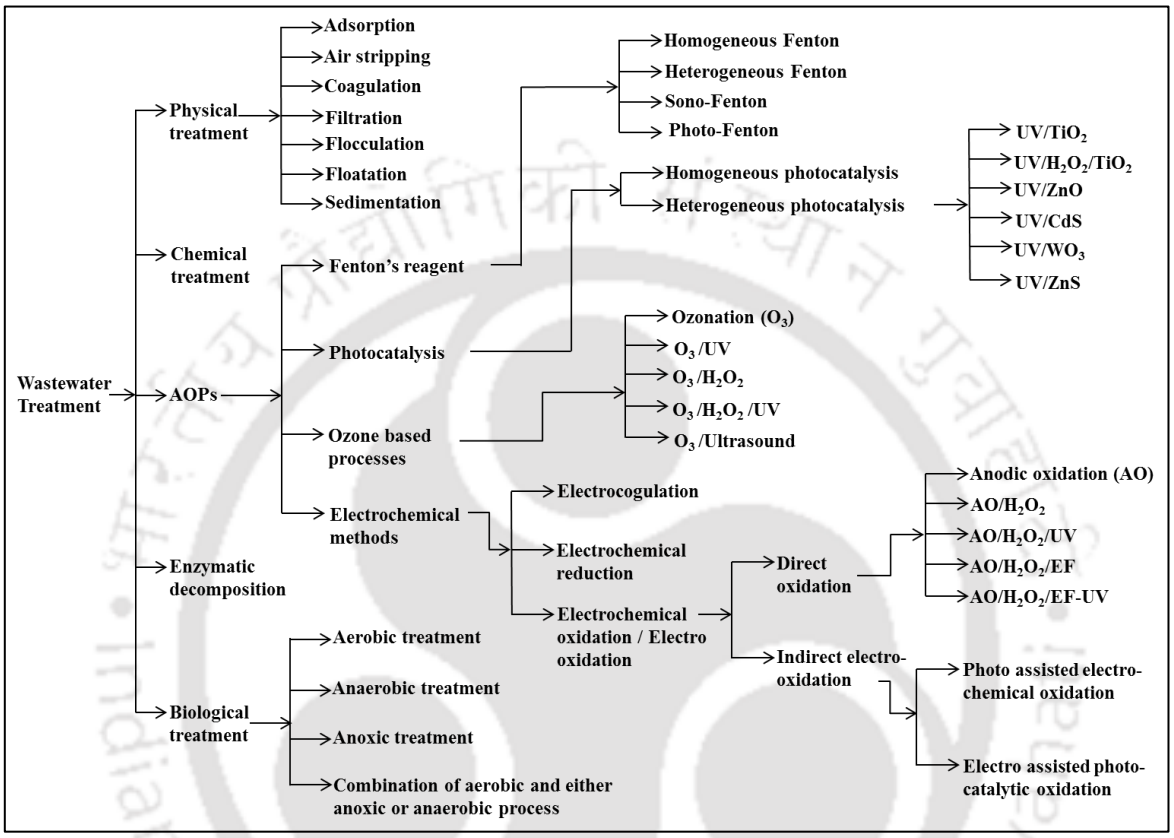

Figure 1.1: Common techniques for removal of organic pollutants from wastewater.

In Fenton and Fenton-like AOPs, H_2O_2 is used mostly as a precursor of the hydroxyl radicals ($^{\bullet}OH$) generation. H_2O_2 has also many other applications in biomedical, clinical, pharmaceutical, food production, and pulp and paper bleaching industries (Jiang and Zhang, 2009). It is used as a mediator in many organic compound synthesis reactions and liquid based fuel cells (Jiang and Zhang, 2009). Moreover, H_2O_2 is considered as an environment-friendly chemical as it breaks down into the water and oxygen after the reaction (Eq. 1.1).

$$2H_2O_2 \rightarrow 2H_2O + O_2 \qquad (1.1)$$

In an electro-Fenton process (EFP), H_2O_2 (Eq. 1.2) and Fe^{2+} (Eq. 1.3) can be electrochemically generated in-situ, separately or simultaneously (Anotai et al., 2006; Qiang et al. 2003). The standard electrode potentials (E^0) of these reactions are shown with respect to the standard Ag/AgCl electrode.

$2H^+ + O_2 + 2e^- \longrightarrow H_2O_2$ (E^0= 0.393 V vs. Ag/AgCl) (1.2)

$Fe^{3+} + e^- \rightarrow Fe^{2+}$ (E^0= 0.482 V vs. Ag/AgCl) (1.3)

H_2O_2 generation is usually carried out by reducing dissolved O_2 (Eq. 1.2) in an acidic solution at a low cathodic potential (Esquivel et al., 2009; Qiang et al., 2002). It could reduce the cost and the hazards during its transportation and handling of concentrated commercial H_2O_2 (Samanta, 2008). Graphite (Qiang et al., 2002; Pozzo et al., 2005), carbon (Wang et al., 2005; Hammami et al., 2007), and gas-diffusion electrodes (Pozzo et al., 2005; Reis et al., 2012) are typically used as cathodes for H_2O_2 formation. But, the popularity of EFP is limited due to a lower current efficiency of H_2O_2 formation. Therefore, various electrocatalysts such as metal nanoparticles (NPs) and metal oxides NPs are developed to enhance the current efficiency of H_2O_2 formation. But, the search is still on to develop a green method for the synthesis of electrocatalysts of H_2O_2 generation.

Table 1.1: Different Fenton and Fenton-like processes with common pH range (Wang et al., 2012).

Reaction type	Reagents	Typical pH range
Classical Fenton	H_2O_2, Fe^{2+}	2–4
Fenton-like	H_2O_2, Fe^{3+} H_2O_2, iron	2–4
Heterogeneous Fenton	H_2O_2, solid iron Electro-generated H_2O_2, free iron ions	Wide range
Homogeneous photo-Fenton	Complex, free iron ions with UV-light irradiation	Acidic to neutral
Heterogeneous photo-Fenton	H_2O_2, solid iron with UV-light irradiation	Wide range
Electro-Fenton	H_2O_2, electro-generated Fe^{2+}	2–4
Heterogeneous Photo-electro-Fenton	Electro-generated H_2O_2 , solid iron with UV-light irradiation	Wide range

Table 1.2: Standard electrode potentials of several oxidizing agents with respect to standard hydrogen electrode (SHE) in aqueous solution at 25 °C (Brillas et al., 2009).

Oxidants	Reduction reaction	Oxidation power (E^o), V
Fluorine	F_2 (g) + $2H^+$ + $2e^-$ → 2HF	3.05
Hydroxyl radical	$^{\bullet}OH + H^+ + e^- \rightarrow H_2O$	2.80
Ozone	O_3 (g) + $2H^+$ + $2e^-$ → O_2 (g) + H_2O	2.075
Hydrogen peroxide	$H_2O_2 + 2H^+ + 2e^- \rightarrow 2H_2O$	1.763
Hydroperoxyl ion (I)	$^{\bullet}OOH + 3H^+ + 3e^- \rightarrow 2H_2O$	1.65
Hydroperoxyl ion (II)	$^{\bullet}OOH + H^+ + 3e^- \rightarrow H_2O_2$	1.44
Chlorine	Cl_2 (g) + $2e^-$ → $2Cl^-$	1.358
Manganese dioxide	$MnO_2 + 4H^+ + 2e^- \rightarrow Mn^{2+} + 2H_2O$	1.23
Oxygen	O_2 (g) + $4H^+$ + $4e^-$ → $2H_2O$	1.229

1.2 H_2O_2 determination and detection

It is outlined in Section 1.1 that H_2O_2 has numerous applications in various industrial processes, including water treatment. Therefore, a sensitive, reliable, rapid, and low cost method of H_2O_2 determination is imperative. The electrochemical methods owe the advantages of easy fabrication, quick sensing, low sample volume, low detection limit, and high selectivity (Xi et al., 2013). However, the direct redox reaction of H_2O_2 at typical solid electrodes is a slow process and, needs a high overpotential. This problem can be overcome by modifying the bare electrode with the suitable electrocatalysts so that the high overpotential for H_2O_2 reduction is decreased (Ensafi et al., 2013).

The enzyme-based electrochemical sensors are employed for faster electron transfer and to lower down the reduction potential. Horseradish peroxidase (Wen et al., 2011), cytochrome c (Luo et al., 2009), haemoglobin (Chen et al., 2007), and myoglobin (Yang et al., 2006) are tested extensively for the fabrication of electrochemical biosensor for H_2O_2 detection due to high sensitivity and selectivity even with the presence of interfering components. However, the enzyme-based electrodes, suffer from instability, high enzyme cost, and complex immobilization technique. The enzyme activity is also significantly dependent on temperature, media pH, and chemical toxicity (Ensafi et al., 2013).

To solve the problems related to H_2O_2 detection by the enzymatic electrochemical methods, the non-enzymatic electrodes mediated with noble metals (Bo et al., 2011), metal oxides (Liu et al., 2013), metal alloys (Sun et al., 2004), and metal NPs (Liu et al., 2011a) as electrocatalysts are developed. But, the synthesis of these catalysts needs the use of costly and hazardous chemicals (Makarov et al., 2014). Therefore, there is a strong synergy between electrocatalytic H_2O_2 generation and H_2O_2 sensing/detection.

1.3 H_2O_2 based processes for water treatment

In this section, a brief outline on the role of H_2O_2 in Fenton and Fenton-like processes is provided.

1.3.1. Fenton reaction

In 1894, the reaction between H_2O_2 and metal as a homogeneous catalyst in dark condition was proposed first by H. J. H. Fenton which is recognized as the Fenton reaction. Later, in 1934 Haber and Weiss realized that $^{\bullet}OH$ is responsible for the Fenton reaction which is based on $^{\bullet}OH$ radical formation under dark condition. The Fenton reaction is widely used for $^{\bullet}OH$ radical formation took place by electron transfer between H_2O_2 and several

transition metals as catalysts (Luecking et al., 1998). The classical Fenton reaction is shown in Eq. 1.4 (Sun and Pignatello, 1993).

$$Fe^{2+} + H_2O_2 \rightarrow Fe^{3+} + {}^{\bullet}OH + OH^{-} \qquad k= 40\text{-}80\ M^{-1}s^{-1} \qquad (1.4)$$

In 1975, Cheves Walling established the real mechanism of the Fenton reaction and stated that in an acid medium, ${}^{\bullet}OH$ radical is produced as follows (Eq. 1.5):

$$Fe^{2+} + H_2O_2 + H^{+} \rightarrow Fe^{3+} + {}^{\bullet}OH + H_2O \qquad k=63\ M^{-1}s^{-1} \qquad (1.5)$$

In radical chemistry, there are three steps of a chain reaction for ${}^{\bullet}OH$ formation– initiation, propagation, and termination reactions. In an initiation reaction, a free radical is produced by a non-radical reactant (Eqs. 1.5 to 1.10). A radical product reacts with another reactant to produce different radicals (Eqs. 1.11 to 1.14) in the propagation step. In a termination reaction, no new radical is generated when a radical react with another radical/reactant (Eqs. 1.15 to 1.23). The original reaction is defined by Haber and Weiss for metal-catalyzed decomposition of H_2O_2 and, the generation of the radicals is illuminated by De Laat and Gallard (1999). Fe^{3+} generated can be reduced (Eqs. 1.6 and 1.19) with an excess H_2O_2 and more radicals are produced. They are known as Fenton like reactions. When the concentration of H_2O_2 is high, newly generated ${}^{\bullet}OH$ radicals react with H_2O_2; then the rate of the generation of ${}^{\bullet}OOH$, $O_2^{\bullet-}$ and HOO^{-} become significantly greater (Watts et al., 2005).

In an acidic medium (pH 2-4), the reaction of H_2O_2 with Fe^{3+} leads to the formation of a Fe(III)-hydroperoxy complex through reaction 1.7 (Evans et al., 1949). If both ${}^{\bullet}OH$ and Fe^{2+} ions are in excess, reaction 1.16 will terminate the chain reaction. H_2O_2 in excess acts as ${}^{\bullet}OH$ scavenger to form ${}^{\bullet}OOH$ (Eq. 1.11) which plays a vital role in the regeneration of Fe^{2+} (Eq. 1.19). Regeneration of Fe^{2+} can also happen as in Eq. 1.6, but at a slower rate. According to Burbano et al. (2008), the production of superoxide radical ($O_2^{\bullet-}$) through reaction 1.13, plays a significant role in the redox cycle of $Fe^{2+}$and Fe^{3+}. It is based on the reactions as in Eqs. 1.19 and 1.23.

At very high concentrations of H_2O_2, diperoxo complexes are formed (Eq. 1.24) (Jones et al., 1959). Gallard et al. (1999) also reported the formation of two complexes in H_2O_2 reaction with Fe^{3+}/ Fe^{2+} (Eqs. 1.7 and 1.24). The formation of these complexes occurs in the chain initiation reaction at pH<3.5 (De Laat and Gallard, 1999). They are decomposed as in Eqs. 1.8 and 1.25. Bray and Gorin (1932) discovered the active intermediate like ferryl ion $[Fe^{IV}O]^{2+}$ through reaction 1.26 (Ensing et al., 2003). These intermediates may react with organic compounds to cause mineralization.

Initiation reactions:

$H_2O_2 + Fe^{3+} \rightarrow Fe^{2+} + {}^{\bullet}OOH + H^+$ $k_2 = 8.4 \times 10^{-6}\ M^{-1}\ s^{-1}$ (1.6)

$H_2O_2 + Fe^{3+} \leftrightarrow Fe(OOH)^{2+} + H^+$ $ke_1 = 3.1 \times 10^{-3}\ M^{-1}s^{-1}$ (1.7)

$Fe(OOH)^{2+} \rightarrow Fe^{2+} + {}^{\bullet}OOH + H^+$ $k = 2.7 \times 10^{-3}\ M^{-1}s^{-1}$ (1.8)

$OH^- + Fe^{3+} \leftrightarrow Fe(OH)^{2+}$ (1.9)

$Fe(OH)^{2+} \rightarrow Fe^{2+} + {}^{\bullet}OH$ (1.10)

Propagation reactions:

$H_2O_2 + {}^{\bullet}OH \rightarrow H_2O + {}^{\bullet}OOH$ $k = 3.3 \times 10^{7}\ M^{-1}\ s^{-1}$ (1.11)

${}^{\bullet}OOH + HOO^- \leftrightarrow {}^{\bullet}OH + OH^- + O_2$ (1.12)

${}^{\bullet}OOH \rightarrow O_2^{\bullet-} + H^+$ $k = 1.58 \times 10^{5} s^{-1}$ (1.13)

$O_2^{\bullet-} + H^+ \rightarrow {}^{\bullet}OOH$ $k = 1 \times 10^{10}\ M^{-1}\ s^{-1}$ (1.14)

Termination reactions:

$H_2O_2 + {}^{\bullet}OOH \rightarrow H_2O + O_2$ (1.15)

${}^{\bullet}OH + Fe^{2+} \leftrightarrow Fe^{3+} + OH^-$ $k = 3.2 \times 10^{8}\ M^{-1}\ s^{-1}$ (1.16)

${}^{\bullet}OH + {}^{\bullet}OH \rightarrow H_2O_2$ $k = 5.2 \times 10^{9} M^{-1}\ s^{-1}$ (1.17)

${}^{\bullet}OH + {}^{\bullet}OOH \leftrightarrow H_2O + O_2$ $k = 0.71 \times 10^{10} M^{-1}\ s^{-1}$ (1.18)

${}^{\bullet}OOH + Fe^{3+} \rightarrow Fe^{2+} + H^+ + O_2$ $k = 2 \times 10^{3} M^{-1}\ s^{-1}$ (1.19)

${}^{\bullet}OOH + Fe^{2+} \leftrightarrow Fe^{3+} + HOO^-$ (1.20)

${}^{\bullet}OOH + {}^{\bullet}OOH \rightarrow H_2O_2 + O_2$ $k = 8.3 \times 10^{5} M^{-1}\ s^{-1}$ (1.21)

${}^{\bullet}OOH + O_2^{\bullet-} + H_2O \rightarrow H_2O_2 + O_2 + OH^-$ $k = 9.7 \times 10^{7} M^{-1}\ s^{-1}$ (1.22)

$O_2^{\bullet-} + Fe^{3+} + 2H^+ \rightarrow Fe^{2+} + O_2$ $k = 1.5 \times 10^{8}\ M^{-1}\ s^{-1}$ (1.23)

$FeOH^{2+} + H_2O_2 \leftrightarrow Fe(OH)(OOH^+) + H^+$ $ke_2 = 2 \times 10^{-4}$ (1.24)

$Fe(OH)(OOH)^+ \rightarrow Fe^{2+} + {}^{\bullet}OOH + OH^-$ (1.25)

$Fe^{2+} + H_2O_2 \leftrightarrow [Fe^{IV}O]^{2+} + H_2O$ (1.26)

Fenton's reagent is inexpensive and easily available. The process is carried out at room temperature and pressure. The energy input is not required to activate H_2O_2 and, it is easy to operate and maintain this process. There is no mass transfer limitation due to its homogeneous catalytic nature and, the reaction time is the shortest among all the AOPs (Gotvajn and Zagorc-Koncan, 2005). The drawback of Fenton reaction is that a low pH (3-4) is required to keep Fe(II)/Fe(III) in solution at the beginning of the operation. Further, a more amount of Fe(II) is required than it is regenerated. Therefore, both solution pH adjustment, and the storage and transportation of H_2O_2 increase the operational and maintenance costs. The iron sludge formed also needs to be cleared at the end of treatment which is expensive.

1.3.2 Photo-Fenton process (PFP)

The dark Fenton process photo-assisted by UV or visible light irradiation is known as Photo-Fenton process (PFP). Many studies use sunlight as the light source because of the high cost of generating the artificial UV light. UV irradiation is classified into three groups based on the wavelength termed as UVA (λ=315-400 nm), UVB (λ=285-315 nm), and UVC (λ<285 nm). UV light can accelerate the mineralization process by (i) photolysis of complexes of Fe^{3+} with some oxidation products (e.g., with oxalic acid) (Zuo and Holgne, 1992) and oxidation by-products formed in Fenton and Fenton-like processes and, (ii) enhancement of Fe^{2+} regeneration from additional photoreduction of Fe^{3+} species (Pignatello, 1992).

However, the degradation action of UV irradiation is complex and can be achieved via photolysis of $Fe(OH)^{2+}$ (Fe^{3+}-hydroxy complex) and complexes of Fe(III) with some oxidation by-products or Fe(III)-carboxylate species. A large amount of $Fe(OH)^{2+}$ produced by Fenton reaction is converted to Fe^{2+}(regeneration) and, $^{\bullet}OH$ is formed by photoreduction (Eqs. 1. 27 and 1.28). $Fe(OH)^{2+}$ absorbs radiation from 300 to 410 nm range. Khandelwal and Ameta (2013) proposed a tentative mechanism for photodegradation of Fast Green FCF dye in PFP (Figure 1.2). The aqueous solution of ferric ions on the exposure to light, dissociates water into a proton and $^{\bullet}OH$ radical (Eq. 1.28). $^{\bullet}OOH$ radicals are formed from the dissociation of H_2O_2 in the presence of light (Eq. 1.29).

$$Fe(OH)^{2+} + h\nu \rightarrow Fe^{2+} + {}^{\bullet}OH \quad (1.27)$$

$$Fe^{3+} + H_2O_2 + h\nu \rightarrow Fe^{2+} + {}^{\bullet}OH + H^{+} \quad (1.28)$$

$$Fe^{3+} + H_2O_2 + h\nu \rightarrow Fe^{2+} + {}^{\bullet}OOH + H^{+} \quad (1.29)$$

The efficiency of the PFP process can be improved by using organic acids-Fe(III) complexes with the additional $^{\bullet}OH$ radical formation by regenerating Fe^{2+}. Zuo and Holgne (1992) set up a common reaction (Eq. 1.30) for the decomposition of oxalic acids through Fe(III)-complexes such as$[Fe(C_2O_4)]^{+}$, $[Fe(C_2O_4)_2]^{-}$, and $[Fe(C_2O_4)_3]^{3-}$. Fe^{3+}-oxalate complex is more efficiently photodegraded under visible radiation (upto 500 nm) and, it has higher quantum yields than Fe^{3+}-hydroxy complexs. Hence, the photoreduction can take place at different wavelengths with different quantum yields.

$$2Fe(C_2O_4)^{(3-2n)} + h\nu \rightarrow 2Fe^{2+} + (2n-1)C_2O_4^{2-} + 2CO_2 \quad (1.30)$$

The main advantage of PFP is cyclic regeneration of consumed Fe^{2+} ions on illumination minimizing sludge generation and increases the degradation rate (Khandelwal and Ameta, 2013). The main drawbacks of PFP are the requirement of expensive UV light

and strong dependency on solution pH. Low pH generally shows high degradation efficiency with minimum sludge production (Andreozzi et al., 1999).

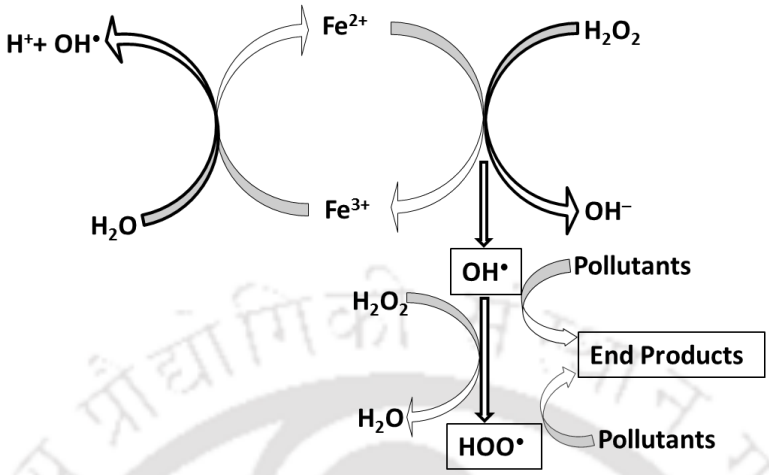

Figure 1.2: A schematic representation of photo-Fenton process for decomposition of contaminants (Khandelwal and Ameta, 2013).

1.3.3 Electro-Fenton process (EFP)

In an electro-Fenton process (EFP), H_2O_2 and Fe^{2+} are on-site generated electrochemically, either separately or concurrently. H_2O_2 is electro-generated by the reduction of dissolved oxygen (Eq. 1.31), and Fe^{2+} is regenerated by Fe^{3+} reduction (Eq. 1.3) or oxidation of a sacrificial iron-anode (Qiang et al., 2003). Sudoh et al. (1986) first developed an H-type EFP cell for the degradation of phenol with the H_2O_2 formation by the reduction of O_2 dissolved in an acidic solution (pH 3). The degradation rate of phenol in EFP is higher than that of in Fenton process.

EFP is operated using different types of two- and three-electrode arrangement in divided and undivided cells. The mechanism of EFP by the catalytic reaction (Eq. 1.4) is propagated by the catalytic action of the Fe^{2+}/Fe^{3+} system as shown in Figure 1.3. Fe^{2+} can be continuously regenerated by four related reactions: (i) reduction of Fe^{3+} with H_2O_2 directly at cathode surface (single electron transfer) (Eq. 1.3), (ii) via electro-generated H_2O_2 in bulk medium (Eq. 1.6), (iii) via hydroperoxyl radical reaction (Eq. 1.19), and (iv) via organic radical inter-mediates, $R^{\bullet}$, (Eq. 1.32).

$$O_2 + 2H^+ + 2e^- \rightarrow H_2O_2 \quad E^0 = 0.867\text{-}68.197 \text{ V vs. Ag/AgCl (acid solution)} \quad (1.31)$$

$$Fe^{3+} + R^{\bullet} \rightarrow Fe^{2+} + R^+ \quad (1.32)$$

H_2O is produced by the reduction of dissolved oxygen in a 4 electron pathway (Eq. 1.33) (Pozzo et al., 2005). The hydroxide ion is formed by the reduction of oxygen in an alkaline medium (Eq. 1.34).

$$O_2 + 4H^+ + 4e^- \rightarrow 2H_2O \qquad E^0=1.427 \text{ V vs. Ag/AgCl} \qquad (1.33)$$

$$O_2 + H_2O + 2e^- \rightarrow OH^- + HOO^- \qquad E^0=-0.065 \text{ V (alkaline solution)} \qquad (1.34)$$

Qiang et al. (2002) reported that two side reactions also occur simultaneously at the cathode: (i) reduction of H_2O_2 to H_2O due to the accumulation of H_2O_2 at the cathode-solution interface (Eq. 1.35), and (ii) H_2 gas evolution (Eq. 1.36). Besides, the electrochemical reduction of H_2O_2 at the electrode surface (Eq. 1.37) and in bulk solution take place (Eq. 1.38) (Gallegos et al., 2005). The oxidation of H_2O releases O_2 gas and protons at the anode (inert) surface (Eq. 1.39).

$$H_2O_2 + 2H^+ + 2e^- \rightarrow 2H_2O \qquad E^0=1.487 \text{ V vs. Ag/AgCl} \qquad (1.35)$$

$$2H^+ + 2e^- \rightarrow H_2 \qquad E^0=-0.195 \text{ V vs. Ag/AgCl} \qquad (1.36)$$

$$H_2O_2 + 2e^- \rightarrow 2OH^- \qquad (1.37)$$

$$2H_2O_2 \rightarrow O_2(g) + 2H_2O \qquad (1.38)$$

$$H_2O \rightarrow 1/2O_2 + 2H^+ + 2e^- \qquad (1.39)$$

In an undivided cell, H_2O_2 decomposition is more. H_2O_2 is oxidized to O_2 at the anode surface via intermediate hydro-peroxy radical (Eqs. 1.40 and 1.41) unlike in a divided cell (Brillas et al., 1995). Even, Fenton's reaction rate also may be dropped resulted from Fe^{2+} oxidation (Eq. 1.42) (Gallegos et al., 2005).

$$H_2O_2 \rightarrow H^+ + {}^{\bullet}OOH + e^- \qquad (1.40)$$

$${}^{\bullet}OOH \rightarrow H^+ + O_2\,(g) + e^- \qquad (1.41)$$

$$Fe^{2+} \rightarrow Fe^{3+} + e^- \qquad (1.42)$$

1.3.4 Photo electro-Fenton (PEP) process

Photo-electro-Fenton (PEF) (or electro-photo-Fenton) process comprises all the features of EFP and PFP. Light causes photolysis of $[Fe(OH)]^{2+}$ and additional ${}^{\bullet}OH$ radicals are generated as outlined before. Furthermore, UV light can induce photodegradation of some intermediates such as Fe(III)-carboxylate complexes as in Eq. 1.30 (Garcia-Segura and Brillas, 2011). Moreover, Fe^{2+} is also regenerated at the cathode surface (Eq. 1.3) enhancing gross ${}^{\bullet}OH$ radical production compared to individual EFP and PFP. The PEP process always exhibits a quicker degradation of contaminants. Table 1.3 corroborates the higher oxidation ability of PEF process compared to EFP for pharmaceuticals, dyes, and herbicides&

pesticides. A greater percentage of TOC reduction is always reported with PEF under comparable conditions.

The solar photo electro-Fenton (SPEF) process uses direct sunlight as a cheap and renewable energy source (Flox et al., 2007). UV radiation is supplied by sunlight and an additional absorption at $\lambda>400$ nm, e.g. for photolysis of Fe(III)-carboxylate complexes, could enhance the degradation rate in SPEF compared to PEF process.

Table 1.3: Time required for total disappearance (t_{TD}) of decontaminants, TOC removal, and MCE in EFP and PEF processes.

Pollutant(s)	Method-anode/cathode	Treatment condition	t_{TD} (min)	TOC removal (%)	MCE (%)	Source
Pharmaceuticals						
Clofibric acid (179 mg/L)	EF-Pt/GDE EF-BDD/GDE PEF-Pt/GDE PEF-BDD/GDE	Fe^{2+} 1 mM 300 mA 35°C 240 min	7 7 7 7	73 93 92 > 96	--	Sires et al., 2007a and 2007b
Chloroxylenol (100 mg/L)	EF-Pt/GDE EF-BDD/GDE PEF-Pt/GDE PEF-BDD/GDE	Fe^{2+} 1 mM 100 mA 35°C 360 min	20 20 20 20	58 82 91 98	--	Skoumal et al., 2008
Salicylic acid (164 mg/L)	EF-Pt/GDE EF-BDD/GDE PEF-Pt/GDE PEF-BDD/GDE	Fe^{2+} 0.5 mM 100 mA 35°C 180 min	30 30 30 30	57 73 97 96	--	Guinea et al., 2008
Ibuprofen (41 mg/L)	EF-Pt/GDE EF-BDD/GDE PEF-Pt/GDE PEF-BDD/GDE	Fe^{2+} 0.5 mM 100 mA 35°C 360 min	40 40 40 40	58 81 83 94	--	Skoumal et al., 2009
Herbide and Pesticides						
2,4-dichloro-phenoxyacetic acid	EF-Pt/GDE EF-BDD/gde PEF-Pt/GDE	Fe^{2+} 1 mM 100 mA 25°C 180 min	--	57 78 90	16 22 25	Brillas et al., 2000
4-chloro-phenoxyacetic acid (4-CPA) (100 mg/L)	EF-Pt/GDE EF-BDD/GDE PEF-Pt/GDE	Fe^{2+} 1 mM 100 mA 35°C 180 min	--	60 75 98	18 22 29	Boye et al., 2002
2-methyl-4-chlorophenoxyacetic acid (MCPA)	EF-Pt/GDE EF-BDD/GDE PEF-Pt/GDE	Fe^{2+} 1 mM 100 mA 35°C 180 min	--	65 76 91	20 24 29	Brillas et al., 2003
2,4,5-trichloro-phenoxyacetic acid	EF-Pt/GDE EF-BDD/GDE PEF-Pt/GDE	Fe^{2+} 1 mM 100 mA 35°C 180 min	--	53 80 99	14 21 26	Boye et al., 2003

BDD: Boron doped diamond, GDE: Gas diffusion electrode, TOC: Total organic carbon, MCE: Mineralization current efficiency

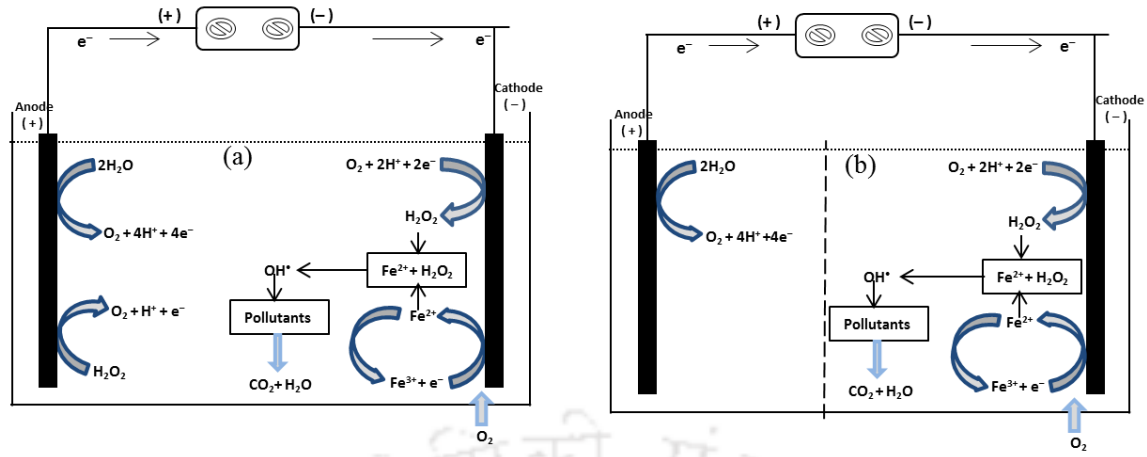

Figure 1.3: A schematic representation of major reactions takes place in EFP: (a) Undivided cell and (b) Divided cell.

1.4 Techniques for H_2O_2 determination and detection

In this section, the performance of different techniques conventionally used for the determination and detection of H_2O_2 is outlined.

1.4.1 Analytical methods (non-electrochemical)

The laboratory methods for the determination of H_2O_2 concentration mostly fall in four different categories: (i) titrametric, (ii) spectrophotometric, (iii) fluorescence and, (iv) chemiluminescence methods.

1.4.1.1 Titration method

In this method, a known concentration and volume of titrator such as $KMnO_4$ and KI is reacted with H_2O_2 to determine its concentration. Likewise, this method is termed either as the permanganate method or iodometric method for the determination of H_2O_2 concentration. The redox reaction takes place for the permanganate method is shown in Eq. 1.43. This method is used for the determination of high H_2O_2 concentration between 0.25 and 70% w/w (Brandhuber and Korshin, 2009).

$$2MnO_4^- (aq) + H_2O_2 (aq) + 4H^+ (aq) \rightarrow 7/2O_2 (g) + 2Mn^+ (aq) + 3H_2O (l) \quad (1.43)$$

In the iodometric method, H_2O_2 is reacted with iodide present in excess in the presence of ammonium molybdate catalyst forming Iodine (I_2) (Eq. 1.44) which is subsequently titrated with a standard thiosulfate solution (Eq. 1.45).

The solution turns pale yellow when iodide reacts with H_2O_2 in an acid medium. The addition of few drops of starch as an indicator changes deep blue colour to a colourless solution at the end of titration. In 1880, Kingzett first developed this method (also known as

Kingzett's method). Like permanganate, this method is also applicable for a high H_2O_2 concentration (0.1 to 6 % w/w) (Brandhuber and Korshin, 2009).

$$H_2O_2 + 2KI + H_2SO_4 \leftrightarrow I_2 + K_2SO_4 + 2H_2O \quad (1.44)$$

$$I_2 + 2Na_2S_2O_3 \leftrightarrow Na_2S_4O_6 + 2NaI \quad (1.45)$$

1.4.1.2 Spectrophotometric method

This method generally gives a rapid response for H_2O_2 determination than the titration method. The spectrophotometric method is commonly used being straightforward and a full spectrum could detect the presence of potential sample contaminants. A low concentration of H_2O_2 can be analysed in an aqueous solution through the change in solution colour by reacting with several compounds such as ammonium metavanadate, pyridine-2,6-dicarboxylic acid and vanadate(V), Eriochrome black T in the presence of peroxidase, and titanic sulphate ($Ti(SO_4)_2$). Ammonium metavanadate in an acidic medium forms a red-orange peroxovanadium cation (λ_{max}=450 nm) and H_2O_2 concentration can be determined as low as 143 µM (Nogueira et al., 2005). Zhu et al. (1997) used Eriochrome black T catalysed by peroxidase for H_2O_2 determination. A colour complex is formed by the reaction between H_2O_2 and Eriochrome black T in the presence of Horseradish peroxidase (HRP) and, the maximum absorption was recorded at 615 nm with a linear range from 0.2 to 10 µM (Zhu et al., 1997). Tanner and Wong (1998) Pyridine-2,6-dicarboxylic acid and vanadate (V) in an acidic solution develops a stable orange–red chelate complex, oxo-peroxo-pyridine-2,6-dicarboxylato-vanadate by reacting with H_2O_2. The maximum optical absorption is found at 432 nm. In the case of titanic sulphate method, a yellow colour complex of Ti^{4+} (λ_{max}=400 nm) is formed with the reaction between $Ti(SO_4)_2$ and H_2O_2. But, this method doesn't give accurate results at a lower H_2O_2 concentration with a higher optical path length and, the absorption properties of the sample may be changed with temperature and pH variation (Amin and Olson, 1966).

1.4.1.3 Fluorescence method

In this technique, several fluorescent substrates such as 3-(p-hydroxyphenyl)propionic acid (HPPA) (Sakuragawa et al., 1998), coumarin compounds (Corbett, 1989; Abbas et al., 2010), and HRP (Mohanty et al., 1997) are used for the fluorometric determination of H_2O_2. Corbett (1989) used the fluorescent substrate like scopoletin (7-hydroxy-6-methoxy-2H-1-benzopyran-2-one) to determine H_2O_2 and achieves a limit of quantification of 0.15 nM of H_2O_2. Later, Mohanty et al. (1997) found that N-acetyl-3,7-dihydroxyphenoxazine (A6550) has several advantages over scopoletin as a substrate for the detection of H_2O_2 including, a

10-fold higher sensitivity, better temperature stability, and overall greater stability of the fluorescent product. Sakuragawa et al. (1998) used HRP immobilized on the chitosan carrier for the fluorometric determination of H_2O_2 using HPPA as a fluorescent substrate. They achieve the determination limit of 50 ng/cm^3 with a linear range of 50 to 1000 ng/cm^3. In 2010, Abbas and his research group developed a fluorometric method for the determination of low H_2O_2 concentration present in milk. Fenton's reaction oxidizes non-fluorescent coumarin to highly fluorescent 7-hydroxycoumarin leading to a highly sensitive fluorometric signal. A linear range of H_2O_2 determination is reported from 0.02 to 20 µM with a detection limit as low as 0.005 µM (Abbas et al., 2010).

1.4.1.4 Chemiluminescence method

In the past decade, chemiluminescence sensors are widely studied for H_2O_2 detection. Generally, these types of sensors are fabricated based on the reaction between luminol and H_2O_2 which is catalysed by an enzyme i.e., HRP and haemoglobin. In fact, lucigenin, esters of acridinium and oxalate also can be used instead of luminol. Luminol(5-amino-2, 3-hyhidro-1, 4-phathlazinedione ($C_8H_7N_3O_2$) is a chemical phosphor that produces chemiluminescence (emit a blue glow that can be seen in a darkened room) when mixed with an appropriate oxidizing agent like H_2O_2 in the presence of a catalyst. Diaz et al. (1998) obtained a detection limit of H_2O_2 of 0.11 mM using 0.15 mM luminol and HRP. However, this method is complex and requires an expensive and advanced instrumentation (Brandhuber and Korshin, 2009). Li et al. (2001) reported a detection limit of 0.13 µM using haemoglobin. Kiba et al. (2003) observed a rapid H_2O_2 determination catalysed by HRP in a micro-machined flow cell.

1.4.2 Electrochemical methods

H_2O_2 is an electrochemically active species. The electrochemical methods can overcome many of the drawbacks laid by the previous methods for the determination of H_2O_2. Electrochemical techniques own advantages of easy preparation, fast detection, low consumption, and high selectivity and sensitivity (Liu et al., 2011a). The direct electrochemical reduction or oxidation of H_2O_2 at ordinary solid electrodes is a slow process and requires a large overpotential. An efficient approach is to overcome this problem to modify the bare electrode with suitable electro-catalysts to decrease high overpotential of H_2O_2 detection (Wang et al., 2015). A brief outline on enzymatic and non-enzymatic electrochemical H_2O_2 sensing is given in the following sub-sections.

1.4.2.1 Enzymatic electrochemical sensor

For the decrease of reaction potential and faster electron transfer kinetics, the enzyme-based electrochemical sensors are employed. Horseradish peroxidase (Wen et al., 2011), cytochrome C (Luo et al., 2009), haemoglobin (Chen et al., 2007), and myoglobin (Yang et al., 2006) are tested extensively for the fabrication of electrochemical biosensor for H_2O_2 detection owing to high sensitivity and selectivity even in the presence of interfering components. However, the enzyme based electrodes, suffer from instability, high enzyme cost, and complex immobilization technique. The enzyme activity is also significantly dependent on temperature, media pH, and toxic chemicals (Ensafi et al., 2013).

1.4.2.2 Non-enzymatic electrochemical sensor

In order to solve the problems related to H_2O_2 detection by enzymatic electrochemical methods, considerable attention has been paid to develop non-enzymatic electrodes mediated with noble metals, metal alloys, and metal NPs as the electro-catalysts. Some of them are described below.

Prussian blue (ferric hexacyanoferrate): Prussian blue catalyzes H_2O_2 reduction at low potential. Prussian blue exhibits polycrystal like structure which allows passage of the small molecules through its lattice while bigger molecules are restricted. It is electrochemically coated on the working electrode surface followed by layering with enzymes, stabilizers or selectivity improvers, etc. The disadvantage behind using Prussian blue in H_2O_2 sensing is its instability in the neutral and alkaline medium (Karyakin et al., 2001; Ricci and Palleschi, 2005).

Metal hexacyanoferrate: Metal hexacyanoferrates include copper, nickel, cobalt, chromium, vanadium, ruthenium, and manganese hexacyanoferrates. They are comparatively similar or having lower capability for H_2O_2 reduction compared to Prussian blue. But, metal hexacyanoferrates possess more electrochemical stability over a wide range of pH. It shows good electrocatalytic activity in the electrolytes media containing alkali metal cations such as lithium, rubidium, sodium or cesium. However, Prussian blue performs well only in the solution containing K^+ (Garjonyte and Malinauskas, 1998; Ferreira et al., 2004).

Metals: Metal catalysts such as palladium (Pd), rhodium (Rh), iridium (Ir), ferrum (Fe), platinum (Pt), and the substrates made up of carbon based nanomaterials such as ordered mesoporous carbon or carbon nanotubes are also used because of their high electrochemical activity, high conductivity, and high surface area (Chandra et al., 2009; Hrapovic et al., 2004; Wang et al., 2015).

Bimetals: Recently, bimetallic nanoparticles as the electrocatalysts in H_2O_2 sensing are in great demand. The introduction of another metal brings changes in particle size, shape, surface morphology, chemical, and physical properties. In comparison to mono-metal catalysts, bimetal catalysts exhibit greater electrocatalytic activity, selectivity, and greater deactivation resistance (Wang et al., 2011a; Xu et al., 2011; Rajkumar et al., 2011; Liu et al., 2011a).

Metal oxides: Transition metal oxides such as cobalt oxide, nickel oxide, titanium dioxide, manganese oxide, copper oxide, etc. have shown good electrocatalytic activity towards the detection of H_2O_2. Most of them require high overpotential for the electrocatalytic oxidation of H_2O_2. This is the major disadvantage behind the use of metal oxides as the electro-catalysts in H_2O_2 sensing (Jiang et al., 2009).

1.5 Current status of EFP involving H_2O_2 generation

It is seen that EFP is a promising technique for the in-situ generation of H_2O_2 which leads to the formation of $^{\bullet}OH$ radicals. AO processes generate $^{\bullet}OH$ directly on the anode surface. The coupled processes may enhance the gross rate of $^{\bullet}OH$ radicals formation.

1.5.1 EFP parameters affecting H_2O_2 formation

The generation rate of H_2O_2 is influenced significantly by a number of parameters such as solution pH, temperature, supporting electrolyte, applied potential, inter electrode distance, and O_2 sparging rate. The primary focus of H_2O_2 generation studies is its implication for the wastewater treatment in the presence of iron catalyst.

1.5.1.1 Effect of pH

The optimal value of pH ranges commonly between 2 and 4. At pH< 2, Fe^{2+} concentration is more in solution. Fe^{2+} cannot discompose H_2O_2 to $^{\bullet}OH$ as H_2O_2 is converted into an electrophilic $H_3O_2^+$ (oxonium ion) (Eq. 1.46) (Zhou et al., 2007) by capturing one proton with the formation of stable complexes leading to deactivation of catalysts. At 2<pH<3, the Fenton process is usually more effective due to Fe^{2+} regeneration (Eq. 1.6) thorough reaction between Fe^{3+} and H_2O_2 (Pignatello, 1992). H_2 is evaluated at low pH reducing the number of active sites for H_2O_2 generation (Eq. 1.35) (Wang et al., 2010). H_2O_2 is rapidly decomposed to O_2 and water at higher pH because H_2O_2 is unstable in a basic medium (Chapter 3). Some workers have investigated the effect of inorganic acids which are used for pH adjustment. H_2SO_4, $HClO_4$, and HCl are commonly employed for this purpose. Diagne et al. (2007) observed that TOC removal is accelerated in perchloric acid media than

in H_2SO_4 media. Fe^{2+} forms complexes, with H_2O_2 and SO_4^{2-} at low pH (< 3) but perchlorate does not form complexes with Fe(III).

$$H_2O_2 + H^+ \rightarrow 2H_3O_2^+ \quad (1.46)$$

1.5.1.2 Cathodic potential (E_{cat}) and current density

Two important factors i.e., electrode potential and current density are directly associated with the formation of H_2O_2 and regeneration of Fe^{2+} ions. Higher current density increases the amount of H_2O_2 production which in turn is converted to $^{\bullet}OH$ radicals in the electrolyte medium. E_{cat} value is usually selected to get the highest H_2O_2 production rate before H_2 evolution (Eq. 1.47) depending upon the cathode material. Also, the higher electro-regeneration of Fe^{2+} (Eq. 1. 31) with increasing current enhances the efficiency of Fenton chain reactions (Zhang et al., 2007).

But at a higher current density, the discharge of O_2 at the anode (Eq. 1.48) and evolution of H_2 at the cathode (Eq. 1.47) occur, leading to inhibition of main reactions (Eqs. 1.32 and 1.49) (Zhang et al., 2007). $^{\bullet}OH$ radicals also can be formed at a higher O_2 overpotential (Eq. 1.49).

$$2H_2O + 2e^- \rightarrow H_{2(g)} + 2OH^- \qquad E^0 = -1.027 \text{ V vs. Ag/AgCl} \quad (1.47)$$

$$2H_2O \rightarrow 4H^+ + O_2 + 4e^- \quad (1.48)$$

$$H_2O \rightarrow {}^{\bullet}OH + H^+ + e^- \quad (1.49)$$

El-Desokya et al. (2010) reported that azo-dyes degradation is much faster at E_{cat} = −1.0 V vs. SCE than −0.5 V. More negative applied potentials than −1.2 V vs. SCE commence the side reaction of H_2 evolution. Similarly, the degradation rate of picloram increases with the rise of applied current from 30 to 300 mA. The $4e^-$ reduction of O_2 leading to the formation of H_2O (Eq. 1.33) begins to compete with the formation of H_2O_2 (Eq. 1.32) at higher current (> 300 mA) (Ozcan et al., 2008a).

1.5.1.3 Electrode spacing

The spacing between two electrodes in an electrolytic cell displays a slight effect on H_2O_2 electro-generation. To avoid the short-circuiting between anode and cathode, the appropriate electrodes distance is required. The decrease in spacing between the electrodes leads to a lower ohmic drop. So, there is an equivalent decrease of cell voltage and energy consumption (Fockedey and Lierde, 2002).

1.5.1.4 Electrode materials

The common cathode materials used for H_2O_2 generation are active carbon fibre (Wang et al., 2005), carbon felt (Oturan, 2000), graphite felt (Do and Chen, 1994), carbon polytetrafluoroethylene (C-PTFE) gas diffusion electrode (GDEs) (Brillas et al., 1998), reticulated vitreous carbon (De Leon and Pletcher, 1995), mercury pool (Oturan et al., 1999; Oturan and Pinson, 1995), and carbon sponge (Ozcan et al., 2008b). The anode materials include graphite, Pt (Pozzo et al., 2005), metal oxides such as PbO_2 (Kaba et al., 1990), doped SnO_2 (Stucki et al., 1991), boron-doped diamond (BDD), RuO_2/Ti mesh, and Ti rod coated IrO_2/RuO_2. Pt is commonly used due to its excellent conductivity and chemical stability at high overpotential in a corrosive media (Panizza and Cerisola, 2009) but it is extremely costly.

The cell current efficiency of H_2O_2 generation and the mineralization efficiency are significantly varied with the type of electrode materials. In a divided cell, a cation permeable membrane is placed between the cathodic and anodic electrodes to prevent H_2O_2 oxidation on the anode surface. EFP with Pt anode is not potent enough to mineralize the pollutants due to the formation of stable complexes of Fe^{3+} with the by-products such as carboxylic acids. Indeed, BDD anode is extensively applied in wastewater treatment because of surface inertness with low adsorption properties, remarkable corrosion stability and much higher O_2 overpotential than that of conventional anodes (Cheng-Chun and Jia-Fa, 2007). The combination of BDD anode and GDE cathode is much more powerful to mineralize the pollutants completely.

1.5.1.5 Oxygen sparging rate

The continuous sparging of O_2 is required for H_2O_2 generation to enhance the current efficiency. An increase in O_2 sparging rate increases the dissolved O_2 concentration and the mass transfer rate of dissolved O_2, leading to an improvement of H_2O_2 production. Wang et al. (2008) showed that the color removal efficiency remains constant at a current density of 68 A/m^2 even when the O_2 sparging rate increases from 0.3 to 0.4 L/min. The color removal begins to be controlled by the kinetics of H_2O_2 production at an O_2 sparging rate > 0.3 L/min.

1.5.1.6 Reaction temperature

H_2O_2 electro-generation and degradation studies are generally performed at room temperature. The optimal temperature is around 35-40°C to avoid H_2O_2 decomposition (Eq. 1.50) (Brillas et al., 2009).

$$2H_2O_2 \rightarrow O_2\,(g) + 2H_2O \qquad (1.50)$$

The increasing temperature decreases O_2 solubility in water. So, H_2O_2 formation decreases. The solubility of H_2O_2 is also low at a higher temperature (Ozcan et al., 2008b; Wang et al., 2010). In contrast, an increase in temperature can enhance the mineralization efficiency.

1.5.1.7 Supporting electrolyte concentration

Higher electrolyte concentration reaction gives a solution conductivity and accelerates the electron transfer rate. Sodium sulphate, sodium perchlorate, sodium chloride, sodium nitrate, and potassium chloride are generally used as the supporting electrolytes. Ghoneim et al. (2011) observed that the decolorization rate of azo dye is faster in SO_4^{2-} solution than in Cl^- solution at the same concentration. Almost 100 % removal of azo dye occurs in 120, 180, and 180 min in Na_2SO_4, NaCl, and KCl solutions, respectively. Daneshvar et al. (2008) reported that the removal efficiency of Orange II in different electrolyte media (0.05 M) follows the order as $ClO_4^{2-} > Cl^- > SO_4^{2-}$. The increase in $NaClO_4$ concentration from 0.05 to 0.1 M does not have any effect on Orange II degradation. Diagne et al. (2007) achieved a faster Methyl parathion degradation in the presence of NO_3^- than that of SO_4^{2-}. A higher Na_2SO_4 concentration leads to higher current density, which is resulted in faster and higher production of H_2O_2 (Zhou et al., 2007).

1.5.1.8 Current efficiency of H_2O_2 generation

Current efficiency (CE_f) is the ratio of electricity consumed by an electrode reaction of interest to total electricity passed through the circuit given by Eq. 1.51.

$$CE_f = \frac{nFC_{H_2O_2}V}{\int_0^t Idt} \times 100 \qquad (1.51)$$

Where, n is the stoichiometric number of electrons transferred, F is Faraday's constant (96487 C/mol), V is the catholyte volume (L), C_{H2O2} is H_2O_2 concentration (M), I is the applied current (A), and η represents the overall current efficiency over a certain period of electrolysis, t (s).

Qiang et al. (2002) obtained about 81% current efficiency at the limiting current density of 6.4 A/m^2 with an optimal condition as E_{cat} = – 0.5 V vs. SCE, pH 2, and O_2 flow rate of 8.2 $\times 10^{-2}$ mol/min. The limiting current density is independent on the cathode geometry and surface area. The current density decreases to 2.1 A/m^2 with a current efficiency of 90% when the air is purged instead of pure O_2. The supporting electrolyte doesn't affect the net generation rate of H_2O_2.

1.5.2 EFP generating H_2O_2 for effluent treatment

The performance of EFP generating H_2O_2 for the decomposition of pharmaceutical compounds is outlined in this section. Some relevant published articles are reviewed and, the focus was on the treatment of pharmaceutically active compounds (PhACs) effluents being the emerging contaminants of the 21st centuries. The key results are provided in the tabular form for H_2O_2 generation and its application for effluent treatment.

The variation of CE_f of H_2O_2 formation using different cathode materials is summarized in Table 1.4. Important studies on EFP for the decomposition of PhACs from aqueous effluent are also summarized in Table 1.5.

Table 1.4: Current efficiency (CE_f) of generation of H_2O_2 in a divided cell.

Anode/ cathode/membrane	Electrolysis conditions	CE_f (%)	Important findings	Source
Pt wire/ graphite plate	Fe^{2+} 0.5 mM 0.5 mA/cm^2 Na_2SO_4 0.5 M O_2 300 mL/min pH 11 & 25°C	93.5	○ Decreasing I_{CD} from 1.25 to 0.5 mA/cm^2 sharply increase CE_f of H_2O_2 from 20 to 77.3 % ○ I_{CD} of oxygen reduction increases when the E_{cat} is more negative than –0.2 V	Do and Chen, 1993
Pt gauze/ RVC/ Nafion 417	E_{cat} –0.55 V Fe^{2+} 0.5 mM Cell current 95 mA NaOH 0.00001 M pH 3 & Room temp	94	○ CE_f dropped to 57 % at -1.4 V and to very low values with more hydrogen evolution	De Leon and Pletcher, 1995
Pt sheet/ PTFE GDE/ Cationic	Fe^{2+} 1.0 mM, Seawater(catholyte) $NaClO_4$ 0.01 M (anolyte) pH 3	80 in 15 min, 50 in 120 min	○ H_2O_2 formation at different solution pH of 2.8, 2.6, and 2 with electrolysis time at cell current of 100, 300, and 450 mA ○ Higher CE_f achieves without Fe^{2+}, its value falls from 80 % in 15 min to 50 % in 2 h	Brillas et al., 2000
Pt /PTFE GDE and Pt/graphite / Cationic	Fe^{2+} 0.17 mM Na_2SO_4 0.04M (catholyte) $NaClO_4$ 0.01 M (anolyte) O_2 130 mL/min pH 3 & Room temp	85 in both cathode	○ Higher CE_f in GDE cathode compared to graphite cathode ○ Higher H_2O_2 production in O_2 flow than in air flow for both the cathodes	Pozzo et al., 2005
Dimensionally stable anode/ PTFE GDE	E_{cat} –1.7 to –2.0 V Cell current 3 A Na_2SO_4 0.05 mM O_2 333.3 mL/min pH 3 25-60°C	98	○ CE_f reduction at high temperature (60°C) and current density especially in alkaline solutions ○ Higher CE_f in preparative electrolysis in membrane reactor in comparison to an undivided cell ○ Higher CE_f in reactor separated with proton-exchange membrane than that with cation-exchange membranes	Aglardze et al., 2007
Pt/ PTFE GDE/ Cationic	Fe^{2+} 1.0 mM E_{cat} –0.85 V Na_2SO_4 0.05M O_2 20 mL/min pH 3 25°C	70	○ Higher CE_f and H_2O_2 production in the divided cell than those in the undivided cell ○ Best performance obtained at –0.9 V with further increase in E_{cat}, the production efficiency drops notably due to side reactions	Pozzo et al., 2008

RVC: Reticulated vitreous carbon, E_{cat} (V vs Ag/AgCl): Cathode potential, I_{CD}: Current density, PTFE: Polytetrafluoroethylene, GDE: Gas diffusion electrode

Table 1.5: Operational condition of EFP in divided and undivided cells.

Pollutant(s)	Anode/cathode/membrane; Treatment condition	Important findings	Source
Clofibric acid (Drug 179 mg/L and TOC 100 mg/L)	Pt /PTFE GDE 33, 100 and 150 mA/cm^2 UVA (300-400 nm) Fe^{2+}1.0 mM Na_2SO_4 0.05 M H_2O_2 pH 3 35°C	○ Faster drug decay with rising current density and falls at higher metabolite concentration ○ Degradation rate falls with pH as: pH 2> pH and 4>>pH 6 ○ Follows pseudo-1st order kinetic with a similar rate constant in EFP and PEF	Sires et al., 2007a
Sulfamethoxazole (50-300 mg/L)	RuO_2/Ti/ACF Cell current 120-500 mA UV365 nm Fe^{2+} upto 0.2 mM Na_2SO_4 0.05M pH 3	○ Decay rate increases with electrolysis time as: AO<AO-H_2O_2<AO-H_2O_2-UVA< EF< PEF ○ TOC reduction upto 80 % in 6 h of electrolysis at 0.360 mA under PEF process	Wang et al., 2011b
Sulfamethazine (0.72 mg/L)	Pt/C-felt Cell current 50-600 mA Fe^{2+} 0.1 mM Na_2SO_4 0.05M O_2 450 mL/min pH 3 18-45°C	○ About 37.3 % degradation without Fe^{2+} and 56.9 % degradation with Fe^{2+} in first 10 min ○ Degradation efficiency raises to 99.1 % with Fe^{2+} in 40 min at 500 mA and 18°C ○ Degradation follows pseudo 1st -order kinetic	Mansour et al., 2012
17β-estradiol (5 mg/L)	Pt/C-felt Cell current 200 mA Fe^{2+} 0.1-1.0 mM Na_2SO_4 0.05 M pH 3	○ Faster disappearance in presence of acetonitrile-water mixture ○ Complete disappearance in 30 min in presence of Fe^{2+}, Cu^{2+}, and Co^{2+}in 50 min ○ Higher degradation rate at 0.2 mM Fe^{2+} but decreases at > 0.2 mM Fe^{2+}	Naimi and Bellakhal, 2012
Acetaminophen (0.033 mg/L)	Ti-IrO_2 or RuO_2/Stainless steel Fe^{3+} 0.01-01 mM H_2O_2 5-25 mM pH 2-4 15°C	○ Box–Behnken design results confirm that $Fe^{2+}$and H_2O_2 concentrations positively affect drug removal efficiencies in Fenton and EFP ○ At a high H_2O_2 to Fe^{2+} molar ratio (1500), degradation efficiency in EFP is higher than Fenton process at pH 2 ○ Degradation efficiency increases from 12 to 84 % in Fenton at pH 2 and 20 to 94 % in EFP at pH 4	Su et al., 2012
Paracetamol, Salicylic acid (1 mg/L)	BDD/GDE(EF) or BDD/Pt (electro-oxidation) 10 and 50 mA/cm^2 Fe^{3+} 0.15 mM Na_2SO_4 0.05 M O_2 300 mL/min pH 3	○ Electro-oxidation shows rapid drugs decay in real water matrix than ultrapure water ○ Higher drugs decay in EFP using real water matrix ○ Complete disappearance in about 5 min increase in current density from10 to 50 mA/cm^2	Sires et al., 2013

TOC: Total organic carbon, PTFE: Polytetrafluoroethylene, GDE: Gas diffusion electrode, ACF: Activated carbon fiber, BDD: Boron doped diamond

1.5.3 H_2O_2 generation in EFP and anodic oxidation (AO)

1.5.3.1 Direct $^{\bullet}OH$ radical generation in AO

There are two basic approaches for the electrochemical degradation of organic matters: (i) direct AO where the pollutants are adsorbed on the surface of the electrode and (ii) indirect oxidation in the bulk liquid mediated by electrochemically generated H_2O_2 as in EFP.

The most popular direct electrochemical method is the AO with low a concentration of organic pollutants (Flox et al., 2006). Generally, AO is carried out either in an anodic compartment of a divided cell or in an undivided cell (Figure 1.4). Most of the researchers use classical anode electrodes such as Pt (Arapoglu et al., 2003), doped SnO_2 (Stucki et al., 1991), doped and undoped PbO_2 (Zhou et al., 2005), IrO_2 (Martinez-Huitle et al., 2004), RuO_2 (Mohan et al., 2007), and BDD (Panizza and Cerisola, 2005) with a high O_2 overpotential. Pt electrodes are much more stable than SnO_2 or PbO_2 with an extremely low current efficiency for $^{\bullet}OH_{ad}$ production (Kraft et al., 2003). Organic contaminants are destroyed by the adsorbed $^{\bullet}OH$ radical formed as an intermediate from water oxidation to O_2 at the anode surface (Eq. 1.52) (Panizza and Cerisola, 2005).

$$M + H_2O \rightarrow M(^{\bullet}OH) + H^+ + e^- \quad (1.52)$$

$M(^{\bullet}OH)$ denotes the adsorbed hydroxyl radical at the metal anode, M. The electrodes comprise of the active and inactive sites (Canizares et al., 2002). The electrode surface does not change and acts only as a sink of electrons in inactive electrodes like fully oxidized metal oxides (PbO_2 or SnO_2) and BDD whose surface does not take part in the oxidation process (Lv et al., 2013). There are electrode materials where adsorbed $^{\bullet}OH$ radicals transform into the electrode surface and react with M forming higher oxide, MO (Eq. 1.53). MO reacts with organic pollutants and reduces back to the original state, M (Eq. 1.54). Such electrodes are known as active electrodes (Pt, IrO_2, stainless steel, RuO_2, etc.). In the case of the inactive electrode, the adsorbed $^{\bullet}OH$ radical does not react with active site (M). They directly oxidize the organic pollutants to CO_2 (Eq. 1.55) (Lv et al., 2013).

High O_2 overpotential is required for the O_2 evolution. Mainly molecular O_2 is produced during water electrolysis if O_2 overpotential is not high enough (Brillas et al., 2007). Therefore, high oxidation power anodes are required to minimize the extent of the O_2 evolution (Eq. 1.56). The O_2 evolution also may occur as in Eq. 1.57 (Lv et al., 2013).

$$M(^{\bullet}OH) + M \rightarrow MO + H^+ + e^- \quad (1.53)$$

$$MO + R \rightarrow M + RO \quad (1.54)$$

$$M(^{\bullet}OH) + R \rightarrow M + CO_2 + H_2O \quad (1.55)$$

$$2M(^{\bullet}OH) \rightarrow 2M + O_2(g) + 2H^+ + 2e^- \quad (1.56)$$

$$2MO \rightarrow 2M + O_2 \quad (1.57)$$

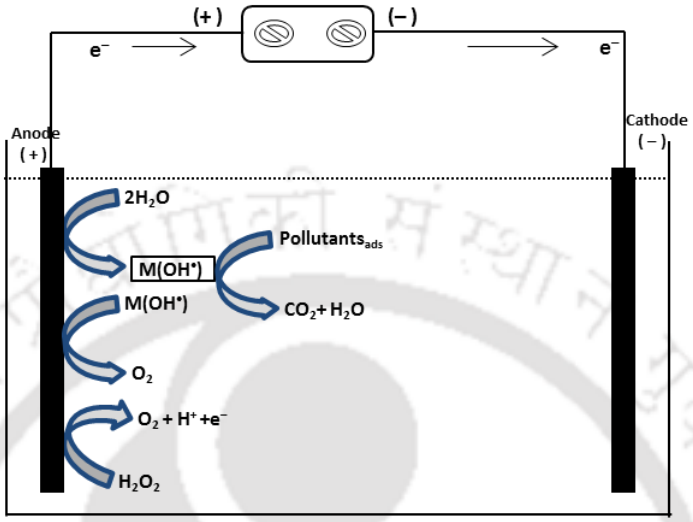

Figure 1.4: Schematic representation of anodic oxidation in an undivided cell.

1.5.3.2 AO for effluent treatment

In 2009, Zhao et al. reported that the direct AO of 30 mg/L diclofenac at BDD anode shows about 72 % mineralization in 4 h with an anodic bias potential (BP) of 4 V. The effects of applied BP and addition of NaCl on diclofenac degradation are investigated. The degradation rate and specific charge composition increase with increasing applied BP. Higher BP accelerates the O_2 evolution reaction. No remarkable degradation is achieved at < 1.2 V, for which H_2O electrolysis nearly does not take place. The addition of NaCl decreases the TOC removal rate. The toxicity of the initial diclofenac solution and samples collected at different reaction time is evaluated by monitoring the changes in the natural emission of luminescent bacteria, *Vibrio fischeri*. Bacterial inhibition increases with the increase in toxic intermediates.

Ciriaco et al. (2009) investigated on ibuprofen degradation. They achieved 60-95% COD and 48-92% TOC removals in 6 h with a higher removal using BDD anode compared to Ti/Pt/PbO_2 at different current densities in a batch cell. The cell CE_f current efficiency and mineralization current efficiency (MCE) for both the electrodes give a similar performance with 20 mA/cm^2. The combustion efficiency is found to be slightly higher with BDD at a lower current density and equal to almost 100 % for both the anodes at 30 mA/cm^2.

Brillas et al. (2010) showed that AO without pH regulation in an undivided cell for diclofenac decomposition with Pt anode acidifies the solution with precipitation of its protonated form. On the contrary, BDD creates the alkaline solution and only attains partial mineralization. A buffer solution of pH 6.5 with at lower diclofenac concentration can be thoroughly decontaminated at BDD electrode. The increase in cell current with BDD accelerates the degradative process but decreases its efficiency.

Murugananthana et al. (2010) revealed the influence of applied current density and nature of supporting electrolytes on AO of ketoprofen at BDD and Pt electrodes. A better degradation occurs in the presence of SO_4^{2-} within 4 h both at BDD and Pt anodes than the NaCl electrolyte due to the formation of active chlorine at the anode surface. Active chlorine evolution is considerably restricted at BDD anode as it exhibits a "non-active" behaviour. Whereas at Pt anode, Cl^- based oxidants are predominantly formed by direct oxidation of Cl^- due to its electrocatalytic activity towards Cl_2 evolution. But, a poor mineralization is achieved in SO_4^{2-} media with Pt compared to BDD.

Wang et al. (2011a) demonstrated that PEF process gives a better performance for the mineralization of sulfamethoxazole in an acidic aqueous solution (pH 3) compared to AO using RuO_2/Ti electrode, AO-E H_2O_2, and AO- H_2O_2-UVA. PEF treatment at a low applied current of 360 mA yields a faster decontamination with 80 % TOC removal in 6 h of electrolysis. About 36, 28, and 25 % TOC removal is achieved in AO-H_2O_2-UVA, AO-E H_2O_2, and AO processes.

Wirzal et al. (2013) used two mixed metal oxide (MMO) titanium based electrodes in three different compositions. Ru-Ir-TiO_2 (20:30:50)-10 micron shows the highest degradation of ampicillin at pH 4. Total degradation is achieved in 15 min of electrolysis time for penicillin G at pH 10. For Ru-Ir-TiO_2 (40:10:50)-10 micron, similar results are obtained, i.e., pH 4 is found to be the best for ampicillin decomposition and pH 12 for penicillin G.

Yahiaoui et al. (2013) worked on tetracycline hydrochloride decomposition on Pb/PbO_2 electrode and coupled anodic oxidation-activated sludge process. The rise in current density and temperature increase the degradation efficiency. But, an increase in the initial drug concentration deteriorates its degradation efficiency. The operating parameters are then optimized through a central composite design. The BOD_5/COD ratio increases substantially from 0.028 initially to 0.41 in 5 h of electrochemical pre-treatment. The biological treatment is then performed aerobically in a mineral medium using 0.5 g/ L of activated sludge for 30 days, leading to an overall decrease of 76 % of dissolved organic carbon (DOC).

1.5.3.3 Synergy in H_2O_2 and $^{\bullet}OH_{ad}$ generation in effluent treatment

Brillas et al. (2000) used EFP and PEF methods in an undivided cell containing a Pt anode and a C-PTFE-O_2-fed cathode. H_2O_2 is electro-generated (Eq. 1.32). EFP is performed with Fe^{2+} addition to the solution. Pollutants are mainly destroyed by the combined action of $^{\bullet}OH$ radicals formed at the anode (Eq. 1.52) and $^{\bullet}OH$ radicals formed in the bulk mediated by H_2O_2 (Eq. 1.5). In PEF process, the solution is irradiated with a UV light, which favours the regeneration rate of Fe^{2+} (Eq. 1.10) and can also photodecompose some complexes of Fe^{3+} formed with organics.

Fockedey and Lierde (2002) studied on COD reduction by coupling anodic and cathodic reactions. They used Sb-doped SnO_2-coated titanium foam for direct AO and an RVC cathode for H_2O_2 production on the cathodic side of a divided cell for phenol oxidation. The coupled process reduces energy consumption to 6.3 kAh to degrade 1 kg phenol when working at 100 A/m^2. The energy consumption is about 5kWh/kg COD reduction. Brillas et al. (2004) investigated on coupled AO and EFP using Pt anode and GDE cathode electrodes where H_2O_2 is electro-generated in an undivided cell for nitrobenzene decomposition. For all the cases, TOC reduction is more rapid with increasing current density. They explained this as the concurrent increase in the generation of adsorbed $^{\bullet}OH$ radical at the anode (Eq. 1.52) and H_2O_2 at cathode (Eq. 1.31) leading to a total higher gross rate of $^{\bullet}OH$ radical formation.

Flox et al. (2006) reported on carmine degradation by EFP and PEF using BDD, and Pt anodes, and C-PTFE O_2 fed cathode. Complete mineralization occurs in EFP with BDD anode, while a partial mineralization is noted with Pt electrode. Mineralization is complete when EFP is carried out with BDD anode and, when Fe^{2+} and Cu^{2+} are used as catalysts in PEF with Pt anode.

Montanaro et al. (2008) used BDD anode and gas diffusion cathode in a divided cell using an anionic membrane to treat phosphates effluent. The anionic membrane allows the passage of OH^- ions from the cathodic to the anodic compartment to maintain the catholyte pH. It minimizes iron precipitation in the cathode cell. The combined treatment in an undivided cell using BDD anode leads to complete oxidation in about 500 min against the same in 1320 min in EFP. The simultaneous anodic and cathodic oxidation in a divided cell allows complete oxidation of effluent in 240 min.

1.5.4 Development of electrocatalysts for enhanced H_2O_2 generation

In the past decades, many transition metals and metal oxides are used in catalysing the oxygen reduction reaction (ORR) for H_2O_2 formation due to its low cost, noble-metal like

catalytic properties, abundance and environmental compatibility, and chemical stability in a wide pH range. Therefore, the stress is given on transition metals and metal oxides catalysed electrochemical H_2O_2 formation.

Assumpcao et al. (2013) tested two methods namely polymeric precursor method (PPM) and sol-gel method (SGM) to synthesize CeO_2 NPs. The carbon reference materials include Printex 6L (P) and Vulcan XC 72 R (V). They observed that the ring current produced with 4 % CeO_2-PPM-P catalyst is higher than that of Vulcan XC 72 R and Printex L6 carbon for H_2O_2 production and it is also higher than that of CeO_2-PPM-V. It improves the energy consumption for 4 % CeO_2-PPM-P. CE_f of 88 % of H_2O_2 generation is obtained and ORR takes place by 2.2 electrons transfer per O_2 molecule at the lowest onset potential of $-E_{cat}$= 0.457 V vs. Ag/AgCl.

Shuan et al. (2013) used Co_3O_4 as an electrocatalyst and reported that the 3d orbitals of Co metal ions could display a significant catalytic effect in ORR. H_2O_2 is formed at a very low cathode potential (0.133 V vs. Ag/AgCl) in an alkaline medium (pH 7).

Carneiro et al. (2015) used the Nb_2O_5/rGO/GDE composite electrode to generate H_2O_2 both in an acid and alkaline media. Reduced graphene oxide (rGO) modified composite electrode exhibits higher electroctalyitc activity toward the reduction of O_2 in an acid media (pH 2) compared to carbon Printex 6L and also a higher reduction current is found at Nb_2O_5/rGO/GDE due to its large effective surface area.

Barros et al. (2015) reported that F_3O_4 NPs supported on graphene (F_3O_4/graphene) and Printex carbon (F_3O_4/Printex) act as a promising catalyst for $2e^-$ ORR to H_2O_2 in an alkaline medium (1 M KOH) at $-E_{cat}$=0.253 V vs. Ag/AgCl. A larger number of functional groups present on the surface of the graphene sheets than Printex carbon provide more anchoring sites for the nucleation and growth of Fe_3O_4 NPs.

Lin et al. (2016) synthesized the cobalt sulfide/partly-graphatized carbon (Co_9S_8/PGC) composite by a simple carbonization method to improve electrocatalytic H_2O_2 generation. H_2O_2 formation takes place at a very low potential of 0.111 V vs. Ag/AgCl at Co_9S_8/PGC electrode compared to PGC. An abundant of oxygen-containing functional groups on the PGC surface improved the wettability and hydrophilicity of Co_9S_8/PGC, contributing to the formation of more catalytic sites in the porous structure. Therefore, the electron transfer between the electrode and solution interface is accelerated. A higher temperature increases the degree of graphitization and Co_9S_8 crystal size which helps for the enhancement of the electrical conductivity of Co_9S_8/PGC.

Table 1.6: Performance comparison of graphite (mostly) based transition metal oxides NPs electrodes for H_2O_2 formation.

Cathode electrode	$-E_{cat}$ (V)	Experimental condition	H_2O_2 formed (mg/L)/ CE_f (%)	NPs synthesis process	Source
Fe_2O_3/ACF	1.2	pH 2-3 Na_2SO_4 0.05M	~0.238/--	Chemical	Li et al., 2009
CeO_2/C-PPM-P	0.457	NaOH 1 M	--/88.8	Sol-gel	Assumpcao et al., 2013
Graphite/Co_3O_4	0.133	pH 7 Na_2SO_4 0.07 M Time 3 h	0.1/--	Hydrothermal	Shuan et al., 2013
Nb_2O_5/rGO/GDE	0.3	pH 2 K_2SO_4 0.1 M Time 5.5 h	--/85.3	Hydrothermal	Carneiro et al., 2015
Fe_3O_4/Graphene	0.253	KOH 1 M Time 5.5 h	--/62	Precipitation	Barros et al., 2015
Co_9S_8/PGC	0.111	pH 5 Na_2SO_4 0.1 M Time 2 h	~ 3/--	Carbonization	Lin et al., 2016

$-E_{cat}$:vs. Ag/AgCl, Co_9S_8: Cobalt sulphide, PGC: Partly graphitized carbon, rGO: Reduced graphene oxide, GDE: Gas diffusion electrode, PPM: Polymeric precursor, P: Printex L6

1.6 Current status of H_2O_2 detection: Role of electrocatalysts

It is already outlined in Section 1.2 of this Chapter that electroanalytical H_2O_2 detection and determination offers low cost, easy operation, high sensitivity and selectivity, and possibility of real-time analysis. Nanostructured materials are used extensively to develop non-enzymatic H_2O_2 sensors due to their unique and excellent electrochemical activity having a large surface to volume ratio and high crystallinity. On the other hand, the enzyme-based sensors could suffer from electrode and enzyme stability being dependent on temperature, pH, and humidity. Therefore, the non-enzymatic electrodes catalysed by noble and transition metals and metal oxides NPs are tested for H_2O_2 detection. The following sections survey the state-of-the-art literatures on metal and metal oxides NPs for electrocatalytic H_2O_2 detection and determination.

1.6.1 Transition and noble metal electrocatalysts

Hrapovic et al. (2004) prepared the Pt NPs (2-3 nm diameters) using the chemical reaction method and employed Pt NPs through single-wall carbon nanotube (SWCNTs) to modify the glassy carbon electrode (GC) in order to improve their electroactivity for H_2O_2 sensing. Nafion was used to solubilize and disperse SWCNTs as the deposition of metal on SWCNTs is difficult because of greater inertness, smaller size, and higher curvature of these materials compared to multiwall carbon nanotubes. The resultant current at the fabricated electrode (GC/SWCNTs + Pt NPs) electrode was higher compared to the GC electrode. They

obtained the detection limit of 25 nM with a sensitivity of 3.57 μA/μM/cm^2 at $-E_{cat}$=0.55 V vs. Ag/AgCl.

Chandra et al. (2009) applied dendrimer to encapsulate Rh NPs for the prevention of agglomeration. They synthesized rhodium nanoparticles in an aqueous solution by the reduction of Rh ions using $NaBH_4$ in the presence of N,N-bis-succinamide-based dendrimer. The dendrimer-encapsulated Rh nanoparticles (Rh-DENs) of uniform size are immobilized onto the surface of glassy carbon electrodes (GCEs) and used for H_2O_2 catalysis. The dendrimer/nanoparticle composite acts like a template/replica system having synergistic effects that exceed those of individual components. The cathodic peak current appeared at a $-E_{cat}$=0.253 V vs. Ag/AgCl at Rh NPs modified GCE support electrode compared to the bare GCE electrode in phosphate buffer (pH 7.0). The use of dendrimer stabilized Rh NPs increases the effective surface area which leads to a high catalytic activity.

Maji et al. (2013) showed that 8±3 nm Ag NPs (S1) exhibits a much better electrocatalytic activity compared to 256±6 nm Ag NPs (S2) towards H_2O_2 sensing. A higher current response is achieved at $-E_{cat}$=0.55 V vs. Ag/AgCl at the Ag NPs(S1)/GC electrode due to smaller particles size having higher active sites and faster electron transfer. It exhibits a quick current response (4 s), wider linear range (10 μM to 6.5 mM) and high sensitivity (5.9 mA/mM).

Wang et al. (2015) found an optimal pH of 7.4 for H_2O_2 detection using Pd NPs modified glassy carbon electrode (GCE) and showed that the electrocatalytic of the electrode is notably affected by Pd NPs coverage on the electrode surface. Pd NPs coverage of 85 % gives strong sensitivity and linear response at a sufficiently low potential which is also similar to Sophia and Muralidharan (2015) reported for Cu NPs modified GCE electrode. The high density arrays of Pd NPs are formed on the carbon surface without agglomeration. A decrease in NP sizes sufficiently reduces the overpotential for H_2O_2 detection. Furthermore, Wang et al. (2015) and Sophia and Muralidharan (2015) investigated the influence of common interfering species such as ascorbic acid (AA), uric acid (UA) and acetaminophen (AP) on the sensor response in order to estimate the selectivity toward H_2O_2 sensing. A concise summery of the key findings of the above studies is provided in Table 1.7.

Table 1.7: Performance comparison of various metals NPs catalysing electrochemical H_2O_2 sensing.

Modified electrode	$-E_{cat}$ (V)	LOD (µM)	LR (mM)	Sensitivity (µA/µM/cm^2)	AR (s)	Source
Pt	0.55	0.025	0.00025-0.01	3.75	--	Hrapovic et al., 2004
Rh	–0.253	5	0.008-0.03	0.031 µA/µM	--	Chandra et al., 2009
Au	–0.4	0.1	0.0005-5.89	0.273	2	Zhang et al., 2011
Ag	–0.5	2.24	0.01-6.5	5.9 mA/mM	4	Maji et al., 2013
Cu	–0.14	3.4	0.008-0.07	--	--	Sophia and Muralidharan, 2015
Pd	–0.12	0.34	0.0001-6	0.051 µA/µM	--	Wang et al., 2015

$-E_{cat}$:vs. Ag/AgCl, LOD: Limit of detection, LR: Linear range, AR: Amperometric response, NPs: Nanopartilces

1.6.2 Bimetallic NPs as electrocatalysts in H_2O_2 detection

The bimetallic NPs could be classified in three different structures, namely, core-shell, alloyed NPs, and heterogeneous structures based on their mixing pattern with the geometric structure (Wang et al., 2011a). The induction of a second metal generates an epic variation in the particle shape and size, surface morphology, and physical and chemical properties**.** The bimetallic NPs such as Au-Pt, Pd-Cu, Pt-Ag, Pt-Cu, Pt-Ir, Pt-Pd, Rh-Pd, and Ru-Rh are in use to fabricate H_2O_2 sensors. Janasek et al. (2002) showed improved operational stability, low background current, and high signal-to-noise ratios using Ru-Rh NPs deposited as a thin layer on the gold foils. Under the flow injection condition, H_2O_2 is detected between 1 and 1000 µM at $-E_{cat}$=0.1 V and between 2 and 500 µM at $-E_{cat}$=–0.25 V vs. Ag/AgCl. Rajkumar et al. (2011) reported on H_2O_2 detection at the Rh-Pd NPs modified GCE. The linearity of H_2O_2 detection is found to be different for the synthetic and real samples even at the same potential of $-E_{cat}$=0.17 V vs. Ag/AgCl. The bimetallic Pt-Pd, Pt-Ir, Pt-Ag core-shell NPs are also commonly employed to develop the electrochemical H_2O_2 sensors. But, the main concern is the insufficient activity and durability of the core–shell nano-architectures, which is largely restricted by the occurrence of easy agglomeration during catalytic reactions (Li et al., 2012). Li et al. (2015) synthesized raspberry-like bimetallic Au-Pt-Au triple layered core-shell NPs on graphene oxide (GO) nanosheets for H_2O_2 sensing. The bi-directional sensor gives the lowest detection limit of 0.02 mM (signal to noise ratio 3) at $-E_{cat}$=–0.5 V and, the lowest response time at $-E_{cat}$=–0.253 V vs. Ag/AgCl catalysed by Au-Pt-Au triple-layered NPs with the two exposed metal surfaces (Au and Pt) consisting of an Au core, a Pt inner shell, and an outer shell composed of Au protuberances on GO nanosheets. The addition of common interfering species such as ascorbic acid (AA), uric acid (UA) and L-tyrosine (LT) doesn't affect the performance of the sensor. The important results using bimetallic NPs for H_2O_2 sensing is summarized in Table 1.8.

Table 1.8: Performance comparison of various bimetallic NPs catalysing electrochemical H_2O_2 sensing.

Modified electrode	$-E_{cat}$ (V)	LOD (µM)	LR (mM)	Sensitivity (µA/µM/cm^2)	AR (s)	Source
Ru-Rh	–0.1 or 2.5	--	0.001-1 or 0.002-0.5	--	--	Janasek et al., 2002
Rh-Pd	–0.17	--	10-460 (LS) 10-340 (RS)	0.3160 µA/µM 0.0560 µA/µM	5	Rajkumar et al., 2011
Pt-Ag	0.9	0.1	0.05-0.8	--	4	Xu et al., 2011
Pd-Cu	0.97	0.1	0.5-8	--		Liu et al., 2011a
Pt-Cu	0.9	0.1	0.05-0.8	--	4	Xu et al., 2011
Pt-Pd	–0.2	0.297	0.0005-270	--	< 3	Wang et al., 2011a
Pt-Ir	0.203		0-10	0.014	--	Chang et al., 2014
Au-Pt	0.5 –0.2.53	0.02 0.25	0.00005-17.5 0.005-110	-- --	3 2	Li et al., 2015

$-E_{cat}$:vs. Ag/AgCl, LOD: Limit of detection, LR: Linear range, AR: Amperometric response, LS: Lab sample, RS: Real sample, NPs: Nanopartilces

1.6.3 Metal oxide electrocatalysts in H_2O_2 sensing

The transition metal oxides NPs such as Co_3O_4, CoO, NiO, CuO, MnO_2, Fe_2O_3, TiO_2, and IrO_2 are also widely investigated for the electrocatalytic H_2O_2 sensing mostly to achieve a lower overpotential (Jiang and Zhang, 2009; Hrbac et al., 2007; Ping et al., 2010). Xu et al. (2010) employed MnO_2-modified vertically aligned multi-walled carbon nanotubes (MnO_2/VACNTs) to detect H_2O_2 using Ag/AgCl as the reference electrode. The MnO_2/VACNTs nanocomposite electrode displays about 10 times higher response current than the bare VACNTs electrode with a linear range of 0.0012 to 1.8 mM (limit of detection 0.8µM) and sensitivity of 1.08 µA/µM/cm^2 at $-E_{cat}$= 0.45 V vs. Ag/AgCl. The higher sensitivity is resulted from the presence of MnO_2 NPs on the VACNTs, which significantly increases the active catalytic area and promotes electron transfer between MnO_2 and VACNT. The TiO_2/multiwalled carbon nanotubes (TiO_2/MWCNTs) electrode provides a large surface area by the presence of MWCNTs and high active catalytic sites by the presence of nanostructured TiO_2 (Jiang and Zhang, 2009). It decreases the overpotential of H_2O_2 detection and enhances the peak current. A low detection limit of 0.4 µM is obtained than that of Xu et al. (2010) because the existence of TiO_2 NPs on the surface of the MWCNTs increases the rate of electron transfer. The TiO_2/MWCNTs electrode also shows a very high selectivity towards the determination of H_2O_2. The inorganic salts namely, sodium sulphate, potassium chloride, and calcium nitrate, and organic compounds, namely, acetic acid, citric acid, uric acid, and d-(þ)-glucose cause negligible interference. Ping et al. (2010) showed that traces of ionic liquid can reduce the overpotential of H_2O_2 sensing. H_2O_2 reduction takes place at a very low potential of –0.14 V vs. Ag/AgCl catalysed by CuO NPs embedded on GCE. N-octylpyridium hexafluorophosphate is used for CuO binding on GCE which also

helps for accelerating the electron transfer rate. Co_3O_4 NPs/MWCNTs modified carbon paste electrode exhibits a low potential of –0.19 V vs. Ag/AgCl for H_2O_2 sensing (Heli and Pishahang, 2014). AA, glucose, dopamaine and UA injection at a high concentration into the electrolyte solution couldn't alter the performance of the sensor (Xu et al., 2010; Ping et al., 2010; Heli and Pishahang, 2014). Al-Hardan et al. (2016) obtained a detection limit of 42 µM (linear range 10-700 µM) using the aluminium doped ZnO nanorods electrode (AZO/ZnO NR). Wang et al. (2009) employed gold nanoparticles (Au NPs) electrodeposited indium tin oxide (ITO) electrode and a detection limit of 2 µM is achieved (linear range 8-300 µM). Lavanya et al. (2012) used Ni doped SnO_2 glassy carbon/HRP electrode for H_2O_2 detection. A detection limit of 43 nM is obtained with a linear range of 0.1 to 300 µM. A brief summary of the outcomes using metal oxides electrocatalysts for H_2O_2 sensing is provided in Table 1.9.

Table 1.9: Performance comparison of various metals oxides NPs catalysing electrochemical H_2O_2 sensing.

Modified electrode	$-E_{cat}$ (V)	LOD (µM)	LR (mM)	Sensitivity (µA/µM/cm^2)	AR (s)	Source
MnO_2/DHP/GCE	+0.65	0.08	0.00012 - 2.16	0.266		Yao et al., 2006
Fe_2O_3/GCE	–0.4	20	0-8.5	--	< 3	Hrbac et al., 2007
TiO_2/MWCNT	0.4	0.4	--	13.4µA/mM	5	Jiang and Zhang, 2009
MnO_2/VACNTs	+ 0.45	0.8	0.0012- 1.8	1.08	--	Xu et al., 2010
CuO/CPE	–0.2	0.5	0.001-2.5	0.393	3-5	Ping et al., 2010
Co_3O_4/MWCNTs	–0.19	2.46	0.02–0.43	1.0028	--	Heli and Pishahang, 2014
NiO nanosheets on graphite	0.33	0.4	0.5- 4	1.077	5	Liu et al., 2015

$-E_{cat}$:vs. Ag/AgCl, LOD: Limit of detection, LR: Linear range, AR: Amperometric response, NPs: Nanopartilces, DHP: Dihexadecyl hydrogen, GCE: Glassy carbon electrode, MWCNT: Multiwalled carbon nanotube, VACNTs: Vertically mutiwalled carbon nanotubes, CPE: Carbon paste electrode

1.6.4 Composite materials as electrocatalysts

The composite electrocatalysts, namely, porphyrin complex of cobalt (CoTRP), DNA hybrid, poly(diallydimethyl ammonium chloride)-graphene (PDDA-G), HRP, and chitosan (CS) are studied to enhance the electron transfer rate during H_2O_2 sensing. Quintino et al. (2005) reported a detection limit of about 0.2 µM in the linear range of 5×10^{-4} to 2.0 mM in the presence of µ-(5,10,15,20-tetra(4-pyridyl)porphyrinatocobalt(III))-tetrakis-(chloro-bis-(2,29-bipyridine)ruthenium(II)) (CoTRP) complex in a batch injection technique. To avoid agglomeration of Ag NPs, Wu et al. (2006) electrodeposited Ag-deoxyribonucleic acid (DNA) hybrid NPs on the GCE and, it improves the sensitivity to 0.773 from 0.0436 µA/µM/cm^2 with a low overpotential of 1.51 V. Both Xin et al. (2013) and Hao et al. (2016) achieve a low H_2O_2 reduction potential of 0.3 and 0.253 V vs. Ag/AgCl using the screen

printed electrode (SPE)/graphene-Nafion/Fe_3O_4-Au-HRP and graphene-Fe_2O_3-CS/GCE electrodes. The surfaces of the electrodes are easily renewed with the aid of an external magnetic field due to the presence of Fe_3O_4 magnetic NPs. Au NPs improve the biocompatibility and prevent cluster aggregation. Hao et al. (2016) got a fast response time (< 2 s) due to the presence of graphene nano-sheets. In fact, Fe_2O_3 NPs promote the transmission rate and adhesive capacity of the target object on the surface of the electrodes. It also facilitates and accelerates the transition of chemical to the electrical signal. UA, AA, and glucose did not cause an observable interference for H_2O_2 detection. The performances of composite catalysts in H_2O_2 sensing are summarized in Table 1.10.

Table 1.10: Performance comparison of various composite NPs catalysing electrochemical H_2O_2 sensing.

Modified electrode	$-E_{cat}$ (V)	LOD (µM)	LR (mM)	Sensitivity (µA/µM/cm^2)	AR (s)	Source
Co_3O_4/CoTRP (GC)	+0.3	0.2	5×10^{-4}-2.0	--	--	Quintino et al., 2005
Ag-DNA/GCE	–0.45	0.6	0.002-2.5	0.773	--	Wu et al., 2006
PDDA-G/Fe_3O_4	–0.4	2.5	0.02–6.25	61.2 $\times10^3$	--	Liu et al., 2011b
SPE/GS-Nafion/Fe_3O_4-Au-HRP	–0.3	12	0.02–2.5	--	~3	Xin et al., 2013
G-Fe_2O_3-CS/GCE	–0.253	1.1	0.001-6.0	0.084	<2	Hao et al., 2016

$-E_{cat}$:vs. Ag/AgCl, LOD: Limit of detection, LR: Linear range, AR: Amperometric response, NPs: Nanopartilces, CoTRP: Tetraruthenated cobalt-porphyrin, GCE: Glassy carbon electrode, PDDA: Poly(diallydimethylammonium chloride), SPE: Screen printed electrode, GS: Graphene sheets, HRP: Horseradish peroxidase, G: Graphene, CS: Chitosan

1.7 Knowledge gap and research objectives

The typical electrocatalysts popularly employed for the generation of H_2O_2 are various transition metal oxides such as Co_3O_4, NiO, SnO_2, SnO, and MnO_2 etc. It is noteworthy that these catalysts also impart strong electrocatalytic activity for H_2O_2 sensing. The primary reason for this dual catalytic activity are (i) more stability in an oxidative environment, (ii) difference in the oxygen defect, oxygen holes and oxygen adsorption in different oxidation states of metal and, (iii) change in spital overlapping between 3d orbital of metal and 2p orbital of O_2. The synthesis process is usually mediated by the use of reducing agents such as sodium borohydrate, hydrazine hydrate, ethylene glycol, polyvinylpyrrolidone, and sodium citrate, followed by the calcination at a higher temperature (400-800 °C). Here, we propose a bio-mediated technique to replace the use of these reducing agents for the synthesis of electrocatalysts for H_2O_2 generation and sensing.

The bio-analytes such as ascorbic acid (Rao and Golder, 2016) and flavonoids (Flick et al., 1978), etc. are extracted in water from the living cells (plant biomass) and employed for the synthesis of Co_3O_4 and NiO NPs electrocatalysts instead of chemical reducing agents.

Sechium edule (Chayote) is an herbaceous perennial climber, and the local climate is highly favourable for the growth of this plant in the North Eastern part of India (Mishra and Das, 2015). The fruit is commonly known as Squash (or simply *S. edule*) in Assam, India. The fruits look similar to pears with a rough skin and the length could be up to 20 cm. *S. edule* contains many natural antioxidants, amino acids, ascorbic acids (AA), and polyphenolic compounds (Ordonez et al., 2003). *S. edule* contain AA and flavonoids as high as 3 and 35 mg per 10 g of dried part, respectively (Siciliano et al., 2004). The fruit extracts show strong reducing power and, it is employed for the antioxidant activity test by converting potassium ferricyanide to potassium ferrocyanide. The analytes present in the extract act as strong electron and hydrogen donors. It could break the radical chain reaction and convert the free radicals to stable products (Ordonez et al., 2006). The bio-analytes are extracted in water from *S. edule* and employed for the synthesis of Co_3O_4 and NiO NPs electrocatalysts in the place of chemical reducing agents. In fact, there is no such earlier report for the synthesis of electrocatalysts in a bio-mediated technique following such a pathway. Likewise, the objectives of the doctoral work are designed as:

Electrocatalytic H_2O_2 generation in an undivided electrolyser

- To elucidate the effect of transition and alkaline metal ions, solution pH, and temperature on the stability of H_2O_2
- To study on electrogeneration of H_2O_2 at isomoulded graphite cathode in an undivided cell and to optimize the process parameters to understand their effects on H_2O_2 formation and decomposition at TiO_2-Ti anode
- To develop a bio-mediated technique for the synthesis of Co_3O_4 and NiO NPs and to determine their physiochemical attributes
- To fabricate modified graphite electrodes to investigate the electrocatalytic activity of Co_3O_4 and NiO NPs for an enhanced H_2O_2 generation
- To investigate the implication of electrogenerated H_2O_2 for the degradation of PhAC wastewater

Electrocatalytic H_2O_2 sensing on graphite support electrode

- To fabricate modified graphite electrodes for Co_3O_4 and NiO NPs catalysed H_2O_2 sensing in a phosphate buffer media
- To derive the fundamental electrochemical parameters and to explore the catalytic action of Co_3O_4 and NiO NPs for H_2O_2 sensing
- To analyse real H_2O_2 samples and to compare with the titanic sulphate spectrophotometric technique
- To explore the effects of common electro-active species interfering with the H_2O_2 sensing

References

Abbas M.E., Luo W., Zhu L., Zou J., Tang H. Fluorometric determination of hydrogen peroxide in milk by using a Fenton reaction system, *Food Chem.* **2010**, 120, 327-331.

Aglardze G.R., Tsurtsumia G.S., Jung B.I., Kim J.S., Gorelishvili G. Comparative study of hydrogen peroxide electro-generation on gas-diffusion electrodes in undivided and membrane cells, *J. Appl. Electrochem.* **2007**, 37, 375-383.

Al-Hardan N.H., Hamid M.A.A., Shamsudin R., Othman N.K., Keng L.K. Amperometric non-enzymatic hydrogen peroxide sensor based on aligned zinc oxide nanorods, *Sensors* **2016**, 16, 1004.1-1004.8.

Amin V.M., Olson N.F. Spectrophotometric determination of hydrogen peroxide in Milk, *J. Dairy Sci.* **1966**, 50, 461-464.

Andreozzi R., Caprio V., Insola A., Marotta R. Advanced oxidation processes (AOP) for water purification and recovery, *Catal. Today* **1999**, 53, 51-59.

Anotai J., Lu M.-C., Chewpreecha P. Kinetics of aniline degradation by Fenton and electro-Fenton processes, *Water Res.* **2006**, 40, 1841-1847.

Arapoglu D., Vlyssides A., Israilides C., Zorpas A., Karlis P. Detoxification of methyl-parathion pesticide in aqueous solutions by electrochemical oxidation, *J. Hazard. Mater.* **2003**, 98, 191-199.

Assumpcao M.H.M.T., Moraes A., De Souza R.F.B., Calegaro M.L., Lanza M.R.V., Leite E.R., Cordeiro M.A.L., Hammer P., Santos M.C. Influence of the preparation method and the support on H_2O_2 electro-generation using cerium oxide nanoparticles, *Electrochim. Acta* **2013**, 111, 339-343.

Barros W.R.P., Wei Q., Zhang G., Sun S., Lanza M.R.V., Tavares C. Oxygen reduction to hydrogen peroxide on Fe_3O_4 nanoparticles supported on Printex carbon and Graphene, *Electrochim. Acta* **2015**, 162, 263-270.

Bo X., Bai J., Qi B., Guo L. Ultra-fine Pt nanoparticles supported on ionic liquid polymer-functionalized ordered mesoporous carbons for nonenzymatic hydrogen peroxide detection, *Biosens. Bioelectron.* **2011**, 28, 77-83.

Boye B., Dieng M.M., Brillas E. Degradation of herbicide 4-Chlorophenoxyacetic acid by advanced electrochemical oxidation methods, *Environ. Sci. Technol.* **2002**, 36 (13), 3030-3035.

Boye B., Dieng M.M., Brillas E. Anodic oxidation, electro-Fenton and photoelectro-Fenton treatments of 2,4,5-trichlorophenoxyacetic acid, *J. Electroanal. Chem.* **2003**, 557, 135-146.

Brandhuber P.J., Korshin G. Methods for the detection of residual concentrations of hydrogen peroxide in advanced oxidation process, **2009**, Wate Reuse Foundation, USA.

Bray W.C., Gorin M.H. Ferryl ion, a compound of tetravalent iron, *J. Am. Chem. Soc.* **1932**, 54, 2124-2125.

Brillas E., Banos M.A., Camps S., Arias C., Cabot P.L., Garrido J.A., Rodriguez R.M. Catalytic effect of Fe^{2+}, Cu^{2+} and UVA light on the electrochemical degradation of nitrobenzene using an oxygen-diffusion cathode, *New J. Chem.* **2004**, 28, 314-322.

Brillas E., Banos M.A., Skoumal M., Cabot P.L., Garrido J.M., Rodriguez R.M. Degradation of the herbicide 2,4-DP by anodic oxidation, electro-Fenton and photoelectro-Fenton using platinum and boron-doped diamond anodes, *Chemosphere* **2007**, 68,199-209.

Brillas E., Bastida R.M., Llosa E., Casado J. Electrochemical destruction of aniline and 4-chloroaniline for wastewater treatment using a carbon-PTFE O_2-fed cathode, *J. Electrochem. Soc.* **1995**, 142 (6), 1733-1741.

Brillas E., Boye B., Dieng M.M. General and UV-assisted cathodic Fenton treatments for the mineralization of herbicide MCPA, *J. Electrochem. Soc.* **2003**, 150, E583-E589.

Brillas E., Calpe J.C., Casado J. Mineralization of 2,4-D by advanced Electro-chemical oxidation processes, *Water Res.* **2000**, 34 (8), 2253-2262.

Brillas E., Garcia-Segura S., Skoumal M., Arias C. Electrochemical incineration of diclofenac in neutral aqueous medium by anodic oxidation using Pt and boron-doped diamond anodes, *Chemosphere* **2010**, 79, 605-612.

Brillas E., Sauleda R., Casado J. Degradation of 4-chlorophenol by anodic oxidation, electro-Fenton, photoelectro-Fenton, and peroxi-coagulation processes, *J. Electrochem. Soc.* **1998**, 145 (3), 759-765.

Brillas E., Sires I., Oturan M.A. Electro-Fenton process and related electrochemical technologies based on Fenton's reaction chemistry, *Chem. Rev.* **2009**, 109, 6570-6631.

Burbano A.A., Dionysiou D.D., Suidan M.T. Effect of oxidant-to-substrate ratios on the degradation of MTBE with Fenton reagent, *Water Res.* **2008**, 42 (12), 3225-3239.

Canizares P., Martinez F., Diaz M., Garcia-Gomez J., Rodrigo M.A. Electrochemical oxidation of aqueous phenol wastes using active and non-active electrodes, *J. Electrochem. Soc.* **2002**, 149, D118-D124.

Carneiro J.F., Paulo M.J., Siaj M., Tavares A.C., Lanza M.R.V. Nb_2O_5 nanoparticles supported on reduced graphene oxide sheets as electrocatalyst for the H_2O_2 electrogeneration, *J. Catal.* **2015**, 332, 51-61.

Chandra S., Lokesh K.S., Nicolai A., Lang H. Dendrimer-rhodium nanoparticle modified glassy carbon electrode for amperometric detection of hydrogen peroxide, *Anal. Chim. Acta* **2009**, 632, 63-68.

Chang S.H., Yeh M.H., Rick J., Su W.N., Liu D.G., Lee J.F., Liu C.C., Hwang B.J. Bimetallic catalyst of PtIr nanoparticles with high electrocatalytic ability for hydrogen peroxide oxidation, *Sens. Actuators B* **2014**, 190, 55-60.

Chen S., Yuan R., Chai Y., Zhang L., Wang N., Li X. Amperometric third-generation hydrogen peroxide biosensor based on the immobilization of hemoglobin on multiwall carbon nanotubes and gold colloidal nanoparticles, *Biosens. Bioelectron.* **2007**, 22, 1268-1274.

Cheng-Chun J., Jia-Fa Z. Progress and prospect in electro-Fenton process for wastewater treatment, *J. Zhejiang Univ. Sci. A* **2007**, 8 (7), 1118-1125.

Ciriaco L., Anjo C., Correia J., Pacheco M.J., Lopes A. Electrochemical degradation of Ibuprofen on Ti/Pt/PbO_2 and Si/BDD electrodes, *Electrochim. Acta* **2009**, 54, 1464-1472.

Corbett J. The Scopoletin assey of H_2O_2, *J. Biochem. Biophys. Methods* **1989**, 18, 290.7-300.7.

Daneshvar N., Aber S., Vatanpour V., Rasoulifard M.H. Electro-Fenton treatment of dye solution containing Orange II: Influence of operational parameters, *J. Electroanal. Chem.* **2008**, 615 (2), 165-174.

Daughton C.G., Ternes T.A. Pharmaceuticals and personal care products in the environment: agents of subtle change, *Environ. Health Perspect.* **1999**, 107, 907-942.

De Laat J., Gallard H. Catalytic decomposition of hydrogen peroxide by Fe(III) in homogeneous aqueous solution: mechanism and kinetic modelling, *Environ. Sci. Technol.* **1999**, 33, 2726-2732.

De Leon C.P., Pletcher D. Removal of formaldehyde from aqueous solutions via oxygen reduction using a RVC cathode cell, *J. Appl. Electrochem.* **1995**, 25 (4) 307-314.

Diagne M., Oturan N., Oturan M.A. Removal of methyl parathion from water by electrochemically generated Fenton's reagent, *Chemosphere* **2007**, 66 (5), 841-848.

Diaz A.N., Peinado M.C.R., Minguez M.C.T. Sol-gel horseradish peroxidase biosensor for hydrogen peroxide detection by chemiluminescence, *Anal. Chim. Acta* **1998**, 363, 221-227.

Do J.S., Chen C.P. In situ oxidative degradation of formaldehyde with electrogenerated hydrogen peroxide, *J. Electrochem Soc.* **1993**, 140 (6), 1632-1637.

Do J.S., Chen C.P. Kinetics of in situ degradation of formaldehyde with electro-generated hydrogen peroxide, *Ind. Eng. Chem. Res.* **1994**, 33, 387-394.

El-Desokya H.S., Ghoneim M.M., El-Sheikh R., Zidan N.M. Oxidation of Levafix CA reactive azodyes in industrial wastewater of textile dyeing by electro-generated Fenton's reagent, *J. Hazard. Mater.* **2010**, 175, 858-865.

Ensafi A.A., Jafari-Asl M., Rezaei B. A novel enzyme-free amperometric sensor for hydrogen peroxide based on Nafion/exfoliated graphene oxide-Co_3O_4 nanocomposite, *Talanta* **2013**, 103, 322-329.

Ensing B., Buda F., Baerends E.J. Fenton-like chemistry in water: oxidation catalysis by Fe(III) and H_2O_2, *J. Phys. Chem. A* **2003**, 107 (30), 5722-5731.

Esquivel K., Arriaga L.G., Rodriguez F.J., Martinez L., Godinez L.A. Development of a TiO_2 modified optical fiber electrode and its incorporation into a photoelectrochemical reactor for wastewater treatment, *Water Res.* **2009**, 43, 3593-3603.

Estrada A.L. Degradation of antibiotics by electrochemical advanced oxidation processes using an activated carbon fiber cathode, **2012**, Doctoral Dissertation, Tohoku University, Japan.

Evans M.G., George P., Uri N. The $[Fe(OH)]^{+2}$ and $[Fe(O_2H)]^{+2}$ complexes, *Trans. Faraday Soc.* **1949**, 45, 230-236.

Fenton H.J.H. Oxidation of tartaric acid in presence of iron, *J. Chem. Soc. Trans.* **1894**, 65 (65), 899-911.

Ferreira M., Fiorito P.A., Oliveira O.N., De Torresi S.I.C. Enzyme-mediated amperometric biosensors prepared with the Layer-by-Layer (LbL) adsorption technique, *Biosens. Bioelectron.* **2004**, 19, 1611-1615.

Flick G.J., Burnette Jr.F.S., Aun L.H., Ory R.L., Angelo A.J.St. Chemical composition and biochemical properties of Mirlitons (*Sechium Edule*) and purple, green, and white eggplants (*Solanum melongena*), *J. Agric. Food Chem.* **1978**, 26, 1000-1005.

Flox C., Ammar S., Arias C., Brillas E., Vargas-Zavala A.V., Abdelhedi R. Electro-Fenton and photoelectro-Fenton degradation of indigo carmine in acidic aqueous medium, *Appl. Catal. B* **2006**, 67, 93-104.

Flox C.; Cabot P.L., Centellas F., Garrido J.A., Rodriguez R.M., Arias C., Brillas E. Solar photoelectro-Fenton degradation of cresols using a flow reactor with a boron-doped diamond anode, *Appl. Catal. B* **2007**, 75 (1-2), 17-28.

Fockedey E., Lierde A.V. Coupling of anodic and cathodic reactions for phenolelectro-oxidation using three-dimensional electrodes. *Water Res.* **2002**, 36 (16), 4169-4175.

Gallard H., De Laat J., Legube B. Spectrophotometric study of the formation of iron(III)-hydroperoxy complexes in homogeneous aqueous solutions, *Water Res.* **1999**, 33 (13), 2929-2936.

Gallegos A.A., Garcia Y.V., Zamudio A. Solar hydrogen peroxide, *Sol. Energy Mater. Sol.* **2005**, 88, 157-167.

Garcia-Segura S., Brillas E. Mineralization of the recalcitrant oxalic and oxamic acids by electrochemical advanced oxidation processes using a boron-doped diamond anode, *Water Res.* **2011**, 45 (9), 2975-2984.

Garjonyte R., Malinauskas A. Electrocatalytic reactions of hydrogen peroxide at carbon paste electrodes modified by some metal hexacyanoferrates, *Sens. Actuators* B **1998**, 46, 236-241.

Ghoneim M.M., El-Desoky H.S., Zidan N.M. Electro-Fenton oxidation of sunset yellow FCF azo-dye in aqueous solutions, *Desalination* **2011**, 274, 22-30.

Gotvajn A.Z., Zagorc-Koncan J. Combination of Fenton and biological oxidation for treatment of heavily polluted fermentation waste broth, *Acta Chim. Slov.* **2005**, 52, 131-137.

Guinea E., Arias C., Cabot P.L., Garrido J.A., Rodriguez R.M., Centellas F., Brillas E. Mineralization of salicylic acid in acidic aqueous medium by electrochemical advanced oxidation processes using platinum and boron-doped diamond as anode and cathodically generated hydrogen peroxide, *Water Res.* **2008**, 42, 499-511.

Haber F., Weiss J.J. The catalytic decomposition of hydrogen peroxide by iron salts, *Proc. Royal Soc. A* **1934**, 147, 332-351.

Hammami S., Oturan N., Bellakhal N., Dachraouia M., Oturan M.A. Oxidative degradation of direct orange 61 by electro-Fenton process using a carbon felt electrode: Application of the experimental design methodology, *J. Electroanal. Chem.* **2007**, 610, 75-84.

Hao C., Shen Y., Wang Z., Wang X., Feng F., Ge C., Zhao Y., Wang K. Preparation and characterization of Fe_2O_3 nanoparticles by solid-phase method and its hydrogen peroxide sensing properties, *ACS Sustain. Chem. Eng.* **2016**, 4, 1069-1077.

Heli H., Pishahang J. Cobalt oxide nanoparticles anchored to multiwalled carbon nanotubes: Synthesis and application for enhanced electrocatalytic reaction and highly sensitive nonenzymatic detection of hydrogen peroxide, *Electrochim. Acta* **2014**, 123, 518-526.

Hrapovic S., Liu Y., Male K.B., Luong J.H.T. Electrochemical biosensing platforms using platinum nanoparticles and carbon nanotubes, *Anal. Chem.* **2004**, 76, 1083-1088.

Hrbac J., Halouzka V., Zboril R., Papadopoulos K., Triantis T. Carbon electrodes modified by nanoscopic iron(III) oxides to assemble chemical sensors for the hydrogen peroxide amperometric detection, *Electroanal.* **2007**, 19, 1850-1854.

Janasek D., Vastarella W., Teuscher U.S.N., Heilmann A. Ruthenium/rhodium modified gold electrodes for the amperometric detection of hydrogen peroxide at low potentials, *Anal. Bioanal. Chem.* **2002**, 374, 1267-127.

Jiang L.-C., Zhang W.-D. Electrodeposition of TiO_2 nanoparticles on multiwalled carbon nanotube arrays for hydrogen peroxide sensing, *Electroanal*. **2009**, 21, 988-993.

Jones P., Kitching R., Tobe M.L., Wynne-Jones W.F.K. Catalytic decomposition of hydrogen peroxide, *Trans*. *Faraday Soc*. **1959**, 79-90.

Kaba L., Hitchens G.D., Bockris J. Electrochemical incineration of wastes, *J. Electrochem. Soc*. **1990**, 137 (5), 1341-1345.

Karyakin A.A. Prussian blue and its analogues: Electrochemistry and analytical applications, *Electroanal.* **2001**, 13, 813-819.

Khandelwal D.H., Ameta R. Use of photo-Fentonreagent in the degradation of basic yellow 2 in aqueous medium, *Res. J. Rec. Sci.* **2013**, 2 (1), 39-43.

Kiba N., Tokizawa T., Kato S., Tachibana M., Tani K., Koizumi H., Edo M., Yonezawa E. Flow-through micro sensor using immobilized peroxidase with chemiluminometric FIA system for determining hydrogen peroxide, *Anal. Sci.* **2003**, 19, 823-827.

Kraft A., Stadelmann M., Blaschke M. Anodic oxidation with doped diamond electrodes: a new advanced oxidation process, *J. Hazard. Mater.* **2003**, 103, 247-261.

Lavanya N., Radhakrishnan S., Sekar C. Fabrication of hydrogen peroxide biosensor based on Ni doped SnO_2 nanoparticles, *Biosens*. *Bioelectron*. **2012**, 36, 41-47.

Li B., Zhang Z., Zhao L. Chemiluminescent flow-through sensor for hydrogen peroxide based on sol–gel immobilized hemoglobin as catalyst, *Anal. Chim. Acta* **2001**, 445, 161-167.

Li N., Cao M.H., Hu C.W. Review on the latest design of graphene-based inorganic materials, *Nanoscale* **2012**, 4, 6205-6218.

Li X.R., Xu M.C., Chen H.Y., Xu J.J. Bimetallic Au@Pt@Au core-shell nanoparticles on graphene oxide nanosheets for high-performance H_2O_2 bi-directional sensing, *J. Mater. Chem. B* **2015**, 3, 4355-4362.

Li Y., Xu D., Oh J., Shen W., Li X., Yu Y. Mechanistic study of co-doped titania with non-metal and metal ions: A Case of C + Mo co-doped TiO_2, *ACS Catal.* **2012**, 2 (3), 391-398.

Lin Y., Yu J., Xing Z., Guo X., Yu X., Tang B., Zou J. Enhanced generation of H_2O_2 and radicals on Co_9S_8/partly-graphitized carbon cathode for degradation of bio-refractory organic wastewater, *Electrochim. Acta* **2016**, 213, 341-350.

Liu A.H., Geng H.R., Xu C.X., Qiu H.J. A three-dimensional hierarchical nanoporous Pd Cu alloy for enhanced electrocatalysis and biosensing, *Anal. Chim. Acta* **2011a**, 703, 172-178.

Liu M., Liu R., Chen W. Graphene wrapped Cu_2O nanocubes: Non-enzymatic electrochemical sensors for the detection of glucose and hydrogen peroxide with enhanced stability, *Biosens. Bioelectron*. **2013**, 45, 206-212.

Liu W., Zhang H., Yang B., Li Z., Lei L., Zhang X. A non-enzymatic hydrogen peroxide sensor based on vertical NiO nanosheets supported on the graphite sheet, *J. Electroanal*. *Chem*. **2015**, 749, 62-67.

Liu X., Zhu H., Yang X. An amperometric hydrogen peroxide chemical sensor based on graphene-Fe_3O_4 multilayer films modified ITO electrode, *Talanta* **2011b**, 87, 243-248.

Luecking F., Koeser H., Jank M., Ritter A. Iron powder, graphite and activated carbon as catalysts for the oxidation of 4-chlorophenol with hydrogen peroxide in aqueous solution, *Water Res.* **1998**, 32 (9), 2607-2614.

Luo Y., Liu H., Rui Q., Tian Y. Detection of extracellular H_2O_2 released from human liver cancer cells based on TiO_2 nanoneedles with enhanced electron transfer of *cytochrome c*, *Anal. Chem.* **2009**, 81, 3035-3041.

Lv J., Feng Y., Liu J., Quc Y., Cui F. Comparison of electrocatalytic characterization of boron-doped diamond and SnO_2 electrodes, *Appl. Sur. Sci.* **2013**, 283, 900-905.

Maji S.K., Dutta A.K., Srivastava D.N., Paul P., Mondal A., Adhikary B., Adhikary U. Electrocatalytic activity of silver nanoparticles modified glassy carbon electrode as amperometric sensor for hydrogen peroxide, *J. Nanosci. Nanotechnol.* **2013**, 13, 4969-4974.

Makarov V.V., Love A.J., Sinitsyna O.V., Makarova S.S., Yaminsky I.V., Taliansky M.E., Kalinina N.O. "Green" nanotechnologies: Synthesis of metal nanoparticles using plants, *Acta Nature* **2014**, 20, 35-44.

Mansour D., Fourcade F., Bellakhal N., Dachraoui M., Hauchard D., Amrane A. Biodegradability improvement of sulfamethazine solutions by means of an electro-Fenton Process, *Water Air Soil Pollut*. **2012**, 223, 2023-2034.

Martınez-Huitle C.A., Brillas E. Decontamination of wastewaters containing synthetic organic dyes by electrochemical methods: A general review, *Appl. Catal. B* **2009**, 87, 105-145.

Martinez-Huitle C.A., Quiroz M.A., Comninellis Ch., Ferro S., De Battisti A. Electrochemical incineration of chloranilic acid using Ti/IrO_2, Pb/PbO_2 and Si/BDD electrodes, *Electrochim. Acta* **2004**, 50, 949-956.

Mishra L., Das K.P. Nutritional evaluation of squash (*Sechium Edule*) germplasms collected from Garo Hills of Meghalaya - North East India, International journal of agriculture, *Environ*. *Biotechnol*. **2015**, 8, 971-975.

Mohan N., Balasubramanian N., Basha C.A. Electrochemical oxidation of textile wastewater and its reuse, *J. Hazard*. *Mater*. **2007**, 147, 644-651.

Mohanty J.G., Jaffe J.S., Schulman E.S., Raible D.G. A highly sensitive fluorescent micro-assay of H_2O_2 release from activated human leukocytes using a dihydroxyphenoxazine derivative, *J. Immunol. Methods* **1997**, 202, 133-141.

Montanaro D., Petrucci E., Merli C. Anodic, cathodic and combined treatments for the electrochemical oxidation of an effluent from the flame retardant industry, *J. Appl*. *Electrochem*. **2008**, 38, 947-954.

Murugananthana M., Latha S.S., Raju G.B., Yoshihara S. Anodic oxidation of ketoprofen-An anti-inflammatory drug using boron doped diamond and platinum electrodes, *J. Hazard. Mater*. **2010**, 180, 753-758.

Naimi I., Bellakhal N. Removal of 17β-estradiol by electro-Fenton process, *Mater. Sci. Appl.* **2012**, 3, 880-886.

Nogueira R.F.P., Oliveira M.C., Paterlini W.C. Simple and fast spectrophotometric determination of H_2O_2 in photo-Fenton reactions using metavanadate, *Talanta* **2005**, 31 (1), 86-91.

Ordonez A.A.L., Gomez J.D., Cudmani N.M., Vattuone M.A., Isla M.I. Antimicrobial activity of nine extracts of *Sechium edule* (Jacq.) Swartz, *Microb. Ecol. Health Dis*. **2003**, 15, 33-39.

Ordonez A.A.L., Gomez J.D., Vattuone M.A., Isla M.I. Antioxidant activities of *Sechium edule* (Jacq.) Swartz extracts, *Food. Chem.* **2006**, 97 (3), 452-458.

Oturan M.A. An ecologically effective water treatment technique using electrochemically generated hydroxyl radicals for in situ destruction of organic pollutants: Application to herbicide 2,4-D, *J. Appl. Electrochem.* **2000**, 30 (4), 475-482.

Oturan M.A., Aaron J.J., Oturan N., Pinson J. Degredation of chlorophenoxyacid herbicides in aqueous media, using a novel electrochemical method, *Pestic. Sci.* **1999**, 55, 558-562.

Oturan M.A., Pinson J. Hydroxylation by electrochemically generated hydroxyl radicals. mono- and polyhydroxylation of benzoic acid: Products and isomers' distribution, *J. Phys. Chem.* **1995**, 99, 13948-13954.

Ozcan A., Sahin Y., Koparal A.S., Oturan M.A. Degradation of picloram by the electro-Fenton process, *J. Hazard. Mater.* **2008a**, 153, 718-727.

Ozcan A., Sahin Y., Koparal A.S., Oturan M.A. Carbon sponge as a new cathode material for the electro-Fenton process: Comparison with carbon felt cathode and application to degradation of synthetic dye basic blue 3 in aqueous medium, *J. Electroanal. Chem.* **2008b**, 616 (1), 71-78.

Panizza M., Cerisola G. Application of diamond electrodes to electrochemical processes, *Electrochim. Acta* **2005**, 51 (2), 191-199.

Panizza M., Cerisola G. Direct and mediated anodic oxidation of organic pollutants, *Chem. Rev.* **2009**, 109 (12), 6541-6569.

Pignatello J. Dark and photoassisted Fe^{3+}-catalyzed degradation of chlorophenoxy herbicides by hydrogen peroxide, *Environ. Sci. Technol.* **1992**, 26, 944-951.

Ping J., Ru S., Fan K., Wu J., Ying Y. Copper oxide nanoparticles and ionic liquid modified carbon electrode for the non-enzymatic electrochemical sensing of hydrogen peroxide, *Microchim. Acta* **2010**, 171, 117-123.

Pozzo A., Palma L., Merli C., Petrucci E. An experimental comparison of a graphite electrode and a gas diffusion electrode for the cathodic production of hydrogen peroxide, *J. Appl. Electrochem.* **2005**, 35, 413-419.

Pozzo A., Petrucci E., Merli C. Electrogeneration of hydrogen peroxide in seawater and application to disinfection, *J Appl. Electrochem*. **2008**, 38, 997-1003.

Qiang Z., Chang J., Huang C. Electrochemical generation of hydrogen peroxide from dissolved oxygen in acidic solutions, *Water Res.* **2002**, 36, 85-94.

Qiang Z., Chang J., Huang C. Electrochemical regeneration of Fe^{2+} in Fenton oxidation processes, *Water Res.* **2003**, 37, 1308-1319.

Quintino M.S.M., Winnischofer H., Araki K., Toma H.E., Angnes L. Cobalt oxide/tetraruthenated cobalt-porphyrin composite for hydrogen peroxide amperometric sensors, *Analyst* **2005**, 130, 221-226.

Rajkumar M., Thiagarajan S., Chen S.M. Electrochemical fabrication of Rh-Pd particles and electrocatalytic applications, *J. Appl. Electrochem*. **2011**, 41, 663-668.

Rao Ch.V., Golder A.K. pH dependent size control, formation mechanism and antimicrobial functionality of bio-inspired AgNPs, *RSC Adv*. **2016**, 6, 95483-95493.

Reis R.M., Beati A.A.G.F., Rocha R.S., Assumpçao M.H.M.T., Santos M.C., Bertazzoli R., Lanza M.R.V. Use of gas diffusion electrode for the in situ generation of hydrogen peroxide in an electrochemical flow-by reactor, *Ind. Eng. Chem. Res.* **2012**, 51, 649-654.

Ricci F., Palleschi G. Sensor and biosensor preparation, optimisation and applications of prussian blue modified electrodes, *Biosens. Bioelectron.* **2005**, 21, 389-400.

Sakuragawa A., Taniai T., Okutani T. Fluorometric determination of microamounts of hydrogen peroxide with an immobilized enzyme prepared by coupling horseradish peroxidase to chitosan beads, *Anal. Chim. Acta* **1998**, 374, 191-200.

Samanta C. Direct synthesis of hydrogen peroxide from hydrogen and oxygen: An overview of recent developments in the process, *Appl. Catal. A* **2008**, 350, 133-149.

Shuan L., Yan G., Lian W.S., Yu Z., Fen F.Y., Johnson D.M., Ping H.Y. Degradation of organic pollutants by a Co_3O_4-graphite composite electrode in an electro-Fenton-like system, *Chin. Sci. Bull.* **2013**, 58, 2340-2346.

Siciliano T., Det Ommasi N., Morelli I., Braca A. Study of flavonoids of *Sechium edule* (*Jacq*) swartz (cucurbitaceae) different edible organs by liquid chromatography photodiode array mass spectrometry, *J. Agric. Food Chem.* **2004**, 52, 6510-6515.

Sires I., Arias C., Cabot P.L., Centellas F., Garrido J.A., Rodriguez R.M., Brillas E. Degradation of clofibric acid in acidic aqueous medium by electro-Fenton and photoelectro-Fenton, *Chemosphere* **2007a**, 66 (9), 1660-1669.

Sires I., Centellas F., Garrido J.A., Rodriguez R.M., Arias C., Cabot P.L., Brillas E. Mineralization of clofibric acid by electrochemical advanced oxidation processes using a boron-doped diamond anode and Fe^{2+} and UVA light as catalysts, *Appl. Catal. B* **2007b**, 72, 373-381.

Sires I., Garrido J.A., Brillas E. Performance of the electro-oxidation and electro-Fenton processes with a BDD anode for the treatment of low contents of pharmaceuticals in a real water matrix, *J. Electrochem.* **2013**, 19 (4), 300-313.

Skoumal M., Arias C., Cabot P.L., Centellas F., Garrido J.A., Rodriguez R.M., Brillas E. Mineralization of the biocide chloroxylenol by electrochemical advanced oxidation processes, *Chemosphere* **2008**, 71 (9), 1718-1729.

Skoumal M., Rodriguez R.M., Cabot P.L., Centellas F., Garrido J.A., Arias C., Brillas E. Electro-Fenton, UVA photoelectro-Fenton and solar photoelectro-Fenton degradation of the drug ibuprofen in acid aqueous medium using platinum and boron-doped diamond anodes, *Electrochim. Acta* **2009**, 54 (7), 2077-2085.

Sophia J., Muralidharan G. Amperometric sensing of hydrogen peroxide using glassy carbon electrode modified with copper nanoparticles, *Mater. Res. Bull.* **2015**, 70, 315-320.

Stucki S., Kotz R., Carcer B., Suter W. Electrochemical waste water treatment using high overvoltage anodes Part II: Anode performance and applications, *J. Appl. Electrochem.* **1991**, 21 (2), 99-104.

Su C.-C., Chang A.-T., Bellotindos L.M., Lu M.-C. Degradation of acetaminophen by Fenton and electro-Fenton processes in aerator reactor, *Sep. Purif. Technol.* **2012**, 99, 8-13.

Sudoh M., Kodera T., Sakai K., Zhang J.Q., Koide K. Oxidative degradation of aqueous phenol effluent with electrogenerated Fenton's reagent, *J. Chem. Eng. Jpn.* **1986**, 19 (6), 513-518.

Sun X., Dong S., Wang E. One-step preparation and characterization of poly (propyleneimine) dendrimer-protected silver nanoparticles, *Macromolecules* **2004**, 37, 7105-7108.

Sun Y., Pignatello J.J. Photochemical reactions involved in the total mineralization of 2,4-D by Fe^{3+}/H_2O_2/UV, *Environ. Sci. Technol.* **1993**, 27, 304-310.

Tanner P.A., Wong A.Y.S. Spectrophotometric determination of hydrogen peroxide in rainwater, *Anal. Chim. Acta* **1998**, 370, 279-287.

Walling C. Fenton's reagent revisited, *Acc. Chem. Res*. **1975**, 8, 125-133.

Wang A., Li Y., Estrada A.L. Mineralization of antibiotic sulfamethoxazole by photoelectro-Fenton treatment using activated carbon fiber cathode and under UVA irradiation, *Appl. Catal. B* **2011b**, 102, 378-386.

Wang A., Qu J., Ru J., Liu H., Ge J. Mineralization of an azo dye acid red 14 by electro-Fenton's reagent using an activated carbonfiber cathode, *Dyes Pigm.* **2005**, 65, 227-233.

Wang C., Liu H., Sun Z. Heterogeneous Photo-Fenton reaction catalyzed by nanosized iron oxides for water treatment, *Int. J. Photoenergy* **2012**, 2012, 1-10.

Wang C.T., Chou W.L., Chung M.H., Kuo Y.M. COD removal from real dyeing wastewater by electro-Fenton technology using an activated carbon fiber cathode, *Desalination* **2010**, 253, 129-134.

Wang C.T., Hu J.L., Chou W.L., Kuo Y.M. Removal of color from real dyeingwaste-water by electro-Fenton technology using a three-dimensional graphite cathode, *J. Hazard. Mater.* **2008**, 152, 601-606.

Wang H., Bo X., Bai J., Wang L.X., Guo L.P. Electrochemical applications of platinum–palladium alloy nanoparticles/large mesoporous carbon, *J. Electroanal. Chem.* **2011a**, 662, 281-287.

Wang J., Chen X.-J., Liao K.-M., Wang G.-H., Han M. Pd nanoparticle-modified electrodes for nonenzymatic hydrogen peroxide detection, *Nanoscale Res. Lett.* **2015**, 10, 311.1-311.6.

Wang J., Wang L., Di J., Tu Y. Electrodeposition of gold nanoparticles on indium/tin oxide electrode for fabrication of a disposable hydrogen peroxide biosensor, *Talanta* **2009**, 77, 1454-1459.

Watts R.J., Asce A.M., Sarasa J., Loge F.J., Asce A.M., Teel A.L. Oxidative and reductive pathways in manganese-catalyzed Fenton's reactions, *J. Environ. Eng.* **2005**, 131 (1), 158-164.

Wen F., Dong Y., Feng L., Wang S., Zhang S., Zhang X. Horseradish peroxidase functionalized fluorescent gold nanoclusters for hydrogen peroxide sensing, *Anal. Chem.* **2011**, 83, 1193-1196.

Wirzal M.D.H., Yusoff A.R.M., Zima J., Barek J. Degradation of ampicillin and penicillin G using anodic oxidation, *Int. J. Electrochem. Sci.* **2013**, 8, 8978-8988.

Wu S., Zhao H., Ju H., Shi C., Zhao J. Electrodeposition of silver–DNA hybrid nanoparticles for electrochemical sensing of hydrogen peroxide and glucose, *Electrochem. Commun.* **2006**, 8, 1197-1203.

Xi F., Zhao D., Wang X., Chen P. Non-enzymatic detection of hydrogen peroxide using a functionalized three-dimensional graphene electrode, *Electrochem. Commun.* **2013**, 26, 81-84.

Xin Y., Fu-Bing X., Hong-Wei L., Feng W., Di-Zhao C., Zhao-yang W. A novel H_2O_2 biosensor based on Fe_3O_4-Au magnetic nanoparticles coated horseradish peroxidase and graphene sheets-Nafion film modified screen-printed carbon electrode, *Electrochim. Acta* **2013**, 109, 750-755.

Xu B., Ye M.-L., Yu Y.-X., Zhang W.-D. A highly sensitive hydrogen peroxide amperometric sensor based on MnO_2-modified vertically aligned multiwalled carbon nanotubes, *Anal. Chim. Acta* **2010**, 674, 20-26.

Xu C., Liu Y., Su F., Liu A., Qiu H. Nanoporous PtAg and PtCu alloys with hollow ligaments for enhanced electrocatalysis and glucose biosensing, *Biosens. Bioelectron.* **2011**, 27, 160-166.

Yahiaoui I., Aissani-Benissad F., Fourcade F., Amrane A. Removal of tetracycline hydrochloride from water based on direct anodic oxidation (Pb/PbO_2 electrode) coupled to activated sludge culture, *Chem. Eng. J.* **2013**, 221, 418-425.

Yang W., Li Y., Bai Y., Sun C. Hydrogen peroxide biosensor based on myoglobin/colloidal gold nanoparticles immobilized on glassy carbon electrode by a Nafion film, *Sens. Actuators B-Chem.* **2006**, 115, 42-48.

Yao S., Xu J., Wang Y., Chen X., Xu Y., Hu S. A highly sensitive hydrogen peroxide amperometric sensor based on MnO_2 nanoparticles and dihexadecyl hydrogen phosphate composite film, *Anal. Chim. Acta* **2006**, 557, 78-84.

Zhang H., Fei C., Zhang D., Tang F. Degradation of 4-nitrophenol in aqueous medium by electro-Fenton method, *J. Hazard. Mater.* **2007**, 145, 227-232.

Zhang Y., Sun Y., Liu Z., Xu F., Cui K., Shi Y., Wen Z., Li Z. Au nanocages for highly sensitive and selective detection of H_2O_2, *J. Electroanal. Chem.* **2011**, 656, 23-28.

Zhao X., Hou Y., Liu H., Qiang Z., Qu J. Electro-oxidation of diclofenac at boron doped diamond: Kinetics and mechanism, *Electrochim. Acta* **2009**, 54, 4172-4179.

Zhou M., Yu Q., Lei L., Barton G. Electro-Fenton method for the removal of methyl red in an efficient electrochemical system, *Sep. Purif. Technol.* **2007**, 573, 380-387.

Zhou M.H., Dai Q.Z., Lei L.C., Ma C., Wang D. Long life modified lead dioxide anode for organic waste water treatment: electrochemical characteristics and degradation mechanism, *Environ. Sci. Technol.* **2005**, 39, 363-370.

Zhu M., Huang X., Liu L., Shen H. Spectrophotometric determination of hydrogen peroxide by using the cleavage of Eriochrome black T in the presence of peroxidase, *Talanta* **1997**, 44, 1407-1412.

Zuo Y., Holgne J. Formation of hydrogen peroxide and depletion of oxalic acid in atmospheric water by photolysis of iron (II)-oxalato complexes, *Environ. Sci. Technol.* **1992**, 26, 1014-1022.

Chapter–2

Materials and Methodologies

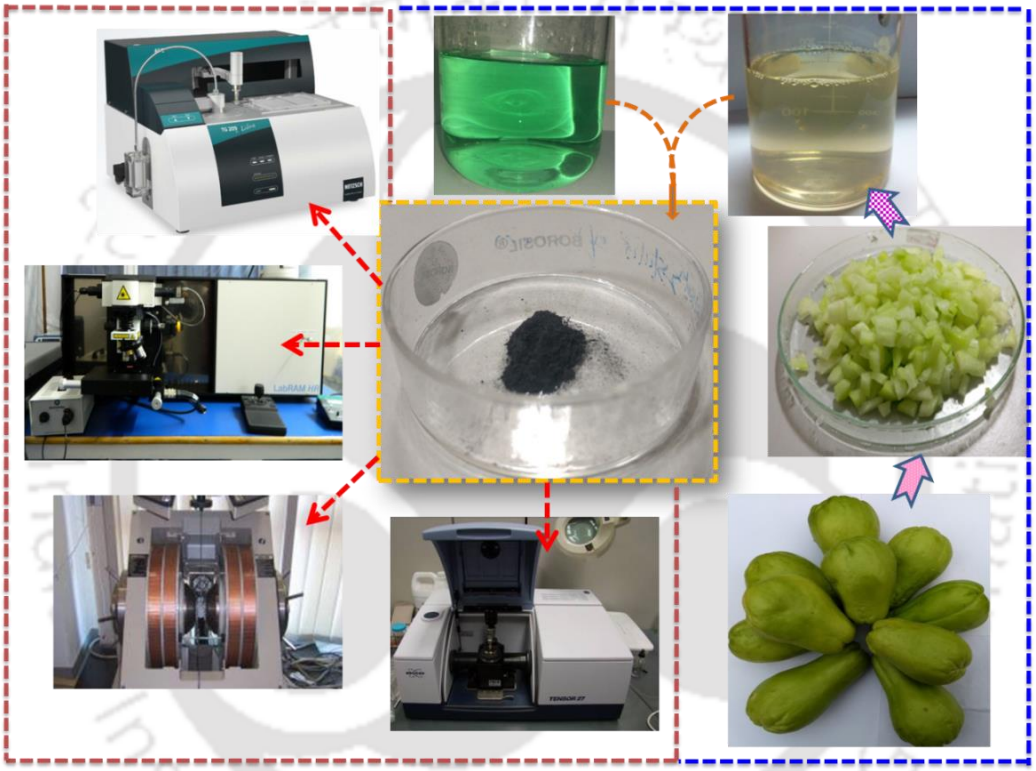

Chapter 2 describes the experimental details including the synthesis processes of Co_3O_4 and NiO NPs, fabrication of carbon paste electrodes, NPs coating on the electrodes surface, and electroanalytical techniques and experimentations on H_2O_2 generation and sensing. Specifications of all reagents and chemicals are documented in this chapter. Any specific change or deviation from what is stated here is detailed in the respective Section(s)/Chapter(s).

2.1 Materials and analytical reagents

All the chemicals employed in this study were of analytical grades and used without further purification. The chemicals and/or any reagents used for specific applications are detailed below. The background for the selection of *Sechium edule* used in this study as the source of the bio-extract/bio-analytes is provided in Section 2.2.

Chemicals used for H_2O_2 decomposition study using trace metals: The chemicals used for H_2O_2 decomposition, namely, copper sulphate ($CuSO_4$, $5H_2O$, assay ≥ 99%), calcium sulphate precipitated powder ($CaSO_4$, $2H_2O$), potassium sulphate (KSO_4, assay ≥ 99%), nickel sulphate ($NiSO_4$, $7H_2O$, assay 94-104%), manganese sulphate ($MnSO_4$, H_2O, assay ≥ 99%) were procured from Merck, Mumbai, India. Initial solution pH was adjusted using 1:5 (v/v) perchloric acid ($HClO_4$, assay ≥ 70%, Merck, Mumbai, India).

Reagents for H_2O_2 formation at commercial graphite plate: Supporting electrolytes (SEs), namely, $NaNO_3$ (assay 99%, Merck, Mumbai, India), NaCl (assay min 99.5%, Merck, Mumbai, India), Na_2SO_4 (assay ≥ 99%, Merck, Mumbai, India) and $NaClO_4.H_2O$ (assay 98-102%, LOBA Chemie, Mumbai, India) were used for H_2O_2 electro-generation studies at iso-moulded commercial graphite as the working electrode (WE). The commercial iso-moulded graphite rod (diameter 6.35 mm) (GM-10, Graphite store, USA) was employed to obtain the cyclic voltammogram and a graphite plate (GM-10, 10.16 cm × 10.16 cm × 3.18 mm) was employed to study the stability of the anode material during H_2O_2 formation. TiO_2 coated Ti (TiO_2–Ti) plates (10 cm × 8 cm × 1 mm) (Titanium Tantalum Products Limited, Chennai, India) were applied for the wastewater treatment as the counter electrode (CE). The solution pH was adjusted using H_2SO_4 (assay 95-98%, Merck, Mumbai, India). Milli-Q water (model: Elix 3) was used to prepare the all reagents and solutions.

Precursors of NiO and Co_3O_4 NPs synthesis: Nickel sulphate heptahydrate ($NiSO_4.7H_2O$, assay 97-104%) (LOBA Chemie, Mumbai, India) and cobalt (II) nitrate hexahydrate ($Co(NO_3)_2.6H_2O$, assay ≥ 97%) (Merck, Mumbai, India) used as the NiO and Co_3O_4 NPs precursors. pH of the precursor solutions were elevated using sodium hydroxide (NaOH, assay 98%) which was purchased from Merck, Mumbai, India.

Reagents employed for graphite paste and modified electrodes fabrication: Graphite powder (<20µm, Sigma Aldrich, Bangalore, India) and paraffin wax (LOBA Chemie, Mumbai, India) were employed for the electrode fabrication (Farahi et al., 2016). Either NiO NPs or Co_3O_4 NPs

(synthesis process outlined in Section 2.5.1) were brush coated on the surface of the working electrode (WE) with the help of Nafion (perfluorosulfonic acid-PTFE copolymer, 5% w/w solution, Alfa Aesar, Haverhill, USA) as a binder (Xia et al., 2014). A copper wire (ϕ 1 mm, conductivity 5.96×10^7 S/m at 20 °C) was inserted in the middle of the mould for the electrical connection.

Phosphate buffer solution (PBS) and H_2O_2 sensing: H_2O_2 sensing was performed in the phosphate buffer solution (PBS) (pH 7.2) (Su et al., 2016). PBS was prepared using 0.1 M sodium dihydrogen phosphate dihydrate ($NaH_2PO_4.2H_2O$, assay 99-100.5%) and 0.1 M disodium hydrogen phosphate (Na_2HPO_4, assay 99%) solutions (28:72 v/v) purchased from Merck, Mumbai, India. Hydrogen peroxide (H_2O_2, assay 30%) employed for the electrochemical sensing studies was purchased from LOBA Chemie, Mumbai, India.

Acetic acid (glacial 99-100%) (Merck, Mumbai, India), ascorbic acid (assay 99-100.5%) (LOBA Chemie, Mumbai, India), dopamine hydrochloride (assay 98%) (Sigma Aldrich, Bangalore, India), ethanol (assay 99.9%) (Changshu Yangyuan Chemicals, China), glucose (assay 99.4%) (Himedia Laboratories Pvt Ltd, Mumbai, India), and uric acid (assay ≥ 99%) (Sigma Aldrich, Bangalore, India) were used as the interfering species (Su et al., 2016) during H_2O_2 sensing for the selectivity study of the fabricated electrodes following a typical amperometric procedure (Section 2.5.5.2).

Chemicals employed for drug decomposition studies: Ciprofloxacin (CIP, assay min 98%) was obtained from Sigma-Aldrich (USA). $FeSO_4.7H_2O$ (assay 99%, Ranbaxy Fine Chemicals Limited, New Delhi, India) was used to prepare the stock solution of Fe^{2+} in the electro-Fenton process (EFP) (Yahya et al., 2014). CIP concentration was determined by High performance liquid chromatography (HPLC) using a mobile phase consisting of acetonitrile (assay min 99.9%, Spectrochem Pvt. Ltd, Mumbai, India) and tri-ethylamine (assay ≥ 99%, Merck, Mumbai, India). O-phosphoric acid (assay ≥ 85%, Merck, Mumbai, India) was used to adjust pH of the mobile phase solution (Giri and Golder, 2014). Potassium hydrogen phthalate ($C_8H_5KO_4$) (KHP) (assay 99%, Merck, Mumbai, India) was used as the standard organic compound to determine the total organic carbon (TOC) of drug solution before and during the EFP. The mobile phase was consisting of ammonium acetate (assay ≥ 98%, Sigma Aldrich, Bangalore, India), acetonitrile (assay min 99.9%, Spectrochem Pvt. Ltd, Mumbai, India), and water to acquire the LC-MS (liquid chromatography and mass spectroscopy) spectra during CIP

degradation (Kumari et al, 2016). pH of this mobile phase was adjusted using formic acid (assay ≥95%, Sigma Aldrich, Bangalore, India). The calibration solution for the instrument was prepared using acetonitrile, methanol (assay 99.8%, Fisher Scientific, Bangalore, India), and water. pH of the calibration solution was adjusted using acetic acid (glacial 99-100%) (Merck, Mumbai, India) (Kumari et al, 2016).

H_2O_2 concentration analysis: TiO_2 (assay ≥ 99%, Sigma Aldrich, Bangalore, India) was employed for the preparation of titanic sulphate reagent ($Ti_2(SO_4)$) which was used for the colourimetric determination of H_2O_2 concentration (Amin and Olson, 1966).

Titanium standard solution: The standard titanium solution ($(NH_4)_2TiF_6$) was procured from Merck, Mumbai, India and employed to obtain the calibration curve within the concentration range from 5 to 100 mg/L.

FTIR analysis reagents: Potassium bromide (KBr) (assay min. 99.5%, Merck, Mumbai, India) was used as the sample carrier to record the FTIR spectra having a 100% transmission window in the range of wave number from 4000 to 400 cm^{-1} (Huheey et al., 1993).

TEM and FESEM analyses: NPs were dispersed in acetone (assay min 99.0%, Himedia Laboratories Pvt Ltd, Mumbai, India) prior to capture the TEM (Transmission electron microscopy) and FESEM (Field emission scanning electron microscopy) micrographs (Section 2.4.10 of this Chapter). The carbon-coated copper grid for TEM analysis was obtained from EMS/Proscitech, Hatfield, UK. The glass slide used for FESEM analysis was procured from JSGW, Haryana, India).

2.2 Selection of *Sechium edule*

In this study, NiO and Co_3O_4 NPs were synthesized using the bio-extract prepared from the fruits of *Sechium Edule* (or simply *S. edule*) (Figure 2.1). It grows abundantly in the North-Eastern part of India, and the fruits are available almost in all the seasons. *S. edule* looks fleshy or fleshy-fibrous and come at different sizes (3-11 cm wide and 4.3-26.5 cm long), colors (whitish, light green, green, dark green and pale yellow), and shapes (elongated pyriform, pyriform, subpyriform subovoid, ovoid, globose, rounded and flattened) (Engels, 1983; Ordonez et al., 2006). The surface of the ripe fruits contains woody ridges or lenticels and, the pulp is pale green or whitish and tastes sweet or insipid in cultivated plants (Saade, 1996). The seed is ovoid, smooth and compressed and, germinates within the fruit.

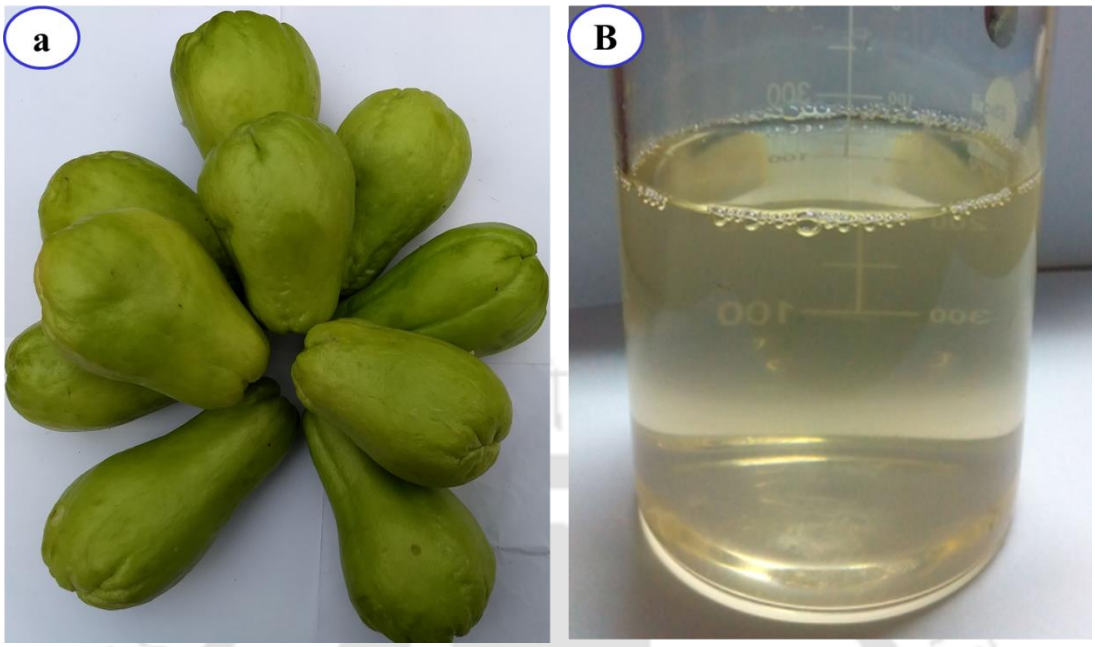

Figure 2.1: (a) Digital photograph of *S. edule*, and (b) Digital photograph of clarified *S. edule* bio-extract.

The *S. edule* plant is a hairy climbing shrub belonging to the family, Cucurbitaceae. It is also popularly known as *Chayote (*Hindi language*), Sayote, Choko, Chocho, Chow-Chow, Isqush (*Nepali*), Piskut (*Khasi language*), Sikut (*Garo language*)* and vegetable pear (Mishra and Das, 2015). *S. edule* is a good source of nutrients and vitamins (Table 2.1). The fruits and seeds have excellent antioxidant activity (Ordonez et al., 2006) and are rich in several important compounds such as ascorbic acid (AA) (0.294 mg/g on the dry basis) (Rao and Golder, 2016a), amino acids (12.9 mg/g on the dry basis), and polyphenols (Flick et al., 1978) (Table 2.1). However, the content of these compounds depends on the degree of maturity, climate, soil, and species variety, but it varies in close proximity for mature squash of the same variety grown in the same geographical site (Cadena-Iniguez et al., 2007). The variation of ascorbic acid (AA) one of the primary analytes present in the organs of squash is provided in Table 2.1. It can be seen that the AA concentration in a mature squash of the same variety varies is very close.

This species used in the present work (Figure 2.1) was originally discovered by Browne (1756) in Jamaica (Browne, 1756) and in 1763, it was classified simultaneously as *Sicyos edulis* by Jacquin (Cadena-Iniguez et al., 2007) and as *Chocho edulis* by Adanson (Cadena-Iniguez et

al., 2007). Later, Jacquin (1788) changed it to *C. edulis* and placed it in genus Chayota. A few years later, Swartz (1800) became the first to include this species in *Sechium*, when he proposed the combination by which it is still known, *Sechium Edule* or *S. edule* (Rao, 2017).

Table 2.1: *S. edule* plant details and chemical composition, and ascorbic acid content in various organs of squash. Data are reported per 100 g of dry matter (Cadena-Iniguez et al., 2007).

Characteristic of *S. edule*			
Botanical name	*Sechium edule*		
Family	Cucurbits		
Genus	Sechium		
Kingdom	Plant		
Tribe	Sicyeae		
Order	Cucurbitales		
Species	*S. edule*		
Composition of *S. edule*			
Composition	**Leaf**	**Fruit**	**Root**
Ascorbic acid (mg)	16	29.8	19
Flavonoid contents (g)	35	19.3	30.5
Energy (cal)	60	26-30	79
Protein (g)	4	0.9-1.1	2
Carbohydrate (g)	4.7	3.5-8.4	17.8
Phosphorous (µg)	108	20-27	34
Calcium (mg)	21.7-69.5	6.1-19	6.1-17.5
Nitrogen (g)	0.49-0.778	0.95-0.156	0.332
Thiamine (mg)	0.043-0.0119	0.03-0.33	0.041-0.08
Roboflavin (mg)	0.124-0.208	0.03-0.37	0.05-0.028
Niacin (mg)	0.919-1.19	0.35-1.1	0.7-1.04

Ascorbic acid (AA) content in various organs of squash, mg				
Leaf	**Fruit**	**Root**		**Source**
16	29.8	19	Country: Brazil Season: Rainy season (February-April)	Sing et al., 2015
-	28	-	Country: India (Sikkim)	Kapoor et al., 2014
-	20	-	Country: Central America Season:	Engels, 1983
-	29.4	-	Country: India (Guwahati)	**Present study**

The major producer countries are Mexico, Costa Rica, Brazil, and the Dominical Republic with 360, 170, 50 and 2.3 thousand tons per year. In Mexico, *S. edule* is in fourth place after avocado, tomato, and coffee as an export product (Cadena-Iniguez et al., 2007). It is also extensively cultivated in India, Australia, Algeria, and New Zealand. In India, it is mostly cultivated in the hill regions of Assam, Meghalaya, Manipur, Mizoram, Nagaland, Sikkim and, West Bengal.

In India, Mizoram is the largest producer of *S. edule* mainly in Silphir area having a cooler climate (8-32 °C) and good annual rainfall (2500-3000 mm) (Singh et al., 2015). In Mizoram, the area of *S. edule* production is increased to 714 hectare (hec) in 2008 from 535 hectare in 2002, and typical production is in between 20 and 25 tons/hec in organic-rich soil. The production of *S. edule* in Assam (India) is about 20-22 tons/hec with a total production area of 110 hec in Assam, and the average production in India is about 10-15 tons/hec (Morton, 1981).

The fruit extracts exhibit strong reducing power and, it coverts potassium ferricyanide to potassium ferrocyanide of about 2000 ASE/mg which was used for the antioxidant activity test (Ordonez et al., 2006). ASE means that reducing power of 1 mg sample is equivalent (E) to reducing power of 1 nmol AA. The analytes present in the extract act as strong electron and hydrogen donors. It could break the radical chain reaction and convert the free radicals to stable products. This particular study along with our recent works for the synthesis of Ag NPs and Pt NPs (Rao and Golder, 2016a; Rao and Golder, 2016b) provided the foundation for the selection of *S. edule* for the bio-mediated synthesis of NiO and Co_3O_4 NPs. The present work primarily focuses on the synthesis of mono-crystalline NiO and Co_3O_4 NPs using the analytes present in the aqueous extract of squash for electrocatalytic H_2O_2 formation and sensing.

2.3 Preparation of bio-extract

The bio-extract was prepared using the mature squash of about 150 g per fruit. An amount of 75 g fruit pieces (5 mm × 4mm × 2.5 mm) after the removal of peels were added to 350 mL deionized water and, the mixture was heated for 12 h at 85-90 ºC (Rao and Golder, 2016b) with stirring at 300 rpm on a magnetic stirrer (Tarsons Products Pvt. Ltd., Kolkata, India). AA didn't show much degradation during the extraction below this temperature (Plaza et al., 2011; Wawire et al., 2011). After that, the bio-extract was filtered out using 2 μm filter paper (Prefilter AP25, Glass fiber filters with binders, Millipore, Germany) and, a volume of 390 mL

bio-extract (pH 5.63) was collected. The fresh bio-extract was prepared before each experiment. The schematic flow diagram of the bio-extract preparation process is shown in Figure 2.2.

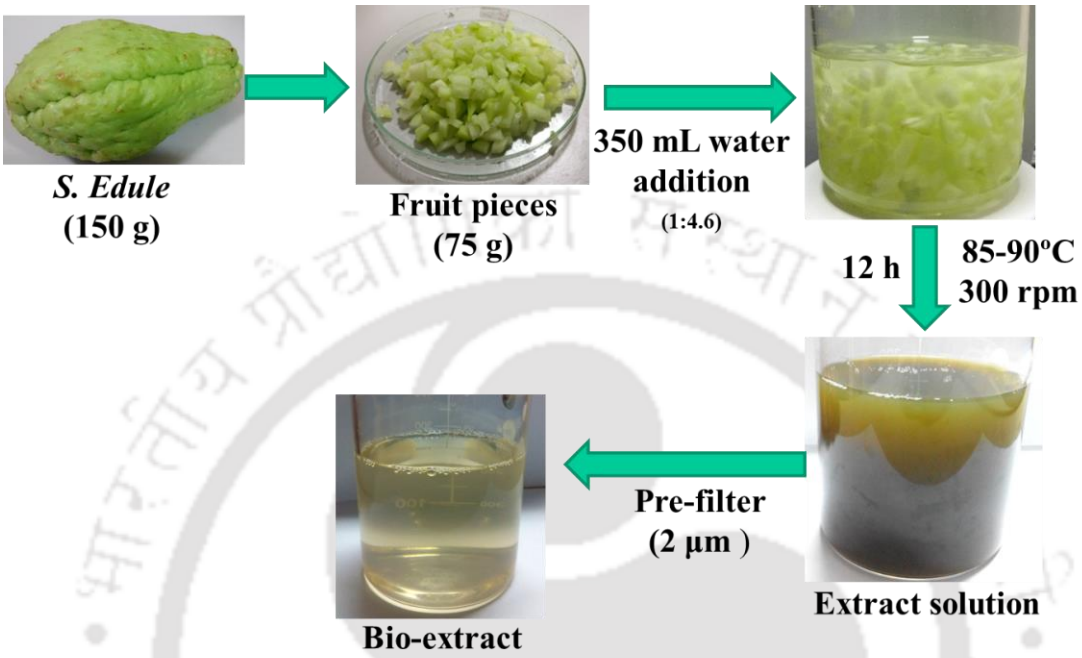

Figure 2.2: Schematic diagram showing the steps involved in bio-extract preparation using *S. edule*.

2.4 Analytical techniques

2.4.1 Atomic absorption spectroscopy (AAS)

The TiO_2–Ti anode was corroded during the H_2O_2 electro-generation study in the case of commercial graphite and TiO_2–Ti system. The concentration of Ti in the supporting electrolyte was analysed by AAS (240FS, M/s Varian instrument, Australia). A calibration curve was developed using the standard Ti solution within a concentration range of 5 to 100 mg/L (Figure 2.3). An acetylene (99.0% purity, pressure 11 psi)-nitrous oxide (99.5% purity, pressure 50 psi) flame was used. The calibration curve was freshly prepared by an appropriate dilution of the stock solution before each experiment.

2.4.2 Optical microscopy

The surface morphology of the electrode (graphite and TiO_2-Ti) was studied by capturing the optical microscopic images (DM 2500M, Leica Microsystem Ltd., Mumbai, India) before

and after the reaction during H_2O_2 generation. The arithmetic average surface roughness (Ra) of the electrodes was determined using Gwyddion 2.45 software (version 2).

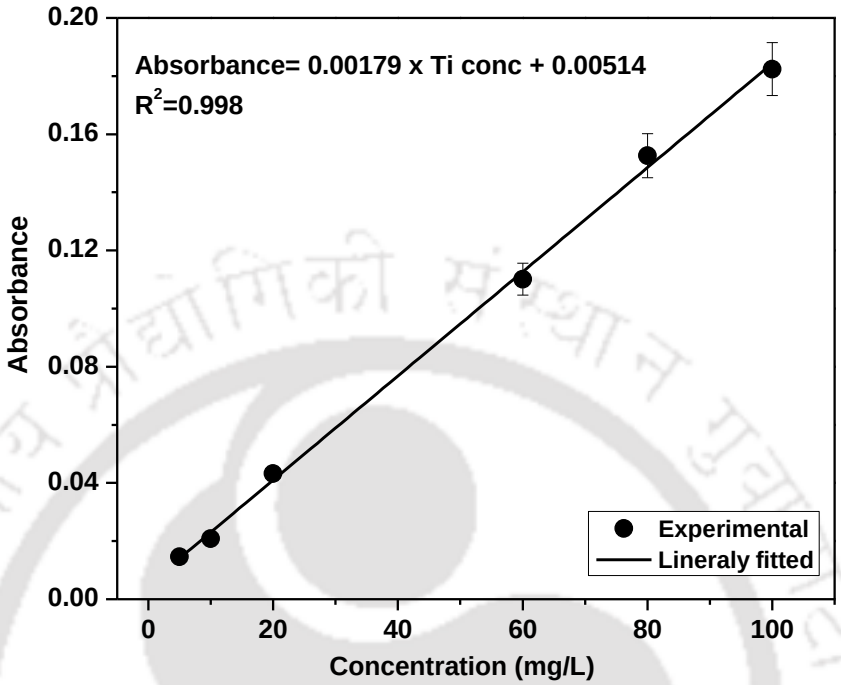

Figure 2.3: Calibration curve developed for the determination of Ti concentration using AAS in the flame mode of operation.

2.4.3 X-ray diffraction (XRD)

The phase purity and crystalline structures of un-calcined and calcined metal oxide NPs were studied by XRD (D8 Advance, Bruker Axis, Germany) with a monochromatic high-intensity Cu Kα1 radiation (λ=1.54Å) at 40 kV and 40 mA with a scanning speed of 0.5 step/s over a scan range from 10 to 85° 2θ angles. An amount of about 20 mg dried sample was used to capture the diffractogram.

2.4.4 Raman spectroscopy

The Raman spectra of synthesized metal oxide NPs were measured by Laser Micro-Raman System (LabRam HR, Horiba Jobin Vyon, USA) in the Raman shift range of 100-3000 cm^{-1}.

2.4.5 Thermogravimetric analysis (TGA)

The mass losses of NiO and Co_3O_4 NPs and, control specimens with the temperature were studied by the Thermogravimetric analysis (TGA) (TG 209 F1 Libra, Netzsch, Selb,

Germany). An amount of 10 mg sample was used in the temperature range of 30 to 800 °C. A heating rate of 10 °C/min with an N_2 flow rate of 20 mL/min was applied (Rao and Golder, 2016b).

2.4.6 Fourier transforms infrared spectroscopy (FTIR)

The FTIR spectra of NiO and Co_3O_4 NPs were obtained using IR Affinity-1 FTIR spectrometer (Shimadzu, Japan) in the KBr pellet method. KBr salt was dried at 105 ºC in a hot air oven before analysis. At the beginning, the background correction was done with the pure KBr pellet by scanning from 400 to 4000 cm^{-1} with a resolution of 4 cm^{-1}. The KBr salt and sample was grinded at a ratio of 99:1 (w/w) in a clean mortar and pestle for better homogenization. It was then transferred to the pellet casting die. The pressure of 5 to 7 tons was imposed to create a thin pellet.

2.4.7 BET surface analyser

The specific surface area was found out by using Brunauer–Emmett–Teller (BET) analyzer (SA 3100, Beckman Coulter, Switzerland) from the nitrogen adsorption isotherm. The samples were degassed at 150 °C for 5 h before nitrogen adsorption. The parameters like pore size, pore volume, and Barrett–Joyner–Halenda (BJH) surface area, adsorption-desorption curve were obtained from the BET analysis.

2.4.8 UV-Vis spectroscopy

The concentration of H_2O_2 was measured by the UV-Vis spectrophotometry (UV-2600, Shimadzu, Tokyo, Japan) with an optical path length of 1 cm during its electro-generation by the titanic sulphate ($Ti(SO_4)_2$) method (Amin and Olson, 1966). A yellow coloured complex of Ti^{4+} and H_2O_2 was formed in the presence of $TiSO_4$ reagent. The absorbance was recorded at 410 nm. A series of standard solution (0 to 50 mg/L) of H_2O_2 was prepared for the calibration of the instrument. A linear relationship was found as H_2O_2 concentration = 43.95 × Absorbance [mg/L] (R^2=0.998) (Figure 2.4). The liquid sample was withdrawn from the reactor at every 20 min (when TiO_2–Ti and graphite plate were used) or 30 min (when fabricated electrode was used) up to 2 h during H_2O_2 electro-generation studies.

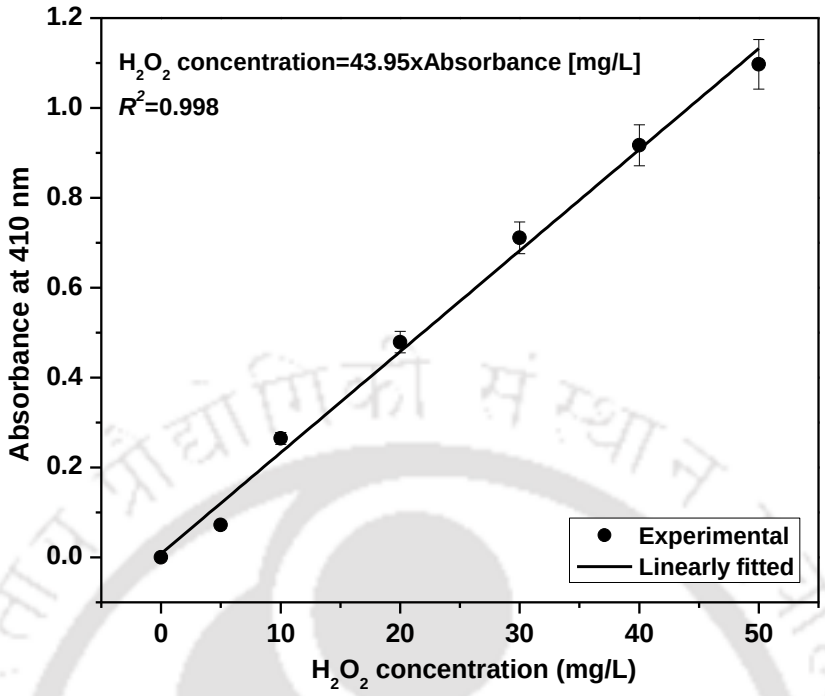

Figure 2.4: Calibration curve developed for the determination of H_2O_2 concentration from the UV-Vis spectroscopy by recording the absorbance at λ_{max}=410 nm.

The diffuse reflectance spectra of NiO and Co_3O_4 NPs (solid samples) were obtained to determine the band gap energy using the same instrument with a solid sample module. The absorption edge for NiO NPs was found between 302 and 398 nm wavelengths. Similarly for Co_3O_4 NPs, two absorption bands were also found at 350-600 and 600-800 nm. The optical bandgap (E_g) for individual NPs was calculated from the indirect transition model (Eq. 2.1) (Motahari et al., 2015).

$$(Ahv)^2=B(hv-E_g) \quad (2.1)$$

where, A is optical absorbance, hv is photon energy (eV), B is a constant specific to the material. The bandgap was determined by extrapolating the linear region of the $(Ahv)^2$ versus hv curve).

2.4.9 Vibrating sample magnetometry (VSM)

The magnetic properties of synthesized metal oxide NPs were determined by vibrating sample magnetometer (VSM) (7410 series, Lakeshore, USA) in the magnetic field range of −15 to +15 kOe at room temperature. The software, IDEASVSM, supplied by the manufacturer of the

instrument was employed to program the measurement sequence starting from zero magnetic field to maximum applied field. The exciter (7410 series, Lakeshore, USA) was vibrated at a frequency of 72 Hz and, the signal received from the hall probe and the pick-up coils is converted into the magnetic moment of the sample. The magnetic field is increased automatically in the user-defined steps for obtaining the magnetic hysteresis (M-H) loop.

2.4.10 Electron and atomic force microscopies

The particle size and surface morphologies of both NiO and Co_3O_4 NPs were analyzed by using Transmission electron microscopy (TEM) (EM 2100, JEOL, Tokyo, Japan). A quantity of about 20 mg particles was dispersed in 10 mL acetone and soaked well for few minutes. The suspension was then placed in an ultrasonic bath (50 Hz, Jeio Tech Co. Ltd., Seol, Korea) for about 30 min to segregate individual particles. One drop suspension was deposited carefully on the carbon-coated copper grid, and the film on the TEM grid was left for 2 min. This grid was allowed to dry in a hot air oven (ROV/DG, Reico Equipment and Instrument Pvt. Ltd., Kolkata, India) for overnight at 50-60 °C. High resolution TEM (HRTEM) and, selected area diffraction pattern (SAED) were acquired using the same instrument.

The above sample preparation procedure was adopted for Field emission scanning electron microscopy (FESEM) (Sigma, Zeiss, Jena, Germany) using a glass slide instead of a copper grid. The surface morphologies of metal oxide NPs were also recorded by atomic force microscope (AFM) (5500 series, Agilent, USA).

2.4.11 High performance liquid chromatography (HPLC)

C_{18} HPLC column (150 mm length, ∅ 3.5 mm) was used for the analysis of concentration of CIP drug. HPLC instrument (26462, Simadzu, Japan) equipped with a UV-visible detector was employed for the chromatographic determination. Acetonitrile, water, and tri-ethylamine (20:80:0.1 v/v/v) at a flow rate of 1 mL/min was used as the mobile phase and scanned at a wavelength of 280 nm (Hubicka et al., 2013; Giri and Golder, 2014). pH was adjusted to 3.0 using 5% (v/v) o-phosphoric acid. The scanning was performed at a wavelength of 254 nm (Feldmann et al., 2008). The retention time of CIP was found at 7.2 min (Figure 2.5a). The calibration curve (Figure 2.5b) of CIP was developed within the concentration range from 1.0 to 15 mg/L and the calibration curve equation was obtained as Peak-area = 1474.98×[CIP] + 673.33 (R^2= 0.99).

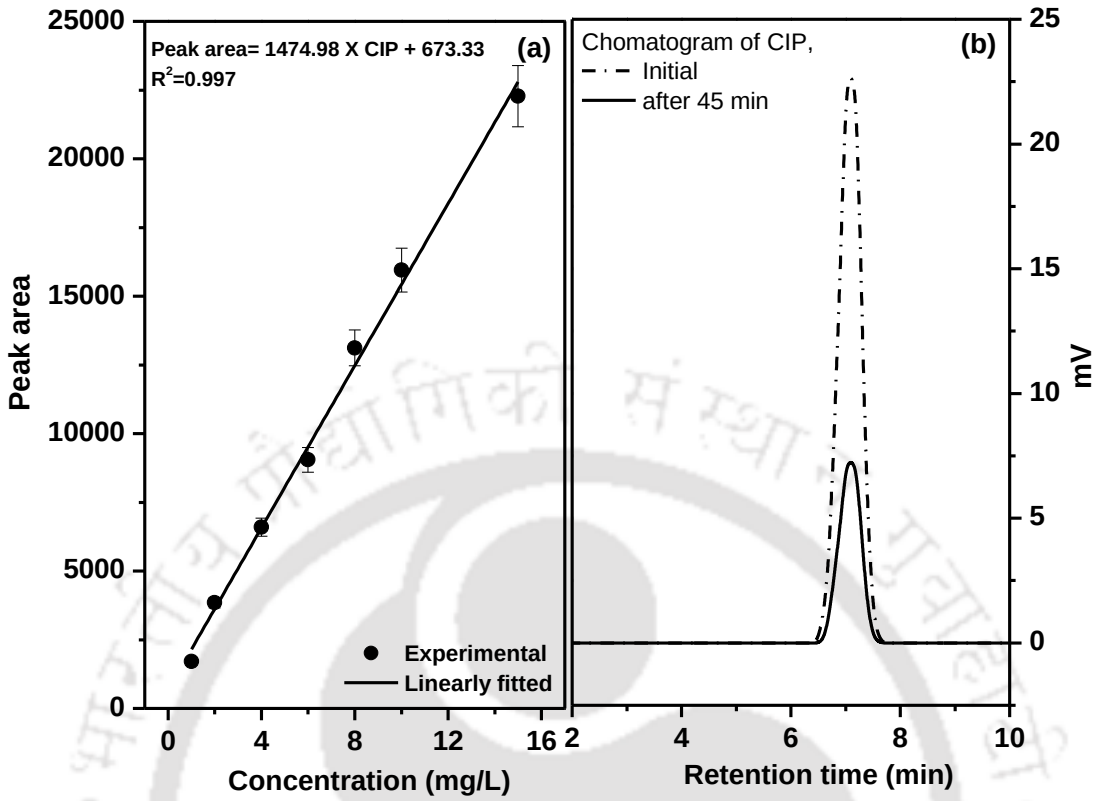

Figure 2.5: (a) Calibration curves of CIP concentration and (b) Chromatogram of pure CIP (15 mg/L) at room temperature before and after 45 min of reaction.

2.4.12 Total organic carbon (TOC) analysis

TOC analyser of O.I. Analytical (1030C, Aurora, USA) was used for the determination of TOC before and after the experiments during CIP decomposition studies. The non-dispersive infrared (NDIR) method was adopted for detection. TOC concentration of the sample was calculated by comparing its carbon content with potassium hydrogen phthalate (KHP) used as a standard compound. The calibration curve was determined as Peak-area= 27016.98 [TOC (mg/L)] + 449977.95 with R^2 = 0.99 in the range of 0.5 to 25 mg/L of TOC (Figure 2.6). The details are provided in the earlier work of the same research group (Giri, 2014).

2.4.13 Liquid chromatography-mass spectroscopy (LC-MS)

The chromatographic separation was performed using a HPLC (3100, Thermo Scientific, San Jose, USA) system tandem with a triple quadrupole Orbitrap mass spectra-mass spectra (MS-MS) system. It is composed of an ultimate 3000 rapid separation LC (Dionex Inc., Sunnyvale, CA, USA) attached to a Thermo Exactive plus Orbitrap triple quadrupole Mass

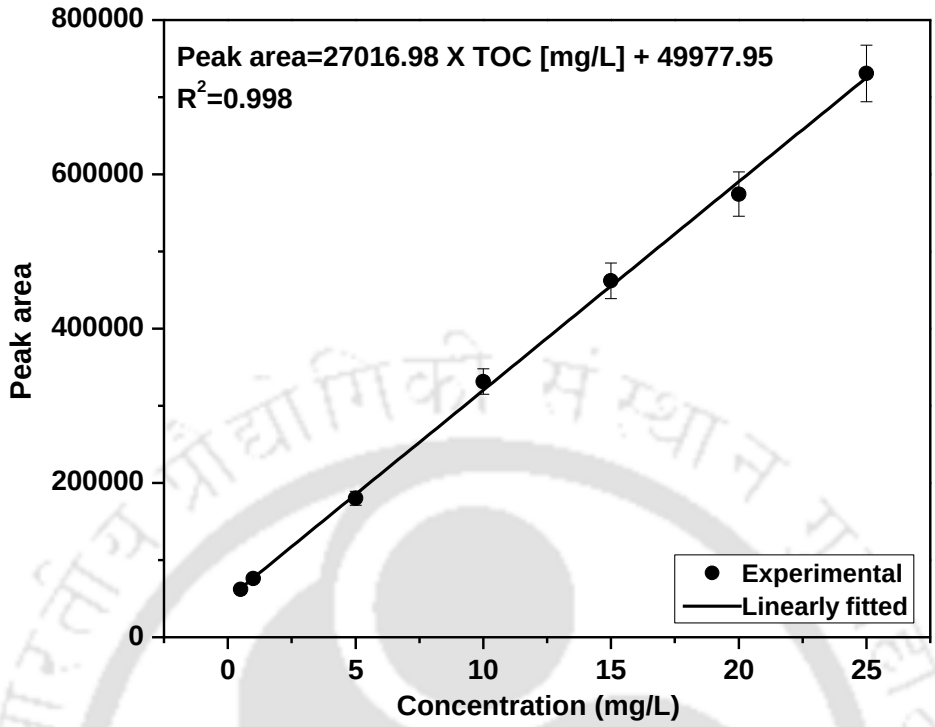

Figure 2.6: Calibration curve developed for the determination of TOC during CIP decomposition.

spectrometer (Thermo Scientific) equipped with an electrospray ionization (ESI) interface. A Hypersil Gold C18 column (150 mm ×3.00 mm, Thermo, USA) was used for the chromatographic separation at 25 °C equipped with an RS-3000 auto sampler (Dionex Inc., Sunnyvale, CA, USA). The mobile phase A was consisting of 10 mM ammonium acetate in water at pH 5.0 adjusted with 0.01% formic acid. The mobile phase B was 100% acetonitrile. A gradient mobile phase flow rate of 0.5 mL/min was maintained as: (i) 95% A for first 2 min, (ii) 5 to 95 % B from 2 to 8 min, (iii) 95% B for 8 to 9 min and, (iv) return back to 5% B in last 1 min (Kumari et al., 2016). The mass spectra were recorded using a photodiode array (PDA) detector. The Xcalibur software supplied with the instrument was used for data acquisition and processing.

2.5 Experimental procedure

In this section, the detail methodologies of NiO and Co_3O_4 NPs synthesis, electrodes fabrication and electrochemical analyses are outlined.

2.5.1 Synthesis of NiO and Co_3O_4 NPs

In a typical experiment, an equal volume of 50 mM $NiSO_4$ (pH ~3.85) and as-prepared bio-extract was mixed by the vigorous stirring (300 rpm) for 10 min. pH of this mixture was increased from 4.65 to 11 by the drop-wise addition of 2 M NaOH. The residue after 48 h of continuous stirring at 65-70 ºC was cooled down to room temperature and, collected by centrifugation at 4000 rpm for 5 min (K 70, REMI Instruments Ltd., India). It was then dispersed in a deionized water-ethanol solution (30:70 %) and sonicated for 10 min (50 Hz, Jeio Tech Co. Ltd., Seol, Korea). The residue was recovered by centrifugation as stated before. This procedure was repeated thrice to eliminate uncoordinated biomolecules present in residue (Rao and Golder,

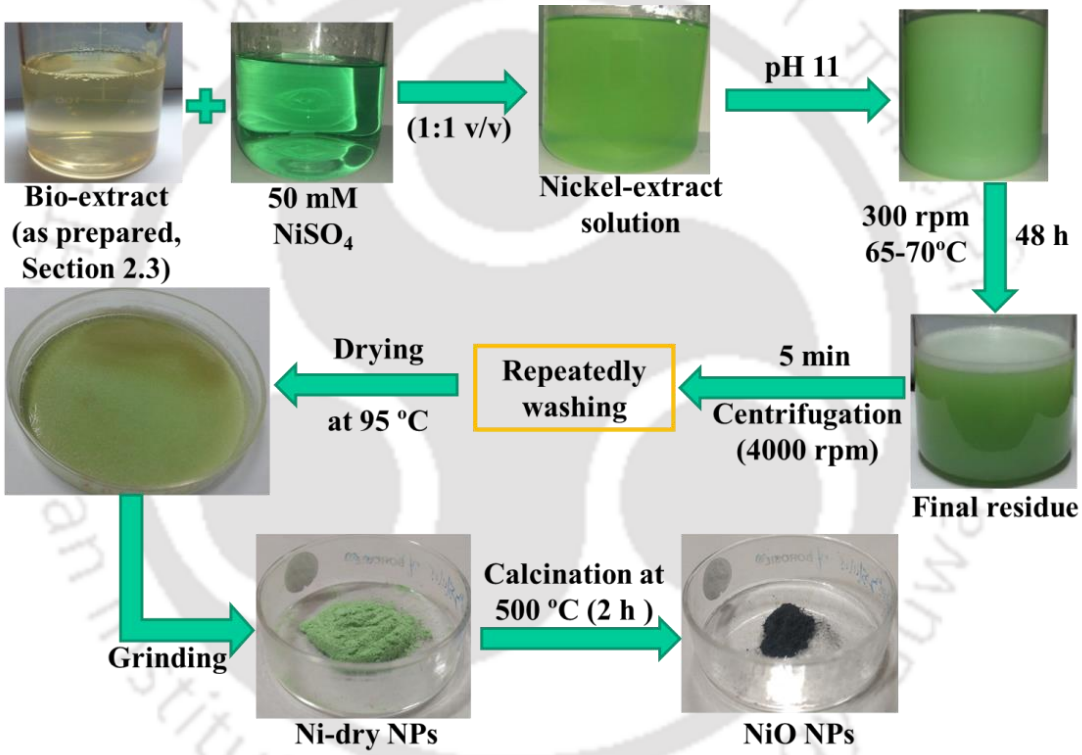

Figure 2.7: Schematic diagram showing various steps of NiO NPs synthesis using the analytes extracted from *S. edule*.

2016b). The so called clean residue was dried (termed as Ni-dry) at 95 ºC in a hot air oven (ROV/DG, Reico Equipment and Instrument Pvt. Ltd., Kolkata, India) and, then calcined at 500 ºC for a period 2 h (Wang et al., 2017) in a muffle furnace (LEF-115P-2, Daihan Labtech Co., Ltd., Namyanglu-City, South Korea) for the formation of NiO NPs. The experimental steps for the synthesis of NiO NPs are schematized in Figure 2.7. In the case of control experiment

(termed as Ni-control), the same procedure was followed, however, without the use of bio-extract/analytes. NiO NPs were also prepared using commercial AA of 10 mM (Barve et al., 2014) instead of using the bio-extract without changing other experimental condition.

A similar methodology was adopted for the synthesis of Co_3O_4 NPs and, an amount of 50 mM Co(II) solution (pH 5.16) was taken in a typical experiment. At the end of the experiment, the residue was first dried at 95 ºC in a hot air oven and, then calcined at 500 and 700 ºC for a period 6 and 12 h in a muffle furnace (Patil et al., 2012; Sharifi et al., 2013). Co_3O_4/700℃/6h denotes the Co_3O_4 NPs calcined at 700 ℃ for 6 h and, the similar nomenclature was used for the NPs calcined at different temperature and time. The flow diagram of Co_3O_4 NPs synthesis is schematized in Figure 2.8.

Figure 2.8: Schematic diagram showing the steps of Co_3O_4 NPs synthesis.

2.5.2 Graphite paste electrode and modified electrode fabrications

A quantity of 3.75 g graphite and 2.25 g paraffin wax were mixed uniformly by heating at 60 °C for 15-20 min (Farahi et al., 2016). The mixture was compacted into a rectangular wooden mould (55 mm × 8 mm × 4 mm), and the hot graphite-paraffin paste was compacted in the mould. This process is schematically shown in Figure 2.9a. A copper wire (ϕ 1 mm, conductivity 5.96×10^7 S/m at 20 °C) was inserted in the middle of the mould for the electrical

connection and, it was then cooled to room temperature. The solidified electrode (or simply graphite electrode) was then removed from the mould (Zayed and Arida, 2013).

An amount of 10 mg NiO NPs was dispersed in 1 mL 0.5 % Nafion solution and homogenized by sonication (40 kHz) for 2 h and, the suspension was then brush-coated on the surface of the graphite electrode. The modified electrode (termed as graphite/NiO NPs electrode) was then left for 12 h in room temperature for drying. The graphite/NiO NPs electrode was washed gently with deionized water and, air-dried before the use (Xia et al., 2014). The process schematics are illustrated in Figure 2.9b. The same methodology was adopted for the electrode surface modification using Ni-control (termed as graphite/Ni-control electrode) and Ni-dry particles (termed as graphite/Ni-dry electrode), and Co_3O_4 NPs (termed as graphite-Co_3O_4/ calcination temperature/calcination time).

Figure 2.9: (a) Schematic diagram for the fabrication of graphite support electrode and (b) NiO NPs immobilization on the support electrode.

2.5.3 Test procedure for H_2O_2 decomposition study

The decomposition behaviour of H_2O_2 was tested at the beginning before electro-catalysed H_2O_2 generation and sensing. For the decomposition study, the concentration of H_2O_2 was taken as 60 and 600 mg/L. A volume of 40 mL H_2O_2 solution at different pH was taken in 50 mL capacity poly-propylene tubes (Tarsons Products Pvt. Ltd., Kolkata, India). pH was

adjusted using 2 M NaOH and 0.5 M H_2SO_4. All the tubes were tightly capped and covered by Al-foil to protect from light. The experimental temperature was maintained at 30, 50, and 70 °C in a thermostatic water-bath (RWB/T, Integrated Electrolife System, Kolkata, India). The final H_2O_2 concentration was determined after 10 h by diluting the sample, whenever required, in proper concentration range. The background cations, namely, K^+, Cu^{2+}, Ca^{2+}, Mn^{2+}, Co^+, and Ni^{2+} were added in the range of 2 to 10 mg/L both at acidic and alkaline pH for a reaction time of 10 h to observe the effect of these trace metal ions on H_2O_2 decomposition.

2.5.4 Cyclic voltammetry (CVs) of H_2O_2 formation

2.5.4.1 Graphite/graphite and graphite/TiO_2–Ti electrodes system

The cyclic voltammetry (CV) was performed in a 220 mL capacity undivided three-electrode cell using a potentiostat/galvanostat (AUTOLAB 302N, Metrohm Autolab B.V, Netherlands) at room temperature. A pictorial image of the experimental set up is illustrated in Figure 2.10. In this case, the graphite rod of 6.35 mm diameter and Pt-wire were used as the WE and CE (graphite/Pt) to avoid the interference of TiO_2-Ti corrosion on the redox potentials. Ag/AgCl (3 M KCl) was employed as the reference electrode (RE). The reference electrode was inserted into a Luggin capillary filled with 3 M KCl solution and placed in the closest vicinity by contacting the tip of the Luggin capillary to the surface of WE. The diameter of the WE was selected to ensure H_2O_2 formation controlled by O_2 diffusion (Qiang et al., 2002). The distance between the WE and CE was 0.5 cm. The concentration of supporting electrolyte (SE) was 0.5 M

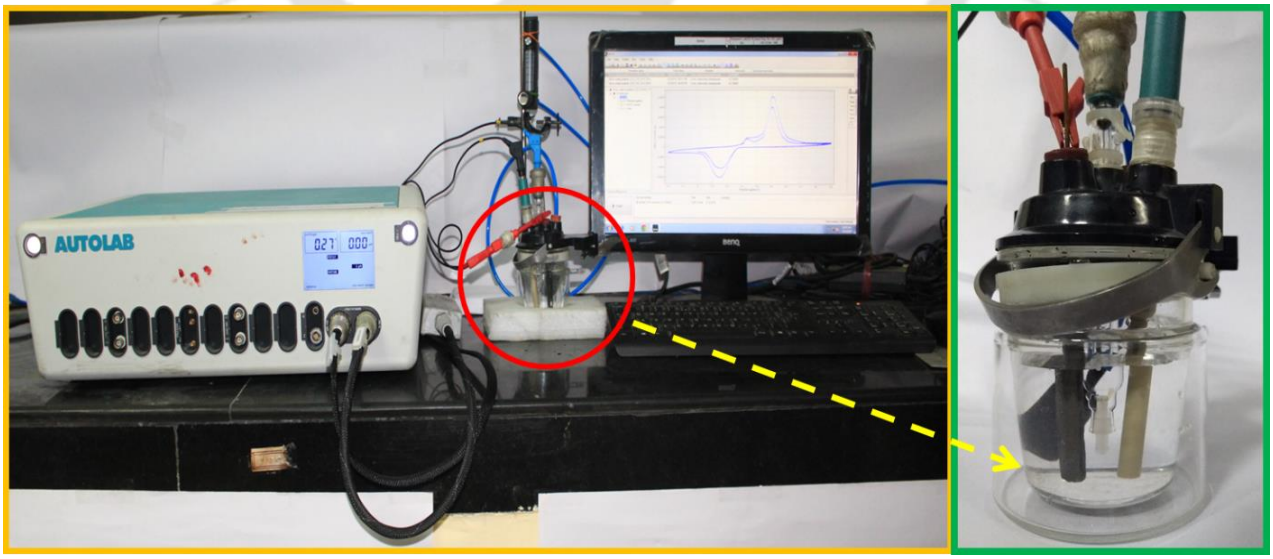

Figure 2.10: Pictorial image of experimental set up employed in this study.

and pH was adjusted to 2.5 as outlined before. The cyclic voltammogram was recorded after DO saturation by continuous bubbling of oxygen (99.995% purity) at the bottom of the WE at a flow rate of 1.2 LPM. The CV was obtained by sweeping from $-E_{cat}$ = 1.5 to –1.5 V vs. Ag/AgCl using $NaNO_3$ and NaCl as the SE and from $-E_{cat}$ = 2.0 to –2.0 V vs. Ag/AgCl using Na_2SO_4 and $NaClO_4$ as the SE at a scan rate 50 mV/s in 190 mL SE solution. The software (NOVA version 1.11) provided with the instrument by the manufacturer was used to monitor the electrochemical experiments and for data recording.

2.5.4.2 CV experiments in fabricated electrode system

A 220 mL capacity undivided three-electrode cell was also employed consisting of WE (graphite, graphite/Ni-control, graphite/Ni-dry or graphite/NiO NPs), Pt CE (2 mm diameter) and Ag/AgCl (3 M KCl) RE to record the CVs for investigating the electrochemical behaviour of H_2O_2 generation using the potentiostat/galvanostat at room temperature. The experiments were conducted using the same electrochemical cell of 190 mL capacity containing 0.5 M Na_2SO_4 as the SE. The selection of SE was based on H_2O_2 electro-generation studies with the graphite/graphite and graphite/TiO_2–Ti system (Section 2.5.3.1). O_2 (99.99 % purity) purging with a flow rate of 1.0 LPM was continued from 20 min before the beginning of the experiment. The scan rate and pH of the SE solution was varied from 1 to 200 mV/s and 1.5 to 4.5, respectively. pH of the electrolyte solution was adjusted using the dilute H_2SO_4 solution (0.5 M). A similar method was followed for the graphite-Co_3O_4 NPs electrode system (Co_3O_4 NPs catalysed system) with a potential range of $-E_{cat}$ = –0.1 to 0.5 V.

2.5.5 CVs of H_2O_2 sensing

The cyclic voltagrams were recorded using the same electrochemical cell of 190 mL capacity containing 0.1 M PBS (pH 7.2) (Su et al., 2016). The concentration of H_2O_2 was varied from 1 to 1000 µM. N_2 purging was continued from 20 min before the beginning of the experiment at a flow rate of 1.2 LPM. The scanning (1 -100 mV/s) was performed by employing the same potentiostat/galvanostat. The fabricated electrodes (graphite-Co_3O_4 NPs or graphite-NiO NPs) were used as the WE against Pt wire (2 mm diameter) as the CE, and Ag/AgCl (3 M KCl) as the RE. All the experiments were carried out at room temperature.

The selectivity of Co_3O_4 and NiO NPs modified electrodes towards H_2O_2 detection was tested through the addition of acetic acid, ascorbic acid, dopamine, glucose, and uric acid with a

concentration of 0.1 mM to cause force interference. The experiment was started following a typical amperometric procedure (Section 2.5.5.2 of this Chapter) with the successive addition (every 50 s) of 1 mM H_2O_2 in 0.1 M PBS at $-E_{cat} = -0.117$ V vs. Ag/AgCl with the Co_3O_4 NPs modified electrodes. It was at $-E_{cat} = -0.129$ V with the NiO NPs modified electrodes. The interfering compounds were added in between 400-700 s and 1000-1300 s for the Co_3O_4 NPs modified electrode. In the case of NiO NPs modified electrode, acetic acid, ascorbic acid, and dopamine were added in between 300 and 450 s, 900 and 1050 s, 600 and 750 s, and 1200 and 1350 s.

2.5.6 Chronoamperometric test

2.5.6.1 H_2O_2 generation in graphite/graphite and graphite/TiO_2–Ti electrodes system

Two combinations of electrodes, i.e., graphite/graphite and graphite/TiO_2-Ti as the WE and as the CE were used, with an effective area of 69 cm^2 against Ag/AgCl as the RE. The electrodes spacing between the WE and CE was 2 cm. The cathode potentials ($-E_{cat}$) were precisely controlled with respect to the reference electrode and it was varied from 0.1 to 0.7 V vs. Ag/AgCl using a potentiostat/galvanostat. The $-E_{cat}$ and the response current were recorded using NOVA software (version 1.11). Before electrolysis, the electrolyte solution was pre-saturated with DO by sparging high purity compressed O_2 (99.99%) at 4 LPM flow rate for 15 min. Thereafter, O_2 was sparged continuously near the WE.

The chronoamperometric experiment was carried out at room temperature in the batch mode using a 4 L capacity three-electrode electrolyser made of Perspex. The electrolyte solution volume was 2 L. The cell was placed on a magnetic stirrer and agitated continuously at 300 rpm. The solution pH was adjusted using H_2SO_4 solution (2 M). NaCl, $NaClO_4$, $NaNO_3$, and Na_2SO_4 were added individually as SE. The concentrations of SEs were taken as 0.05, 0.08, and 0.1 M. The solution pH varied from 0.5 to 4.5 in the case of only NaCl and $NaClO_4$. For the rest of the studies, it was selected based on the highest amount of H_2O_2 formation with NaCl and $NaClO_4$. pH was fixed at 2.5. The electrolysis was carried out for 2 h, and samples were withdrawn at every 20 min to analyse for H_2O_2 concentration, Ti^{4+} corrosion, pH variation, and DO saturation level.

The current efficiency (CE_f) was determined by the ratio of electrical current required for H_2O_2 formation to the total current passed through the cell (Eq. 2.2) (Qiang et al., 2002).

$$CE_f = \frac{nFC_{H_2O_2}V}{\int_0^t Idt} \times 100,\% \quad (2.2)$$

where, n = stoichiometric number of electrons transfer for H_2O_2 formation, F = Faraday's constant (96485 C/mol), $C_{H_2O_2}$= mole of H_2O_2 formed, I= cell current (A) supplied for the time period of t (s). Here, it is important to mention that the rate of H_2O_2 formation is governed by the DO transport from the bulk to the WE surface (Qiang et al., 2002).

2.5.6.2 H_2O_2 generation and sensing in fabricated electrode system

The amperometric test of H_2O_2 formation was carried out for a period of 2 h following the same procedure, but at a fixed potential ($-E_{cat}$) of 0.268 V vs. Ag/AgCl which was selected from CV tests with graphite/NiO NPs as the WE. In the case of the graphite/Co_3O_4 NPs electrode, $-E_{cat}$ was fixed at 0.146 V for H_2O_2 electro-generation. The CE_f of H_2O_2 formation was also calculated using Eq. 2.1.

On the other hand, the amperometric test of H_2O_2 sensing was conducted following the same procedure, but at a fixed potential of –0.117 V vs. Ag/AgCl with graphite/Co_3O_4 NPs electrode. It was at –0.129 V with graphite/NiO NPs electrode. An equal amount of 1 µM H_2O_2 was added to the solution at very 50 s for a total test period of 4000 s. The selectivity, reproducibility, and repeatability of the fabricated electrode were tested using the amperometric technique.

2.5.7 Implication of electro-generated H_2O_2 for drug decomposition

The simultaneous generation (Section 2.5.5.2) and utilization of H_2O_2 was tested for the degradation of an antibiotic drug, ciprofloxacin (CIP) in the EFP. The background for the selection of CIP in the present study is outlined in Section 4.2.3.1 of Chapter 4. The optimized reaction parameters for the degradation of CIP were selected based on the earlier studies of the same research group (Giri and Golder, 2014). It was the initial CIP concentration of 15 mg/L, pH of 2.5, Fe(II) of 0.03 mM, and room temperature of 25±2 °C. Fortunately, the optimal pH of H_2O_2 electro-generation was also found to be 2.5 (Section 2.5.5.2). An appropriate amount of CIP was dissolved in dilute sulfuric acidic solution (Larsson et al., 2007; Giri and Golder, 2014), and it was further diluted in 0.08 M Na_2SO_4 solution of a total volume of 190 mL. The electrode potential ($-E_{cat}$ vs. Ag/AgCl) was fixed at 0.268 and 0.146 V for the NiO and Co_3O_4 NPs catalysed systems for the EFP which was selected from H_2O_2 electro-generation studies (Section

2.5.5.2). O_2 (99.99 % purity) purging with a flow rate of 1.0 LPM was continued from 20 min before the beginning of the experiment. The reaction time of the EFP was limited up to 45 min. At 1, 5, 10, 20 and 45 min of electrolysis, 5 mL samples were taken out and, the reaction was stopped immediately after the collection of samples by the addition of 0.5 mL of 0.1 N NaOH at 5:0.5 (v/v) (Giri and Golder, 2014; Giri and Golder, 2015). Iron sludge appeared due to pH elevation (pH 11.9) from NaOH addition was separated out by centrifugation and, the clear supernatant was analysed for CIP concentration and TOC. The mass spectra were recorded only for the sample collected after 45 min of EFP with both the Co_3O_4 NPs catalysed systems.

References

Amin V.M., Olson N.F. Spectrophotometric determination of hydrogen peroxide in Milk, *J. Dairy Sci.* **1966**, 50, 461-464.

Barve A.K., Gadegone S.M., Lanjewar M.R., Lanjewar R.B. Synthesis and characterization of nickel oxide based nanocomposite material, International Journal of Engineering Research and Applications (IJERA) (ISSN: 2248-9622), 2014.

Cook O.F The chayote: a tropical vegetable. USDA Division Botany Bulletin **1901**, 18, 1-31.

Engels J.M.M. Variation in *Sechium edule* in Central America, *J. Amer. Soc. Hort. Sci*. **1983**, 108, 706-710.

Farahi A., Achak M., Gaini L., Mhammedi M.A., Bakasse M. Silver particles-modified carbon paste electrodes for differential pulse voltammetric determination of paraquat in ambient water samples, *J. Assoc. Arab Univ. Basic Appl. Sci*. **2016**, 19, 37-43.

Flick G.J., Burnette Jr.F.S., Aung L.H., Ory R.L., Angelo A.J.St. Chemical composition and biochemical properties of Mirlitons (*Sechium edule*) and purple, green, and white eggplants (Solanum melongena), *J. Agric. Food Chem*. **1978**, 26, 1000-1005.

Giri A.S. Advanced oxidation processes for treatment of pharmaceutical wastewater, PhD Thesis, IIT Guwahati, **2014**.

Giri A.S., Golder, A.K. Ciprofloxacin degradation from aqueous solution by Fenton oxidation: reaction kinetics and degradation mechanisms, *RSC Adv*. **2014**, 4, 6738-6745.

Giri A.S., Golder A.K. Decomposition of drug mixture in Fenton and photo-Fenton processes: comparison to singly treatment, evolution of inorganic ions and toxicity assay, *Chemosphere* **2015**, 127, 254-261.

Huheey J.E., Keiter E.A., Keiter R.L. Inorganic chemistry: principles of structure and reactivity, Fourth Edition, **1993**.

Kapoor C., Kumar A., Pattanayak A., Gopi R., Kalita H., Avasthe R.K., Bihani S. Genetic diversity in local chow-chow (*Sechium edule sw*.) germplasm of Sikkim, *Indian J. Hill Fmg*. **2014**, 27, 130-134.

Kumari S., Elancheran R., Kotoky J., Devi R. Rapid screening and identification of phenolic antioxidants in Hydrocotyle sibthorpioides Lam. by UPLC–ESI-MS/MS, *Food Chem*. **2016**, 203, 521-529.

Larsson D.G.J., de Pedro C., Paxeus N. Effluent from drug manufactures contains extremely high levels of pharmaceuticals, *J. Hazard. Mater*. **2007**, 148, 751-755.

Mishra L., Das K.P. Nutritional evaluation of squash (*Sechium edule*) germplasms collected from Garo Hills of Meghalaya – North East India, International Journal of Agriculture, *Environ. Biotechnol*. **2015**, 8, 971-975.

Moffettt J.W., Zika R.G. Reaction kinetics of hydrogen peroxide with copper and iron in seawater, *Environ. Sci. Technol*. **1987**, 21 (8), 804-810.

Motahari F., Mozdianfarda M.R., Salavati-Niasari M. Synthesis and adsorption studies of NiO nanoparticles in the presence of H_2acacen ligand for removing Rhodamine B in wastewater treatment, *Process Saf. Environ. Prot.* **2015**, 93, 282-292.

Ordonez A.A., Gomez J.D., Isla M.A. Antioxidant activities of *Sechium edule* (Jacq.) Swartz extracts, *Food Chem.* **2006**, 97, 452-58

Patil V., Joshi P., Chougule M., Sen S. Synthesis and Characterization of Co_3O_4 Thin Film, *Soft Nanosci. Lett.* **2012,** 2, 1-7.

Petlicki J., Palusova D., Van de Ven T.G.M. Physicochemical aspects of catalytic decomposition of hydrogen peroxide by manganese compounds, *Ind. Eng. Chem. Res.* **2005**, 44 (7), 2002-2010.

Plaza L., Sanchez-Moreno C., De Ancos B., Elez-Martinez P., Martin-Belloso O., Cano M.P. Carotenoid and flavanone content during refrigerated storage of orange juice processed by high-pressure, pulsed electric fields and low pasteurization, *LWT - Food Sci. Technol.* **2011**, 44, 834-839.

Qiang Z., Chang J.-H., Huang C.-P. Electrochemical generation of hydrogen peroxide from dissolved oxygen in acidic solution, *Water Res.* **2002**, 36, 85-94.

Rao Ch.V., Golder A.K. Development of a bio-mediated technique of silver-doping on titania, *Colloids Surf. A* **2016a**, 506, 557-565.

Rao Ch. V. Bio-inspired route of metal nanoparticles systensis and photocatalysts doping, PhD Thesis, IIT Guwahati, **2017**.

Rao Ch.V., Golder, A.K. pH dependent size control, formation mechanism and antimicrobial functionality of bio-inspired AgNPs, *RSC Adv.* **2016b**, 6, 95483-95493.

Saade R.L. Chayote (Jacq.) Sw., Promoting the conservation and use of underutilized and neglected crops. 8, International Plant Genetic Recourses Institute, Italy, **1996**.

Sharifi S.L., Shakur H.R., Mirzaei A., Salmani A., Hosseini M.H. Characterization of cobalt oxide Co_3O_4 nanoparticles prepared by various methods: effect of calcination temperatures on size, dimension and catalytic decomposition of hydrogen peroxide, *Int. J. Nanosci. Nanotechnol.* **2013**, 9, 51-58.

Shiga T.M., Peroni-Okita F.H.G., Carpita N.C., Lajolo F.M., Cordenunsi B.R. Polysaccharide composition of raw and cooked chayote (*Sechium edule Sw.*) fruits and tuberous roots, *Carbohydr. Polym.* **2015**, 130, 155-165.

Singh B.K., Ramakrishna Y., Verma V.K. Chow-Chow (*Sechium edule*): Best alternative to shifting cultivation in Mizoram, *Indian J. Hill Fmg* **2015**, 28, 158-161.

Su C.-Y., Lan W.-J., Chu C.-Y., Liu X.-J., Kao W.-Y., Chen C.-H. Photochemical green synthesis of nanostructured cobalt oxides as hydrogen peroxide redox for bifunctional sensing application, *Electrochim. Acta* **2016**, 190, 588-595.

Wang H.-Q., Fan X.-P., Zhang X.-H., Huang Y.-G., Wu Q., Pan Q.-C., Li Q.-Y. In situ growth of NiO nanoparticles on carbon paper as a cathode for rechargeable Li-O_2 batteries, *RSC Adv.* **2017**, 7, 23328-23333.

Wawire M., Oey I., Mathooko F., Njoroge C., Shitanda D., Hendrickx M. Thermal stability of ascorbic acid and ascorbic acid oxidase in African cowpea leaves (Vigna unguiculata) of different maturities, *J. Agric. Food Chem.* **2011**, 59, 1774-1783.

Xia S., Yua M., Hu J., Feng J., Chen J., Shi M., Weng X. A model of interface-related enhancement based on the contrast between Co_3O_4 sphere and cube for electrochemical detection of hydrogen peroxide, *Electrochem. Commun.* **2014**, 40, 67-70.

Yahya M.S., Oturan N., Kacemi K.E., Karbane M.E., Aravindakumar C.T., Oturan M.A. Oxidative degradation study on antimicrobial agent ciprofloxacin by electro-Fenton process: Kinetics and oxidation products, *Chemosphere* **2014**, 117, 447-454.

Zayed S.I.M., Arida H.A.M. Preparation of carbon paste electrodes and its using in voltammetric determination of amiloride hydrochloride using in the treatment of high blood pressure, *Int. J. Electrochem. Sci* **2013**, 8, 1340-1348.

Chapter–3

H_2O_2 Electro-generation on Isomoulded Graphite and Stability of Counter Electrode

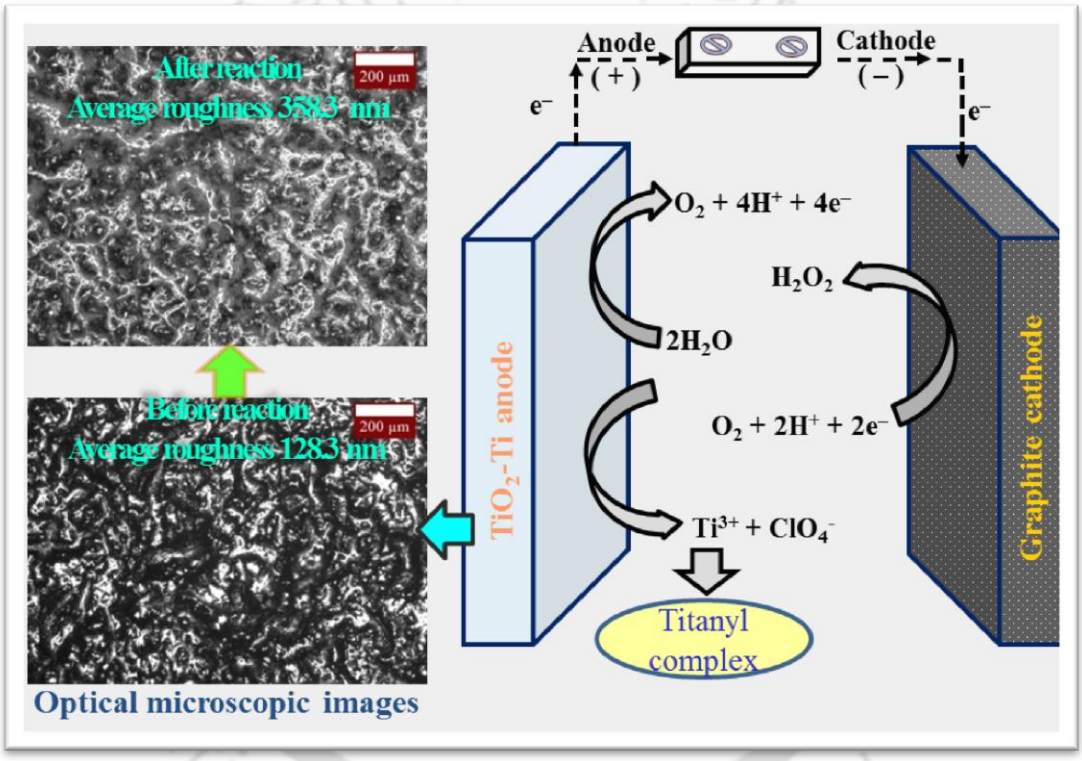

Chapter 3 comprises of two parts. In the first part, the effects of pH, temperature, supporting electrolytes (SEs), and traces of metals ions such as Na^+, Ca^{2+}, Ni^{2+}, Co^{2+}, Cu^{2+}, etc. on the decomposition of H_2O_2 were investigated in an aqueous stream as it could markedly influence the performance of both H_2O_2 electro-generation and sensing. High purity isomoulded graphite plate was used as the cathode material. The anode was either isomoulded graphite plate or TiO_2-coated Ti (TiO_2-Ti).

3.1 Specific background

Hydrogen peroxide (H_2O_2) is known as an 'environmentally friendly' chemical as it doesn't leave any toxic residues (Section 1.1, Chapter 1). Self-decomposition of hydrogen peroxide is influenced by temperature, reaction time, pH, H_2O_2 concentration, and water quality (Khan, 2006). Decomposition of H_2O_2 generally occurs very slowly in an aqueous solution at low pH. In the presence of metal catalysts or in a basic medium, hydrogen peroxide breaks into oxygen and water in an exothermic reaction. The decomposition of H_2O_2 takes place in a basic medium according to the reaction 1.1 of Chapter 1 (Eq. 1.1). The presence of trace metals also can catalytically initiate H_2O_2 decomposition both at acidic and alkaline pH (Qiang et al., 2002) and, very frequently, they are introduced from acids and bases used for the fixing of solution pH. H_2O_2 and free metal ions predominate at low pH. HO_2^- and hydroxylated metal complexes prevail at an alkaline condition.

The major applications of H_2O_2 include its use as a precursor for the hydroxyl radical formation ($^{\bullet}OH$) (Eq. 1.4, Chapter 1) in the AOPs (EF, AO, etc.) during wastewater treatment. The carbonaceous materials, namely, carbon felt, carbon nanotubes, graphite, graphite felt, and reticulated vitreous carbon electrodes are usually used as cathodes due to their non-toxicity, high conductivity, good stability, and low catalytic activity of H_2O_2 decomposition (Brillas et al., 2009). Graphite is much cheaper than gas-diffusion and modified carbon-nanotube-based electrodes. Therefore, many researchers prefer the uses of graphite and modified-graphite electrodes when the treatment of a large volume of wastewater is concerned (Wang et al., 2010). Moreover, the gas-diffusion electrodes suffer from a small surface area, and in the case of the closed packed carbon-nanotube-based electrodes, bundles and ropes are formed (Pajootan et al., 2014).

In the case of AO, the organic contaminants are destroyed mostly by the $^{\bullet}OH$ radicals formed on the anode surface as an intermediate from water oxidation to O_2 (Panizza et al., 2005). The classical anode materials include the combinations of various metals such as titanium (Ti), ruthenium (Ru), lead (Pb), iridium (Ir), tin (Sn), and their oxides. The AO coupled with the EF processes both in divided and undivided cells are tested by many researchers (Brillas et al., 2004; Flox et al., 2006a; Fockedey et al., 2002; Montanaro et al., 2008). Fockedey et al. (2002) used Sb-doped SnO_2-coated Ti foam and reticulated vitreous carbon for phenol degradation in a divided cell using 0.25 M Na_2SO_4 as the SE. In addition, the coupled oxidations reduce the

energy consumption. The total mineralization of Indigo Carmine dye owing to the destruction of Fe^{3+}-oxalate and Fe^{3+}-oxamate complexes in 0.05 M Na_2SO_4 SE solution is reported for the combined AO and EF processes using a BDD anode and as well as in PEF process with Pt anode using Fe^{2+} and Cu^{2+} catalysts (Flox et al., 2006b). The boron doped diamond anode and gas diffusion cathode for the degradation of phosphates from a 400 mg/L SO_4^{2-} solution using an anionic membrane minimizes iron precipitation in the cathode chamber leading to complete oxidation (Montanaro et al., 2008).

It is also reported that the rate of AO of tannery wastewater is strongly affected by the type of anode materials (Szpyrkowicz et al., 2005). The Ti/Pt-Ir and Ti/PdO-Co_3O_4 anodes outperformed Ti/PbO_2 and Ti/RhO_x-TiO_2. TiO_2-Ti anodes are prone for the anodic corrosion that could yield various Ti ions such as Ti^{2+}, Ti^{3+}, and Ti^{4+} (Lee et al., 2012). Ti^{3+} can react with ClO_4^- (Eq. 3.1) in an acidic medium and such reaction usually proceeds through an initial complexation leading to the formation of titanyl ions and chlorate radical (Eq. 3.2) (Duke and Quinney, 1954; Urbansky, 1998).

$$8Ti^{3+} + ClO_4^- + 8H^+ \rightarrow 8Ti^{4+} + Cl^- + 4H_2O \quad (3.1)$$

$$Ti^{3+} + ClO_4^- \rightarrow TiO^{2+} + ClO_3^{\bullet} \quad (3.2)$$

A yellow colored complex is also formed by the reaction between Ti^{4+} and H_2O_2 (Eq. 3.3). In fact, this reaction is used for the colorimetric determination of H_2O_2 (Eisenberg, 1943; Peralta et al., 2013). Moreover, ClO_4^- contaminations can be found not only in water but also in food and food items such as lettuce, spinach, cereals, wines, beer, bottled water, dairy and breast milk (Dyke et al., 2007). On the other hand, the use of $NaClO_4$ as a SE in the EFP is preferred as ClO_4^- ions don't complex with Fe^{2+}/Fe^{3+} (Qiang et al., 2002; Thiam et al., 2015).

$$Ti^{4+} + H_2O_2 + 2H_2O \rightarrow H_2TiO_4 + 4H^+ \quad (3.3)$$

Therefore, the selection of a suitable SE for the simultaneous EFP and AO, in particular, while using Ti-based material is a prudent research area as it could affect bulk reactions as well as the stability of the electrode during H_2O_2 generation. However, to the best of our knowledge, there are no reports on the influence of ClO_4^- on H_2O_2 electro-generation when the coupled oxidation processes using the TiO_2-Ti anode are concerned.

However, most of the researchers generally use Fe^{2+} and Fe^{3+} in an acid solution to generate hydroxyl radical from H_2O_2 for the oxidation of different refractory contaminants in the dark as well as in the presence both UV and solar light. Likewise, this study was undertaken at

the beginning (before electro-catalysed H_2O_2 generation and sensing, Chapters 4 and 5) to investigate the effect of pH, temperature, and common trace metal ions on the decomposition of H_2O_2 which could markedly affect its stability and generation of $^{\bullet}OH$ radical (Section 1.7, Chapter 1). The formation of $^{\bullet}OH$ by such side reactions can transmit misconception on the performance of the main reaction.

This work also investigates the influence of different SEs such as $NaClO_4$, Na_2SO_4, NaCl, and $NaNO_3$ in an undivided electrolyzer in order to study on the: (i) fundamental electrochemical process for the formation of H_2O_2 by O_2 reduction using cyclic voltammetry, (ii) H_2O_2 formation using graphite/TiO_2-Ti as the cathode/anode combination and its comparison to graphite/graphite system, and (iii) stability of TiO_2-Ti anode affecting H_2O_2 formation (Section 1.7, Chapter 1).

3.2 Results and discussion

3.2.1 Stability of aqueous H_2O_2

3.2.1.1 Effect of temperature and pH on H_2O_2 decomposition

The effect of temperature and pH on stability of H_2O_2 is shown in Figure 3.1. It can be seen that the percentage H_2O_2 decomposition was <10 % at pH<8 at different reaction temperature. Stability of hydrogen peroxide was decreased greatly with the increase in temperature. About 27, 34, and 69 % H_2O_2 were decomposed at 30, 50, and 70 °C with 60 mg/L initial H_2O_2 and pH 12. However, the same was increased to 34, 51, and 96 % with 600 mg/L initial H_2O_2 at the identical experimental condition. It is also evident from this figure that H_2O_2 was degraded at an extremely faster rate at pH> 8 and, it was unstable at pH 12 at the higher concentration.

H_2O_2 was more stable at low pH, and it can be stored for long time. At a high pH value, H_2O_2 was unstable due to the formation of a reactive nucleophile perhydroxy anion (HOO^-) (Eq. 3.4). Free metals ions also could form hydroxo complexes in an alkaline medium. More H_2O_2 was consumed by a side reaction through the decomposition of HOO^- (Eq. 3.5) (Aleboyeh et al., 2005). HOO^- could further decompose as in Eqs. 3.6 and 3.7. Formation of HOO^- was increased with the rise of temperature. Khan (2006) reported that the ratio of perhydroxy anion to H_2O_2 (0.7:1) at 0 °C moved to 0.3:1 at 40 °C because of HOO^- decomposition. Qiang et al. (2002) showed that H_2O_2 self–decomposition was suppressed at 10 °C.

$$H_2O_2 + OH^- \leftrightarrow H_2O + HOO^- \quad (3.4)$$

$$H_2O_2 + HOO^- \rightarrow H_2O + OH^- + O_2 \quad (3.5)$$

$$H_2O_2 + HOO^- \rightarrow H_2O + {}^{\bullet}OH + O_2^{\bullet-} \quad (3.6)$$

$${}^{\bullet}OH + O_2^{\bullet-} \rightarrow OH^- + O_2 \quad (3.7)$$

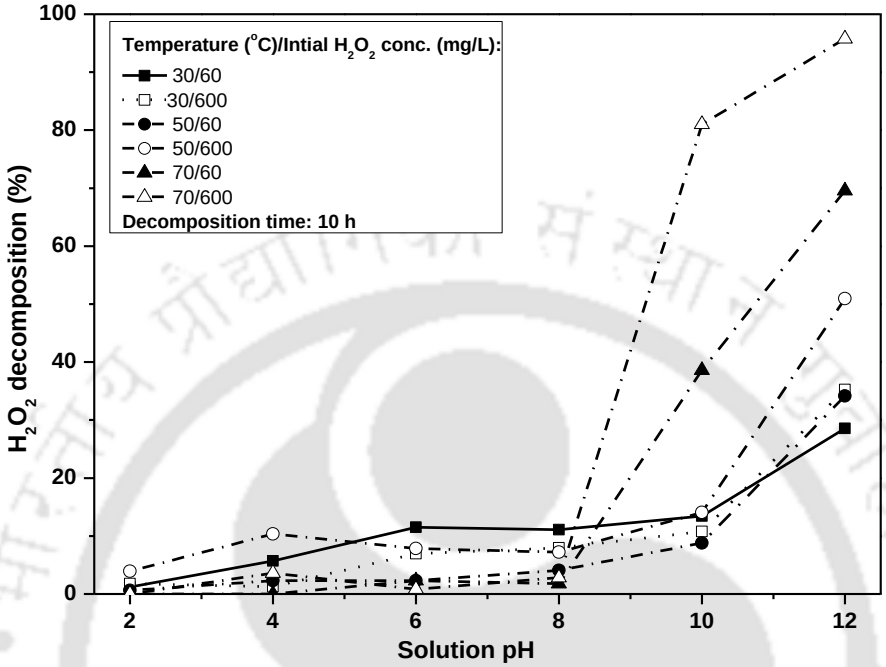

Figure 3.1: Decomposition of H_2O_2 at various temperature and pH. Experimental condition: Working solution 40 mL and decomposition time 10 h.

An excess of H_2O_2 concentration could affect the decomposition of HOO^- as well as the decomposition of H_2O_2 with hydroxyl radical formation. An elevated H_2O_2 concentration enhanced the chain reaction which induced a series of propagation reactions in which per-hydroxyl radical (${}^{\bullet}OOH$), a weak nucleophile, superoxide radical anion ($O_2^{\bullet-}$) and perhydroxy anion were formed (Eqs. 3.8 to 3.10).

$$H_2O_2 + {}^{\bullet}OH \leftrightarrow H_2O + {}^{\bullet}OOH \quad (3.8)$$

$${}^{\bullet}OOH \rightarrow O_2^{\bullet-} + OH^+ \quad (3.9)$$

$${}^{\bullet}OOH + O_2^{\bullet-} \rightarrow HOO^- + O_2 \quad (3.10)$$

Even the walls of glassware or other surface of apparatus could affect the stability of H_2O_2. Feng et al. (2012) reported that pH of the H_2O_2 solution was increased when the solution was stored in a glass container due to the extraction of alkali from the glass container. To protect H_2O_2 decomposition, Nicoll and Smith (1955) washed all glasswares using 5 % NaOH, water, 5 % (v/v) HCl acid at about 60 °C, 5 % (v/v) HNO_3 at 60 °C, and finally several times with

deionized water. To avoid such contamination, polypropylene (Tarsons Products Pvt. Ltd., Kolkata, India) containers were used instead of glasswares in the present work.

3.2.1.2 Effect of mono- and bi-valents metal ions on H_2O_2 decomposition

Low concentration of catalytic impurities such as Cu^{2+}, Fe^{2+}, Ni^{2+}, etc. could significantly decompose H_2O_2. The effect of various metal ions on H_2O_2 decomposition is shown in Figures 3.2. H_2O_2 was essentially stable in the presence of Ni^{2+}, Ca^{2+}, and K^+ ions at pH 4. However, it was markedly increased when Cu^{2+} and Mn^{2+} ions were present even at low pH. Figure 3.2 displays that H_2O_2 decomposition was increased from 40 to 70 % when Cu^{2+} concentration was varied from 2 to 10 mg/L. The same was between 2 to 48 % with Mn^{2+} ions. H_2O_2 decomposition was augmented at a high pH in the presence of trace metal. The enhanced H_2O_2 decomposition in the presence of Cu^{2+} (or Fe^{2+}) ions is shown through Eqs. 3.11 and 3.16. Cu^{2+} ions react with H_2O_2 forming O_2 and H_2O (Moffettt and Zika, 1987). Mn^{2+} ions also could be oxidized to its oxide by H_2O_2 in an aqueous solution depending on solution pH (Eq. 3.17) (Petlicki et al., 2005). An interesting observation was seen that H_2O_2 was stable an alkaline medium with the addition of a trace amount of Ni^{2+} and Co^{2+} ions (Figure 3.3).

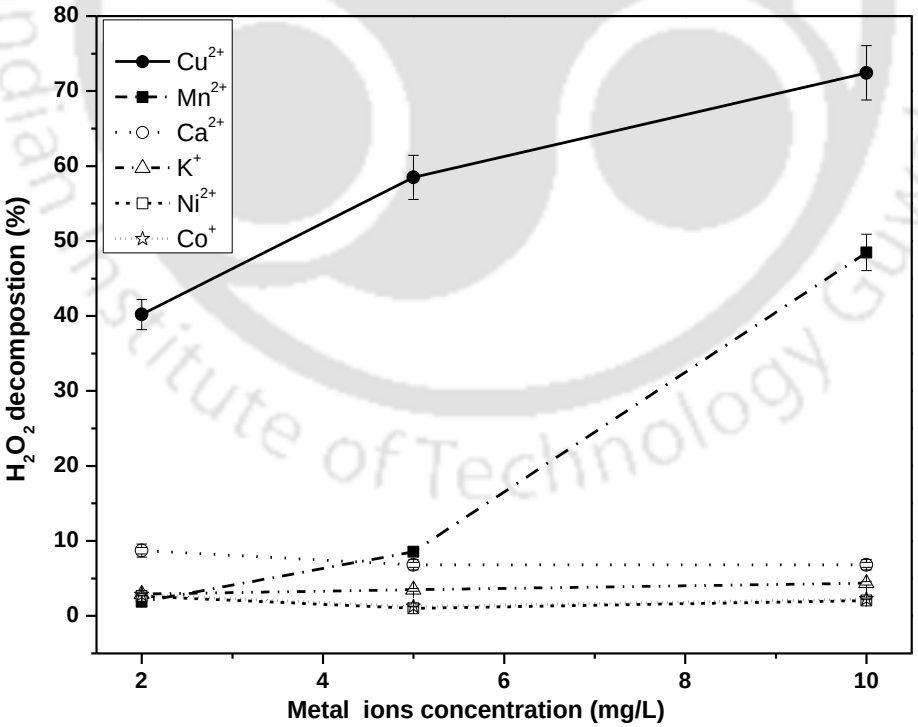

Figure 3.2: Decomposition of H_2O_2 at different metal ions concentration at pH 4. Experimental condition: Working solution 40 mL, room temperature (25±2 °C) and decomposition time 10 h.

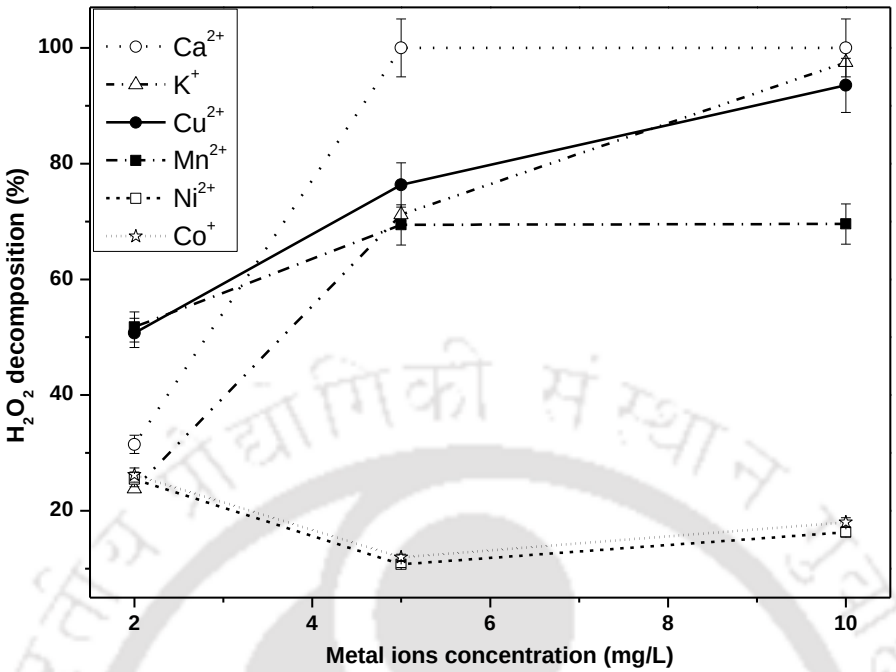

Figure 3.3: Decomposition of H_2O_2 at different metal ions concentration at pH 10. Experimental condition: Working solution 40 mL, room temperature (25±2 °C) and decomposition time 10 h.

These similar results were observed by Nicoll and Smith (1955). H_2O_2 decomposition at a higher pH was caused by OH^- ions itself or by the catalytic reactions induced by the presence of metal impurities. OH^- ion itself is an initiator of H_2O_2 decomposition at a higher pH. The effect of Ni^{2+} and Co^{2+} ion on H_2O_2 decomposition was very small due to a low catalytic activity in an alkaline, but the catalytic activities of other metal ions like Cu^{2+}, Ca^{2+}, K^+, Fe^{2+}, and Mn^{2+} increase with the increase in alkalinity.

$$H_2O_2 \leftrightarrow H^+ + HO_2^- \quad (3.11)$$

$$Cu^{2+} + HO_2^- \rightarrow Cu^+ + HO_2 \quad (3.12)$$

$$HO_2 \leftrightarrow H^+ + O_2^- \quad (3.13)$$

$$Cu^{2+} + O_2^- \rightarrow Cu^+ + O_2 \quad (3.14)$$

$$Cu^+ + H_2O_2 \rightarrow Cu^{2+} + {}^{\bullet}OH + OH^- \quad (3.15)$$

$${}^{\bullet}OH + H_2O_2 \rightarrow H_3O^+ + O_2^- \quad (3.16)$$

$$Mn^{2+} + H_2O_2 + 2OH^- \rightarrow MnO_2 + 2H_2O \quad (3.17)$$

3.2.2 Cyclic voltammogram (CV) and H_2O_2 formation

The CV is a useful tool for the identification of redox reactions at a particular condition. A set of experiments was performed with different SEs. Figure 3.4 illustrates the CV curves. The

scanning was performed between $-E_{cat}$ =2 to –2 V vs. Ag/AgCl at 50 mV/s scan rate. In the case of $NaNO_3$, one pair of oxidation and one of reduction peaks were observed, and the current was decreased while going to the next cycle due to the decrease in pre-adsorbed DO (Figure 3.4a). The equilibrium concentration of DO is proportional to the O_2 partial pressure in the supplied gas stream. The DO was found to be around 18-23 mg/L with pure O_2 sparging at pH 2.5 with all SEs. The anodic peak labelled as A at 1.274 V was indicating O_2 oxidation in the 1st cycle, but it disappeared in the next cycle. Another anodic peak labelled as B at 0.89 V was due to the decomposition of H_2O_2 to O_2. The cathodic peak labelled as C at $-E_{cat}$ =–0.745 V was due to O_2 reduction. On the other hand, one oxidation and one reduction peaks appeared in the case of Na_2SO_4 (Figure 3.4b). The anodic peak (D) similar to A was also found with $NaNO_3$. The cathodic peak (labelled as E) appeared at $-E_{cat}$ =–0.918 V.

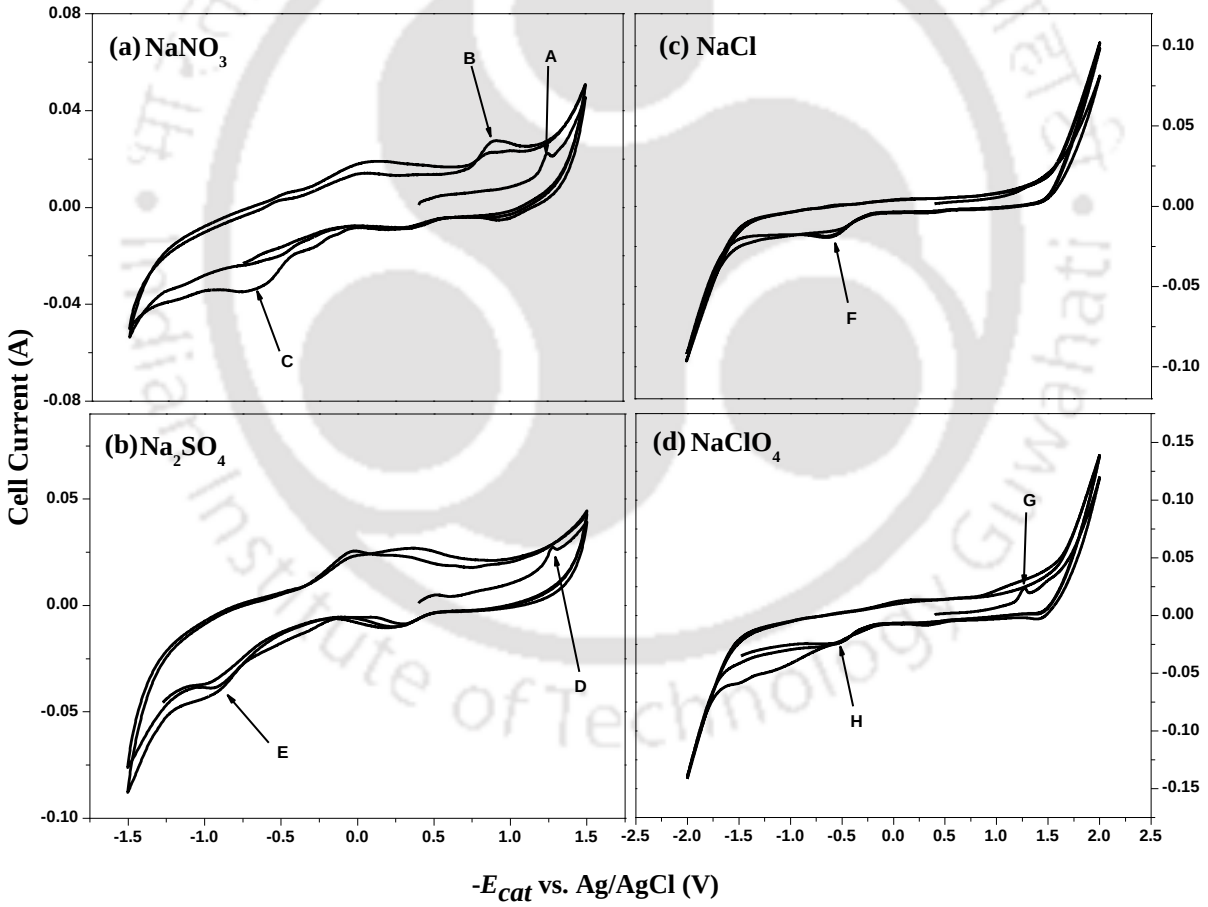

Figure 3.4: Cyclic voltammograms with graphite as WE and Pt as CE by sweeping from 1.5 to –1.5 V vs. Ag/AgCl (a and b) and from 2.0 to –2.0 V vs. Ag/AgCl (c and d). Experimental condition: Scan rate 50 mV/s, SEs 0.5 M, pH 2.5, O_2 flow rate 1.2 LPM, and electrolyte 190 mL.

No oxidation peak was identified in the CV when NaCl was used (Figure 3.4c). The cathodic peak labelled as F appeared at $-E_{cat}$ =–0.655 V. With $NaClO_4$, the anodic peak labelled as G was at 1.274 V, and the cathodic peak (H) was found at $-E_{cat}$ =–0.527 V (Figure 3.4d). Therefore, the overpotential of O_2 reduction forming H_2O_2 varied with SEs in the order as Na_2SO_4 > $NaNO_3$ > NaCl > $NaClO_4$.

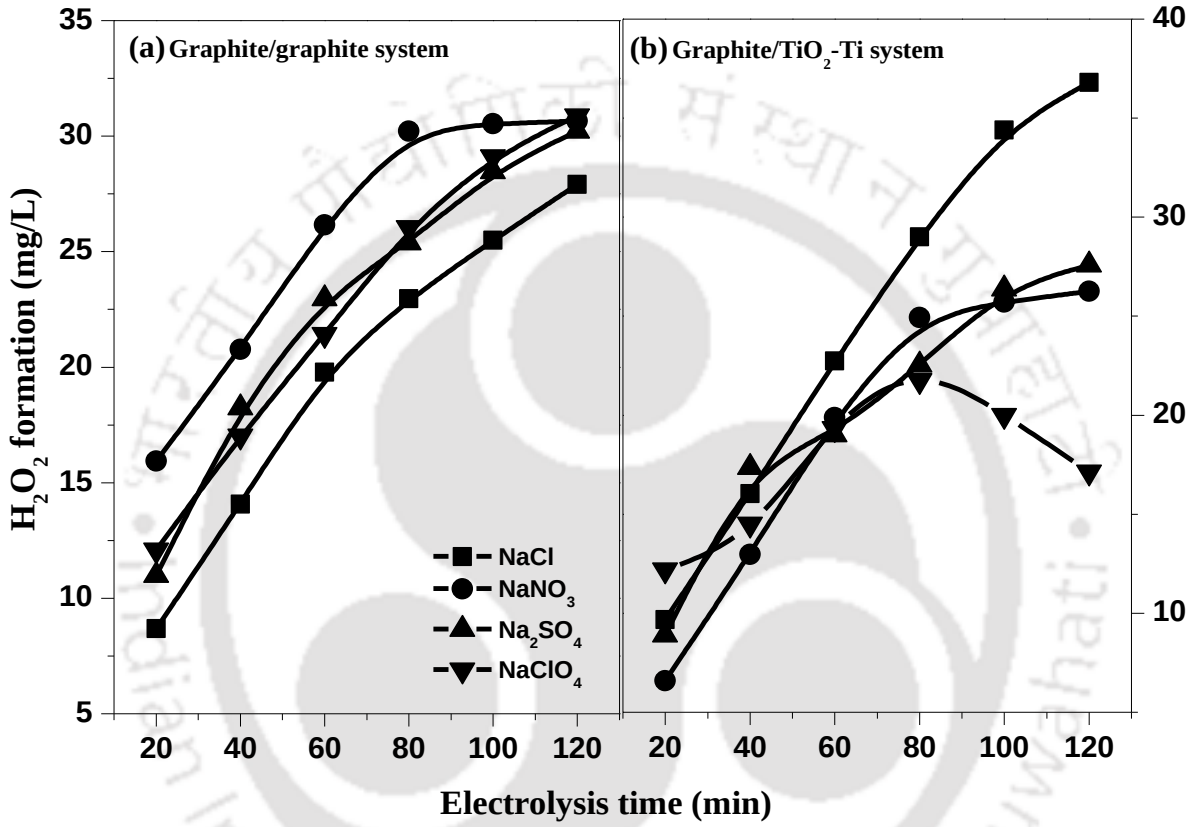

Figure 3.5: H_2O_2 formation with electrolysis time. (a) Graphite/graphite system with $-E_{cat}$ = –0.6 V and; (b) Graphite/TiO_2–Ti system with $-E_{cat}$ =–0.5 V. Experimental condition: SE 0.08 M, stirrer speed 300 rpm, pH 2.5, O_2 flow rate 4 LPM, and electrolyte 2 L.

3.2.3 H_2O_2 formation and current efficiency

3.2.3.1 Influence of SEs and stability of Ti-O_2 anode

The concentration of SEs was fixed at 0.08 M at the beginning of the experiments. The results are shown in Figure 3.5 with both the graphite/graphite and graphite/TiO_2-Ti systems. The accumulation of H_2O_2 remained steady at 30 mg/L of its concentration with $NaNO_3$ after 80

min due to an increase in H_2O_2 anodic- and self-decomposition (Brilllas et al., 2000) with the graphite/graphite system (Figure 3.5a) (Alverez-Gallegos and Pletcher, 1999). However, the rate of H_2O_2 formation was gradual with NaCl, Na_2SO_4, and $NaClO_4$, with a minimum yield in the case of NaCl (28 mg/L H_2O_2 in 120 min) (Figure 3.5a). On the other hand, both Na_2SO_4 and $NaNO_3$ showed about 27 mg/L H_2O_2 formation after 120 min in the case of the graphite/TiO_2-Ti system. A steady rate of 0.32 (mg/L)/min of H_2O_2 formation fell down to 0.12 (mg/L)/min after 90 min with NaCl and, there was around 37 % more H_2O_2 formation compared to Na_2SO_4 and $NaNO_3$ with the graphite/TiO_2-Ti system (Figure 3.5b). So, the chlorinated SEs, i.e., NaCl and $NaClO_4$ showed a reverse effect on H_2O_2 formation with the graphite/TiO_2-Ti and graphite/graphite systems. The anodic liberation of Cl_2 was usually more at the graphite electrode (Eq. 3.18) than at the mixed metal oxide electrode in which Cl_2 discharge took a different reaction pathway (Eq. 3.19).

$$2Cl^-(aq) \rightarrow Cl_2(g) + e^- \quad \text{(graphite anode)} \qquad (3.18)$$

$$TiO_2(^{\bullet}OH) + Cl^- \rightarrow TiO_2 + \tfrac{1}{2}Cl_2 + OH^- \qquad (3.19)$$

There is a report on about 44 % more Cl^- depletion from 0.01 M NaCl solution during AO of an azo dye (Karuppiah and Raju, 2009). H_2O_2 generation was about 25-38 % more with $NaClO_4$ at 20 min of electrolysis (Figure 3.5b). H_2O_2 formation was found to increase up to 80 min to 21.8 mg/L from 12.2 mg/L at 20 min. After that, H_2O_2 started decomposing and its concentration came down to 17 mg/L in 120 min when $NaClO_4$ was used (Figure 3.5b).

Many authors prefer to use $NaClO_4$ and $NaNO_3$ in the EF process instead of NaCl as the later could oxidize Fe^{2+} (Loaiza-Ambuludi et al., 2013; Sarala and Venkatesha, 2013). Figure 3.6a shows the UV-vis spectra of the electrolyte solution at 2 h of electrolysis when $NaClO_4$ was used as the SE. The maximum absorbance peak appeared at 380 nm. The solution turned yellow within 80 min of operation. The concentration of Ti ions in the SE solution was also determined, and Ti was detected only with $NaClO_4$ (Figure 3.6b). Within first 1 h, Ti was not detected but after that it was increased linearly (correlation coefficient of 0.96) and a concentration of 4.3 mg/L was determined in 2 h of electrolysis with a strong yellowish color of the solution. So, Ti^{4+} could form a yellow color complex with H_2O_2 (Eq. 3.3). ClO_4^- ions also could react with Ti^{3+} forming a titanyl complex. The reaction proceeded through an initial complexation after which Ti^{3+} was oxidized to a titanyl ion, TiO^{2+} (Eq. 3.20) (Duke and Quinney, 1954).

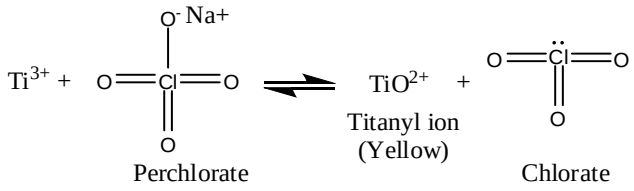

(3.20)

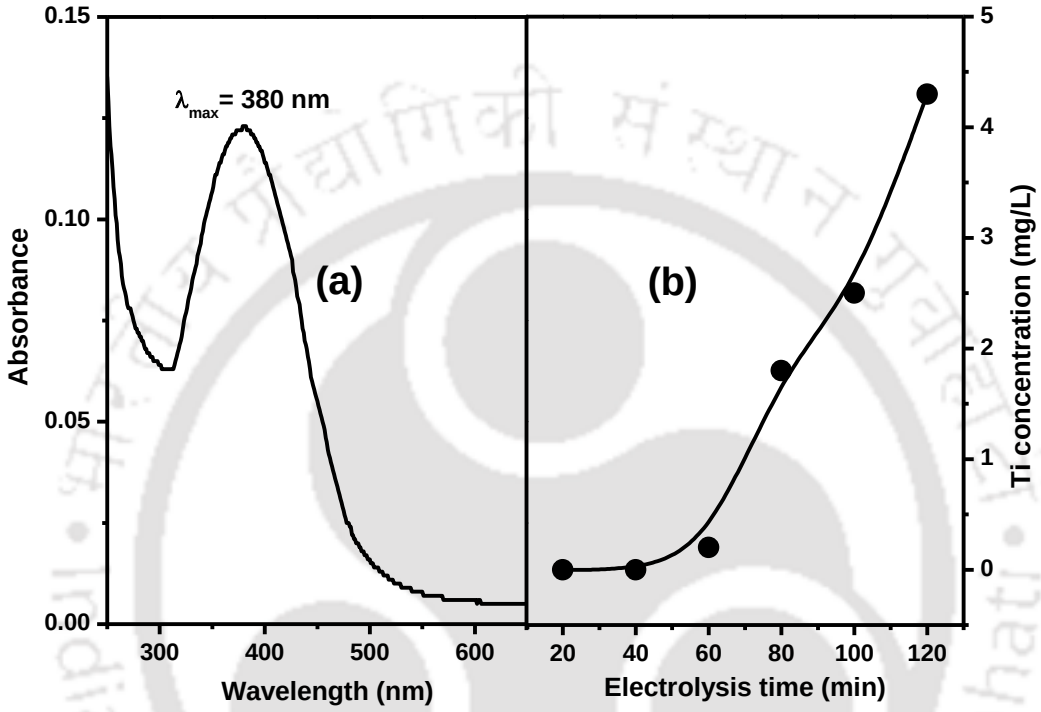

Figure 3.6: (a) UV-Vis spectra of electrolyte solution after 2 h of electrolysis with TiO_2-Ti as CE and (b) Variations of Ti concentration with electrolysis time with graphite/TiO_2-Ti system after 2 h of electrolysis. Experimental condition: $NaClO_4$ 0.08 M, $-E_{cat}$ =–0.5 V, stirrer speed 300 rpm, pH 2.5, O_2 flow rate 4 LPM, and electrolyte 2 L.

The optical microscopic images of TiO_2-Ti and graphite plates used as the CEs are shown in Figure 3.7. The surface corrosion of TiO_2-Ti is clearly visible (Figures 3.7a and 3.7b). The arithmetic average surface roughness (Ra) was determined using Gwyddion 2.45 software (version 2). Ra was increased from 128.3 to 358.3 nm after 2 h of reaction with TiO_2-Ti. Ra of the fresh graphite electrode was 163.3 nm and no variation was determined after the electrolysis (Figures 3.7c and 3.7d).

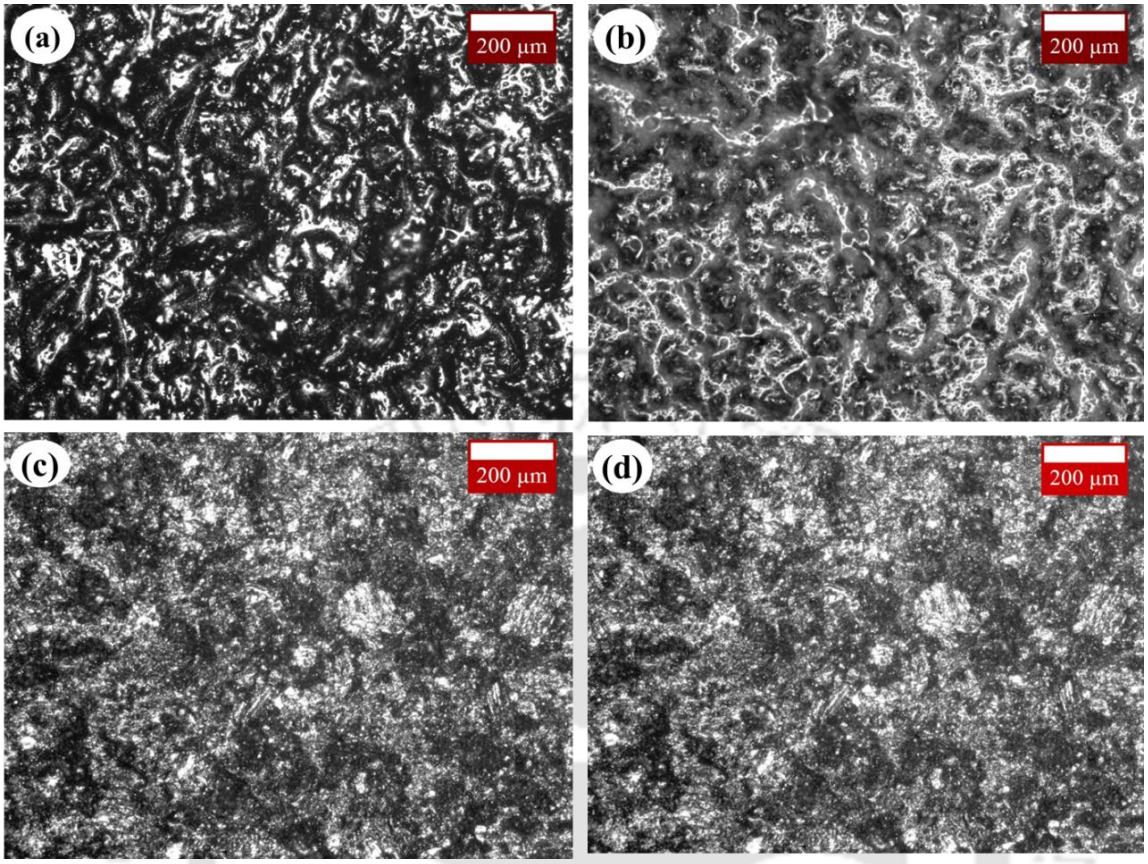

Figure 3.7: Optical microscopic images of both TiO_2-Ti (a and b) and graphite CEs (c and d) before (a and c) and after 2 h (b and d) of electrolysis. Experimental condition: SE 0.08 M, $-E_{cat}$ =–0.5 V with graphite/TiO_2-Ti system, $-E_{cat}$ =–0.6 V with graphite/graphite system, stirrer speed 300 rpm, pH 2.5, O_2 flow rate 4 LPM, and electrolyte 2 L.

$NaClO_4$ in the case of the graphite/TiO_2-Ti system caused a severe reduction in the current efficiency (CE_f, Eq. 2.2 of Chapter 2) of H_2O_2 formation, and it decreased to 10.5 % after 2 h from 52 % at 20 min of electrolysis (Figure 3.8a). CE_f was found to be the highest with H_2O_2 formation using NaCl for the graphite/TiO_2-Ti system (Figure 3.8a), with 59.5 % at 20 min of electrolysis. It decreased to 41.9 % at 120 min, which was 30-15 % higher compared to all other SEs in both the electrode combinations. Na_2SO_4 exhibited the highest CE_f (3-12 % higher) even though H_2O_2 formation was more with $NaNO_3$ because of a higher cell current (Figure 3.9) with the graphite/graphite system (Figure 3.8b). An initial CE_f of 63.3 % at 20 min with Na_2SO_4 came down to 29.9 % in 120 min, and the difference was marginal (5 %) with $NaClO_4$. Therefore, $NaClO_4$ was selected for further studies with the graphite/graphite system as ClO_4^- doesn't

complex with iron during the Fenton oxidation. This is why the influence of different concentrations of NaCl was studied further with TiO_2-Ti as the CE.

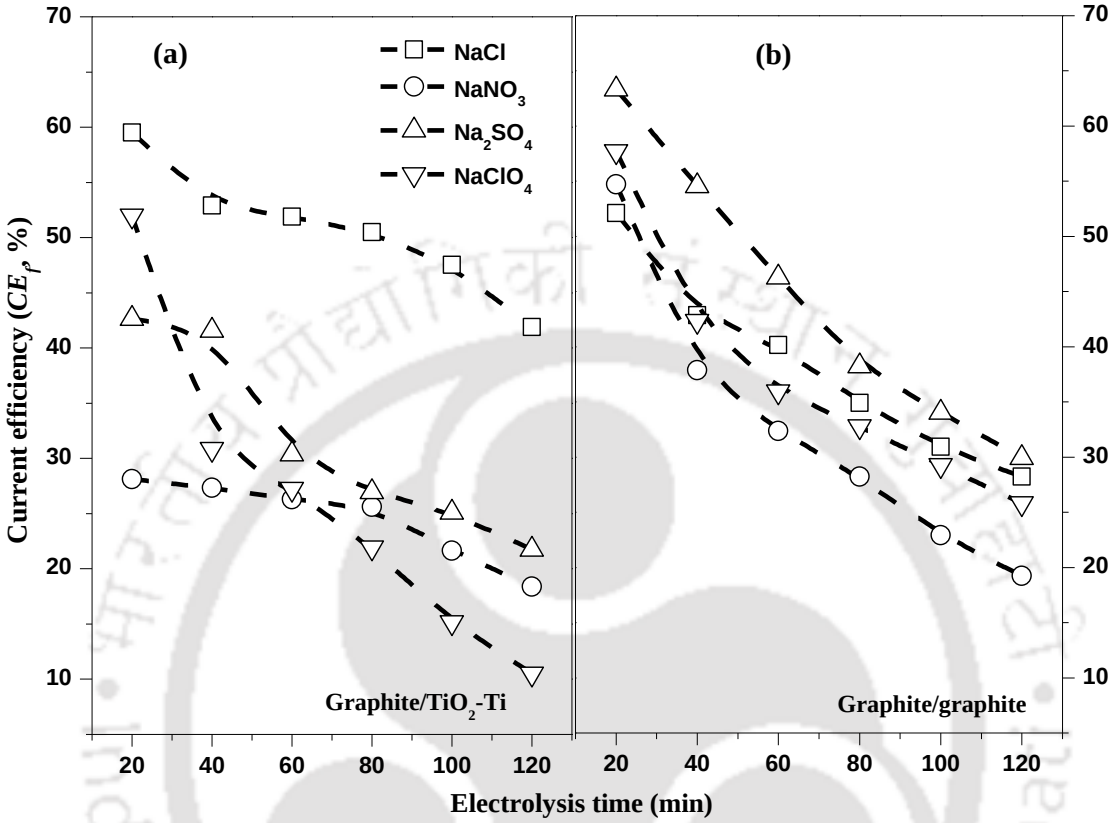

Figure 3.8: Current efficiency (CE_f) with electrolysis time calculated from Figure 3.5: (a) graphite/graphite system with $-E_{cat}$ =–0.6 V and (b) graphite/TiO_2-Ti system with $-E_{cat}$ =–0.5 V. Experimental condition: SE 0.08 M, stirrer speed 300 rpm, pH 2.5, O_2 flow rate 4 LPM, and electrolyte 2 L.

The effect of SEs concentrations on the formation of H_2O_2 and CE_f is shown in Figures 3.10a and 3.10b. The H_2O_2 formation was found to be the same at 0.05 and 0.10 M SE with both the electrode combinations, but CE_f was 5-13 % more at 0.05 M SE. H_2O_2 concentration was increased gradually with electrolysis time while the CE_f fell down. A notable reduction in H_2O_2 formation was found with an increase in the SE concentration from 0.08 to 0.10 M. The predominant chlorine species at pH < 3 is HOCl, and ClO^- is significant at pH > 6 (Czarnetzki and Janssen, 1992; Barazesh et al., 2015). So, at a higher concentration of NaCl (Figure 3.10a), more chloride based reactive species like Cl_2 (Cl^-/Cl_2: E^0 =1.163 V vs. Ag/AgCl) and HOCl

(Cl_2/HOCl: E^0 =1.433 V vs. Ag/AgCl) were formed because these reactions were thermodynamically more favourable (Chatzisymeon et al., 2010). A stringent smell of free chlorine was also detected during electrolysis. It resulted in H_2O_2 decomposition (Eq. 3.21). So, CE_f was dropped with a further increase in NaCl concentration even though a higher concentration of NaCl exhibited a higher mass transfer co-efficient of oxygen transport.

$$Cl_2 + H_2O_2 \rightarrow 2HCl + O_2 \quad (3.21)$$

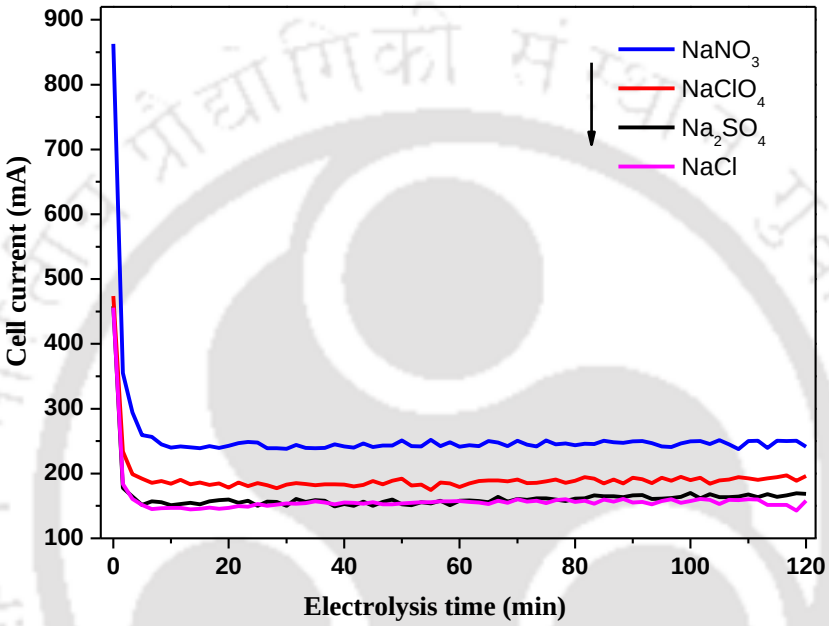

Figure 3.9: Cell current variation with electrolysis time at different supporting electrolyte. with graphite/graphite system. Experimental condition: $-E_{cat}$ =–0.6 V, SE 0.08 M, pH 2.5, stirrer speed 300 rpm, O_2 flow rate 4 LPM, and electrolyte 2 L.

The concentration of O_2 at the cathode surface is depleted rapidly (<5 s) after the start of electrolysis. So, the steady valley of cell current essentially implies the limiting current (i_L) of O_2 reduction reaction forming H_2O_2 and, i_L for macroscopic electrodes can be expressed by Eq. 3.22 (Qiang et al., 2002; Li et al., 1997).

$$i_L = k_m nFA(C_{DO,bulk} - C_{DO,surface}) \quad (3.22)$$

Where, k_m is the mass transfer coefficient (m/s), n is the number of electron transferred, F is the Faraday's constant (96487 C/mol), A is the effective cathode area (m^2), $C_{DO,bulk}$ and $C_{DO,surface}$ (=zero) are the bulk and surface concentration of DO (mol/m^3). D represents the diffusion coefficient (m^2/s) of DO. An equilibrium bulk concentration of DO ($C_{DO,bulk}$) was found as 1.28 mol/m^3 throughout the experiment.

k_m was found to be 9.6×10^{-5}, 9.9×10^{-5} and 10.4×10^{-5} m/s with 0.05, 0.08, and 0.10 M NaCl with the graphite/TiO_2-Ti system. In the case of graphite as the CE, similar results were obtained when $NaClO_4$ was used (Figure 3.10b). The increase in $NaClO_4$ concentration from 0.08 to 0.10 M provided a higher current, which induced the formation of H_2O instead of H_2O_2 (Zhou et al., 2007). k_m was 10.4×10^{-5}, 12.5×10^{-5}, and 14.7×10^{-5} m/s with $NaClO_4$ concentration of 0.05, 0.08, and 0.10 M using the graphite/graphite system. It also was observed that CE_f was reduced by 48.4 and 26.2 % at 20 and 120 min of electrolysis with 0.10 M $NaClO_4$ compared to 0.08 M. According to these results, 0.08 M was used for all subsequent experimental studies. In fact, this is the concentration used to study the role of different SEs on the formation of H_2O_2 (Figures 3.5 and 3.10).

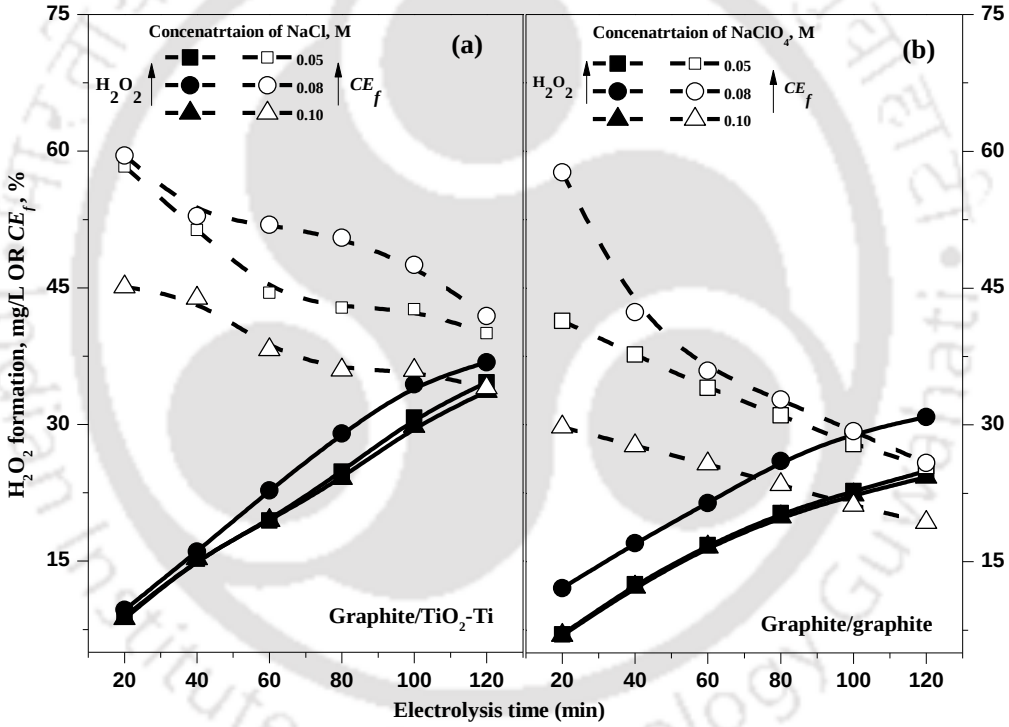

Figure 3.10: Variations of H_2O_2 formation and current efficiency (CE_f) with electrolysis time using NaCl with graphite/TiO_2-Ti system and $NaClO_4$ with graphite/graphite system at 300 rpm stirrer speed, 4 LPM O_2 flow rate, and 2 L electrolyte. Effect of SE concentration at pH 2.5: (a) using NaCl at $-E_{cat}$ =–0.5 V and (b) using $NaClO_4$ at $-E_{cat}$ =–0.6 V.

3.2.3.2 Optimal pH for H_2O_2 electro-generation

pH strongly affected H_2O_2 formation as well as the competition between water and chloride oxidation at TiO_2-Ti anode. The highest H_2O_2 formation was found at pH 2.5 at both

anode materials (Figures 3.11a and 3.11b). However, CE_f was the highest (at least 14 % more) at pH 3.5, and it was the lowest (at least 5 % less) at pH 4.5 (Figures 3.11a and 3.11b). The variations of pH were about +0.2 and –0.2 units at pH above and below 2.5 with both the CEs. Chlorine quickly reacts with peroxides forming O_2 (Eq. 3.20) (Polcaro et al., 2008). H_2O_2 solvates a proton thus, forming an oxonium ion ($H_3O_2^+$) at a lower pH (< 2.5) (Eq. 1.46, Chapter 1). On the other way, it led to a decrease in H_2O_2 formation obviously of H^+ insufficiency at a higher pH (> 2.5).

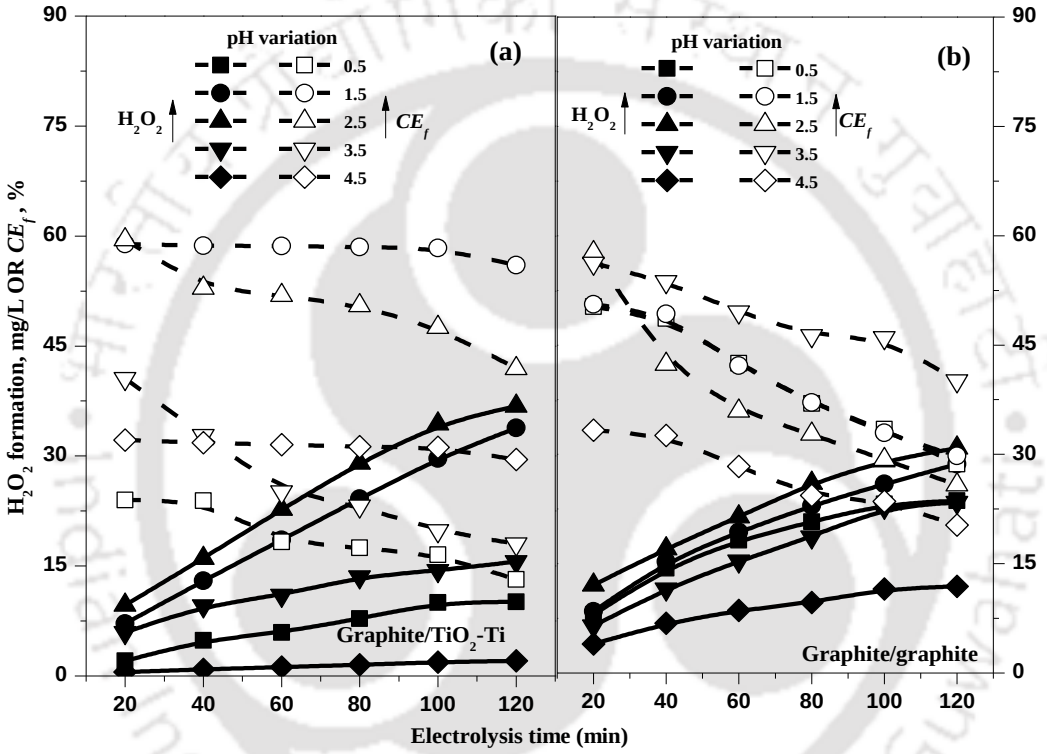

Figure 3.11: Variations of H_2O_2 formation and current efficiency (CE_f) with electrolysis time using NaCl with graphite/TiO_2-Ti system and $NaClO_4$ with graphite/graphite system at 300 rpm stirrer speed, 4 LPM O_2 flow rate, and 2 L electrolyte. Effect of pH: (a) using 0.08 M NaCl at $-E_{cat}$ =–0.5 V, and (b) using 0.08 M $NaClO_4$ at $-E_{cat}$ =–0.6 V.

3.2.3.3 Effect of $-E_{cat}$ on cell current and H_2O_2 formation

The influence of $-E_{cat}$ on H_2O_2 formation was studied between $-E_{cat}$ =–0.3 and –0.7 V vs. Ag/AgCl with both the electrode systems. The results are shown in Figures 3.12a and 3.12b. The rate of H_2O_2 formation at $-E_{cat}$ =–0.5 and –0.6 V was found to be closer with TiO_2-Ti (Figure 3.12a). It was $-E_{cat}$ =–0.6 V with graphite as the CE (Figure 3.12b), however, the difference was

marginal. The yield of H_2O_2 was about of 30.87 and 36.8 mg/L in 2 h with the graphite/graphite and graphite/TiO_2-Ti systems, respectively. Higher -E_{cat} (> 0.6 V vs. Ag/AgCl) caused decomposition of H_2O_2 on both the electrodes and in the bulk solution (Eq. 1.37, Chapter 1) (Brilllas et al., 2000), and Cl_2 formation is also expected to be more. An increase in the formation of Cl_2 (Eq. 3.17) could enhance the HClO generation (Eq. 3.23) which decompose H_2O_2 to O_2 (Eq. 3.24). Furthermore, a portion of H_2O_2 could be anodically oxidized to $^{\bullet}$OOH radicals at a higher potential (Martinez-Huitle and Brillas, 2009).

$$2Cl_2 + H_2O \leftrightarrow HOCl + H^+ + Cl^- \quad (3.23)$$

$$HOCl + H_2O_2 \rightarrow Cl^- + O_2 + H_2O + H^+ \quad (3.24)$$

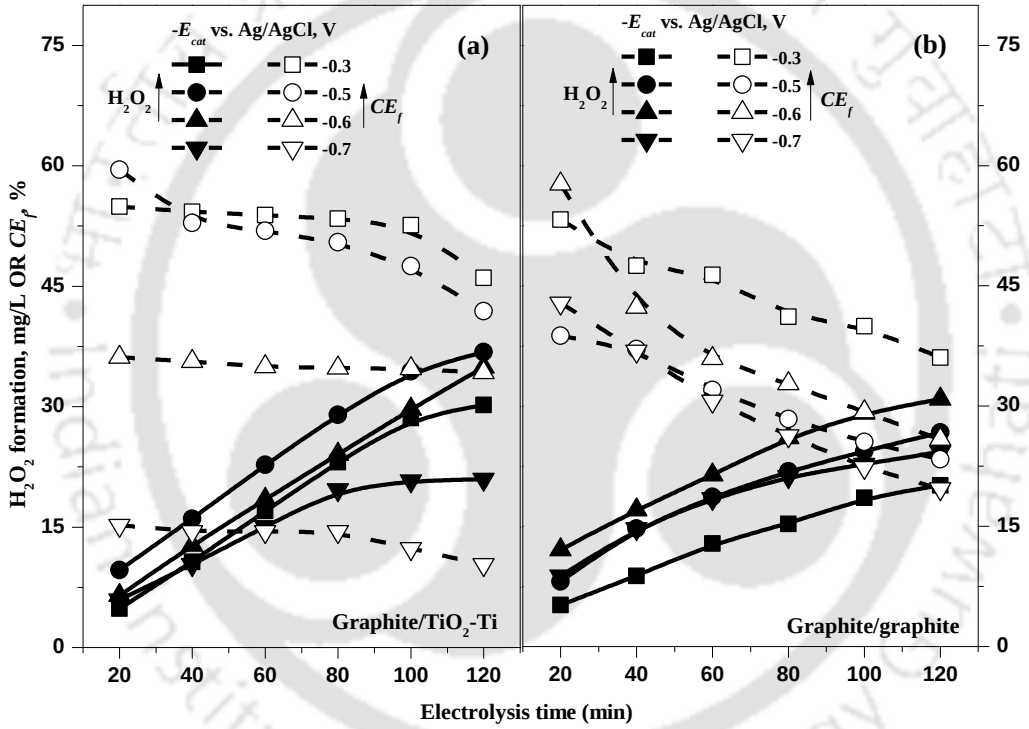

Figure 3.12: Variations of H_2O_2 formation and current efficiency (CE_f) with electrolysis time using NaCl with graphite/TiO_2-Ti system and $NaClO_4$ with graphite/graphite system at 300 rpm stirrer speed, 4 LPM O_2 flow rate, and 2 L electrolyte. Effect of different –E_{cat} at pH 2.5: (a) using 0.08 M NaCl, and (b) using 0.08 M $NaClO_4$.

The cell current was increased gradually with an increase in –E_{cat} vs. Ag/AgCl from –0.3 V (Figure 3.13). An increase in the cell current was significant at –E_{cat} =–0.7 V. It implied a significant reduction of H_2O_2 to H_2O (E^0 =1.578 V vs. Ag/AgCl) and H_2 evolution (E^0 =–0.198 V vs. Ag/AgCl) at –E_{cat} =–0.7 V in the case of graphite/TiO_2-Ti system. The

reduction of H_2O_2 to H_2O was gradually promoted by the accumulation of H_2O_2. At a higher current, CE_f was decreased considerably with an increase in $-E_{cat}$ vs. Ag/AgCl because of parasitic reactions. But, CE_f was low for the cathode potential of 0.7 V vs. Ag/AgCl. It was the reason for the lower H_2O_2 production (Figure 3.12a) and high cell current (Figure 3.13a). At $-E_{cat} < -0.5$ V, a higher CE_f of 8-30 % was noted even though H_2O_2 formation was around 33 % lower at $-E_{cat} = -0.3$ V than $-E_{cat} = -0.7$ V after 120 min. Similar result was observed after 2 h of operation by Zhou and co-workers (Zhou et al., 2013). They claimed that an increase in the cell current was caused by the parasitic reactions (Eqs. 1.40 and 1.41, Chapter 1), and it resulted in H_2O_2 decomposition (Brillas and Casado, 2002). The highest CE_f of 57.7 % in the first 20 min was at $-E_{cat} = -0.6$ V. An increase in the cell current was notable at $-E_{cat} > -0.3$ V with the graphite/graphite system (Figure 3.13b) against $-E_{cat} = -0.7$ V with the graphite/TiO_2-Ti system. It signifies that the parasitic reactions were induced even at a relatively low $-E_{cat}$ (> –0.3 V) with the graphite/graphite system.

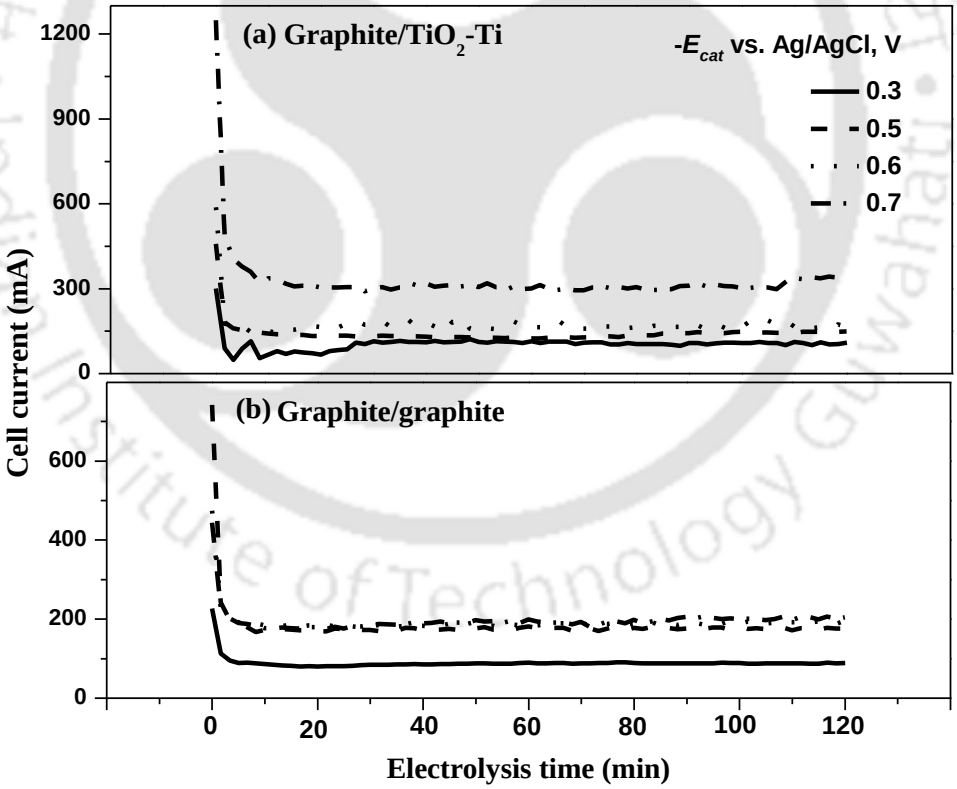

Figure 3.13: Cell current variations with electrolysis time at different $-E_{cat}$: (a) 0.08 M NaCl with graphite/TiO_2-Ti system and (b) 0.08 M $NaClO_4$ with graphite/graphite system. Experimental condition: pH 2.5, stirrer speed 300 rpm, O_2 flow rate 4 LPM, and electrolyte 2 L.

3.3 Major findings

The use of an inappropriate supporting electrolyte in an undivided cell for the combined AO and EF process could destroy the efficiency of the process as it could limit the life of the electrode, decompose the analyte, and scavenge the radicals. The following are the key conclusions of this chapter.

- Significant self-decomposition of H_2O_2 was observed at pH> 8 and temperature > 50 °C. Decomposition of H_2O_2 was accelerated in an alkaline media at an elevated temperature.
- At low pH (< 4), H_2O_2 was fairly stable in the presence of K^+, Ca^{2+}, Co^{2+}, and Ni^{2+} ions. However, a trace amount of Cu^{2+} and Mn^{2+} could catalytically increase H_2O_2 decomposition.
- H_2O_2 became essentially unstable at a higher pH with all trace metal ions tested except Co^{2+} and Ni^{2+} ions having a low catalytic effect even for long time storage at a high pH.
- The overpotential of O_2 reduction was the highest with Na_2SO_4 as the supporting electrolyte and it was the lowest with $NaClO_4$ with the graphite/Pt combination as evidenced from the CV. However, NaCl exhibited the highest yield of H_2O_2 formation followed by Na_2SO_4 and $NaNO_3$ but $NaClO_4$ suppressed the generation of H_2O_2, in particular, at a later stage of the reaction (> 80 min) with the graphite/TiO_2-Ti system.
- The use of $NaClO_4$ as a supporting electrolyte may be avoided as it could destroy the Fenton's reagent by reactive oxygen species formation at TiO_2-Ti anode. However, specific anodes like boron- doped diamond may be used for the coupled AO and EF process. NaCl outperformed $NaClO_4$ for H_2O_2 generation but the use of Cl^- may cause complex formation with Fe(II)/Fe(III) in the case of coupled Fenton oxidation and AO, and Cl^- also may lead to H_2O_2 decomposition. Even though, the yield of H_2O_2 was comparable between Na_2SO_4 and $NaNO_3$ but Na_2SO_4 exhibited a superior current efficiency. In the case of graphite/graphite system, the influence of the SEs on the increasing order of the current efficiency was found as Na_2SO_4 > NaCl > $NaClO_4$>> $NaNO_3$.
- A higher H_2O_2 yield with NaCl was in accordance with the mass transfer coefficient of DO transport which was increased at a higher Cl^- concentration with the graphite/TiO_2-Ti system, with similar results with $NaClO_4$ in the case of graphite/graphite system. It varied from 9.6×10^{-5} to 10.4×10^{-5} and, 10.4×10^{-5} to 14.7×10^{-5} m/s with NaCl and $NaClO_4$, respectively, for the graphite/TiO_2-Ti and graphite/graphite electrode combinations.

- The optimal conditions were determined as pH 2.5, $-E_{cat}$ =–0.6 V vs. Ag/AgCl, 0.08 M SE, and O_2 flow rate 4 LPM with the graphite/graphite system. Graphite/TiO_2-Ti system exhibited almost the same optimal condition except – E_{cat} =–0.5 V vs. Ag/AgCl. The highest concentration of H_2O_2 formation was 36.8 and 30.9 mg/L at 2 h with the graphite/TiO_2-Ti and graphite/graphite systems using NaCl and $NaClO_4$ as the SEs.

References

Aleboyeh A., Moussa Y., Aleboyeh H. The effect of operational parameters on UV/H_2O_2 decolourisation of acid blue 74, *Dyes Pigm*. **2005**, 66 (2), 129-134.

Alverez-Gallegos A., Pletcher D. The removal of low level organics via hydrogen peroxide formed in a reticulated vitreous carbon cathode cell. Part 2: The removal of phenols and related compounds from aqueous effluents, *Electrochim Acta.* **1999**, 44, 2483-2492.

Barazesh J.M., Hennebel T., Jasper J.T., Sedlak D.L. Modular advanced oxidation process enabled by cathodic hydrogen peroxide production, *Environ. Sci. Technol.* **2015**, 49, 7391-7399.

Brillas E., Bonos M.A., Camps S., Arias C., Cabot P.L., Garrido J.A., Rodriguez R.M. Catalytic effect of Fe^{2+}, Cu^{2+} and UVA light on the electrochemical degradation of nitrobenzene using an oxygen-diffusion cathode, *New J. Chem.* **2004**, 28, 314-322.

Brillas E., Calpe J.C., Casado J. Mineralization of 2,4-D by advanced electrochemical oxidation processes, *Water Res.* **2000**, 34, 2253-2262.

Brillas E., Casado J. Aniline degradation by Electro-Fenton and peroxi-coagulation processes using a flow reactor for wastewater treatment, *Chemosphere* **2002**, 47, 241-248.

Brillas E., Sires I., Oturan, M.A. Electro-Fenton process and related electrochemical technologies based on Fenton's reaction chemistry, *Chem. Rev.* **2009**, 109, 6570-6631.

Chatzisymeon E., Fierro S., Karafyllis I., Mantzavinos D., Kalogerakis N., Katsaounis A. Anodic oxidation of phenol on Ti/IrO_2 electrode: Experimental studies, *Catal Today* **2010**, 151, 185-189.

Czarnetzki L.R., Janssen L.J.J. Formation of hypochlorite, chlorate and oxygen during NaCl electrolysis from alkaline solutions at a RuO_2/TiO_2 anode, *J. Appl. Electrochem.* **1992**, 22, 315-324.

Duke F.R., Quinney P.R. The kinetics of reduction of perchlorate ion by Ti(III) in dilute solution, *Am. Chem. Soc.* **1954**, 76, 3800-3803.

Dyke J.V., Ito K., Obitsu T., Hisamatsu Y., Dasgupta P.K., Blount B.C. Perchlorate in dairy milk. Comparison of Japan versus the United States, *Environ. Sci. Technol.* **2007**, 41, 88-92.

Eisenberg G.M. Colorimetric determination of hydrogen peroxide, *Ind. Eng. Chem. Anal. Ed.* **1943**, 15, 327-328.

Feng S., Xin X., Fan Z., Man-ping J., Zhengang W. Effect of pH value on adiabatic decomposition characteristics of hydrogen peroxide, *Chem. Eng.* (*China*) **2012**, 40 (276), 49-52.

Flox C., Ammar S., Arias C., Brillas E., Vargas-Zavala A.V., Abdelhedi R. Electro-Fenton and photoelectro-Fenton degradation of indigo carmine in acidic aqueous medium, *Appl. Catal. B* **2006b**, 67, 93-104.

Flox C., Cabot P.L., Centellas F., Garrido J.A., Rodrıguez R.M., Arias C., Brillas E. Electrochemical combustion of herbicide mecoprop in aqueous medium using a flow reactor with a boron-doped diamond anode, *Chemosphere* **2006a**, 64, 892-902.

Fockedey E., Lierde A.V. Coupling of anodic and cathodic reactions for phenolelectro-oxidation using three-dimensional electrodes, *Water Res.* **2002**, 36, 4169-4175.

Karuppiah M.T., Raju G.B. Anodic degradation of CI reactive blue 221 using graphite and $IrO_2/TaO_2/RuO_2$ coated titanium electrodes, *Ind. Eng. Chem. Res.* **2009**, 48, 2149-2156.

Khan A.F. Study on effect of heavy metals and the stabilisation of hydrogen peroxide bleach bath by polycarboxylic acid, amino polycarboxylic acid, poly amino-phosphonic acid and their salts, Karachi, **2006**.

Lee C., Batchelor B., Park S.H., Han D.S., Abdel-Wahab A., Kramer T.A. Reduction of perchlorate using zero-valent titanium (ZVT) anode: reaction mechanism, *Adv. Environ. Res.* **2012**, 1, 37-55.

Li Z.M., Shea P.J., Comfort S.D. Fenton oxidation of 2,4,6- trinitrotoluene in contaminated soil slurries. *Environ. Eng. Sci*. **1997**, 14, 55-66.

Loaiza-Ambuludi S., Panizza M., Oturan N., Ozcan A., Oturan M.A. Electro-Fenton degradation of anti-inflammatory drug ibuprofen in hydroorganic medium, *Electroanal. Chem.* **2013**, 702, 31-36.

Martınez-Huitle C.A., Brillas E. Decontamination of wastewaters containing synthetic organic dyes by electrochemical methods: A general review, *Appl. Catal. B* 2009, 87, 105-145.

Moffettt J.W., Zika R.G. Reaction kinetics of hydrogen peroxide with copper and iron in seawater, *Environ. Sci. Technol*. **1987**, 21 (8), 804-810.

Montanaro D., Petrucci E., Merli C. Anodic, cathodic and combined treatments for the electrochemical oxidation of an effluent from the flame retardant industry, *J. Appl. Electrochem.* **2008**, 38, 947-954.

Nicoll W.D., Smith A.F. Stability of dilute alkaline solutions of hydrogen peroxide, *Ind. Eng. Chem*. **1955**, 47 (12), 2448-2554.

Pajootan E., Arami M., Rahimdokht M. Discoloration of wastewater in a continuous electro-Fenton process using modified graphite electrode with multi-walled carbon nanotubes/surfactant, *Sep. Purif. Technol*. **2014**, 130, 34-44.

Panizza M., Cerisola G. Application of diamond electrodes to electrochemical processes, *Electrochim. Acta.* **2005**, 51, 191-199.

Peralta E., Natividad R., Roa G., Marin R., Romero R., Pavon T. A comparative study on the electrochemical production of H_2O_2 between BDD and graphite cathodes, *Sustain. Environ. Res.* **2013**, 23, 259-266.

Petlicki J., Palusova D., Van de Ven T.G.M. Physicochemical aspects of catalytic decomposition of hydrogen peroxide by manganese compounds, *Ind. Eng. Chem. Res*. **2005**, 44 (7), 2002-2010.

Polcaro A.M., Vacca A., Mascia M., Ferrara F. Product and by-product formation in electrolysis of dilute chloride solutions, *J. Appl. Electrochem.* **2008**, 38, 979-984.

Qiang Z., Chang J., Huang C. Electrochemical generation of hydrogen peroxide from dissolved oxygen in acidic solutions, *Water Res.* **2002**, 36 (1), 85-94.

Sarala P., Venkatesha T.V. Effect of cathode materials on electrochemical degradation of Luganil Blue N and acid red I. Port, *Electrochim. Acta.* **2013**, 31, 175-183.

Szpyrkowicz L., Kaul S.N., Neti R.N., Satyanarayan S. Influence of anode material on electrochemical oxidation for the treatment of tannery wastewater, *Water Res.* **2005**, 39, 1601-1613.

Thiam A., Sires I., Garrido J.A., Rodriguez R.M., Brillas E. Effect of anions on electrochemical degradation of azo dye Carmoisine (Acid Red 14) using a BDD anode and air-diffusion cathode, *Sep. Purifi. Technol.* **2015**, 140, 43-52.

Urbansky E.T. Perchlorate chemistry:Implications for analysis and remediation, *Biorem J.* **1998**, 2, 81-95.

Wang C.T., Chou W.L., Chung M.H., Kuo Y.M. COD removal from real dyeing wastewater by electro-Fenton technology using an activated carbon fiber cathode, *Desalination* **2010**, 253, 129-134.

Zhou L., Hu Z., Zhang C., Bi Z., Jin T., Zhou M. Electro-generation of hydrogen peroxide for electro-Fenton system by oxygen reduction using chemically modified graphite felt cathode, *Sep. Purif. Technol.* **2013**, 111, 131-136.

Zhou M., Yu Q., Leia L., Barton G. Electro-Fenton method for the removal of methyl red in an efficient electrochemical system, *Sep. Purif. Technol.* **2007**, 57, 380-387.

Chapter-4

Synthesis of NiO and Co_3O_4 Nanoparticles Catalysing Electrochemical H_2O_2 Formation

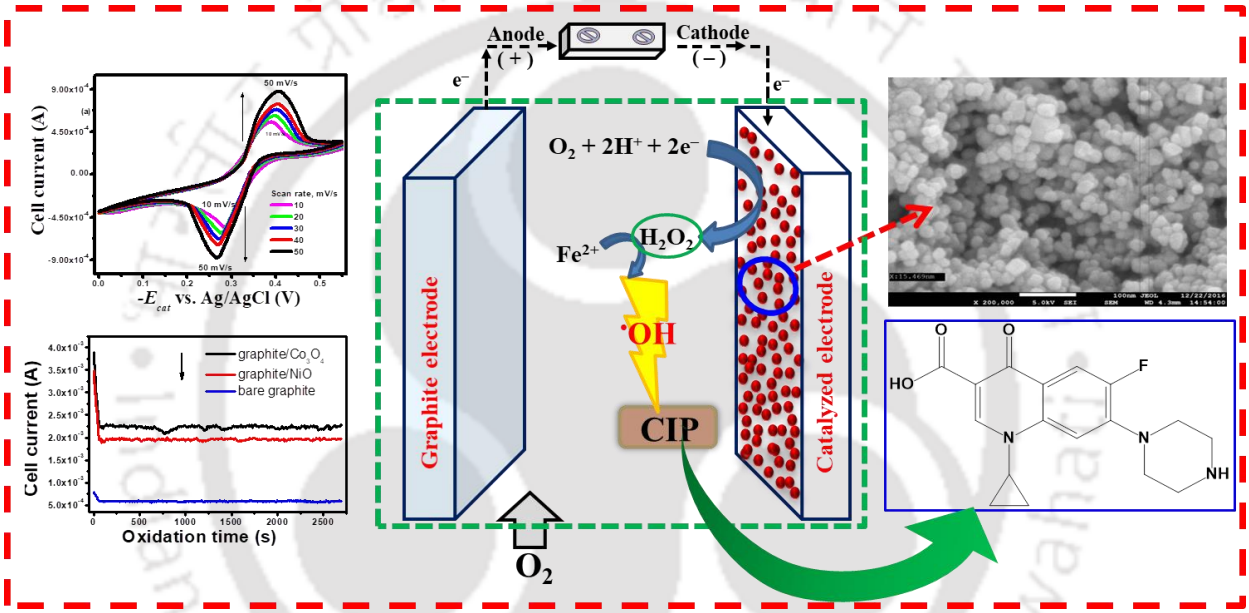

Chapter 4 is divided into three major parts. The first part investigates the physiochemical attributes of NiO and Co_3O_4 NPs and the mechanism of its formation. Studies on H_2O_2 electrogeneration catalysed by NiO NPs were performed in the second part, and the results obtained were then compared with Co_3O_4 NP catalysed H_2O_2 generation. The last part reports on the application of H_2O_2 generated (in the second part) for the degradation of ciprofloxacin (CIP), an antibiotic drug, in the electro-Fenton process (EFP).

4.1 Specific background

The current efficiency (CE_f) of H_2O_2 generation in both the systems (graphite/TiO_2-Ti and graphite/graphite) was quite low even at the beginning of the experiment (28 to 63 %), and there was a quick fall of CE_f with the progress of electrolysis (Section 3.2.3, Chapter 3). The probable reasons are that traditional carbonaceous materials suffer from high overpotential of O_2 reduction (Section 3.2.2, Chapter 3) and slow kinetics of electron transfer (Chen et al., 2012). These limitations are subdued in many extents with the development of nano-structured materials which are used as electrocatalysts in H_2O_2 synthesis (Li et al., 2009; Shuan et al., 2013). Therefore, the current researches are intensified towards the development and synthesis of various electrocatalysts such as metal nanoparticles (NPs) and metal oxides NPs to enhance the current efficiency of H_2O_2 formation, and these catalysts can be easily immobilized on the surface of a tiny electrode (Barros et al., 2015; Carneiro et al., 2015).

The transition metal oxides nanostructures such as Co_3O_4, CuO, NiO, and MnO_2 show strong electrocatalytic activity and faster electron-transfer reactions for an improved H_2O_2 generation (Jia et al., 2009; Assumpcao et al., 2013). The synthesis of such materials is relatively easy and cheaper than noble metals and carbon nanostructures. In particular, both NiO NPs and Co_3O_4 spinel NPs have many potential applications in heterogeneous catalysis, ceramic pigments and dyes, energy storage and gas sensing, lithium-ion batteries, and fuel cell electrodes and electrochromic devices due to their easily interchangeable oxidation states (Bhatt et al., 2011; Al-Sehemi et al., 2014). *Moreover, Ni(II) and Co(II) ions exhibit a very low catalytic activity for the decomposition of H_2O_2 even at a higher pH and reaction temperature* (Section 3.2.1, Chapter 3). A strong interfacial interaction between catalysts (here NiO and Co_3O_4 spinel NPs) and graphite (electrode base/catalyst support) also could facilitate the interfacial charge transfer process (Chen et al., 2017a). According to the most of the studies, the morphology, crystallography, and the size of NPs mostly affect their catalytic activities (Duan et al., 2012; El-Kemary et al., 2013; Liu et al., 2013). The common techniques involved in the synthesis of the *S. edule* nano-structured NiO and Co_3O_4 materials are sol-gel method, solvo-/hydrothermal method, thermal decomposition method, chemical spray pyrolysis, microemulsion, and microwave irradiation (Section 1.6.3, Chapter 1).

In this Chapter, the aqueous fruit extract of *S. edule* (Section 2.2, Chapter 2) was employed for the synthesis of NiO and Co_3O_4 NPs in place of using chemical reductants such as sodium

borohydride, hydrazine and ethylene glycol, and capping agents such as polyvinylpyrrolidone and sodium citrate (Chinnasamy et al., 2005; Li et al., 2009; Ryu et al., 2010; El-Kemary et al., 2013; Medvedeva et al., 2017). To understand the mechanism of NPs formation mediated by these plant-based analytes, the (control) experiments were conducted for synthesizing NiO and Co_3O_4 NPs without the use of analytes. The characterizations of NPs were performed through XRD, TGA, FTIR, UV-Vis and Raman spectroscopies, VSM, BET isotherm, SEM, and HRTEM (Section 2.4, Chapter 2). The support electrode of NPs was made of high-purity graphite which was fabricated by the conventional carbon paste method, and the NPs were embedded in the support electrode with the help of Nafion as a binder material (Xia et al., 2014).

The fundamental electrochemical parameters of the redox couple reactions of H_2O_2 generation by dissolved oxygen (DO) reduction at graphite/NiO NPs cathode using NiO NPs were derived using cyclic voltammetry tests in tandem with the bare-support and control electrodes/experiments. After that, the results obtained using graphite/NiO NPs electrode were compared with Co_3O_4 NP catalysed H_2O_2 generation. The effects of scanning rate and proton concentration on the yield and current efficiency of H_2O_2 generation were investigated in details by the chronoamperometry experiments. The effective surface area of the working electrode (WE) was varied from 3.3 to 5.9 cm^2 to determine the limiting current density and the co-efficient of DO mass transfer for the generation of H_2O_2. In this study, Na_2SO_4 was chosen as the SE by considering the environmental impact of $NaClO_4$ (Section 3.1, Chapter 3) and the potential of Cl_2 release in the case of NaCl (Section 3.2.3.1, Chapter 3). Na_2SO_4 also exhibited a relatively higher CE_f than $NaNO_3$. The concentration of SE was fixed at 0.08 M optimized from the earlier study (Section 3.2.3.1, Chapter 3).

In the last part of this Chapter, degradation and mineralization of CIP was performed in EFP with the addition of Fe^{2+} and in-situ generation of H_2O_2 catalysed by NiO and Co_3O_4 NPs. After that, the decomposition mechanism of CIP was proposed and validated by the mass spectra of the reaction products (intermediates) identified after the reaction. A brief introduction for the selection of CIP is appended herewith in the following paragraphs.

CIP is a second-generation fluoroquinolones class of antibiotic drug (Gupta and Garg, 2018). It is widely administered in India mainly to treat bacterial infections. CIP is also used as a food additive at sub-therapeutic doses to promote growth and to improve the feed efficiency (Ellis et al., 2006). CIP works through the interference of the synthesis of protein and DNA that

stops DNA to rewind. In the year 2017, the production of CIP reached to 40% units in India (Raghavan, 2017) and around 70 % of CIP produced is consumed (Meyer et al., 2000; Yahya et al., 2014). The units of antibiotics sold in India are increased by 40 % between 2005 and 2009, and a major fraction of it is sold without a proper medical recommendation (Hernando et al., 2006). It is found that 30 to 90 % of the administered antibiotics can be evacuated even in the unmetabolized form. CIP is frequently identified in hospital wastewater, sewage treatment plant effluent, and surface water (Golet et al., 2002; Christian et al., 2003; Li et al., 2013). CIP is also strongly adsorbed on sewage sludge with as high as 6.3 mg/kg dry of matter (Golet et al., 2002). The concentration of CIP in the effluent stream from bulk drug production sites in Patancheru, near Hyderabad (India) was many hundred times higher the toxicity level to some bacteria (Larsson et al., 2007).

The unregulated disposals of unused and expired medicines are the primary inception route of PhACs into the environment from hospitals and clinical facilities (Chang et al., 2010). The direct rejection of the used syringe into the hospital drain off is an important source of PhACs into the environment (Huseyin et al., 2006). The residues of PhACs also enter into the aquatic environment due to their incomplete elimination in the water treatment plant (Goutama et al., 2007). The runoff from agricultural fields often contains eroded soil, fertilizers, pharmaceuticals and pesticides that together form a major source of water pollution (Giri et al., 2011). It poses direct risks to human health via contaminated drinking water, and they may also foster conditions for pathogens to develop antibiotic resistances.

4.2 Results and discussions

4.2.1 Characteristics of NiO and Co_3O_4 NPs

4.2.1.1 TGA of synthesized NPs and calcination temperature

The TGA profile of Ni-dry particles before calcination is shown in Figure 4.1a. Mass losses mostly took place in two steps between 40 to 120 and 230 to 380 °C as evident from the differential thermogravimetric (DTG) analysis (Figure 4.1b). The evaporation of adsorbed water was found to be 4 % (< 120 °C). The major mass loss of 25 % was observed in the second temperature step. This was attributable to the thermal decomposition of $Ni(OH)_2$ to NiO (Eq. 4.1) with the removal of sulphate species (Cha et al., 2012). The removal of organic constituents like AA, carbohydrates, carbonates, resistive aromatic complexes, and lignins usually occur

within this temperature range (Carballo et al., 2008). So, it was highly likely that the decomposition of these compounds/ bio-extract adsorbed on NiO NPs took place simultaneously with the formation of NiO NPs within the same temperature range. The mass loss was invariant beyond 420 ºC with an incremental heating time of 42 min (heating rate 10 °C/min). It justifies the selection of calcination temperature of 500 °C for the formation of NiO NPs within 2 h (Cha et al., 2012). It was also in accordance with the sharp and distinct XRD pattern observed for NiO NPs (Section 4.2.1.2, Chapter 4). Ni-control particles also exhibited a similar the mass loss trend (Figure 4.1a). But, the shift in the peak position (Figure 4.1b) may be of other species of Ni such as NiOOH were present even after the calcination (mass loss was also lower).

$$Ni(OH)_2 \xrightarrow{\text{Calciantion}} NiO + H_2O \qquad (4.1)$$

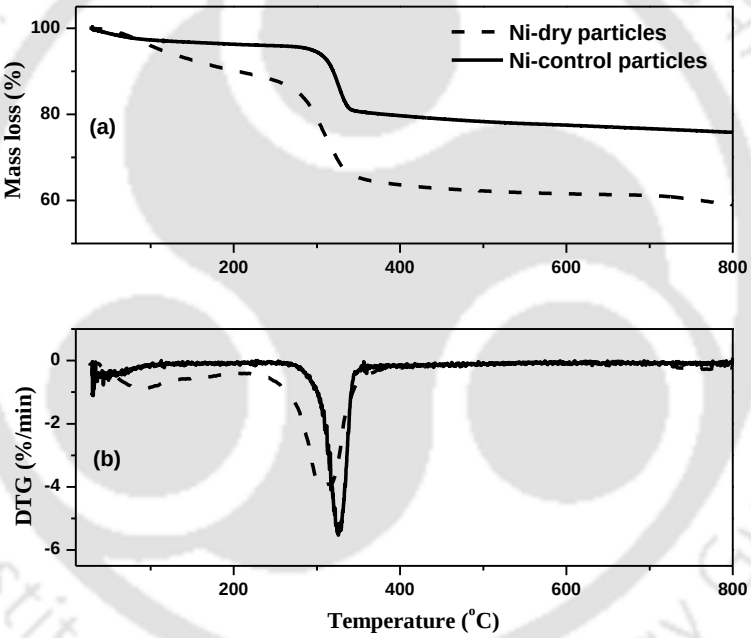

Figure 4.1: (a) TGA profiles, and (b) DTG analysis of Ni-dry particles before calcination and Ni-control particles after the calcination.

The TGA of Co-dry particles is shown in Figure 4.2a. It can be seen that the mass loss took place at four temperature steps as evident from the differential thermogravimetric (DTG) profile (Figure 4.2b). The initial mass loss of about 4 % was attributable to the evaporation of adsorbed water below 120 °C. Like NiO NPs, the next mass loss of 11 % appeared at 220-330 ºC. The simultaneous removal of bio-organic salt like carbonates and decomposition of resistive

aromatic complexes (Carballo et al., 2008) along with desorption of O_2 and H_2O from CoOOH and $Co(OH)_2$ forming Co_3O_4 (Yang et al., 2010) took place at 330-455 ºC, and a mass loss of 21 % was recorded. There was about 15 % mass loss between 455 and 615 ºC. The formation of Co_3O_4 was mostly complete in this region, and no further mass loss was observed beyond 700 °C. It corroborates the XRD pattern of Co_3O_4/700 ºC/6h NPs (Section 4.2.1.2, Chapter 4).

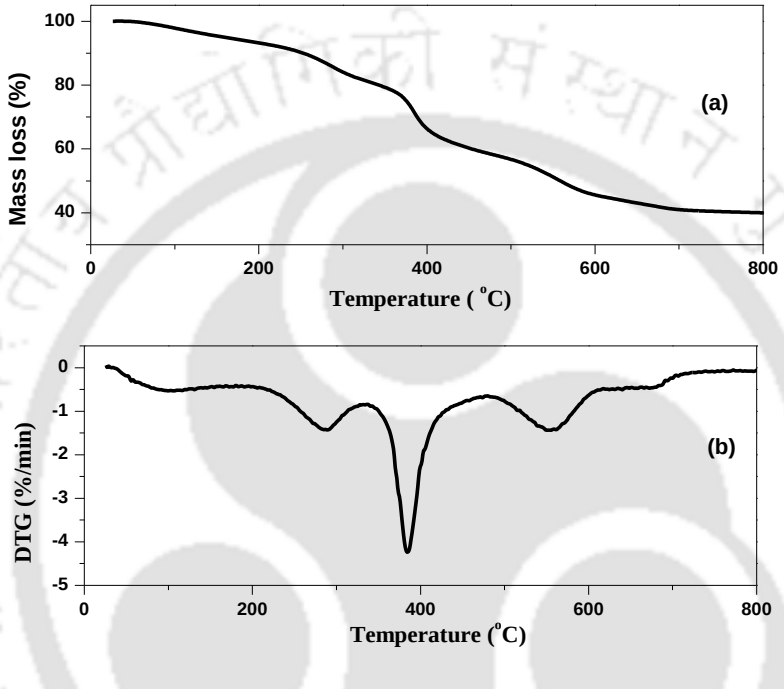

Figure 4.2: (a) TGA of Co-dry particles without calcination, and (b) DTG profile of Co-dry particles.

4.2.1.2 Crystalline nature of NiO and Co_3O_4 NPs

The phase purity and crystalline structures of Ni-dry, Ni-control, and NiO NPs are illustrated in Figure 4.3. No distinct diffraction peak was found in the case of Ni-dry particles due to its amorphous nature (Figure 4.3a). The sharp and intense diffraction peaks appeared at 2θ=37.15, 43.2, 62.8, 75.2, and 79.5° (Figure 4.3b) for diffraction from (111), (200), (220), (311), and (222) planes of the simple cubic crystals of NiO NPs (JCPDS card file 1010095). It was evident from the XRD pattern that NiO NPs were free from impurities but, the elemental composition NiO seems to be non-stoichiometric (Motahari et al., 2015) being blackish in colour (Figure 2.7, Chapter 2). The average crystallite size of NiO NPs was found to be 25.8 nm from the Debye Scherrer equation (Eq. 4.2) (Alagiri et al., 2012).

$$\tau = \frac{k\lambda}{\beta Cos\theta} \qquad (4.2)$$

Where, τ is the crystallite size (nm); k = 0.94, a crystallite shape factor; λ = X-ray wavelength; and β = full width at half maximum of the diffraction peak at the diffraction angle, θ.

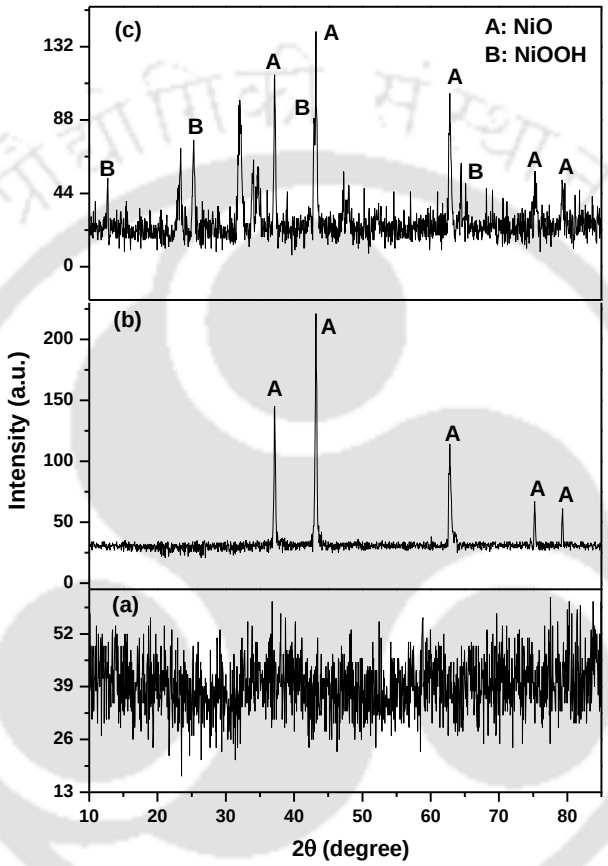

Figure 4.3: X-ray diffractograms of (a) Ni-dry (without calcination), (b) NiO (calcined at 500 °C for 2 h), and (c) Ni-control (without bio-extract) particles.

But for Ni-control, strong XRD peaks of NiOOH was identified at 2θ=12.7, 25.3, 43.0, and 65.15° for the diffraction from the (111), (222), (212), and (101) planes (Barnard et al., 1980; Handan et al., 2013). The unidentified impurities also appeared at 2θ=23.4, 31.9, 34.1, 34.9, and 47.3° (Figure 4.3c). Ni(II)-AA complex is formed in an aqueous solution (Benetis et al., 1981) near the neutral pH (Eq. 4.3). At a higher pH, $Ni(OH)_2$ could be formed by the ligand exchange between AA^- and OH^- (Eq. 4.4) which is similar to Cl^- and OH^- exchange for the

formation of $Ni(OH)_2$ using hydrazine (Huang et al., 2009). At pH> 10, AA^- is converted to 2,3-diketogulonic acid (2,3-DKG, Eq. 4.4) (Rao and Golder, 2016). The concentration of AA (*m/z* 177.6) was abundant in the fresh bio-extract at pH 11 but, it didn't appear in the mass spectra after NiO synthesis (Figure 4.4). At the same time, pyruvic acid (*m/z* 88.15), glyceric acid (*m/z* 107.9), and xylonic acid (*m/z* 167.5) were identified after the reaction, and these compounds are usually formed from the degradation of 2,3-DKG (Zhang et al., 2014; Rao and Golder, 2016). After that, NiO NPs were produced formed from the calcination of $Ni(OH)_2$ (Eq. 4.1). The chemical synthesis of NiO NPs involve the use of hydrazine hydrate (El-Kemary et al., 2013), sodium borohydride (Lui et al., 2013), and polyols (Chinnasamy et al., 2005). The crystallite size found in this work is in well accordance to those studies, and this new method also doesn't compromise with the purity of particles.

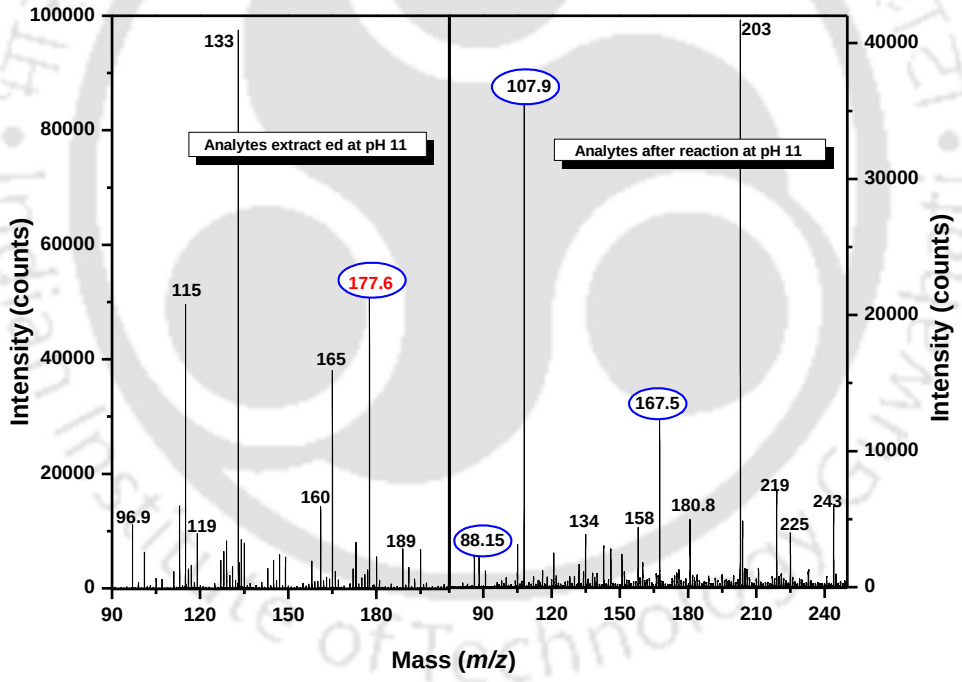

Figure 4.4: Mass spectra of analytes extracted at pH 11 and after 48 h of reaction in the presence of Ni-precursor at the same pH.

NiO NPs formed using the commercial AA is shown in Figure 4.5. The particles displayed poor crystallinity even at the same calcination temperature (500 ºC) and time of 2 h

compared to NiO NPs formed using the bio-extract of *S. edule* as a result of natural capping agents present in it.

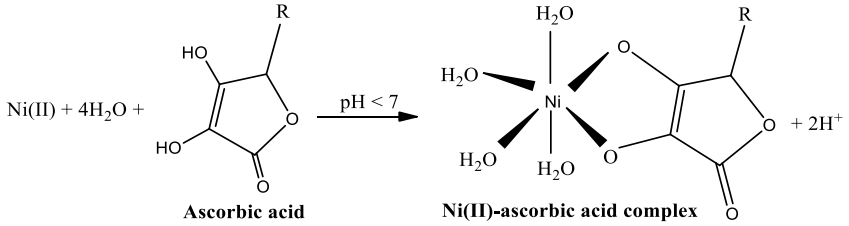

(4.3)

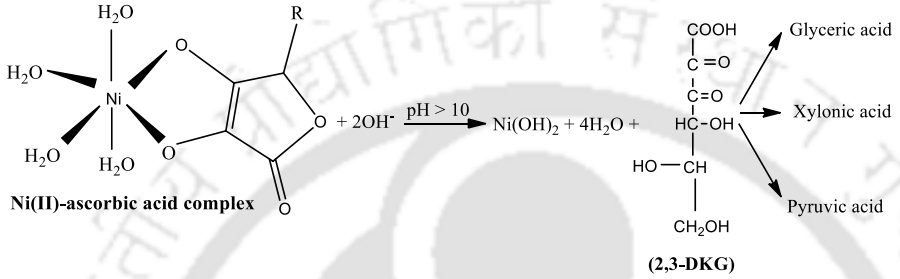

(4.4)

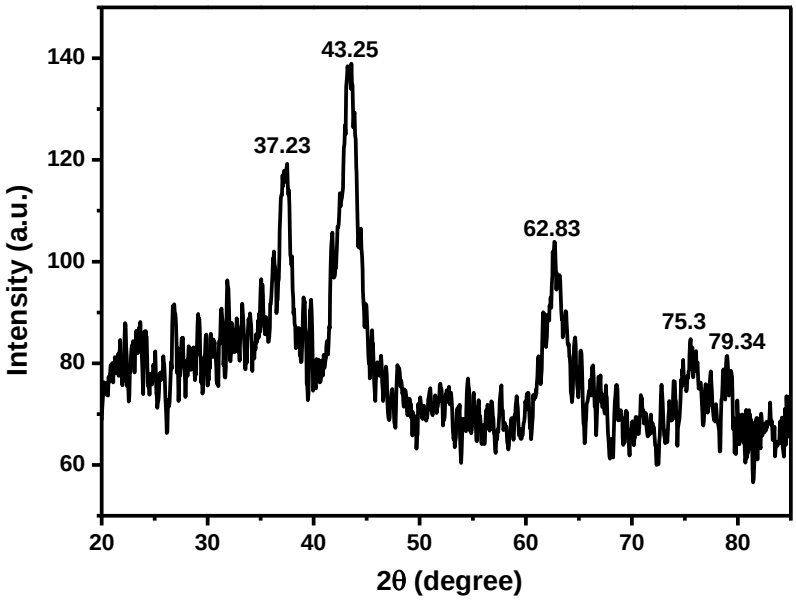

Figure 4.5: X-ray diffractogram of NiO NPs (calcined at 500 °C for 2 h) prepared by using commercial AA.

The XRD patterns of Co_3O_4 NPs are shown in Figure 4.6. No diffraction peak was found without calcination due to the amorphous nature of the particles (Figures 4.6a). The diffraction peaks were improved slightly with the increase in calcination time from 6 to 12 h at 500 °C

because of phase transformation from amorphous to the crystalline phase (Figures 4.6b and 4. 6c). The sharp peaks at 2θ of 18.8, 30.98, 36.45, 44.5, 55.02, 59.02, and 64.47° were ascribed to the simple cubic phase of Co_3O_4 NPs (JCPDS card file 94715) (Tang et al., 2008) for Co_3O_4/700°C/6h NPs (Figures 4.6d). It corresponds to the crystal planes of (111), (220), (311), (400), (422), (511), and (440) of crystalline Co_3O_4. The diffraction peaks were also notably broadened because of the small size effect of the Co_3O_4 NPs for the calcination at 700 °C. The crystalline sizes of Co_3O_4 NPs were determined by the Scherrer equation (Eq. 4.2).

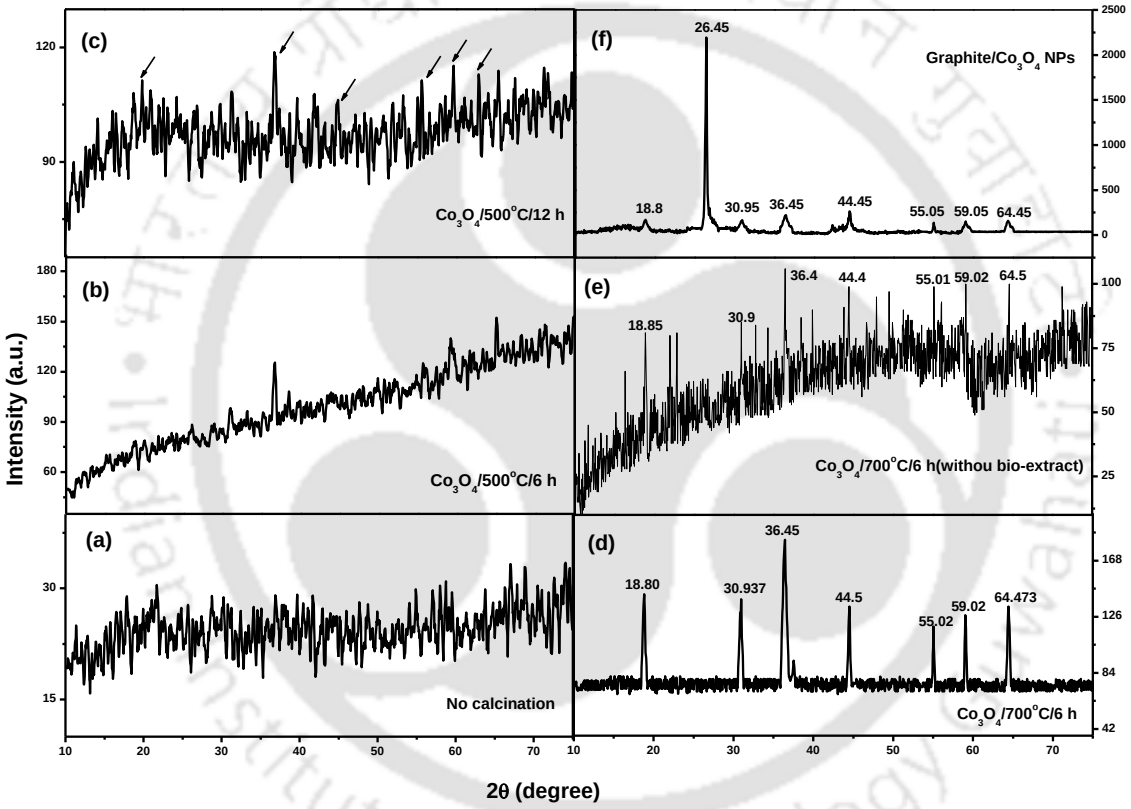

Figure 4.6: X-ray diffractograms of (a) Co-dry particles (without calcination), (b) Co_3O_4/500°C/6h NPs, (c) Co_3O_4/500°C/12h NPs, (d) Co_3O_4/700°C/6h NPs, (e) Co_3O_4/700°C/6h control particles without bio-extract, and graphite-Co_3O_4/700°C/6h composite material.

The high thermal energy would orient the crystallites in proper equilibrium sites (Allaedini and Muhammad, 2013), and the crystallinity was increased with the increase in calcination temperature. The crystal size for Co_3O_4/700°C/6h NPs was much smaller than it was

synthesized by precipitation method followed by calcination at 700 °C for 3-4 h (Sharifi et al., 2013). The migration of grain boundaries would also take place at a higher temperature which results in coalescence of small grains (Sing et al., 2016). A control experiment was performed for the synthesis of Co_3O_4 NPs in the absence of the bio-extract following the same synthesis protocol. The particles formed were calcined at 700 °C for 6 h, and the XRD diffractogram is shown in Figure 4.6e. It was evident that impurities such as CoOOH and traces of $Co(OH)_2$ were present with the Co_3O_4 NPs. The crystallinity of Co_3O_4 NPs was also poor even with the calcination at 700 °C for 6 h. CoOOH was predominantly present at pH 11 (Eqs. 4.5 to 4.7) which appeared in the diffractogram (Ozkaya et al., 2009; Sharifi et al., 2013). Ascorbic acid is an ideal electron donor. It could convert CoOOH to $Co(OH)_2$ (Eq. 4.8) along with the formation of 2,3-diketogulonic acid (2,3-DKG) (Rao and Golder, 2016) which in turn was converted to Co_3O_4 after calcination (Eq. 4.9) (Sharma and Ghose, 2016). The average crystal size of particles was found to be 39 nm for Co_3O_4/700°C/6h NPs. As expected, graphite-Co_3O_4/700°C/6h NPs showed the characteristic diffraction peaks of both graphite (2θ= 26.45°) and Co_3O_4 NPs (Figures 4.6f).

$$Co(NO_3)_2 + 2NaOH \rightarrow Co(OH)NO_3 + 2NaNO_3 \quad (4.5)$$

$$Co(OH)NO_3 + NaOH \rightarrow Co(OH)_2 + NaNO_3 \quad (4.6)$$

$$3Co(OH)_2 + 2NaNO_3 \xrightarrow{OH^-} 2CoOOH + Co(OH)_2 + H_2O + Na_2NO_2 \quad (4.7)$$

$$\text{Ascorbic acid} + CoOOH \xrightarrow{OH^-} Co(OH)_2 + \text{2,3DKG} + H_2O \quad (4.8)$$

$$3Co(OH)_2 \xrightarrow{\text{Calciantion}} Co_3O_4 + 2H_2O + H_2\uparrow \quad (4.9)$$

4.2.1.3 Raman spectra of synthesized NPs

The Raman spectrum of NiO NPs is shown in Figure 4.7. Four vibrational bands i.e. one photon (1P) TO and LO at 519 cm^{-1}, two photon (2P) 2TO at 734 cm^{-1}, TO+LO at 902 cm^{-1}, and 2LO at 1078 cm^{-1} modes could be identified from the spectrum (Mironova-Ulmane et al., 2007). The Raman peak at about 519 cm^{-1} could be assigned to Ni–O stretching mode as 1P band due to the presence of surface defects. The two-magnon (2M) band at 1487 cm^{-1} was arising from the 2M vibration associated with the Ni^{2+}-O^{2-}-Ni^{2+} super-exchange interaction (Duan et al., 2012). The presence of a mild 2M vibration indicates that the NiO NPs could behave like a weak ferromagnet. The results are in agreement with the NiO NPs synthesized by the sol-gel method using agarose polysaccharide (Alagiri et al., 2012).

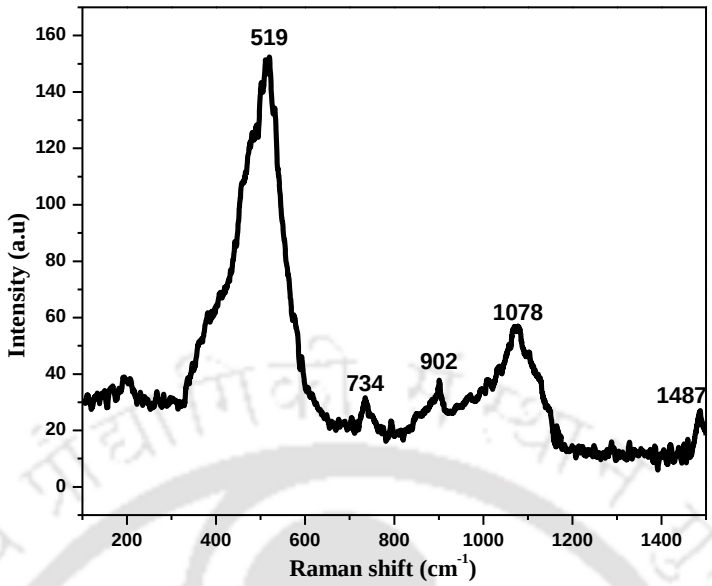

Figure 4.7: Raman spectra of NiO NPs after calcination at 500 °C for 2 h.

The Raman spectra of Co_3O_4 NPs are presented in Figure 4.8. The peaks at 194.1, 482.28, 519.60, 621.38 and 689.55 cm^{-1} are assigned to F_{2g}, E_g, F_{2g}, F_{2g} and A_{1g} modes of Co_3O_4/700°C/6h (Jia et al., 2009; Diallo et al., 2015). These Raman active peaks depict the Co_3O_4 cubic spinal crystal structure. Co_3O_4 crystallizes in the normal spinal crystal structure of $Co^{2+}(Co^{3+})_2O_4^{2-}$ with Co^{2+} ($3d^7$) and Co^{3+} ($3d^6$) located at the tetrahedral and octahedral sites, respectively (Diallo et al., 2015). The Raman mode at 689.55 cm^{-1} (A_{1g}) was attributed to the characteristics octahedral sites, and the E_g and F_{2g} modes were likely related to the combined vibrations of the tetrahedral site and octahedral oxygen motions. The Raman band at 689.55 cm^{-1} was highly polarized. Also, the different calcination temperature greatly affected Co_3O_4 crystal formation. Only a peak at 519.60 cm^{-1} appeared without calcination because of the formation of cobalt oxide-complex or $Co(OH)_2$ (Yang et al., 2010). The similar Raman peaks were clearly found at around 482.16, 519.60 and 689.68 cm^{-1} for Co_3O_4/500 °C/12 h, and the relatively minor peaks were obtained at 194.1 cm^{-1} and 621.48 cm^{-1} for Co_3O_4/500°C/6h. The peaks observed at around 850 to 898 cm^{-1} might be in the presence of impurities, and it disappeared at a higher calcination temperature of 700 °C. The composite material (graphite-Co_3O_4/700°C/6h) was scrapped out from the electrode surface. The D-peak at 1350.17 cm^{-1}, G-peak at 1580.13 cm^{-1} and 2D-peak at 2703.59 cm^{-1} of composite material were due to the characteristic Raman shift of graphite. Graphite-Co_3O_4/700°C/6h also exhibited similar Raman shifts of Co_3O_4/700°C/6h NPs.

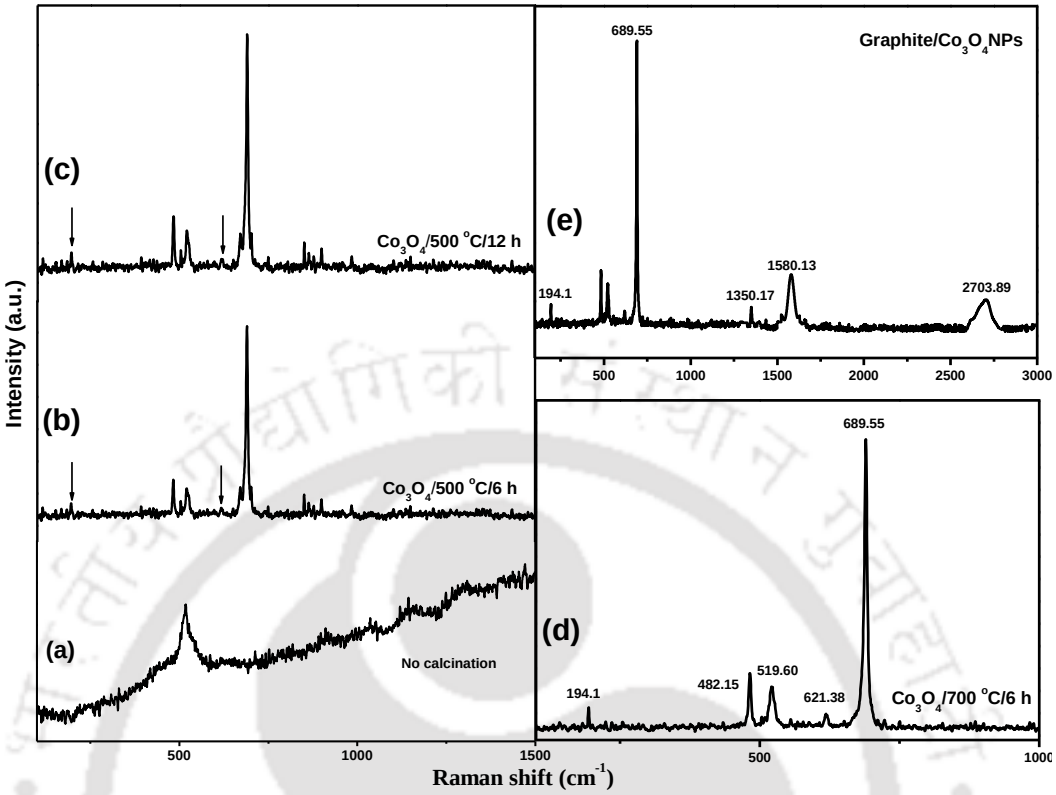

Figure 4.8: Raman spectra of of (a) Co-dry particles (without calcination), (b) Co_3O_4/500°C/6h NPs, (c) Co_3O_4/500°C/12h NPs, (d) Co_3O_4/700°C/6h NPs, and (e) graphite-Co_3O_4/700°C/6h composite material.

4.2.1.4 Morphologies and particle size of NiO and Co_3O_4 NPs

The SEM, TEM, and HRTEM micrographs of NiO NPs are illustrated in Figure 4.9. The SEM micrograph (Figure 4.9a) shows the well dispersed irregular particles but the majority of the NiO NPs were spherical in nature. The particle size was found in the range from 2.98 to 26.9 nm with an average diameter of 12.11 nm (Figure 4.10a). A few dense aggregates were also found suggesting a significant migration of grain boundaries during calcination. The TEM micrograph also reveals irregular NiO NPs of nearly spherical shapes with distinct particles boundaries (Figure 4.9b). The particles appeared to be highly crystalline in nature with an interplanar lattice spacing of 0.239 nm (Figure 4.9c) for the (111) plane of NiO NPs (Liu et al., 2013). The mean particle size was found as 14.48 nm with the diameter varying from 7.1 to 32.61 nm (Figure 4.10b). The particle size well matches with the microwave-assisted synthesis of NiO NPs (Al-Sehemi et al., 2014).

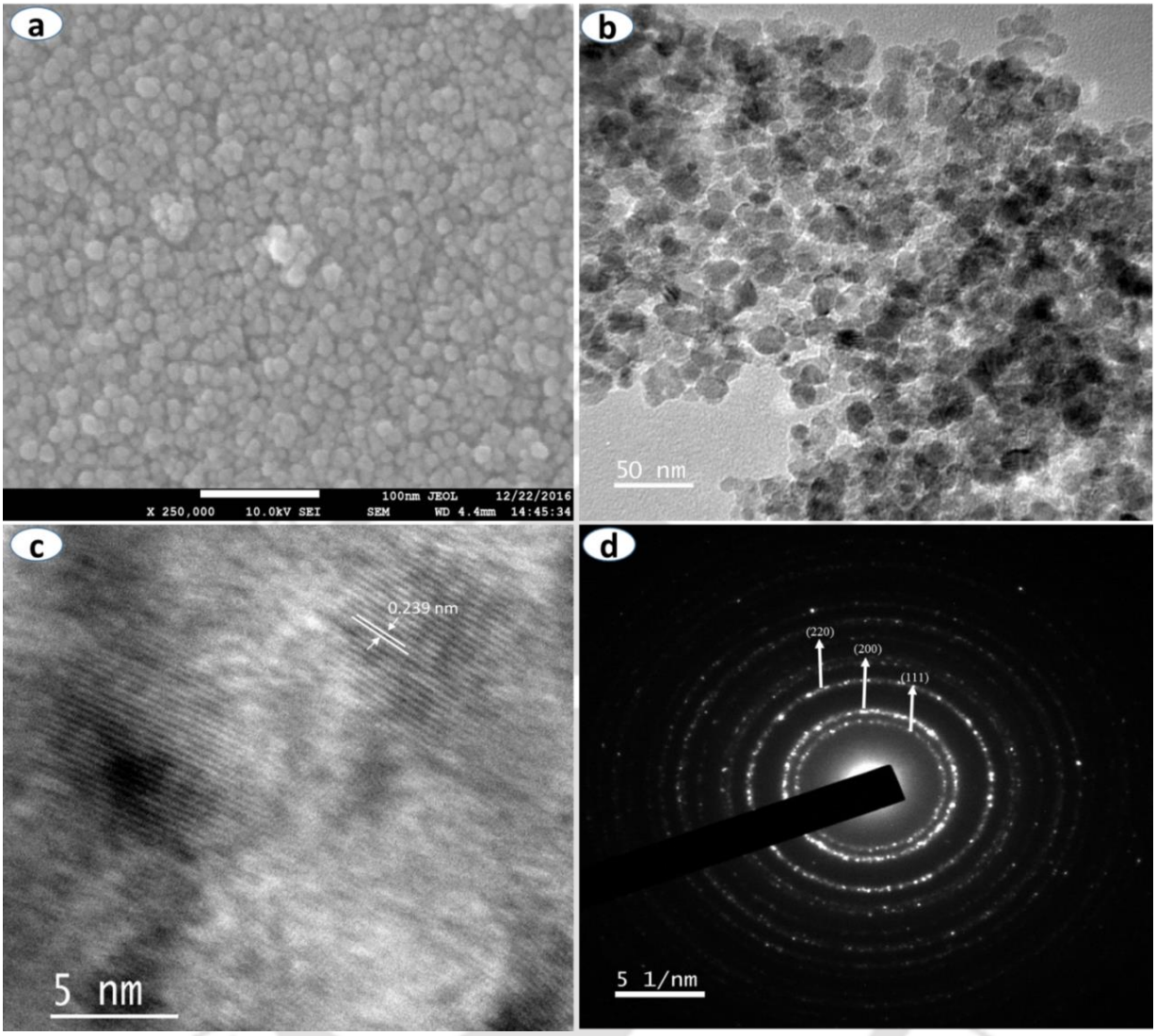

Figure 4.9: (a) SEM micrograph, and (b) TEM, (c) HRTEM, and (d) SAED micrographs of NiO NPs.

The intense SAED (selected area electron diffraction) rings corresponded to the electron diffraction from the (111), (200), and (220) lattice planes of NiO NPs (Figure 4.9d) (Sharma et al., 2013) which was also consistent with XRD patterns (Figure 4.3).

TEM micrograph of NiO NPs formed using the commercial AA (Figure 4.11a) shows that the particles didn't exhibit the defined grain boundaries due to the presence of amorphous particles. The clear lattice spacing also lacked as evident from the HRTEM micrograph (Figure 4.11b).

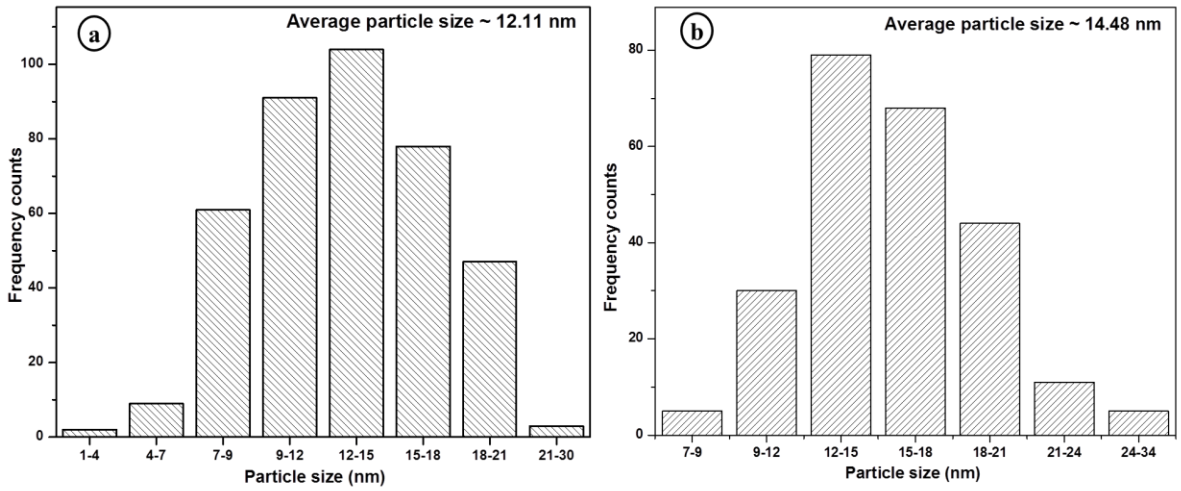

Figure 4.10: Particle size distribution of NiO NPs from (a) SEM and (b) TEM micrographs.

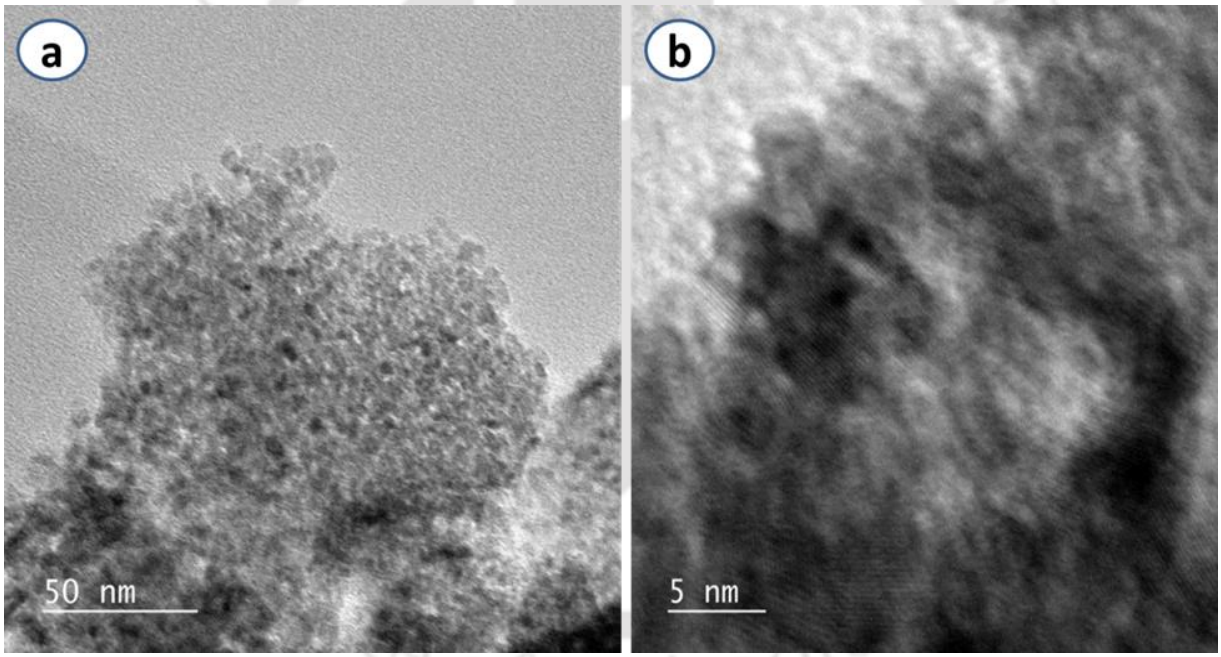

Figure 4.11: (a) TEM and (b) HRTEM micrographs of NiO NPs prepared by using commercial AA.

The SEM micrographs Co_3O_4/500°C/6h, Co_3O_4/500°C/12h, and Co_3O_4/700°C/6h NPs are illustrated in Figure 4.12. The particles were mostly present in irregular aggregates for Co_3O_4/500°C/6h NPs due to the presence of a significant amount of amorphous phases and weak migration of grain boundaries (Figure 4.12a). The particles size ranged from 5.8 to 38.1 nm with

an average diameter of 20.8 nm (Figure 4.13a). The grain boundaries became more distinct with the increase in the orientation of crystallites for Co_3O_4/500°C/12h NPs (Figure 4.12b), and the average particles size was increased to 28.12 nm because of the merger of small grains (Figure 4.13b). The Co_3O_4/700°C/6h particles were consisting of mostly sphere-like morphologies with well-defined boundaries and relatively lower aggregation (Figure 4.12c). The particle size was in the range from 13.86 to 44.17 nm with an average diameter of 31.25 nm (Figure 4.13c) which is smaller than the thermochemical technique (Allaedini and Muhammad, 2013).

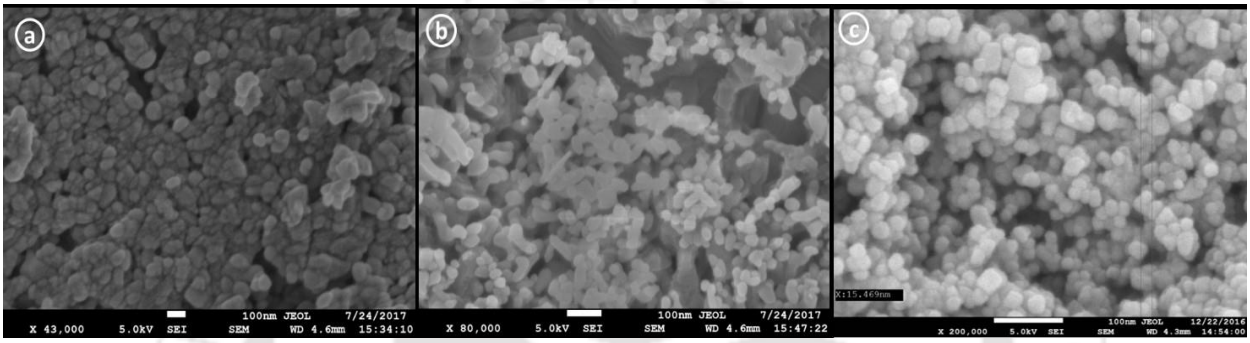

Figure 4.12: SEM micrographs of (a) Co_3O_4/500°C/6h, (b) Co_3O_4/500°C/12h, and (c) Co_3O_4/700°C/6h NPs.

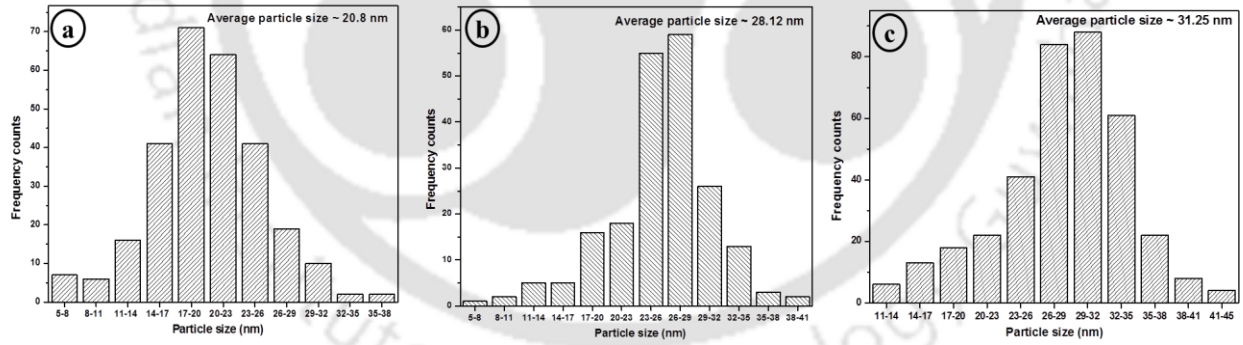

Figure 4.13: Particle size distribution of (a) Co_3O_4/500°C/6h, (b) Co_3O_4/500°C/12h, and (c) Co_3O_4/700°C/6h NPs from SEM micrographs.

The strong aggregates of overlapping particles were evident from the TEM micrograph of Co_3O_4/500°C/6h NPs (Figure 4.14a). The particles of amorphous nature were found with unclear lattice structure (Figure 4.14b). Similarly, the diffused halo ring from the selected-area electron diffraction (SAED) pattern suggested its amorphous nature (Li et al., 2014). Co_3O_4/500°C/12h NPs exhibited relatively distinct shapes (Figure 4.14c) with appearance of crystalline particles as

evidenced by the high resolution (HR) TEM micrograph with a lattice spacing of 0.459 nm for the (111) plane of the Co_3O_4 phase (Figure 4.14d). Co_3O_4/700°C/6h NPs were composed of dispersed mixed shape particles (Figure 4.14e) with highly crystalline Co_3O_4 structure (Figure 4.14f). The particle sizes obtained from the SEM (Figure 4.13) and TEM micrographs (Figure 4.15) showed an excellent agreement (Sharma et al., 2015).

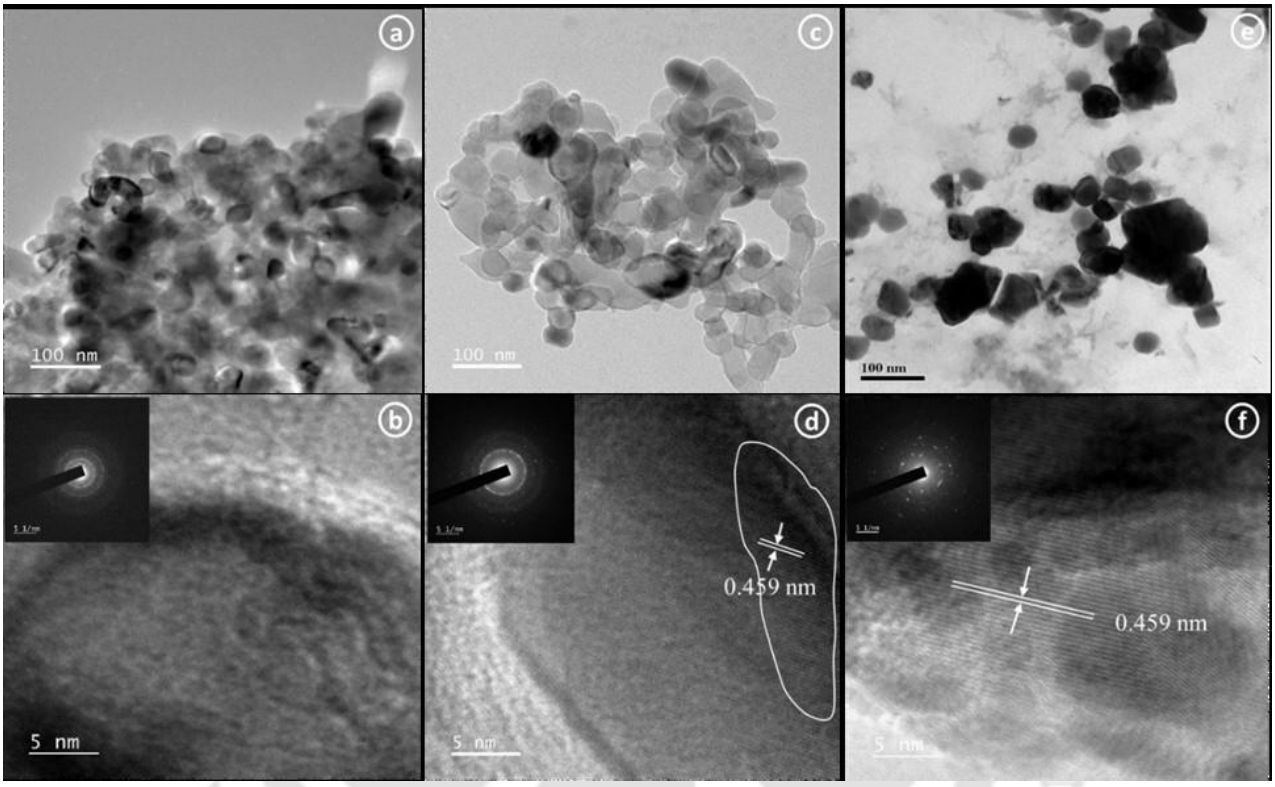

Figure 4.14: TEM and HRTEM micrographs of (a, b) Co_3O_4/500°C/6h NPs, (c, d) Co_3O_4/500°C/12h, and (e, f) Co_3O_4/700°C/6h NPs with SAED as insets in HRTEM micrographs.

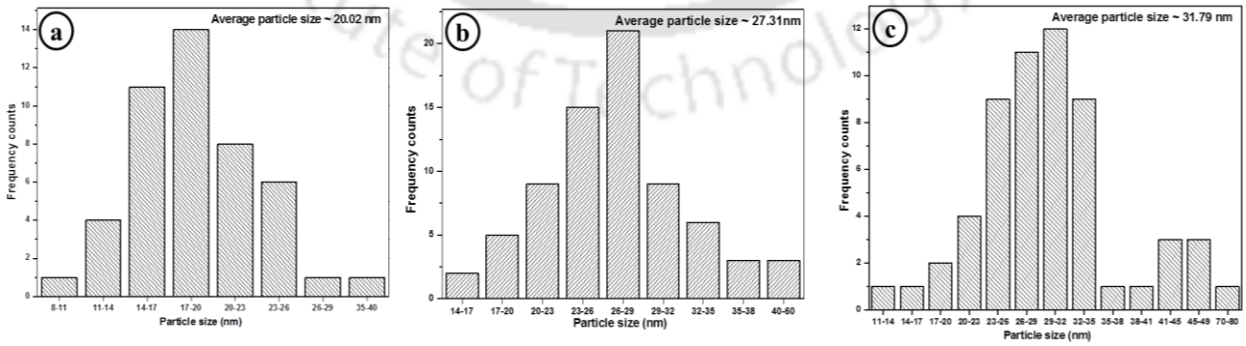

Figure 4.15: Particle size distribution of (a) Co_3O_4/500°C/6h, (b) Co_3O_4/500°C/12h, and (c) Co_3O_4/700°C/6h NPs from TEM micrographs.

The single particle line profile analysis gave the size of Co_3O_4 NPs to be 21.4 nm from the AFM micrographs (Figures 4.16a and 4.16b). The RMS roughness of Co_3O_4 NPs was found to be 1.5739 nm. The particles size ranged from 2.58 to 54.2 nm (Figure 4.16c).

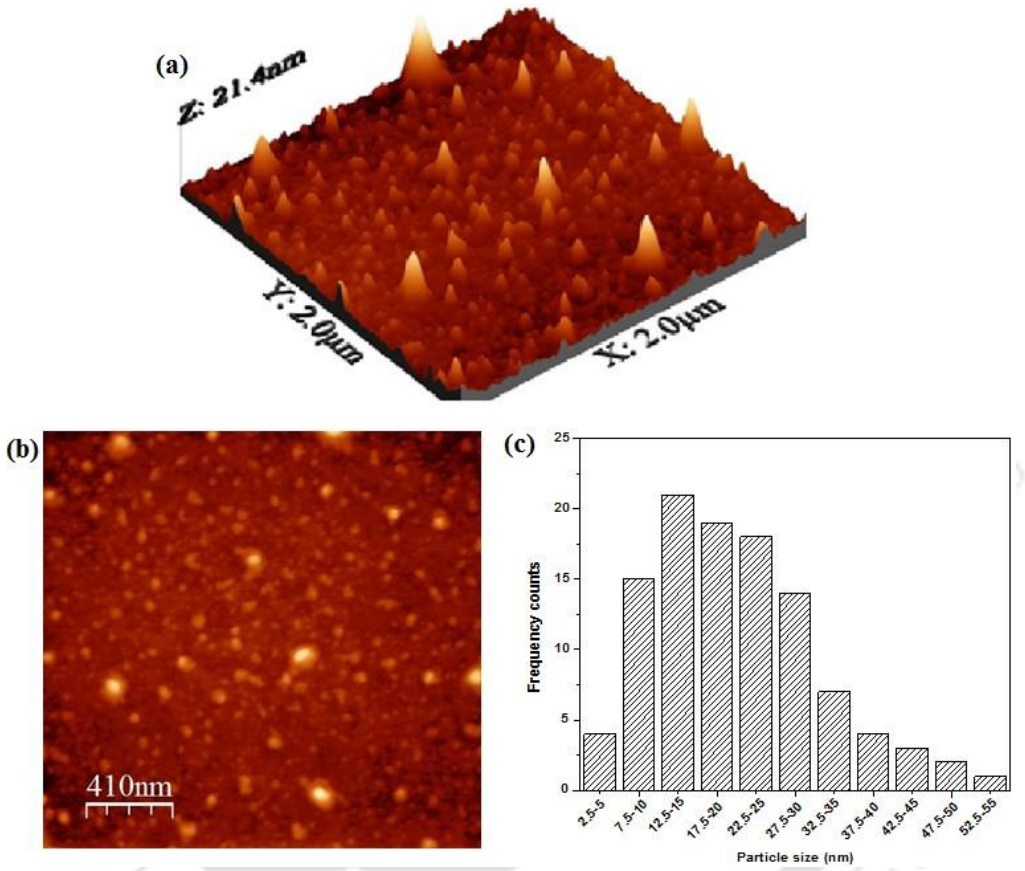

Figure 4.16: (a) AFM micrograph (3D) and (b) AFM micrograph (2D) of Co_3O_4 NPs calcined at 700 °C for 6 h, and (c) particle size distributions of Co_3O_4 NPs calcined at 700 °C for 6 h from AFM micrographs.

4.2.1.5 BET isotherm and pore size distribution

The N_2 adsorption-desorption isotherm and Barrett–Joyner–Halenda (BJH) pore size distribution of NiO NPs are shown in Figure 4.17. The adsorption isotherm can be classified as type IV (Brunauer Deming-Deming-Teller (BDDT) classification) with H_2 hysteresis at a relative pressure (P/P_0) between 0.5 and 1.0 which is a typical characteristic isotherm of mesoporous materials (Figure 4.17a). The BET surface area was calculated as 74.117 m^2/g with a total pore volume of 0.152 cm^3/g. The pore size distribution determined from the adsorption

section of the isotherm by the BJH method ensured a loose mesoporous structure (2 to 20 nm in size) as shown in Figure 4.17b. The micropores (1.52 to 2 nm) volume was found to be 0.115 cm^3/g, and the mesopores distribution was observed up to 59.6 nm with an average diameter of 6.74 nm. The surface area of NiO NPs was little higher than it was synthesized by the solvothermal process (Ai and Zeng, 2013). So, it could improve the diffusion of reaction species for an enhanced electrocatalytic activity (Wang et al., 2016).

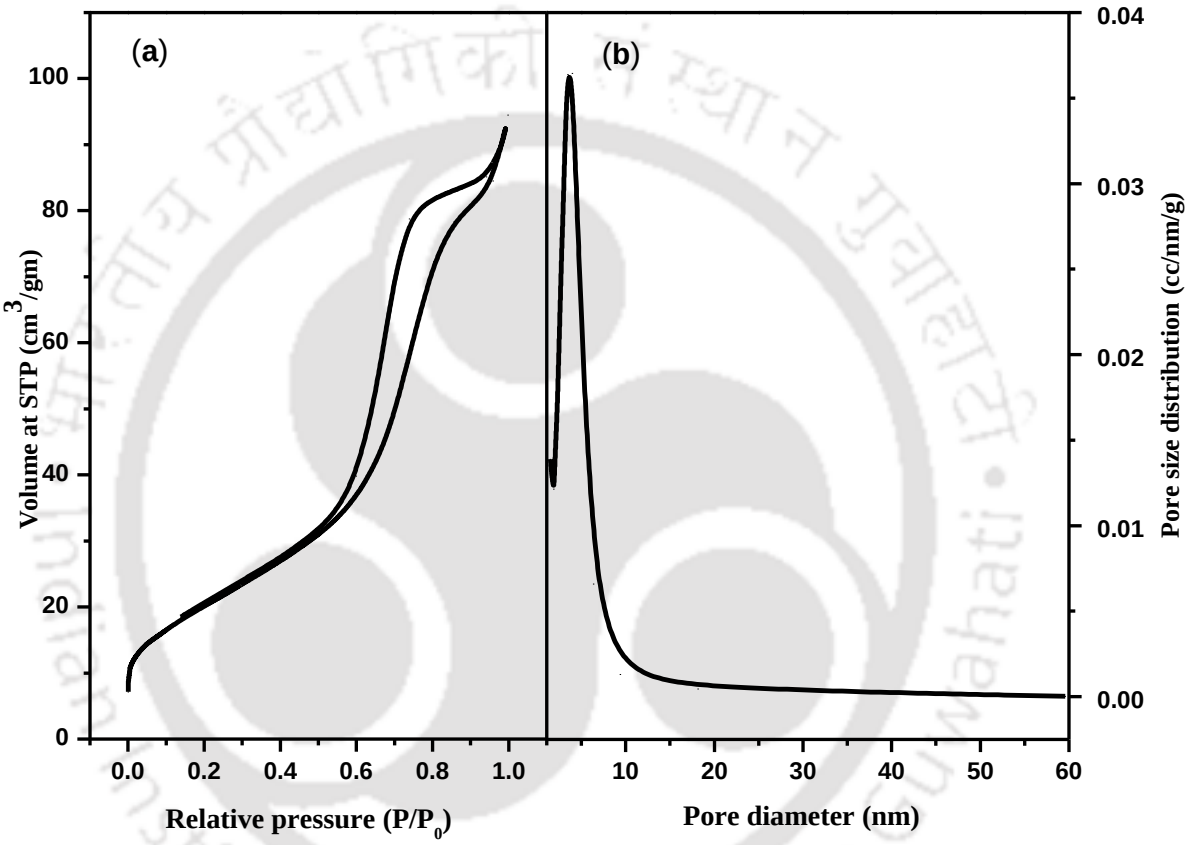

Figure 4.17: (a) BET isotherm of NiO NPs, and (b) its pore size distribution.

Figure 4.18a shows the nitrogen adsorption-desorption isotherms of Co_3O_4/700°C/6h. The adsorption isotherm can be classified as type IV (BDDT classification) with a H_2 hysteresis. The BET surface area was found to be 15.784 m^2/g with a total pore volume 0.1296 cm^3/g (Figure 4.18b). The surface area of Co_3O_4/700°C/6h NPs was relatively lower than the value reported by Esswein et al. (2009) using the thermochemical method.

It was found that Co_3O_4/700°C/6h NPs consisted of both micropores and mesopores. The micropores diameters ranged from 0.6 to 2 nm with 90 % pore volume, and the mesopores

diameters came between 2 and 28 nm (Figure 4.18b). The average pore diameters were found as 1 and 8.58 nm, respectively, which fall well within the pores size used by many researchers for H_2O_2 sensing (Chen et al., 2009; Tu et al., 2017). However, the lower pores diameter could lead to O_2 trapping within the pores (Gonçales et al., 2013) formed during H_2O_2 reduction at the electrode surface, and the larger pores reduce the effective sites of the reaction.

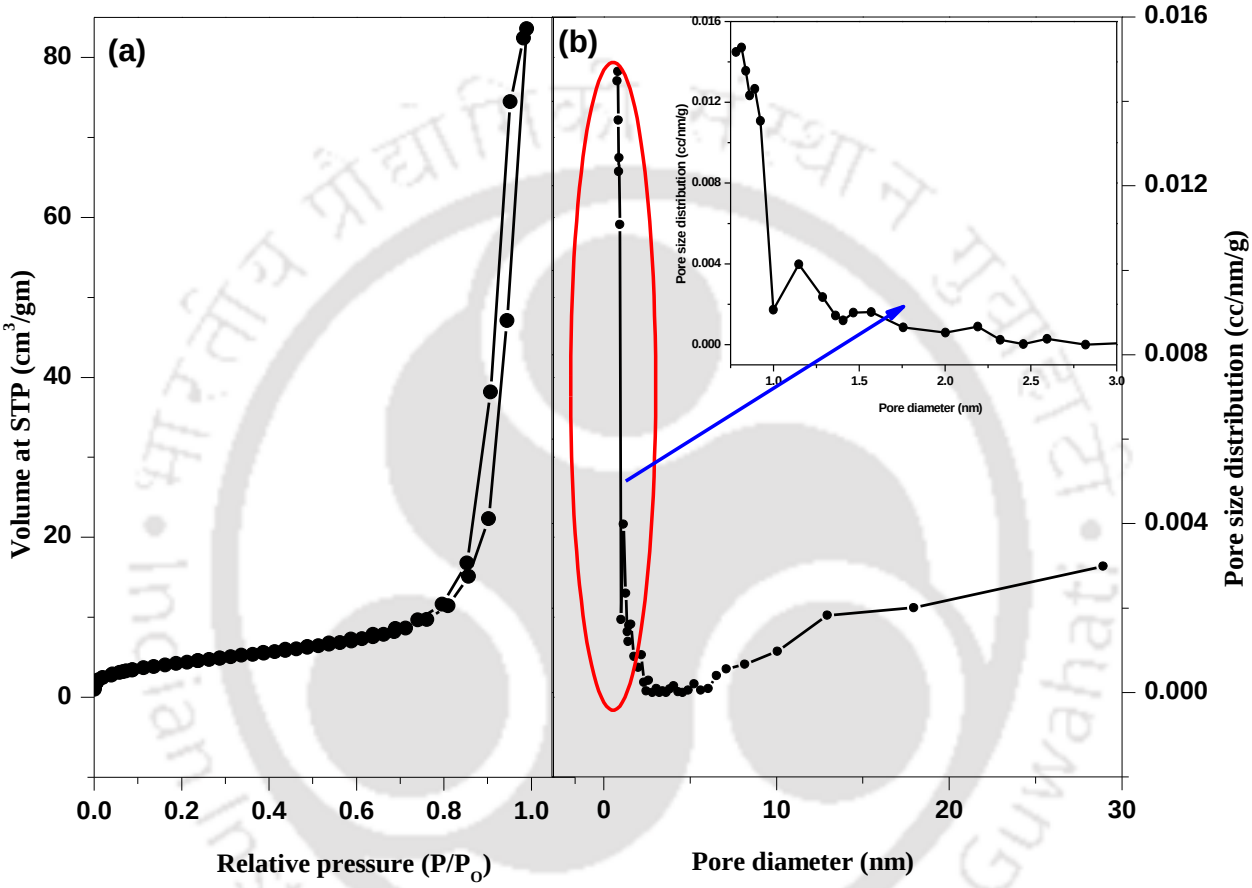

Figure 4.18: (a) BET isotherm of Co_3O_4 NPs calcined at 700 ℃ for 6, and (b) pore size distribution.

4.2.1.6 FTIR spectra and particles interactions

The FTIR spectra of Ni-dry particles and NiO NPs are shown in Figure 4.19. An intense peak at 3646 cm^{-1} for the Ni-dry particles (Figure 4.19a) was attributed to the -OH stretching vibration which was most likely for the presence of $Ni(OH)_2$ (Motahari et al., 2015). This peak vanished after the calcination (Figure 4.19b). The absorption peak at around 598 cm^{-1} was expected to be for the Ni-O-H stretching band (Rahdar et al., 2015). The absorption peak at 466 cm^{-1} was for the Ni-O stretching vibration mode of NiO_6 octahedral in the cubic NiO structure

(Al-Sehemi et al., 2014). The peaks at 3430 and 3415, and 1644, and 1635 cm^{-1} appeared from the vibration of O–H bond of the –OH group and H–O–H bending vibrations of adsorbed water molecules (El-Kemary et al., 2013). The peak at 1378 and 1385 cm^{-1} was probably for the interaction of $Ni(OH)_2$/NiO NPs with KBr (Al-Sehemi et al., 2014). It was likely that the absorption peak at 1094 and 1117 cm^{-1} was originated by the C-O stretching vibration from the adsorption of atmospheric CO_2 as Ni-dry/NiO NPs has a strong tendency to physically adsorb H_2O and CO_2 (El-Kemary et al., 2013).

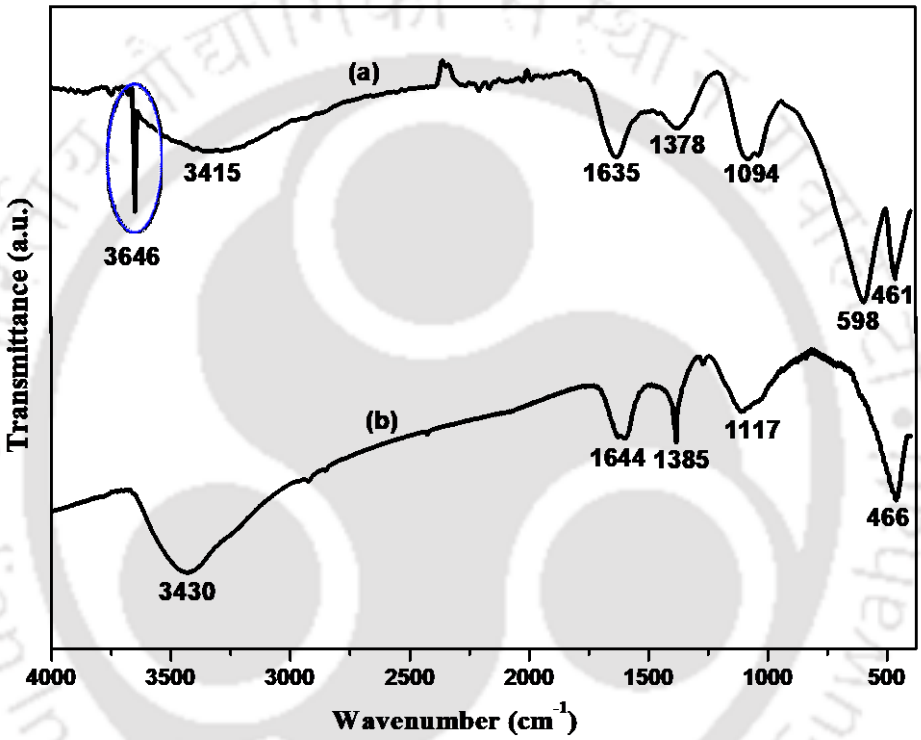

Figure 4.19: IR spectra of (a) Ni-dry particles (before calcination) and (b) NiO NPs (after calcination of Ni-dry) at 500 ℃ for 2 h.

The FTIR spectra of Co_3O_4 NPs display two sharp bands at 571.16 and 664.68 cm^{-1} (Figure 4.20) originating from the stretching vibration of the metal-oxygen bonds (ν(Co-O)) in the spinel lattice (Sharifi et al., 2013). The band at 571.16 cm^{-1} was attributed to Co^{3+} in an octahedral hole, and the latter band at 664.68 cm^{-1} was for Co^{2+} in a tetrahedral hole (Ozkaya e al., 2009).

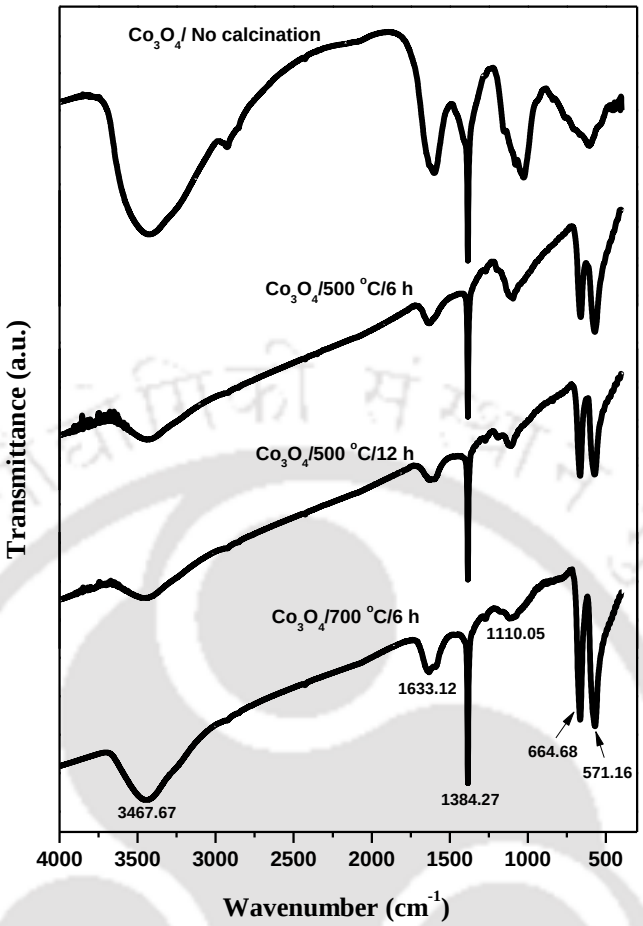

Figure 4.20: IR spectra of Co_3O_4 NPs with different calcination temperatures.

4.2.1.7 Magnetic properties of NiO and Co_3O_4 NPs

The fingerprint of IR absorption at 571.16 and 664.68 cm^{-1} for the cubic spinel structure of Co_3O_4 with Co^{2+} ($3d^7$) and Co^{3+} ($3d^6$) located at tetrahedral and octahedral sites, respectively, was fully developed after the calcination at 500 °C. It is clear that the intensity of these two bands was increased with a higher calcination temperature. The band 3467.12 cm^{-1} was assigned to the stretching vibrations of the hydroxyl group (-OH) due to water absorption by the nanoparticles (Mu et al., 2013). The band at 1633.12 cm^{-1} was because of the –OH stretching mode of water which was absorbed either by the sample or KBr (Kandalkara et al., 2009). Furthermore, the band at 1110 cm^{-1} could be assigned to H_2O absorption (Sharifi et al., 2013).

The VSM hysteresis loop of NiO NPs at room temperature with the magnetic field (-15 to 15 kOe) is shown in Figure 4.21a. The magnetization didn't get saturated even at the maximum applied magnetic field of 15 kOe, and the magnetization of 0.35 emu/g was found. This

unsaturated magnetic behavior of NiO NPs indicates the possibility of a superparamagnetic (week ferromagnetic) single domain nature of the particles. So, the value of the coercive field was obtained as 0.31 kOe with the remanent magnetization of 0.03 emu/g. It suggests that the uncompensated surface spins caused change in the magnetic order of NiO NPs (Rajesh et al., 2014). The results were in accordance with the Raman spectroscopy (Figure 4.7) and NiO NPs synthesized by the coprecipitation method (Rahal et al., 2017).

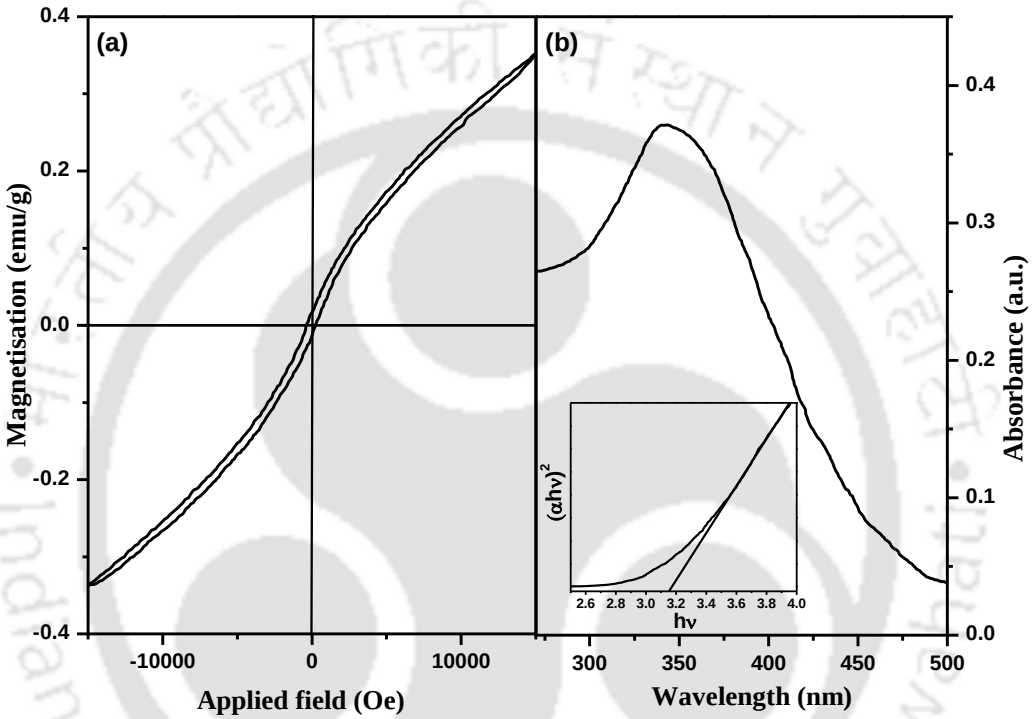

Figure 4.21: (a) VSM hysteresis loop, and (b) UV-vis spectrum of NiO NPs (inset (b): Tauc plot for the bandgap calculation).

The UV-vis spectrum of NiO NPs is illustrated in Figure 4.21b. The absorption edge was found between 302 and 398 nm wavelength. The strong absorption peak at 339 nm (UV region) was resulted from the electronic transition from the top of a valence band (compose of oxygen 2p band) to the bottom of a conduction band (compose of Ni 3d band) in NiO NPs (Alagiri et al., 2012). It suggests that the synthesized NiO NPs could impart a promising photocatalytic activity (Farhadi and Roostaei-Zaniyani, 2011). The optical bandgap (E_g) was calculated from the indirect transition model (Eq. 2.1, Chapter 2) (Motahari et al., 2015).

The bandgap was determined by extrapolating the linear region of the $(Ahv)^2$ versus hv curve (Figure 4.21b (inset)). E_g was found to be 3.15 eV (Rahal et al., 2017). It was observed that the as-synthesized NiO NPs had a significantly lower E_g than bulk NiO (4.0 eV) because of chemical defects or vacancies in the intergranular regions providing a new energy level (Song and Gao, 2008). A lower band gap increases the electrical conductivity at room temperature (Mohanraj et al., 2017) which is an important parameter for NiO NPs catalyzed H_2O_2 formation.

The magnetic properties of Co_3O_4 NPs are shown in Figure 4.22a. It demonstrates that all the samples were a very weak ferromagnetic, and the calcination did not change the magnetic behavior of the nanoparticles, but it increased the amount of magnetization with higher calcination temperature under the same applied magnetic field. The magnetizations of 0.15, 0.29 and 0.37 emu/g were found for Co_3O_4/500°C/6h, Co_3O_4/500°C /12h and Co_3O_4/700°C/6h NPs at the maximum applied magnetic field of 15 kOe. The magnetization of Co_3O_4/700°C/6h NPs was little higher than that reported by Farhadi et al. (2013) because of uncompensated surface spins of Co_3O_4 NPs. The saturation magnetization was gradually increased with the increase in crystal size (Hu et al., 2011). The increase in particle size decreased the proportion of the non-collinear magnetic structure in which the magnetic moments were aligned with the direction of the external magnetic field at a higher calcination temperature (Xavier et al., 2013).

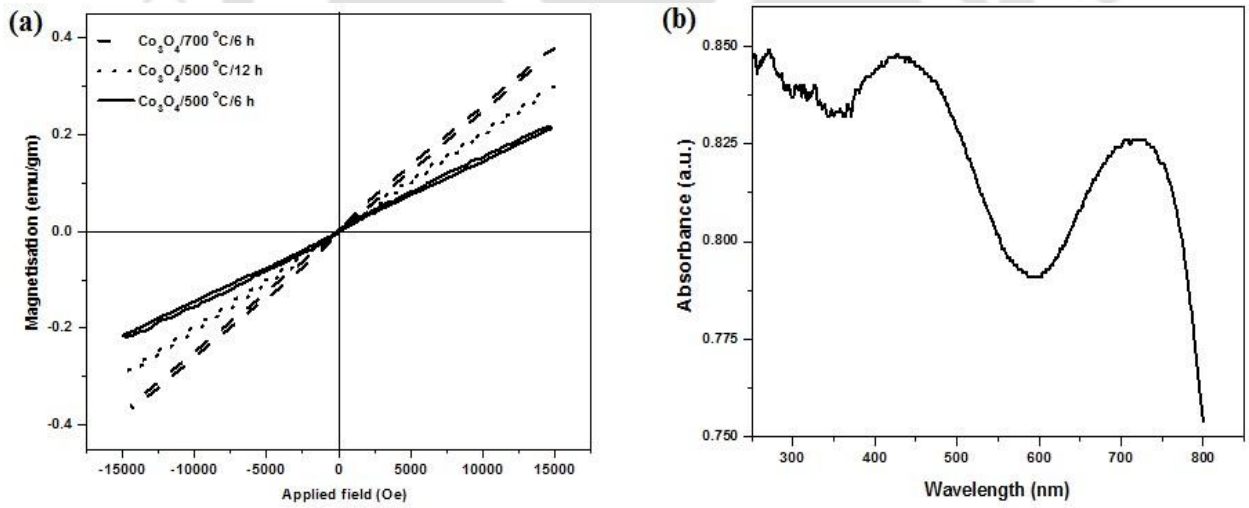

Figure 4.22: (a) VSM hysteresis loop of Co_3O_4 NPs determined at room temperature with different calcination temperatures, and (b) UV-vis spectrum of Co_3O_4 NPs.

The UV-Vis absorption spectroscopy was studied to measure the band gap energy of Co_3O_4 NPs. Figure 4.22b depicts a UV-vis spectra of Co_3O_4 NPs with two wide absorption

bands. The bands at 350 to 600 nm and 600 to 800 nm could be assigned to the O^{2-} to Co^{2+} and the O^{2-} to Co^{3+} charge transfer processes which ensured the p-type semiconductor. The corresponding band gaps were found to be 1.42 and 2.53 eV (Sharma et al., 2015). The absorption peaks at about 427 and 739 nm were similar to an earlier study using a hybrid PVD/PECVD method in which Co_3O_4 NPs was embedded in an amorphous silicon oxide matrix (Naveen and Selladurai, 2015).

4.2.2 Catalytic activity of NiO and Co_3O_4 NPs for H_2O_2 generation

4.2.2.1 Cyclic voltammetry and optimization of reaction condition

Cyclic voltammograms (CVs) for the H_2O_2 formation at the graphite, graphite/NiO NPs, graphite/Ni-control, and graphite/Ni-dry cathodes are illustrated in Figure 4.23. The CVs was obtained with 190 mL 0.5 M Na_2SO_4 SE by sweeping from -E_{cat}=0.0 to 0.55 V vs. Ag/AgCl at pH 2.5 with a scan rate of 50 mV/s (Figure 4.23a). The O_2 flow rate of 1.0 LPM was maintained, and the equilibrium concentration of DO in the bulk solution was found as 41 mg/L. No obvious redox peaks were identified at the (bare) graphite cathode in this typical potential range for carbonaceous materials. On the other hand, graphite/NiO NPs cathode exhibited the distinct redox peaks (Figure 4.23b). The O_2 reduction took place at $-E_{cat}$= 0.268 V vs. Ag/AgCl, and the oxidation peak was found at 0.402 V vs. Ag/AgCl. The CV was also recorded in the absence of O_2 (Figure 4.24) at pH 2.5 in 0.5 M Na_2SO_4 SE solution by sweeping from -0.05 to 0.4 V vs. Ag/AgCl. An oxidation peak was found at 0.322 V for the oxidation NiO to NiOOH (Eq.4.10), and the peak potential of NiOOH reduction to NiO (Eq. 4.11) was found at 0.143 V vs. Ag/AgCl. It confirms that the peak potential of $-E_{cat}$= 0.268 V vs. Ag/AgCl was for the O_2 reduction to H_2O_2 (Figure 4.23b). It also implies that H_2O_2 couldn't be oxidized in the vicinity of this potential.

$$NiO + OH^- \rightarrow NiOOH + e^- \quad (4.10)$$

$$NiOOH + e^- \rightarrow NiO + OH^- \quad (4.11)$$

The possible mechanism for the electrocatalytic activity of NiO NPs for H_2O_2 formation is shown through Eqs. 4.12 to 4.14. This process involves a proton insertion reaction (Eq. 4.12) at the acidic pH, and the molecular O_2 was adsorbed on a single site of NiOH (Eq. 4.13), and the O=O bond was not broken in the adsorption step. The electron transfer reaction for the reduction of adsorbed O_2 is shown in Eq. 4.14. The overall pathway involves a two-electron reduction for

the formation of H_2O_2 (Roche et al., 2007). Here, the Ni(II)/Ni(III) species acted either as oxygen donor or acceptor.

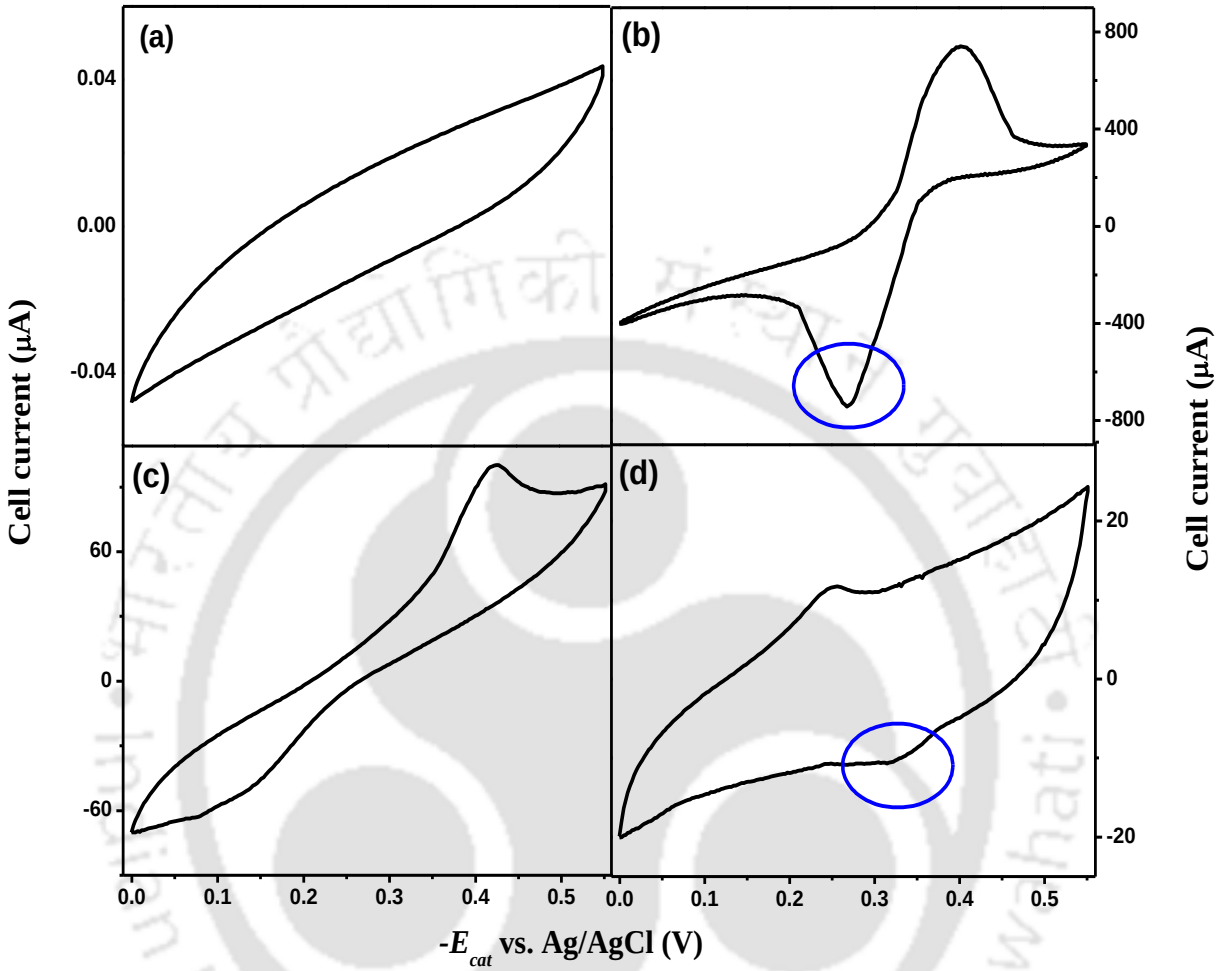

Figure 4.23: Cyclic voltammograms with (a) bare graphite, (b) graphite/NiO NPs, (c) graphite/Ni-control, and (d) graphite/Ni-dry cathodes by sweeping from $-E_{cat}$= 0.0 to 0.55 V vs. Ag/AgCl, cathode area 4.7 cm^2, 0.5 M Na_2SO_4 SE, pH 2.5, O_2 flow rate 1.0 LPM, and electrolyte 190 mL.

The graphite/Ni-control cathode also exhibited a fair oxidation peak at 0.156 V vs. Ag/AgCl but no distinct reduction peak (Figure 4.23c) was identified even with the coexistence of NiO and NiOOH (Figure 4.3c) in comparison to the graphite/NiO cathode. The corresponding cell current was also lower by two order magnitudes. The reduction peak observed at 0.314 V vs. Ag/AgCl and the oxidation peak at 0.146 V vs. Ag/AgCl at graphite/Ni-dry cathode (Figure 4.23d) was likely for the redox couple reactions of Ni(II)/Ni(III) species, and a lower oxidation

potential than the reduction potential is indicative of the existence of multiple redox reactions of $Ni(OH)_2$/NiOOH and NiO/NiOOH couples (Monk, 2010).

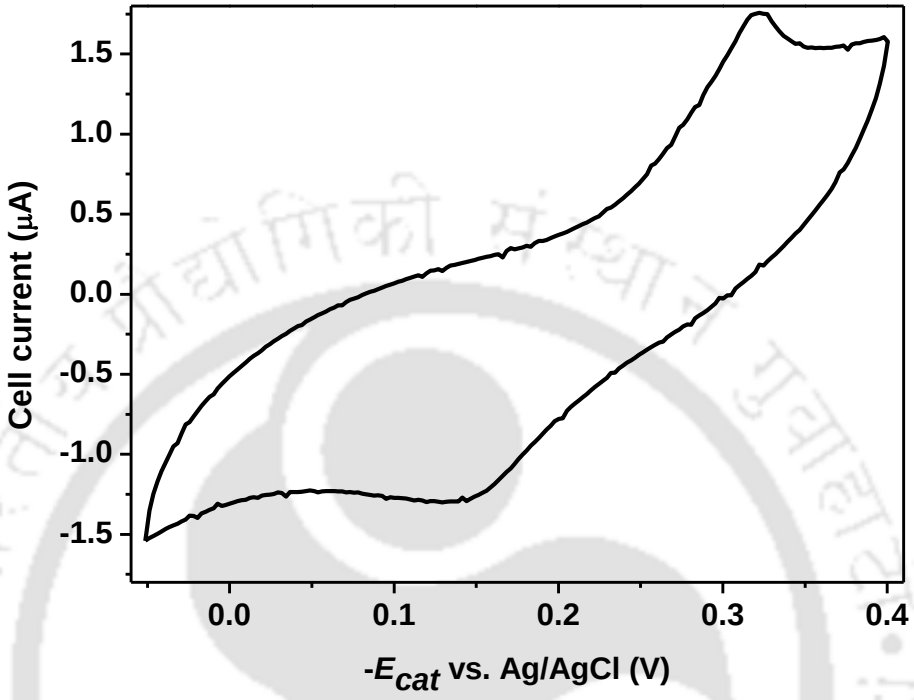

Figure 4.24: Cyclic voltammograms obtained in the 'absence of O_2' with graphite/NiO NPs cathode by sweeping from $-E_{cat}$= 0.32 to 0.48 V vs. Ag/AgCl, cathode area 4.7 cm^2, 0.5 M Na_2SO_4 SE, pH 2.5, N_2 flow rate 1.0 LPM, and electrolyte 190 mL.

The enhanced electrocatalytic activity of graphite/NiO cathode might be for the decrease in the interval of charge-transfer between Ni metal and O_2 that may come down by the covalence of the Ni-oxygen bond. A probable reason is the change in spatial overlapping between the 3d orbital of Ni metal and 2p orbital of O_2 (Chen et al., 2017a).

$$NiO + H^+ + e^- \leftrightarrow NiOH \quad (4.12)$$

$$NiOH + O_2 \leftrightarrow NiOH\text{--}O_{2,ads} \quad (4.13)$$

$$NiOH\text{--}O_{2,ads} + H^+ + e^- \rightarrow NiO + H_2O_2 \quad (4.14)$$

So, the further test was performed only with the graphite/NiO NPs cathode. Scan rates were varied from 10 to 50 mV/s with the sweeping potentials from $-E_{cat}$= 0.0 to 0.55 V vs. Ag/AgCl (Figure 4.25a).

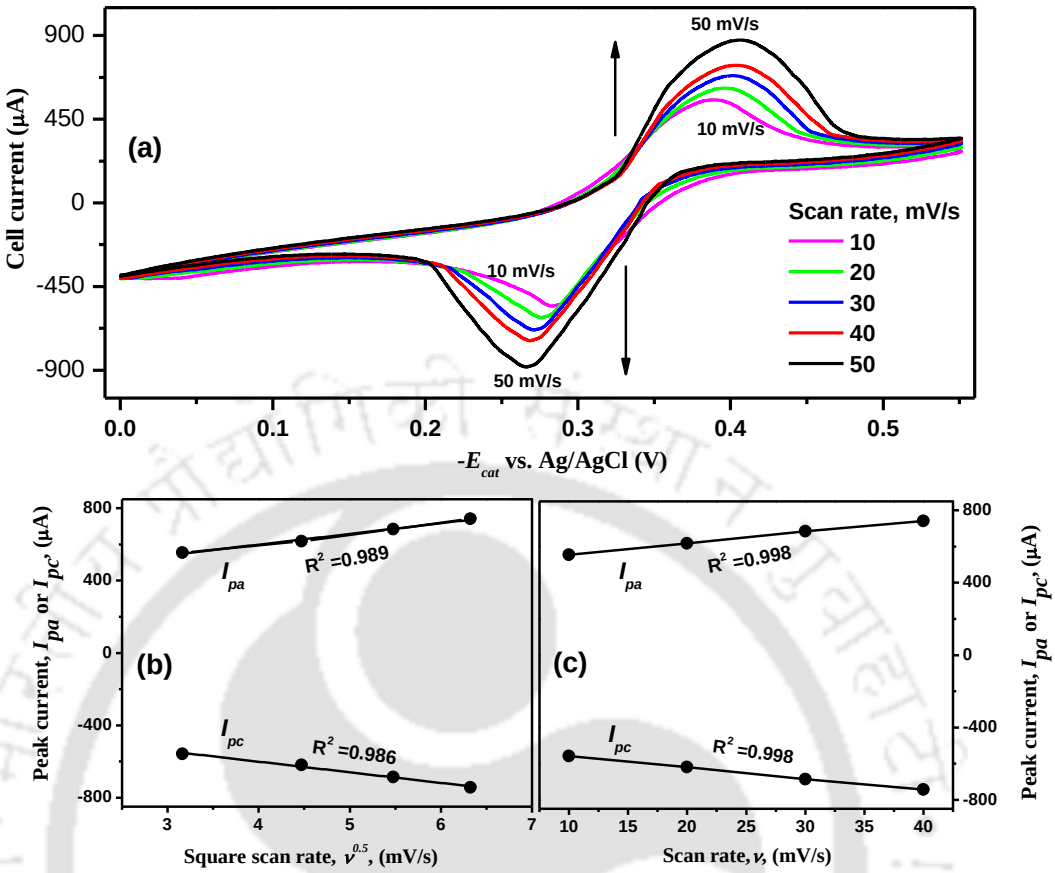

Figure 4.25: (a) Cyclic voltammograms with graphite/NiO NPs cathode at different scan rates by sweeping from $-E_{cat}$= 0.0 to 0.55 V vs. Ag/AgCl, cathode area 4.7 cm^2, 0.5 M Na_2SO_4 SE, pH 2.5, O_2 flow rate 1.0 LPM, and electrolyte 190 mL, (b) Variation of corresponding redox peak current (from Figure 4.25a) with the square root of the scan rate ($\nu^{0.5}$), and (c) Variation of redox peak current with the scan rate (ν).

The redox couple reactions were found to be quasi-reversible (Casado et al., 2016), and the ratio of the anodic peak current (I_{pa}) to the cathodic peak current (I_{pc}) varied from 1.01 to 1.05 (Figure 4.25a). Both the anodic peak current (I_{pa}) and cathodic peak current (I_{pc}) were gradually increased with the increase in scan rate, and it exhibited a fairly linear relationship with the square root of the scan rate up to 40 mV/s (Figure 4.25b) according to the Randles–Sevcik equation (Bard and Faulkner, 2001). The peak currents were also varied linearly with the scan rate (Figure 4.25c). It implies that the O_2 diffusion controlled redox reactions took place in a surface confined redox system (Helia and Pishahang, 2014). At a higher scan rate, the electrons movement is slow, and there is a perceptible 'time lag' between the potential at the voltage

source (here potentiostat) and that at the electrode-solution interface (Monk, 2010). So, the peak potentials were shifted slightly towards more extreme potentials giving a stretched shape of the CV.

Figure 4.26 illustrates the influence of pH (1.5, 2.5, 3.0, and 4.5) on O_2 reduction at the graphite/NiO NPs cathode. pH 2.5 was favorable for the O_2 reduction reaction with the sharp redox peaks, but the peak width was broadened both at a high and low pH. The peak currents were also the highest at pH 2.5, and it decreased notably at $4.5 \leq pH \leq 1.5$. The proton insufficiency at a higher pH caused the decrease in O_2 reduction efficiency. So, the peak current was decreased. A lower pH also induced H_2 evolution (Eq. 1.36, Chapter 1) (Qiang et al., 2003). The highest pH drop at the end of the experiment was found to be around 0.2 units. The O_2 reduction potential of $-E_{cat}$=0.268 V vs. Ag/AgCl was not influenced by the electrolyte pH but, the oxidation reaction took place at a lower potential with the increase in electrolyte pH (Figure 4.26) as pH at the vicinity of the anode was affected by the formation of H_3O^+.

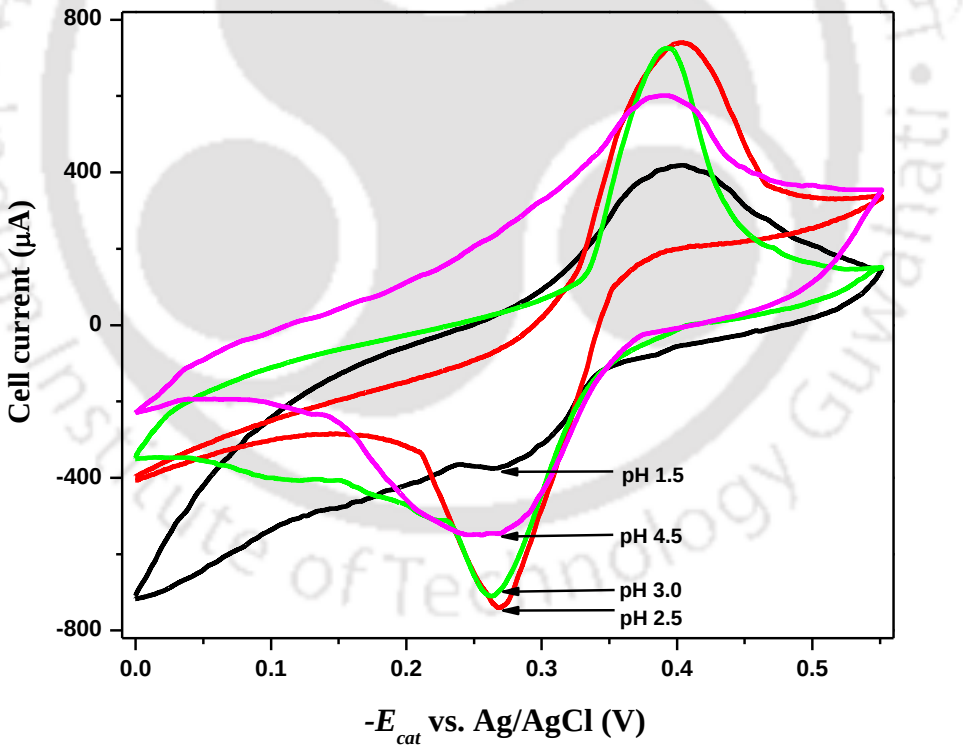

Figure 4.26: Cyclic voltammograms with graphite/NiO NPs cathode at different pH of SE media by sweeping from $-E_{cat}$= 0.0 to 0.55 V vs. Ag/AgCl, cathode area 4.7 cm^2, 0.08 M Na_2SO_4 SE, 40 mV/s scan rate, O_2 flow rate 1.0 LPM, and electrolyte 190 mL.

The optimal pH of 2.5 along with the other operating parameters (except the scanning rate) in the case of the graphite/Co_3O_4/700°C/6h NPs electrode was also adopted for the graphite/Co_3O_4 NPs electrode system. The symbol 'Co_3O_4 NPs' simply signifies 'Co_3O_4/700°C/6h NPs' in the subsequent studies. NPs Scan rates were varied from 10 to 50 mV/s by the sweeping the potentials from $-E_{cat}$= –0.1 to 0.5 V vs. Ag/AgCl (Figure 4.27). It was fairly observed that both I_{pa} and I_{pc} were gradually increased with the increase in the scan rate like the graphite/NiO NPs electrode, and the peak potentials were also shifted slightly towards

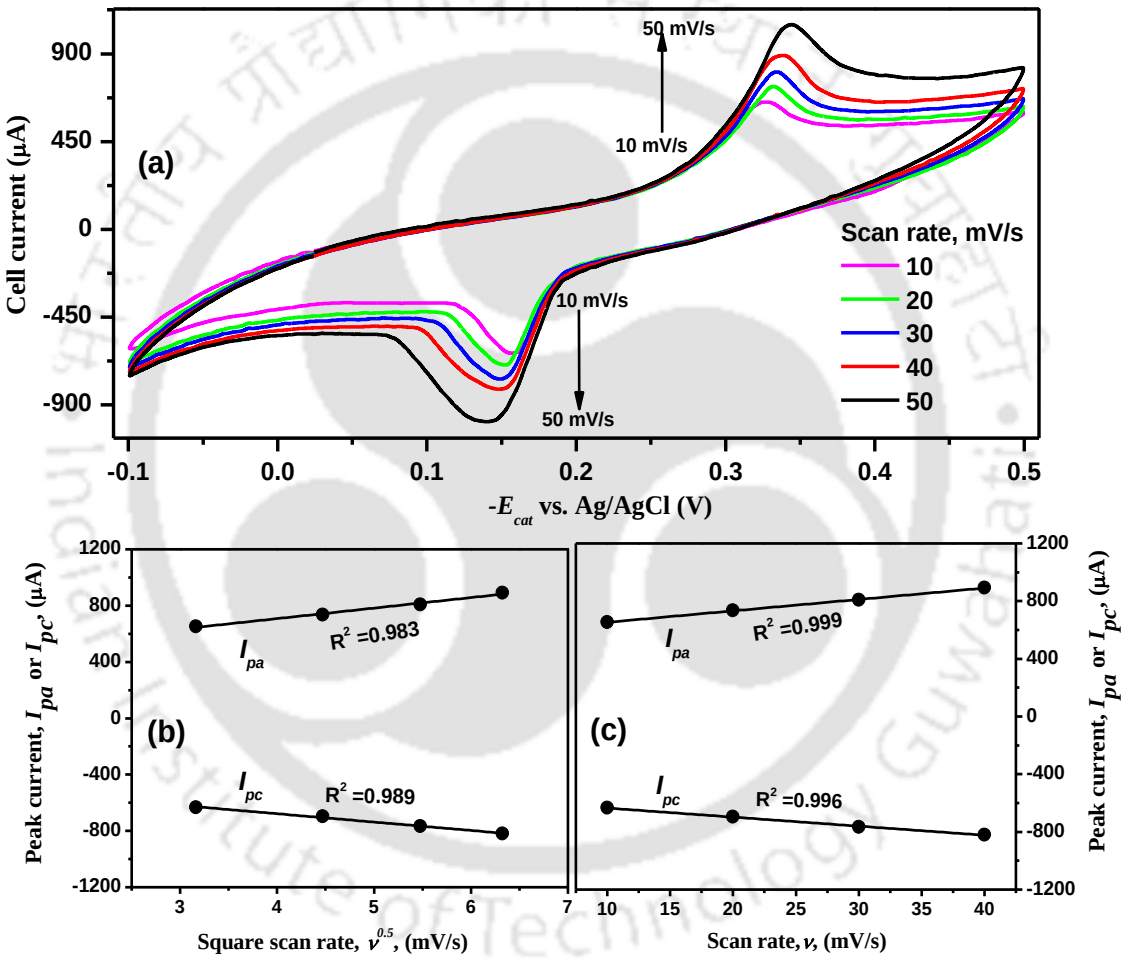

Figure 4.27: (a) Cyclic voltammograms with graphite/Co_3O_4 NPs electrode at different scan rates by sweeping from $-E_{cat}$= –0.1 to 0.5 V vs. Ag/AgCl, WE area 4.7 cm^2, 0.5 M Na_2SO_4 SE, pH 2.5, O_2 flow rate 1.0 LPM, and electrolyte 190 mL, (b) Variation of corresponding redox peak current (from Figure 4.27a) with the square root of the scan rate ($\nu^{0.5}$), and (c) Variation of redox peak current with the scan rate (ν).

the extreme (more positive or more negative) at a higher scan rate. Furthermore, the peak currents were linearly increased with the scan rate and square root of the scan rate. A linear dependency of peak currents with the scan rate indicates a surface confined redox reaction, and a linear dependency on the square root of the scan rate suggests that the redox reactions took place in the diffusion controlled regime of H_2O_2 from bulk to the electrode/solution interface. In this case, the O_2 reduction peak was found at $-E_{cat}$= 0.146 V vs. Ag/AgCl, and the oxidation peak at 0.339 V vs. Ag/AgCl at the scan rate of 40 mV/s. The current formation with the graphite/Co_3O_4 NPs electrode was little higher than that with the graphite/NiO NPs electrode.

4.2.2.2 Chronoamperometry and enhancement of CE_f of H_2O_2 generation

The chronoamperometry tests were performed at $-E_{cat}$= 0.268 V vs. Ag/AgCl and pH 2.5 (Section 4.2.2.1, Chapter 4) to enhance the rate of H_2O_2 formation and to avoid the unwanted side reaction. The kinetic profile of H_2O_2 formation at areas different of the cathode electrode is presented in Figure 4.28a. The higher initial cell current was resulted from the cathode surface DO pre-saturation (Qiang et al., 2002), and it reached the valley within 50 s irrespective of the type of cathodes. A 3.5 folds increase in the steady cell current was observed with graphite/NiO NPs cathode compared to the bare graphite electrode with the same area of 4.7 cm^2 (Figure 4.28a). A large number of microporous NiO NPs and its large surface area significantly enhanced both the electron transfer and H_2O_2 generation. The amount of H_2O_2 formed was about of 7.25, 6.04, and 4.95 mg/L after 2 h of electrolysis with 5.9, 4.7, and 3.3 cm^2 area of graphite/NiO NPs cathode.

The CE_f (Eq. 2.2, Chapter 2) of H_2O_2 formation is illustrated in Figure 4.28c. The CE_f with the graphite/NiO NPs cathode was found to be 87 % which was only 26 % with the bare graphite cathode having the same surface area. The highest CE_f of 89 % was achieved with a bigger cathode of 5.9 cm^2. The decay of CE_f was narrow (only 5-7 %) with a smaller cathode and also with the time of electrolysis up to 2 h. It implies that the amount of H_2O_2 grown up was proportional to the electric charge consumption with a large cathode (Figure 4.28a). The CE_f came down slightly with the time of electrolysis probably of the evocation of H_2O_2 decomposition (Eq. 1.37, Chapter 1) with the accumulation of H_2O_2 (Qiang et al., 2002). So, the catalytic activity of NiO NPs forming H_2O_2 was almost invariant to the surface area of its immobilization and time of electrolysis. The CE_f didn't change much (only 3.4 % fall) even after reuse of the same electrode in a cycle of 10 days up to 1 month.

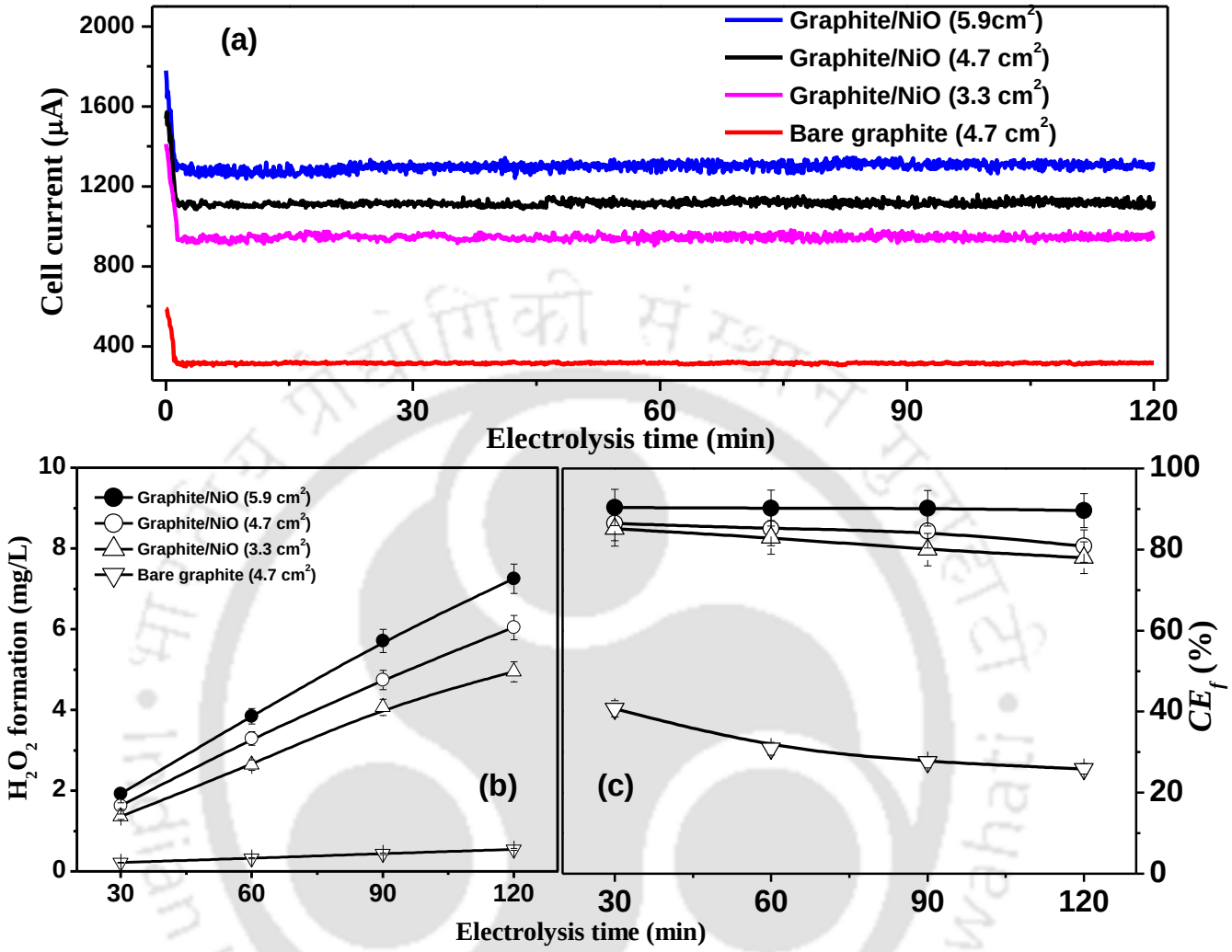

Figure 4.28: (a) Cell current variation with different areas of graphite/NiO NPs cathode and bare graphite, (b) H_2O_2 formation, and (c) Current efficiency (Eq. 2.2, Chapter 2) with electrolysis time calculated from H_2O_2 formation (Figure 4.28b) ($-E_{cat}$ = 0.268 V vs. Ag/AgCl, 0.08 M Na_2SO_4 SE, pH 2.5, 40 mV/s scan rate, O_2 flow rate 1.0 LPM, and electrolyte 190 mL).

SEM micrograph after the stability test was recorded, and it was compared with the SEM micrograph of the unused graphite/NiO NPs cathode (Figure 4.29). There were insignificant changes in the surface morphology. Therefore, the loss of NiO NPs from the electrode surface (Sadiek et al., 2012) was not that significant after the stability test.

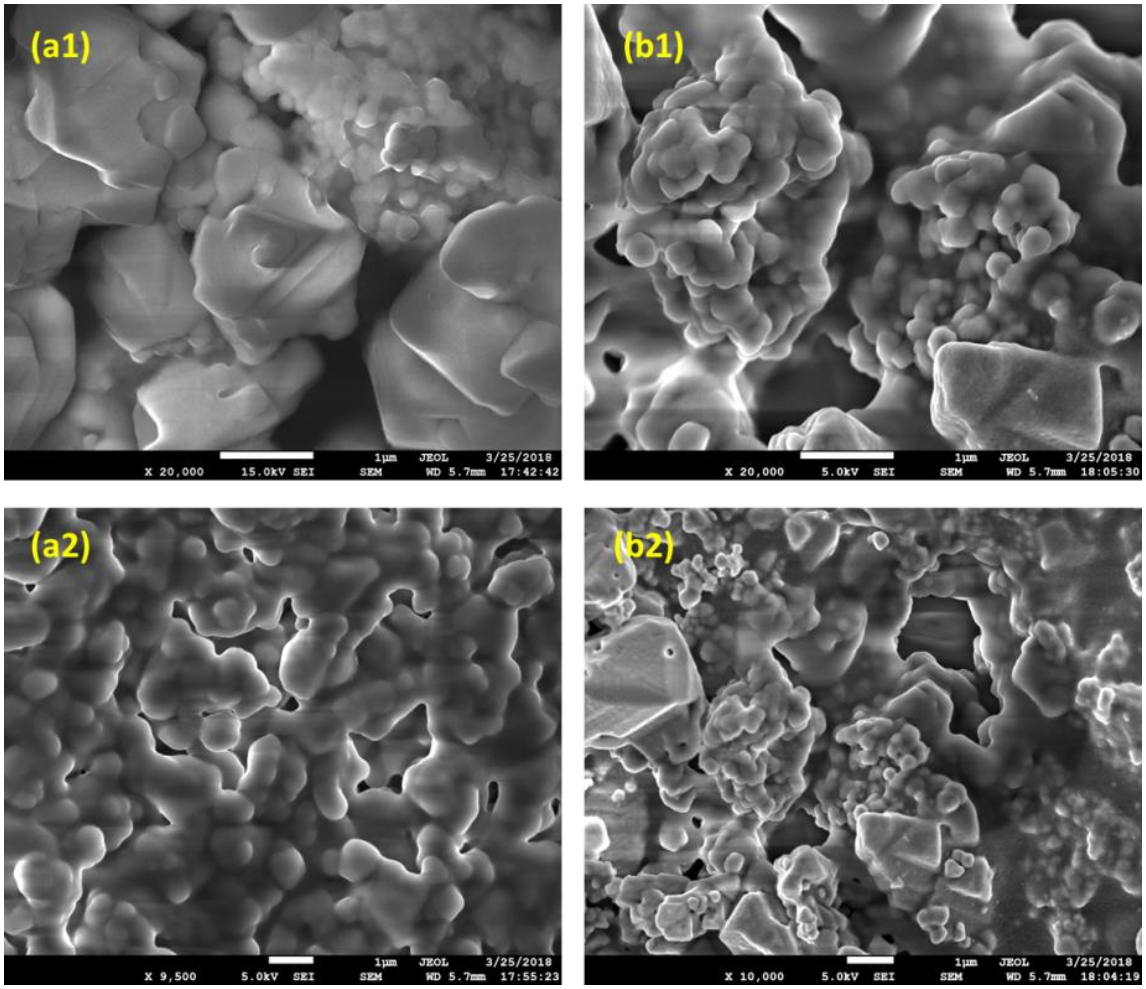

Figure 4.29: SEM micrographs of graphite/NiO NPs cathode before (a1-a2) and after (b1-b2) the stability test.

The chronoamperometry tests using the graphite/Co_3O_4 NPs electrode were also carried out in 0.08 M Na_2SO_4 electrolyte solution at pH 2.5 and $-E_{cat}$= 0.146 V vs. Ag/AgCl. The cell current reached the steady valley within 50 s irrespective to the surface area of electrode. However, the higher surface area of the cathode enhanced H_2O_2 formation (Figure 4.30a). The amount of H_2O_2 formed was about of 9.1, 7.0, and 5.8 mg/L after 2 h of electrolysis with 5.9, 4.7, and 3.3 cm^2 area of the graphite/Co_3O_4 NPs cathode (Figure 4.30b). The variation of the CE_f (Eq. 2.2, Chapter 2) of H_2O_2 generation is presented in Figure 4.30c. CE_f in the case of graphite/Co_3O_4 NPs cathode didn't decrease much with the electrolysis time as it was the graphite/NiO NPs cathode. CE_f was found to be 91, 83, and 79 % with 5.9, 4.7, and 3.3 cm^2 area of the graphite/Co_3O_4 NPs cathode after 2 h of electrolysis (Figure 4.30c).

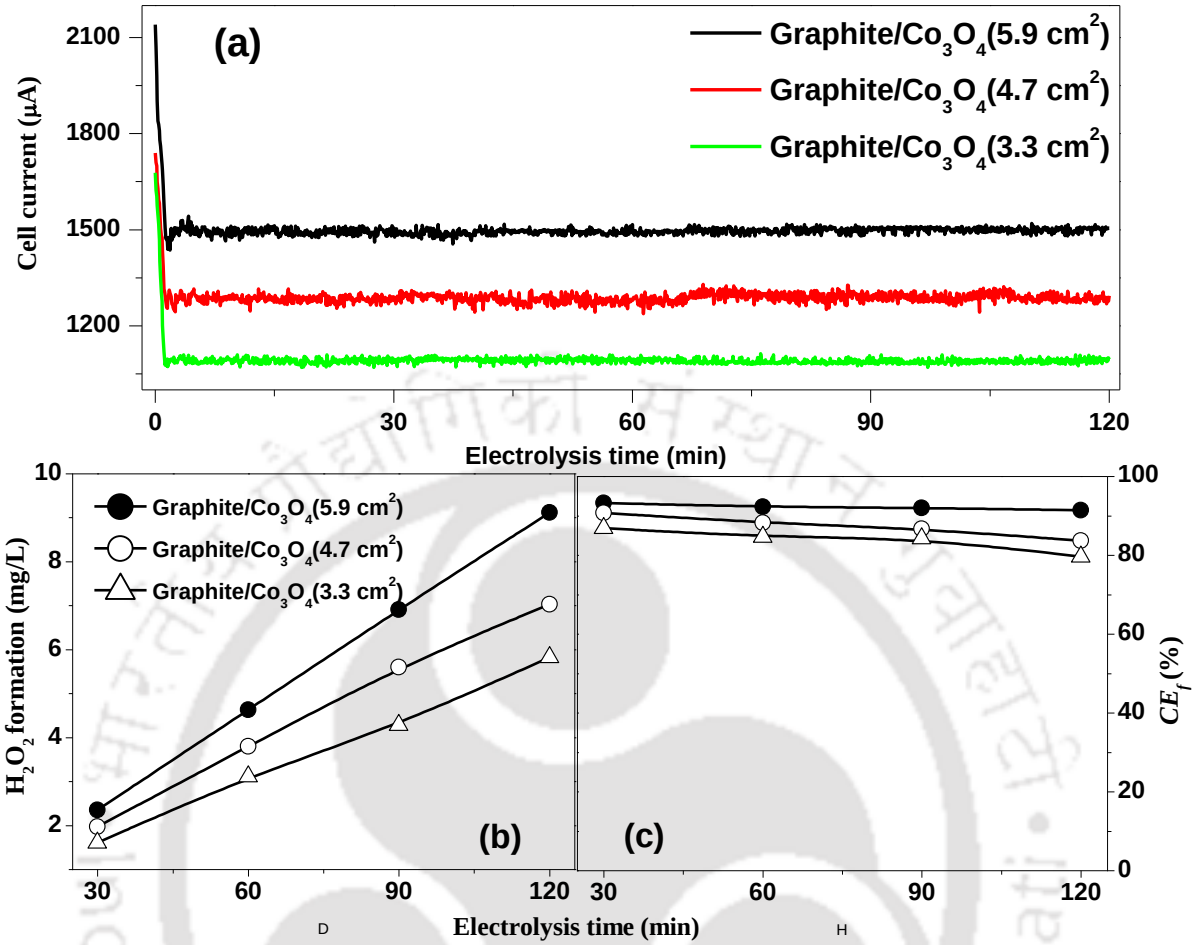

Figure 4.30: (a) Cell current variation with different areas of graphite/Co_3O_4 NPs cathode, (b) H_2O_2 formation, and (c) current efficiency (Eq. 2.2, Chapter 2) with electrolysis time calculated from H_2O_2 formation (Figure 4.30b) ($-E_{cat}$ = 0.146 V vs. Ag/AgCl, 0.08 M Na_2SO_4 SE, pH 2.5, 40 mV/s scan rate, O_2 flow rate 1.0 LPM, and electrolyte 190 mL).

A comparison with graphite/NiO and graphite/Co_3O_4 NPs cathodes to different composite electrodes for the formation of H_2O_2 is summarized in Table 4.1. It is evident that both NiO and Co_3O_4 NPs catalyst exhibited superior electrocatalytic activities over the different transition metal oxides and graphene nanocomposites for H_2O_2 formation. A CE_f of as high as 27 % was achieved over the Fe_3O_4/graphene electrode. The performance of the gas diffusion and polymer-precursor electrodes were comparable with the present work (Table 4.1).

Table 4.1: Performance comparison of graphite/NiO NPs electrode with the published literatures for H_2O_2 formation.

Cathode electrode	$-E_{cat}$ vs. Ag/AgCl, V	Experiment Condition	H_2O_2 formed (mg/L)/ CE_f (%)	NPs synthesis process	Source
Fe_2O_3/ACF	1.2	pH 2-3 Na_2SO_4 0.05M	~0.238/--	Chemical	Li et al., 2009
CeO_2/C-PPM-P	0.457	NaOH 1M	--/88.8	Sol-gel	Assumpcao et al., 2013
Graphite/Co_3O_4	0.133	pH 7 Na_2SO_4 0.07 M Time 3 h	0.1/--	Hydrothermal	Shuan et a., 2013
Au/graphite	0.653	pH 3 Na_2SO_4 0.5 M Time 2 h	59/70	--	Mounia and Djilali, 2014
Nb_2O_5/rGO/GDE	0.3	pH 2 K_2SO_4 0.1M Time 5.5 h	--/85.3	Hydrothermal	Carneiro et al., 2015
Fe_3O_4/Graphene	0.253	KOH 1M Time 5.5 h	--/62	Precipitation	Barros et al., 2015
Co_9S_8/PGC	0.111	pH 5 Na_2SO_4 0.1 M Time 2 h	~ 3/--	Carbonization	Lin et al., 2016
Graphite/NiO NPs	**0.268**	**pH 2.5 Na_2SO_4 0.08 M Time 2 h**	**7.25/89**	**Bio-inspired**	**Present work**
Graphite/Co_3O_4 NPs	**0.146**	**pH 2.5 Na_2SO_4 0.08 M Time 2 h**	**9.12/91**		

Co_9S_8: Cobalt sulfide; PGC: Partly graphitized carbon; rGO: Reduced graphene oxide; GDE: Gas diffusion electrode; PPM: Polymeric precursor; P: Printex L6

4.2.2.3 Limiting current density of H_2O_2 formation and mass-transfer parameters

The formation of H_2O_2 in the limiting current region is governed by the film diffusion of DO between the cathode-solution interfaces rather than by the electron transfer (Qiang et al., 2002). The concentration of O_2 at the cathode surface was depleted rapidly (< 50 s) after the start of electrolysis. So, the steady valley of cell current essentially implied the limiting current (i_L) of O_2 reduction reaction forming H_2O_2, and i_L for macroscopic electrodes can be expressed by Eq.

3.22 (Chapter 3) (Li et al., 1997; Qiang et al., 2002). Further, the thickness of the diffusion layer (δ) can be estimated from Eq. 4.15.

$$k_m = \frac{D}{\delta} \tag{4.15}$$

A linear relationship (R^2 =0.992) was found between the limiting current and area of graphite/NiO NPs cathodes. So, the slope of this line is the limiting current density (1.42 A/m^2) (Figure 4.31a) which was independent on the cathode surface area (Qiang et al., 2002), and k_m determined with this value is 0.955×10^{-5} m/s. Subsequently, δ was found as 209 µm considering D as 2.0×10^{-9} m^2/s (Kinoshita, 1992). The limiting current density was found to be 1.60 A/m^2 in the case of the graphite/Co_3O_4 NPs electrode (Figure 4.31b), and k_m and δ were determined as

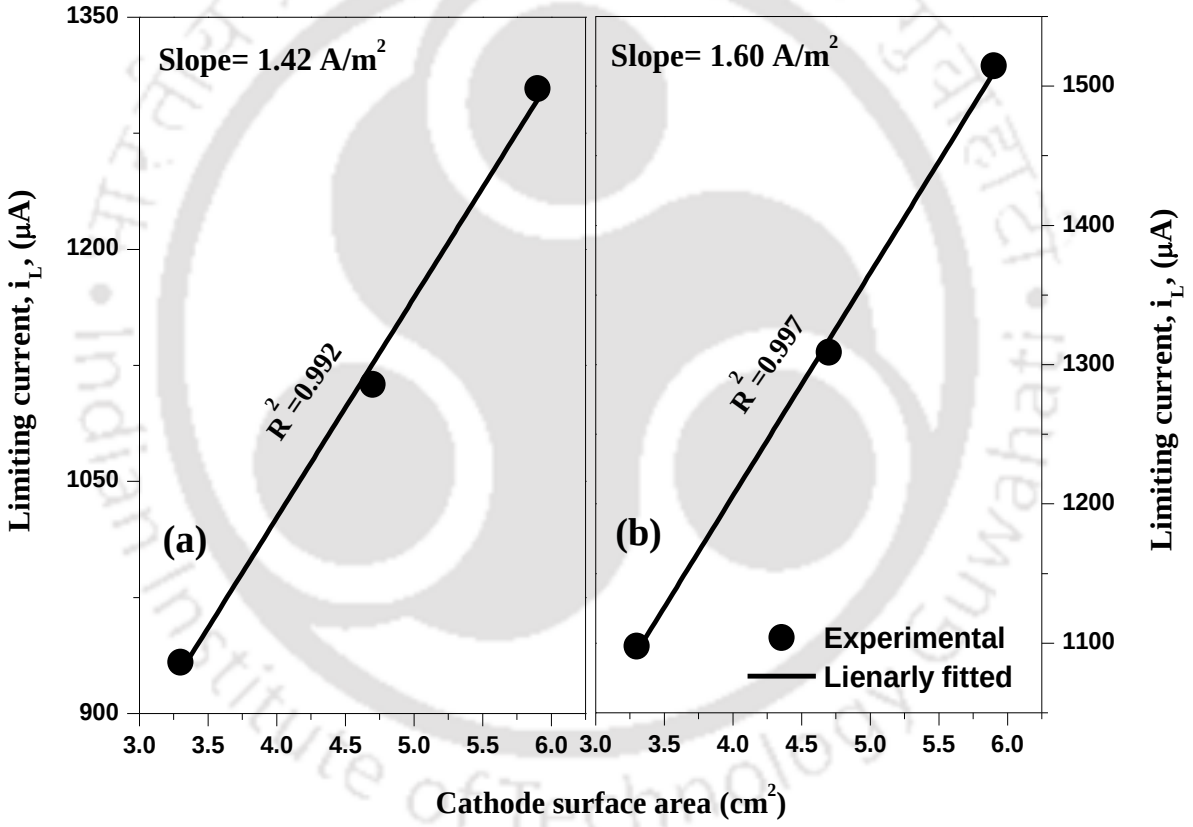

Figure 4.31: Variation of limiting current with different surface areas of (a) graphite/NiO cathode at $-E_{cat}$ = 0.268 V vs. Ag/AgCl and (b) graphite/Co_3O_4 NPs cathode at $-E_{cat}$ = 0.146 V vs. Ag/AgCl (0.08 M Na_2SO_4 SE, pH 2.5, 40 mV/s scan rate, O_2 flow rate 1.0 LPM, and electrolyte 190 mL).

1.13×10^{-5} m/s and 177 µm. The value of k_m and δ gives the microscopic insight of the fabricated graphite/NiO and graphite/Co_3O_4 NPs cathodes for the H_2O_2 formation by O_2 reduction in an acidic electrolyte. These results are in close agreement with earlier studies (Qiang et al., 2002; Lopes et al., 2016)

CE_f of H_2O_2 generation was much higher (~30 % more) in the case of NiO and Co_3O_4 NPs catalysed systems than graphite/TiO_2-Ti and graphite/graphite systems as obtained in the earlier study (Section 3.2.3.3, Chapter 3). Both NiO and Co_3O_4 NPs exhibited a low catalytic activity for the decomposition of H_2O_2 (Section 3.2.1.2, Chapter 3); so, the decrease in CE_f with the progress of H_2O_2 generation was significantly low than the bare graphite cathode (Section 3.2.3.3, Chapter 3). The mass transfer coefficient (k_m) also was increased by 4 and 3.4 folds with the use of Co_3O_4 and NiO NPs as electrocatalysts.

4.2.3 Application of H_2O_2 in electro-Fenton process

4.2.3.1 CIP degradation in NiO and Co_3O_4 NPs catalysed system

The experimental details for the decomposition of CIP in EFP are provided in Section 2.5.7 of Chapter 2. The CIP degradation experiments were carried out in-situ along with the generation of H_2O_2 at the graphite/NiO NPs and graphite/Co_3O_4 NPs cathodes, and a fixed quantity of Fe(II) (0.03 mM) was added just before the beginning of electrolysis. The cell current variation with the oxidation time at different electrodes is shown in Figure 4.32a. The removals of CIP and TOC at different time intervals are depicted in Figures 4.32b and 4.32c. Initially (< 10 min), the rate of degradation of CIP was faster, and thereafter, it progressed slowly with both the electrodes which was in accordance with a higher CE_f of the H_2O_2 formation at the initial stage of electrolysis (Figures 4.28 and 4.30). So, the formation of $^{\bullet}OH$ radicals (Eq. 1.4, Chapter 1) took place at a higher rate. The abundance of Fe^{2+} ions was also more, but it was gradually converted to Fe^{3+} with the progress of reaction (Eq. 1.16, Chapter 1), and the rate of CIP decomposition was decreased. The decomposition of CIP was about of 73 % with the graphite/NiO NPs electrode in 45 min. It was marginally higher (78 %) at the graphite/Co_3O_4 NPs electrode possibly of higher H_2O_2 electrogeneration, which in turn contributed to the formation more $^{\bullet}OH$ radicals (Ai et al., 2007). Only 48 % CIP degradation took place at the bare graphite electrode. Wang et al. (2018) reported a similar extent of CIP oxidation in 120 min with

an initial concentration of 200 mg/L in the photoelectron Fenton process. But, the $Ce_xZr_{1-x}O_2$/RGO composite electrode took 1 h to obtain the similar efficiency (Li et al., 2017).

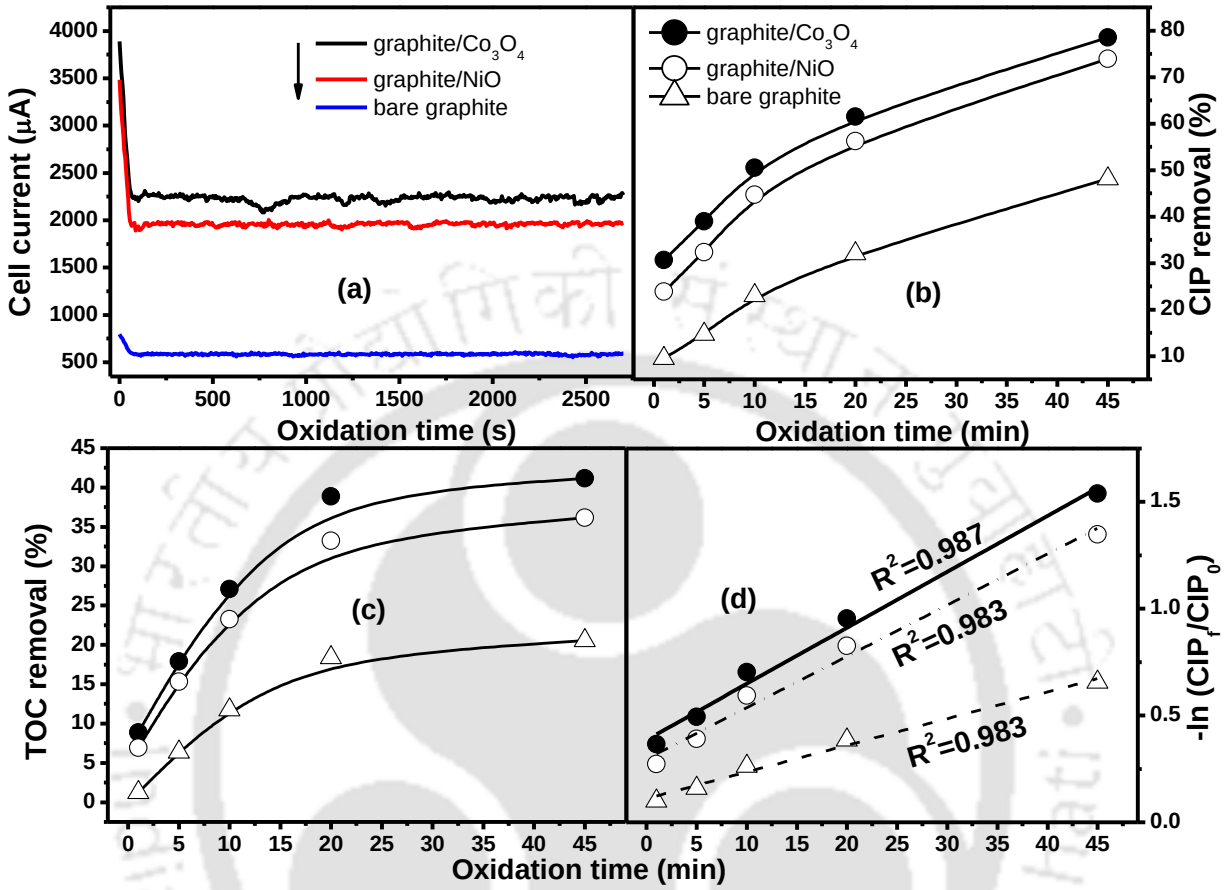

Figure 4.32: (a) Cell current variation with oxidation (H_2O_2 generation) time, (b) CIP removal with oxidation (H_2O_2 generation) time, (c) TOC removal, and (d) Best-fit pseudo-first order kinetic plots of CIP decomposition as shown in Figure 4.32b with electrolysis time using graphite/NiO NPs ($-E_{cat}$ = 0.268 V vs. Ag/AgCl), graphite/Co_3O_4 NPs ($-E_{cat}$ = 0.146 V vs. Ag/AgCl) and bare graphite ($-E_{cat}$ = 0.6 V vs. Ag/AgCl) with 15 mg/L initial CIP concentration, 0.03 mM Fe^{2+}, 0.08 M Na_2SO_4 SE, pH 2.5, 40 mV/s scan rate, O_2 flow rate 1.0 LPM, and electrolyte 190 mL.

TOC removal was found to be only 35 % against 73 % CIP degradation for the graphite/NiO NPs electrode after 45 min of oxidation. TOC reduction was about 46 % (CIP decomposition of 78 %) with the graphite/Co_3O_4 NPs electrode (Figure 4.32c). There was only 20 % TOC reduction with the bare graphite electrode. The extent of mineralization was significantly lower than the corresponding CIP decomposition due to the following reasons: (i) formation of intermediates which were resistant to oxidation by $^{\bullet}OH$ radicals (Wang et al., 2018;

Chen et al., 2017), (ii) diminution of the oxidation reaction rate because of the lower organic matter concentration (Yahya et al., 2014), and (iii) progress of the parasitic reactions (Eq. 1.16, Chapter 1) that competed with •OH radicals. Large numbers of refractory intermediates were originated (Giri and Golder, 2014) as most of them were attached to the core quinolone structure (Figure 4.33).

The degradation of organic pollutants at a low concentration in EFP typically follows the pseudo-first-order kinetic model (Liu et al., 2015) as •OH radicals are extremely short-lived (half-life is ~1 ns) (Liu et al., 2015). The kinetic model is shown in Eq. 4.16. Here, $[CIP]_0$ and $[CIP]$ are the initial concentration of CIP and its concentration at time '*t*'. Practically, there was no time lag between the formation of H_2O_2 and •OH radicals. So, the electrolysis time and oxidation time of CIP was essentially same. *k* is the pseudo-first-order rate constant.

$$[CIP] = [CIP]_0 e^{-kt} \quad (4.16)$$

The values of *k* were determined by fitting experimental results (Figure 4.32d), and the best-fit plots are shown in Figure 4.32d. The rate constant was found to be 0.0240 1/min for the graphite/NiO NPs cathode, and it was 0.0262 1/min (12 % higher) for the graphite/Co_3O_4 NPs cathode. The value of *k* was almost half (0.0124 1/min) with the bare graphite electrode. Wang et al. (2018) and Chen et al. (2017b) reported significantly higher values of *k* because of the higher Fe^{2+} (catalyst) concentration for the formation of •OH radicals.

4.2.3.2 Mechanistic aspects of CIP degradation

N heteroatom in the piperazine ring of the CIP molecule is typically the specific site of •OH radical attack. It is proposed that CIP was cleaved through three degradation routes (Figure 4.33) like piperazine moiety degradation (path# 1), cyclopropyl group cleavage (path #2), and decarboxylation reaction (path #3). Two strong electron-withdrawing nitrogen substituents, i.e. fluorine and -COOH groups are therein the aromatic ring (Figure 4.33a). On the other way, it indicates that the fluoroquinolone ring is less electron-donating due to the presence of highly electron-withdrawing -F substituent (Klavarioti et al., 2009). In general, the common pathways for the fragmentation of fluoroquinolone compounds are the loss of carboxyl ($[M+H-44]^+$) and fluoride moieties ($[M+H-22]^+$) (Klauson et al., 2010).

There was no significant variation in the number of intermediates and types of intermediates (based on *m/z* ratio) formed in EFPs in which H_2O_2 was generated by the

graphite/Co_3O_4 and graphite/NiO NPs electrode systems. So, the unified mechanisms are proposed in this work.

Intermediates with *m/z* of 306.10, 304.07, 305.13, 302.11, 263.04, 242.09, 186.13, 198.07, 310.1, 344.1, 299.1, 257.03, 256.3, 186.1, 283.1, 327.11, 202.03, 271.24, 257.07, and 225.1 were obtained for the graphite/Co_3O_4 NPs and graphite/NiO NPs electrodes with a retention time of 5.36 min (Figure 4.35). Most of the intermediates were formed through the cleavage of piperazine ring (Figure 4.33a to 4.33c). It seems that an unstable intermediate was originated as shown in Figure 4.33a. The nitrogen atom of piperazine ring with a lone pair electron, abstracted a proton from the solvent at an acidic pH, and the C-C bond was broken.

Fragments with *m/z* ratio of 306.10 (P_1) and 304.07 (P_2) were formed due to partial piperazine ring breaking along with defluorination (-F) followed by hydroxylation reactions (Figure 4.33a). D_3 (*m/z* 239) appeared with the loss of the fluorine atom at position 6 and expulsion of the ethylenediamine molecule (Figure 4.33a). Decarboxylation of CIP followed by hydroxylation reactions led to the formation of P_3 having *m/z* of 305.13. CO_2 was removed through this reaction at an acidic medium (Giri and Golder, 2014). The steric effect between the carbonyl (O=C) and carboxylic (-COOH) groups and the presence of the fluoride group could prompt such a decarboxylation reaction (Vogel et al., 2000; Hesse et al., 2008). P_4 (*m/z* 302.11) molecule was originated from P_3 by the substitution reaction of $^{\bullet}OH$ radicals on the release of -F atom.

Similarly, P_5 to P_7 products were formed through piperazine breaking followed by decarboxylation. P_8 molecule was originated due to the cyclopropyl ring breaking of P_7 fragment as the piperazine ring suffers an angle stress in the presence of the high electronegative fluorine atom that led to the formation of the three-membered cyclic amine ring (Figure 4.33a). Quinolone moiety acts as an electron rich compound due to the presence of $–NH_2$ group which makes it susceptible for the $^{\bullet}OH$ attack because of the electrophile nature of the free radical. P_9 (*m/z* 310.1) and P_{10} (*m/z* 344.1) were yielded from defluorination and oxidation of the piperazine ring, and it also formed P_{11} (*m/z* 299.1) and P_{12} (*m/z* 257.03) compounds on the successive cleavage of the piperazine ring (Figure 4.33b). P_{12} was reduced forming P_{13} along with the ethylene diamine molecule which was mineralized to form CO_2 and NH_3 (Figure 4.33b). Figure 4.33c showed the formation pathways of P_{14} to P_{20} compounds through the hydroxylation and decarboxylation reactions and partial cleavage of piperazine ring.

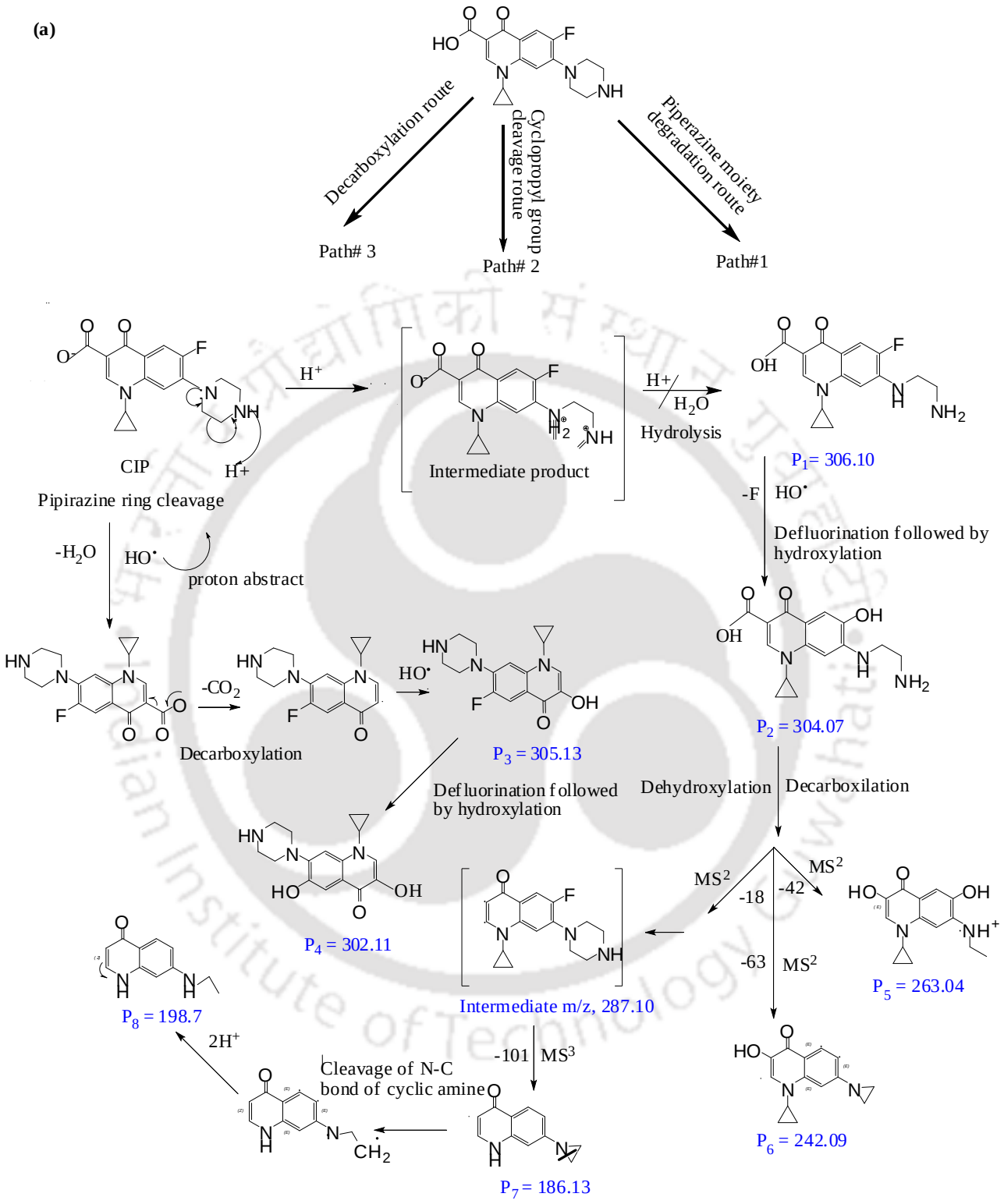

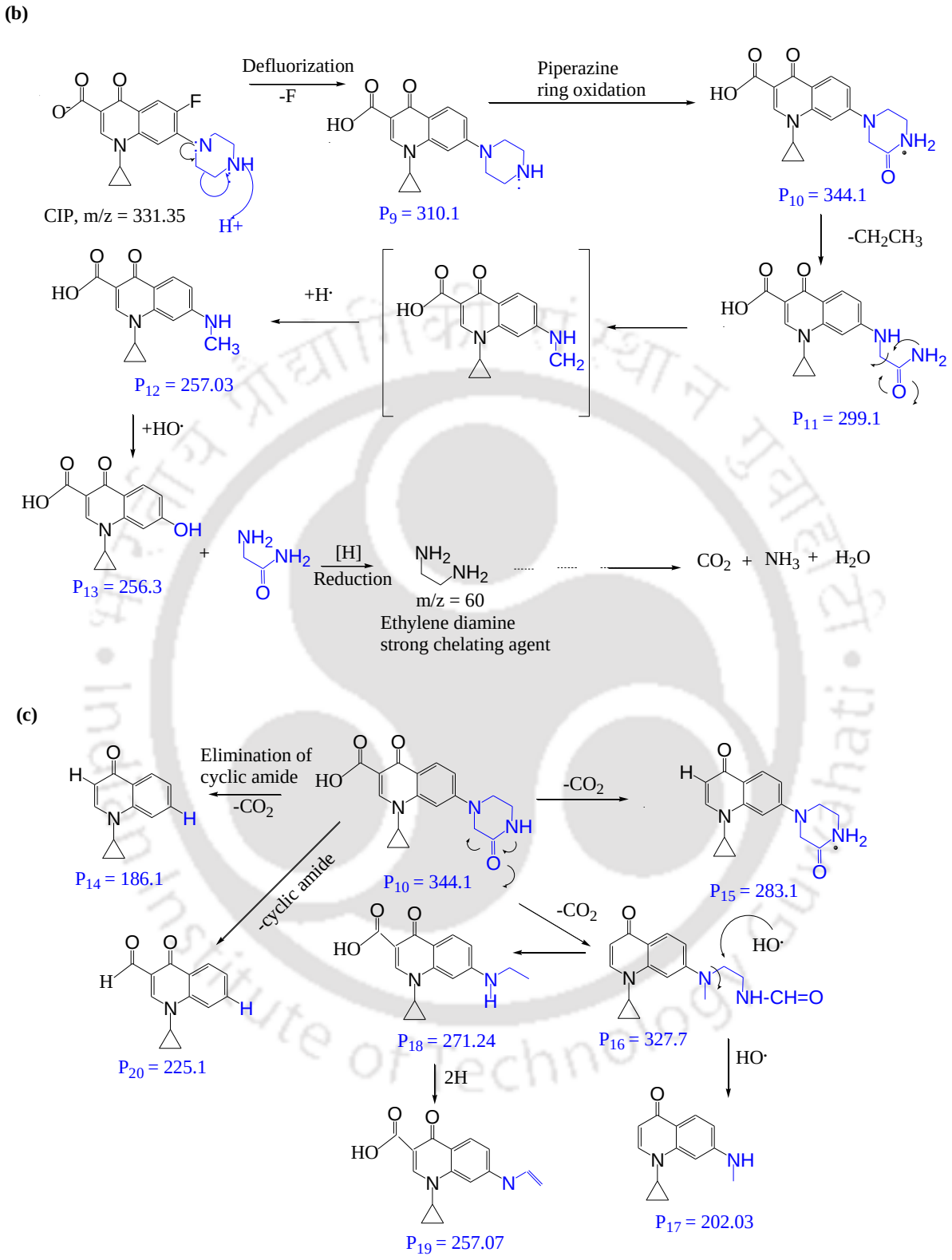

Figure 4.33: Mechanism of CIP degradation (a) Mechanism 1: Piperazine moiety degradation, (b) Mechanism 2: Cyclopropyl group cleavage, and (c) Mechanism 3: Decarboxylation reaction.

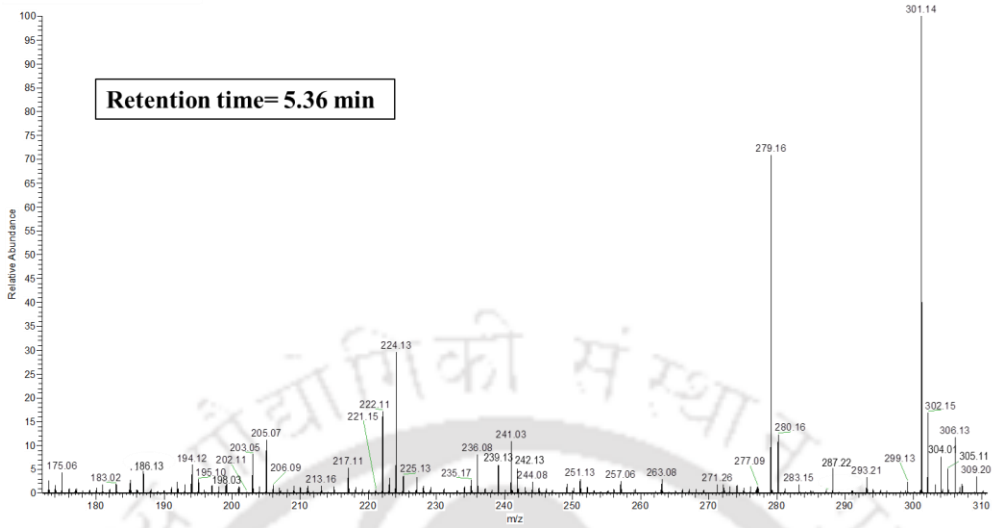

Figure 4.34: Mass spectra of CIP degradation using graphite/Co_3O_4 NPs cathodes ($-E_{cat}$ = 0.146 V vs. Ag/AgCl) with 15 mg/L initial CIP concentration, 0.03 mM Fe^{2+}, 0.08 M Na_2SO_4 SE, pH 2.5, 40 mV/s scan rate, O_2 flow rate 1.0 LPM, oxidation time 45 min, and electrolyte 190 mL.

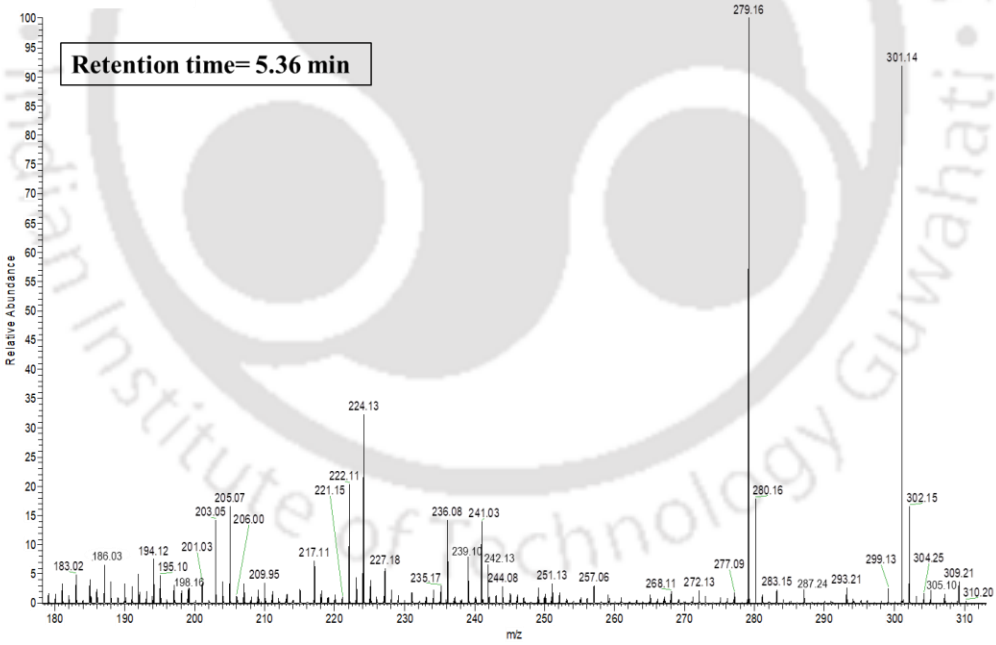

Figure 4.35: Mass spectra of CIP degradation using graphite/NiO NPs electrode ($-E_{cat}$ = 0.268 V vs. Ag/AgCl) with 15 mg/L initial CIP concentration, 0.03 mM Fe^{2+}, 0.08 M Na_2SO_4 SE, pH 2.5, 40 mV/s scan rate, O_2 flow rate 1.0 LPM, oxidation time 45 min, and electrolyte 190 mL.

4.3 Major findings

This work achieved that the analytes present in *S. edule* were as effective as the reductants employed in the conventional chemical methods for the synthesis of NiO and Co_3O_4 NPs, and no external capping agents were needed in this bio-inspired route. Both the NPs exhibited a superior electrocatalytic activity for the synthesis of H_2O_2 in an acidic electrolyte in comparison to different electrocatalysts including the transition metal oxides. The followings are the key findings from the present work.

- Nickel hydroxide was formed through the ligand exchange between the analytes and OH^- ions which was calcined at 500 °C for 2 h for the formation NiO NPs, and the resulting particles were free from contaminants/other nickel species. Similarly, the analytes present in the bio-extract mediated CoOOH reduction to $Co(OH)_2$ for the formation of monocrystalline Co_3O_4 in the calcination process at 700 °C for 6 h.
- NiO NPs were nearly spherical in shapes (2.98 to 26.9 nm) with a weak ferromagnetic property (coercive field 0.31 kOe with 0.03 emu/g remanent magnetization) and high microporosity (75 %). The Co_3O_4 NPs calcined at 700 °C for 6 h at 15 kOe magnetic field exhibited a very weak ferromagnetic property with 0.37 emu/g. TEM micrographs showed that the Co_3O_4 NPs had an average diameter size of 31.79 nm.
- The Raman spectrum also revealed that NiO NPs could behave as a weak ferromagnet due to the presence of a mild 2M vibration in which 2M band was associated with the Ni^{2+}-O^{2-}-Ni^{2+} super-exchange interaction. The Raman spectrum evidenced the Co^{3+} octahedral sites, and the combined vibrations of the Co^{2+} tetrahedral site and octahedral oxygen motions.
- From the cyclic voltammetry, the optimal pH of O_2 reduction for the production of H_2O_2 was found to be 2.5 at $-E_{cat}$=0.268 vs. Ag/AgCl on the graphite/NiO NPs cathode, and the O_2 reduction peak potential didn't get influenced by the solution pH. On the other hand, the graphite/Co_3O_4 NPs cathode generated H_2O_2 at a lower potential of $-E_{cat}$=0.146 vs. Ag/AgCl under the same experimental condition.
- The highest current efficiency of H_2O_2 formation with the larger area (5.9 cm^2) graphite/NiO NPs electrode was found as 89 % at $-E_{cat}$=0.268 vs. Ag/AgCl, pH 2.5, 0.5 M Na_2SO_4 supporting electrolyte and O_2 flow rate 1.0 LPM. But, it was marginally higher with the graphite/Co_3O_4 NPs electrode.

- The limiting current density with the graphite/NiO NPs electrode was determined as 1.42 A/m^2 which was independent on the area of the working electrode. O_2 reduction took place in the diffusion controlled regime, and the corresponding mass transfer coefficient was estimated as 0.955×10^{-5} m/s. From the film theory, the thickness of the O_2 diffusion layer was calculated as 209 µm. The limiting current density was determined as 1.60 A/m^2 in the case of graphite/Co_3O_4 NPs electrode. The mass transfer coefficient and thickness of the diffusion layer were found as $1.1.3\times10^{-5}$ m/s and 1.77 µm, respectively.
- The degradation of CIP was quite impressive (71-78 %) in EFP where H_2O_2 generation was catalyzed by NiO and Co_3O_4 NPs. However, the mineralization efficiency was notably lower due to the formation of the refractory intermediates attached to the quinolone structure.
- The pseudo 1^{st} order kinetic model well fitted the experimental data of CIP cleavage. The values of the rate constant were found as 0.0124, 0.0240, and 0.0262 1/min with the bare graphite, graphite/NiO NPs, and graphite/Co_3O_4 NPs electrode systems, respectively.
- The degradation of the CIP molecule mainly took place through three different pathways such as piperazine moiety breaking, cyclopropyl group cleavage, and decarboxylation reaction. The proposed mechanisms were well supported by the fragments appeared in the mass spectra, and most of the fragments were originated from the cleavage of piperazine ring moiety.

References

Ai L., Zeng Y. Hierarchical porous NiO architectures as highly recyclable adsorbents for effective removal of organic dye from aqueous solution, *Chem. Eng. J*. **2013**, 215-216, 269-278.

Ai Z., Lu L., Li J., Zhang L., Qiu J., Wu M. Fe@Fe_2O_3 core-shell nanowires as iron reagent. 1. Efficient degradation of rhodamine B by a novel sono-Fenton process. *J. Phys. Chem. C* **2007**, 111, 4087-4093.

Alagiri M., Ponnusamy S., Muthamizhchelvan C. Synthesis and characterization of NiO nanopartilces by sol-gel method, *J. Mater. Sci.: Mater. Electron*. **2012**, 23, 728-732.

Allaedini G., Muhammad A. Study of influential factors in synthesis and cobalt characterization of oxide nanoparticles, *J. Nanostructure Chem*. **2013**, 3, 77-92.

Al-Sehemi A.G., Al-Shihri A.S., Kalam A., Du G., Ahmad T. Microwave synthesis, optical properties and surface area studies of NiO nanoparticles, *J. Mol. Struct*. **2014**, 1058, 56-61.

Assumpcao M.H.M.T., Moraes A., De Souza R.F.B., Calegaro M.L., Lanza M.R.V., Leite E.R., Cordeiro M.A.L., Hammer P., Santos M.C., Influence of the preparation method and the support on H_2O_2 electro-generation using cerium oxide nanoparticles, *Electrochim. Acta* **2013**, 111, 339-343.

Bard A.J., Faulkner L.R. Electrochemical methods, 2nd ed., John Wiley and sons, New York, **2001**.

Barnard R., Crickmore G.T., Lee J.A., Tye F.L. The cause of residual capacity in nickel oxyhydroxide electrodes, *J. Appl. Electrochem*. **1980**, 10, 61-70.

Barros W.R.P., Wei Q., Zhang G., Sun S., Lanza M.R.V., Tavares C. Oxygen reduction to hydrogen peroxide on Fe_3O_4 nanoparticles supported on Printex carbon and Graphene, *Electrochim. Acta* **2015**, 162, 263-270.

Benetis N., Holmen K., Kowalewski J., Nordenskiold L., Wahlberg O. Investigation of nickel(II)-ascorbic acid complex formation in aqueous solution using potentiometric measurements, optical spectroscopy and ^{13}C NMR spectroscopy, *Acta Chem. Scand. A* **1981**, 35, 513-520.

Bhatt A.S., Bhat D.K., Tai C.W., Santosh M.S. Microwave-assisted synthesis and magnetic studies of cobalt oxide nanoparticles, *Mater. Chem. Phys*. **2011**, 125, 347-350.

Carballo T., Gil M.V., Gomez X., Gonzalez-Andres F., Moran A. Characterization of different compost extracts using Fourier-transform infrared spectroscopy (FTIR) and thermal analysis, *Biodegrad*. **2008**, 19, 815-830.

Carneiro J.F., Paulo M.J., Siaj M., Tavares A.C., Lanza M.R.V. Nb_2O_5 nanoparticles supported on reduced graphene oxide sheets as electrocatalyst for the H_2O_2 electrogeneration, *J. Catal*. **2015**, 332, 51-61.

Casado N., Hernandez G., Sardon H., Mecerreyes D. Current trends in redox polymers for energy and medicine, *Prog. Polym. Sci*. **2016**, 52, 107-135.

Cha H.G., Sohn J.H., Park Y., Lee K.J., Jung M.H., Lee J.-W., Shin W., Kang M.J., Kim D.Y., Kang Y.S. Hierarchical NiO hollow microspheres: electrochemical and magnetic properties, *RSC Adv*. **2012**, 2, 9786-9790.

Chang X., Meyer M.T., Liu X., Zhao Q., Chen H., Chen, J. Determination of antibiotics in sewage from hospitals, nursery and slaughter house, wastewater treatment plant and source water in Chongqing region of Three Gorge Reservoir in China, Environ. Pollut. **2010**, 158, 1444-1450.

Chen C.-C., Do J.-S., Gu Y. Immobilization of HRP in mesoporous silica and its application for the construction of polyaniline modified hydrogen peroxide biosensor, *Sensors* **2009**, 9, 4635-4648.

Chen M., Wang L., Yang H., Zhao S., Xu H., Wu G., Nanocarbon/composite catalsyts for bifunctional oxygen reduction and evolution in reversible alkaline fuel cells: A mini review, *J. Power Sources* **2017a,** 375, 277-290.

Chen W., Cai S., Ren Q.-Q., Wen W., Zhao Y.-D. Recent advances in electrochemical sensing for hydrogen peroxide: a review, *Analyst* **2012**, 137, 49-58.

Chen Y., Wang A., Zhang Y., Bao R., Tian X., Li J. Electro-Fenton degradation of antibiotic ciprofloxacin (CIP): Formation of Fe^{3+}-CIP chelate and its effect on catalytic behavior of Fe^{2+}/Fe^{3+} and CIP mineralization, *Electrochim. Acta* **2017b**, 256, 185-195.

Chinnasamy C.N., Jeyadevan B., Shinoda K., Tohji K. Synthesis and magnetic properties of face-centered-cubic and hexagonal-close-packed Ni nanoparticles through polyol process, *J. Appl. Phys*. **2005**, 97, 10J309.

Christian T., Schneider R.J., Farber H.A., Skutlarek D., Meyer M.T., Goldbach H.E. Determination of antibiotic residues in manure, soil, and surface waters, *Acta Hydroch. Hydrob*. **2003**, 31, 36-44.

Diallo A., Beye A.C., Doyle T.B., Park E., Maaza M. Green synthesis of Co_3O_4 nanoparticles via Aspalathus linearis: Physical properties, *Green Chem. Lett. Rev*. **2015**, 8, 30-36.

Duan W.J., Lu S.H., Wu Z.L., Wang Y.S. Size Effects on Properties of NiO Nanoparticles Grown in Alkalisalts, *J. Phys. Chem. C* **2012**, 116, 26043-26051.

El-Kemary M., Nagy N., El-Mehasseb I. Nickel oxide nanoparticles: Synthesis and spectral studies of interactions with glucose, *Mater. Sci. Semicond. Process*. **2013**, 16, 1747-1752.

Ellis J. Pharmaceutical and personal care products (PPCPs) in urban receiving water, *Environ. Pollut.* **2006**, 144, 184-189.

Esswein A.J., McMurdo M.J., Ross P.N., Bell A.T., Tilley T.D. Size-dependent activity of Co_3O_4 nanoparticle anodes for alkaline water electrolysis, *J. Phys. Chem. C* **2009**, 113, 15068-15072.

Farhadi S., Roostaei-Zaniyani Z. Simple and low-temperature synthesis of NiO nanoparticles through solid-state thermal decomposition of the hexa(ammine)Ni(II) nitrate, $[Ni(NH_3)_6](NO_3)_2$, complex, *Polyhedron* **2011**, 30, 1244-1249.

Farhadi S., Sepahdar A., Jahanara K. Spinel-type cobalt oxide (Co_3O_4) nanoparticles from the mer-$Co(NH_3)_3(NO_2)_3$ complex: Preparation, characterization, and study of optical and magnetic properties, *JNS* **2013**, 3, 199-207.

Giri A.S., Golder A.K. Ciprofloxacin degradation from aqueous solution by Fenton oxidation: reaction kinetics and degradation mechanisms, *RSC Adv*. **2014**, 4, 6738-6745

Golet E.M., Strehler A., Alder A.C., Giger W. Determination of fluoroquinolone antibacterial agents in sewage sludge and sludge-treated soil using accelerated solvent extraction followed by solid-phase extraction, *Anal. Chem*. **2002**, 74, 5455-5462.

Gonçales V.R., Gaitan M.H., Bragatto A.O.P., Soler-Illia G.J.A.A., Baraldo L.M., Cordoba de Torresi S.I. Correlation between pore size and reactivity of macro/mesoporous iron and copper hexacyanoferrates for H_2O_2 electrocatalysis, *J. Electroanal. Chem*. **2013**, 706, 48-54.

Gupta A., Garg A. Degradation of ciprofloxacin using Fenton's oxidation: Effect of operating parameters, identification of oxidized by-products and toxicity assessment, *Chemosphere* **2018**, 193, 1181-1188.

Handan M.S., Riyanto, Othman M.R. Preparation and characterization of nano size NiOOH by direct electrochemical oxidation of nickel plate, *Int. J. Electrochem. Sci*. **2013**, 88, 4747-4760.

Helia H., Pishahang J. Cobalt oxide nanoparticles anchored to multiwalled carbon nanotubes: Synthesis and application for enhanced electrocatalytic reaction and highly sensitive nonenzymatic detection of hydrogen peroxide, *Electrochim. Acta* **2014**, 123, 518-526.

Hernando M.D., Mezcua M., Fernandez-Alba A.R., Barcelo D. Environmental risk assessment of pharmaceutical residues in wastewater effluents, surface waters and sediments, *Talanta* **2006**, 69 (2), 334-342.

Hesse M., Meier H., Zeeh B., Spectroscopic Methods in Organic Chemistry, Thieme, New York, 2nd ed., **2008**, 4 (7), 17-21.

Hu P., Zhang S., Wang H., Pan D., Tian J., Tang Z., Volinsky A.A. Heat treatment effects on Fe_3O_4 nanoparticles structure and magnetic properties prepared by carbothermal reduction, *J. Alloy Compd*. **2011**, 509, 2316-2319.

Huang G.-Y., Xu S.-M., Xu G., Li L.-Y., Zhang L.-F., Preparation of fine nickel powders via reduction of nickel hydrazine complex precursors, *Trans. Nonferrous Met. Soc. China* **2009**, 19, 389-393.

Huseyin T., Okan B., Selale S., Tolga, H. Use of Fenton oxidation to improve the biodegradability of a pharmaceutical wastewater, *J. Hazard. Mater*. **2006**, 136, 258-265.

Jia W., Guo M., Zheng Z., Yu T., Rodriguez E.G., Wang Y., Lei Y. Electrocatalytic oxidation and reduction of H_2O_2 on vertically aligned Co_3O_4 nanowalls electrode: Toward H_2O_2 detection, *J. Electroanal. Chem*. **2009**, 625, 27-32.

Kandalkara S.G., Gunjakara J.L., Lokhandeb C.D., Joo O.-S. Synthesis of cobalt oxide interconnected flacks and nano-worms structures using low temperature chemical bath deposition, *J. Alloy Compd*. **2009**, 478, 594-598.

Kinoshita K. Electrochemical oxygen technology, John Wiley, New York NY, **1992**.

Klauson D., Babkina J., Stepanova K., Krichevskaya M., Preis S. Aqueous photocatalytic oxidation of amoxiline, *Catal. Taday*. **2010**, 151, 39-45.

Klavarioti M., Mantzavinos D., Kassinos D. Removal of residual pharmaceuticals from aqueous systems by advanced oxidation processes, *Environ. Int.* **2009**, 35, 402-417.

Larsson D.G.J., de Pedro C., Paxeus N. Effluent from drug manufactures contains extremely high levels of pharmaceuticals, *J. Hazard. Mater*. **2007**, 148, 751-755.

Li H.B., Yu M.H., Lu X.H., Liu P., Liang Y., Xiao J., Tong Y.X., Yang G.W. Amorphous cobalt hydroxide with superior pseudocapacitive performance, *ACS Appl. Mater. Interfaces* **2014**, 6, 745-749.

Li J., Ai Z., Zhang L. Design of a neutral electro-Fenton system with Fe@Fe_2O_3/ACF composite cathode for wastewater treatment, *J. Hazard. Mater*. **2009**, 164, 18-25.

Li W., Shi Y., Lihong G., Liu J., Cai Y. Occurrence, distribution and potential affecting factors of antibiotics in sewage sludge of wastewater treatment plants in China, *Sci. Total Environ.* **2013**, 445-446, 306-313.

Li Y., Li Y., Xie B., Han J., Zhan S., Tian Y. Efficient mineralization of ciprofloxacin by using 3D $Ce_xZr_{1-x}O_2$/RGO composite cathode, *Environ. Sci.: Nano* **2017**, 4, 425-436

Li Z.M., Shea P.J., Comfort S.D. Fenton oxidation of 2,4,6- trinitrotoluene in contaminated soil slurries. *Environ. Eng. Sci*. **1997**, 14, 55-66.

Lin Y., Yu J. , Xing Z., Guo X. , Yu X., Tang B. , Zou J. Enhanced generation of H_2O_2 and radicals on Co_9S_8/partly-graphitized carbon cathode for degradation of bio-refractory organic wastewater, *Electrochim. Acta* **2016**, 213, 341-350.

Liu M., Chang J., Sun J., Gao L. Synthesis of porous NiO using $NaBH_4$ dissolved in ethylene glycol as precipitant for high-performance supercapacitor, *Electrochim. Acta* **2013**,107, 9-15.

Liu L., Guo Y., Wang Y., Yanga X., Wang S., Guo H. Hollow NiO nanotubes synthesized by bio-templates as the high performance anode materials of lithium-ion batteries, *Electrochim. Acta* **2013**, 114, 42-47.

Liu Y., Chen S., Quan X., Yu H., Zhao H., Zhang Y. Efficient mineralization of perfluorooctanoate by electro-Fenton with H_2O_2 electro-generated on hierarchically porous carbon, *Environ. Sci. Technol*. **2015**, 49, 13528-13533.

Lopes T., Kucernak A., Malko D., Ticianelli E.A. Mechanistic insights into the oxygen reduction reaction on metal–N–C electrocatalysts under fuel cell conditions, *Chem. Electro. Chem*. **2016**, 3, 1580-1590.

Medvedeva O.I., Kambulova S.S., Bondar O.V., Gataulina A.R., Ulakhovich N.A., Gerasimov A.V., Evtugyn V.G., Gilmutdinov I.F., Kutyreva M.P. Magnetic cobalt and cobalt oxide nanoparticles in hyperbranched polyester polyol matrix, *J. Nanotechnol*. **2017**, 2017, 1-9.

Meyer M.T., Bumgarner J.E., Varns J. L, Daughtridge J.V., Thurman E.M., Hostetler K.A. Use of radioimmunoassay as a screen for antibiotics in confined animal feeding operations and confirmation by liquid chromatography/mass spectrometry, *Sci. Total Environ*. **2000,** 248, 181-187.

Mironova-Ulmane N., Kuzmin A., Steins I., Grabis J., Sildos I., Pars M. Raman scattering in nanosized nickel oxide NiO, J. *Phys. Conf. Series* **2007**, 93, 012039.

Mohanraj V., Jayaprakash R., Chandrasekaran J., Robert R., Sangaiya P. Influence of pH on particle size, band-gap and activation energy of CdS nanoparticles synthesized at constant frequency ultrasonic wave irradiation, *Mater. Sci. Semicond. Process*. **2017**, 66, 131-139.

Monk P.M.S. Fundamentals of electroanalytical chemistry, Wiley India Pvt. Ltd., **2010**, page 167.

Motahari F., Mozdianfarda M.R. , Salavati-Niasari M. Synthesis and adsorption studies of NiO nanoparticles in the presence of H_2acacen ligand, for removing Rhodamine B in wastewater treatment, *Process Saf. Environ. Prot*. **2015**, 93, 282-292.

Mounia A.Y., Djilali Z. Electrogeneration of hydrogen peroxide for electro-Fenton system by oxygen reduction using gold nanoparticle electrodeposited on graphite cathode, *Desalin. Water Treat*. **2014**, 2014, 1-12.

Mu J., Zhang L., Zhao M., Wang Y. Co_3O_4 nanoparticles as an efficient catalase mimic: Properties, mechanism and its electrocatalytic sensing application for hydrogen peroxide, *J. Mol. Catal. A: Chem.* **2013**, 378, 30-37.

Naveen A.N., Selladurai S. Tailoring structural, optical and magnetic properties of spinel type cobalt oxide (Co_3O_4) by manganese doping, *Physica B.* **2015**, 457, 251-262.

Ozkaya T., Baykal A., Koseoglu Y., Kavas H. Synthesis of Co_3O_4 nanoparticles by Oxidation-Reduction method and its magnetic characterization, *Cent. Eur. J. Chem*. **2009**, 7, 410-414.

Qiang Z., Chang J.-H., Huang C.-P. Electrochemical generation of hydrogen peroxide from dissolved oxygen in acidic solution, *Water Res*. **2002**, 36, 85-94.

Qiang Z., Chang J.-H., Huang C.-P. Electrochemical regeneration of Fe^{2+} in Fenton oxidation processes, *Water Res*. **2003**, 37, 1308-1319.

Raghavan K.V. Scoping report on antimicrobial resistance in India, Wanshinton DC, New Delhi, **2017**.

Rahal H.T., Awad R., Abdel-Gaber A.M., El-Said Bakeer D. Synthesis, Characterization, and Magnetic Properties of Pure and EDTA-Capped NiO Nanosized Particles, *J. Nanomater.* **2017**, 2017, 1-9.

Rahdar A., Aliahmad M., Azizi Y. NiO nanoparticles: Synthesis and characterization, *JNS* **2015**, 5, 145-151.

Rajesh A., Raja M.M., Gurunathan K. Spin-Relaxation of NiO Encapsulated Gd_2O_3 Core–Shell Nanoparticles, *Acta Metall. Sin. (Engl. Lett.)* **2014**, 2, 253-258.

Rao Ch.V., Bag S.S., Golder A.K. A biosynthesis route to nearly spherical agnps using chayote fruit extract, *Environ. Prog. Sustain. Energy* **2016**, 36, 192-199.

Rao Ch.V., Golder A.K. pH dependent size control, formation mechanism and antimicrobial functionality of bio-inspired AgNPs, *RSC Adv*. **2016**, 6, 95483-95493.

Roche I., Chainet E., Chatenet M., Vondrak J. Carbon-supported manganese oxide nanoparticles as electrocatalysts for the oxygen reduction reaction (ORR) in alkaline medium: Physical characterizations and ORR mechanism, *J. Phys. Chem. C* **2007**, 111, 1434-1443.

Ryu J., Kim S.-W., Kang K., Beum Park C. Synthesis of diphenylalanine/cobalt oxide hybrid nanowires and their application to energy storage, *ACS Nano* **2010**, 1, 159-164.

Sadiek I.M., Mohammad A.M., El-Shakre M.E., Awad M.I., El-Deab M.S., El-Anadouli B.E. Electrocatalytic evolution of oxygen gas at cobalt oxide nanoparticles modified electrodes, *Int. J. Electrochem. Sci*. **2012**, 7, 3350-3361.

Sharifi S.L., Shakur H.R., Mirzaei A., Salmani A., Hosseini M.H. Characterization of cobalt oxide Co_3O_4 nanoparticles prepared by various methods: effect of calcination temperatures on size, dimension and catalytic decomposition of hydrogen peroxide, *Int. J. Nanotechnol*. **2013**, 9, 51-58.

Sharma J.K., Srivastava P., Singh G., Akhtar M.S., Ameen S. Green synthesis of Co_3O_4 nanoparticles and their applications in thermal decomposition of ammonium perchlorate and dye-sensitized solar cells, *Mater. Sci. Eng. B* **2015**, 193, 181-188.

Sharma R.K., Ghose R. Synthesis of Co_3O_4-ZnO mixed metal oxide nanoparticles by homogeneous precipitation method, *J. Alloy Compd*. **2016**, 686, 64-73.

Sharma S.K., Bahadur J., Patil P.N., Maheshwari P., Mukherjee S., Sudarshan K., Majumder S., Pujari P.K. Revealing the nano-level molecular packing in chitosan-NiO nanocomposite by using positron annihilation spectroscopy and small angle X-ray scattering, *Chem. Phys. Chem*. **2013**, 14, 1055-1062.

Shuan L., Yan G., Lian W.S., Yu Z., Fen F.Y., Johnson D.M, Ping H.Y. Degradation of organic pollutants by a Co_3O_4-graphite composite electrode in an electro-Fenton-like system, *Chin. Sci. Bull*. **2013**, 58, 2340-2346.

Singh R.P.P., Hudiara I.S., Rana S.B. Effect of calcination temperature on the structural, optical and magnetic properties of pure and Fe-doped ZnO nanoparticles, *Mater. Sci.-Poland* **2016**, 34, 451-459.

Song X., Gao L. Facile Synthesis of Polycrystalline NiO Nanorods Assisted by Microwave Heating, *J. Am. Ceram. Soc*. **2008**, 91, 3465-3468.

Tang C.-W., Wang C.-B., Chien S.-H. Characterization of cobalt oxide studied by FT-IR, Raman, TPR and TG-MS, *Thermochim. Acta* **2008**, 473, 68-73.

Tu R., Li L., Zhang S., Chen S., Li J., Lu X. Carbon-modified mesoporous anatase/TiO_2 (B) whisker for enhanced activity in direct synthesis of Hydrogen Peroxide by Palladium, *Catalysts* **2017**, 7, 175-183.

Vogel F., Harf J., Hug A., Von Rohr R.P. The mean oxidation number of carbon (MOC)-A useful concept for describing oxidation processes, *Water Res.*, **2000**, 34, 2689-2702.

Wang A., Zhang Y., Zhong H., Chen Y., Tian X., Li D., Li J. Efficient mineralization of antibiotic ciprofloxacin in acid aqueous medium by a novel photoelectro-Fenton process using a microwave discharge electrodeless lamp irradiation, *J. Hazard. Mater*. **2018**, 342, 364-374.

Wang L., Zhang G., Liu Y, Li W., Lu W., Huang H. Facile synthesis of a mechanically robust and highly porous NiO film with excellent electrocatalytic activity towards methanol oxidation, *Nanoscale* **2016**, 8, 11256-11263.

Xavier S., Thankachan S., Jacob B.P., Mohammed E.M. Effect of sintering temperature on the structural and magnetic properties of cobalt ferrite nanoparticles, *Nanosystems: Phys. Chem. Math.* **2013**, 4, 430-437.

Xia S., Yu M., Hu J., Feng J., Chen J., Shi M., Weng X. A model of interface-related enhancement based on the contrast between Co_3O_4 sphere and cube for electrochemical detection of hydrogen peroxide, *Electrochem. Commun*. **2014**, 40, 67-70.

Yahya M.S., Oturan N., El Kacemi K., El Karbane M., Aravindakumar C.T., Oturan M.A. Oxidative degradation study on antimicrobial agent ciprofloxacin by electro-fenton process: Kinetics and oxidation products, *Chemosphere* **2014**, 117, 447-454.

Yang J., Liu H., Martens W.N., Frost R.L. Synthesis and characterization of cobalt hydroxide, cobalt oxyhydroxide, and cobalt oxide nanodiscs, *J. Phys. Chem. C* **2010**, 114, 111-119.

Zhang A., Liu M., Liu M., Xiao Y., Li Z., Chen J., Sun Y., Zhao J., Fang S., Jia D., Li F. Homogeneous Pd nanoparticles produced in direct reactions: green synthesis, formation mechanism and catalysis properties, *J. Mater. Chem. A* **2014**, 2, 1369-1374.

Chapter- 5

Implications of Co_3O_4 and NiO Nanoparticles for Electrocatalytic H_2O_2 Sensing

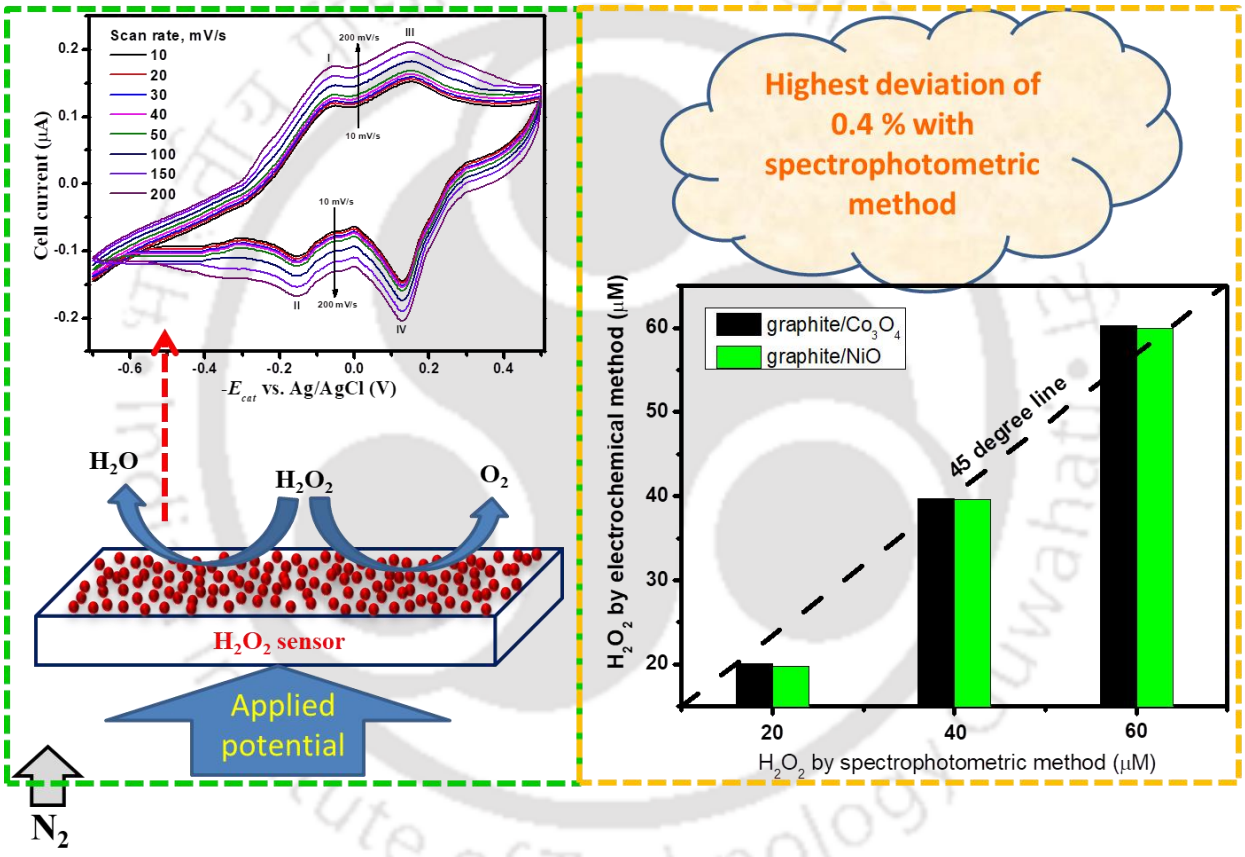

Chapter 5 investigates on H_2O_2 sensing catalysed by Co_3O_4 NPs, and the results obtained were then compared with NiO catalysed H_2O_2 sensing. The results obtained by the electrochemical method were further compared with the spectrophotometric method.

5.1 Specific background

Enzymes are most often used for H_2O_2 sensing, and horseradish peroxidase (HRP) is the most commonly used enzyme (Long et al., 2008), because it offers high sensitivity, selectivity, and faster response (Neal et al., 2017). However, the variation of solution pH and ionic strength, temperature, and exposure to light could cause irreversible loss of HRP activity (Neal et al., 2017). Immobilized HRP loses 60 % of its initial activity with the variation of 4 units of pH (8 to 4), and this loss could be up to 30 % with the change of temperature from 40 to 20 °C (Temocin and Yigitoglu, 2008).

So, various research groups have focused on the development of enzyme-free H_2O_2 sensors (Hao et al., 2016). Towards this goal, simple voltammetric and amperometric methods have been developed for the electrochemical H_2O_2 sensing (Chen et al., 2012). At the early stage of development, high overpotential of redox couple reactions and slow kinetics of electron transfer were the main drawback of this technique (Chen et al., 2012; Neal et al., 2017). These limitations are overcome in many extents with the development of nano-structured materials (Chen et al., 2012; Neal et al., 2017). The state-of-the-art literature for the synthesis metal and metal oxides NPs and its performance for catalysing H_2O_2 sensing in the last fifteen years are summarized in Tables 1.7 to 1.10 (Chapter 1). It is seen that the current research on H_2O_2 sensing is intensified towards electrode modifications for the reduction of overpotential and faster electron transport, but the sensitivity of the working electrode needs improvement, so that H_2O_2 can be detected at a lower concentration with a tiny electrode.

The metal oxides NPs such as Co_3O_4, CuO, NiO, and SnO_2 show a high electrocatalytic activity of H_2O_2 sensing and promote electron-transfer reactions with a lower overpotential (1.2 – 1.8 V) (Jia et al., 2009; Mahmoudiana et al., 2014). The synthesis of such materials is relatively easy and cheaper than noble metals and carbon nanostructures (Miao et al., 2017). Even, the sensors comprising of transition metals are capable of mediating the redox reactions of H_2O_2 sensing.

The cyclic voltammetric study for the electrocatalytic reduction of H_2O_2 was conducted in a phosphate buffer solution (PBS) solution at different concentrations of H_2O_2 to understand the reversibility and mechanism of redox reactions both on the graphite/Co_3O_4 and graphite/NiO NPs electrodes. The chronoamperometric analyses were performed to determine the performance of the modified electrodes for H_2O_2 determination. The close electro-active species, namely,

acetic acid, ascorbic acid, dopamine, ethanol, etc. were tested to study the selectivity of the modified electrode systems. H_2O_2 determination in Co_3O_4 and NiO NPs catalysed electrochemical method was then compared with the titanic sulphate spectrophotometric method at higher H_2O_2 concentration ($7 \leq H_2O_2 \leq 60$ mg/L).

5.2 Results and discussions

5.2.1 Catalytic activity of Co_3O_4 and NiO NPs in H_2O_2 sensing

5.2.1.1 Cyclic voltammetry and optimization of reaction condition

The cyclic voltammograms (CVs) recorded using the graphite and graphite/Co_3O_4 NPs electrodes are illustrated in Figure 5.1a. $-E_{cat}$ was varied from −0.5 to 0.5 V vs. Ag/AgCl with a

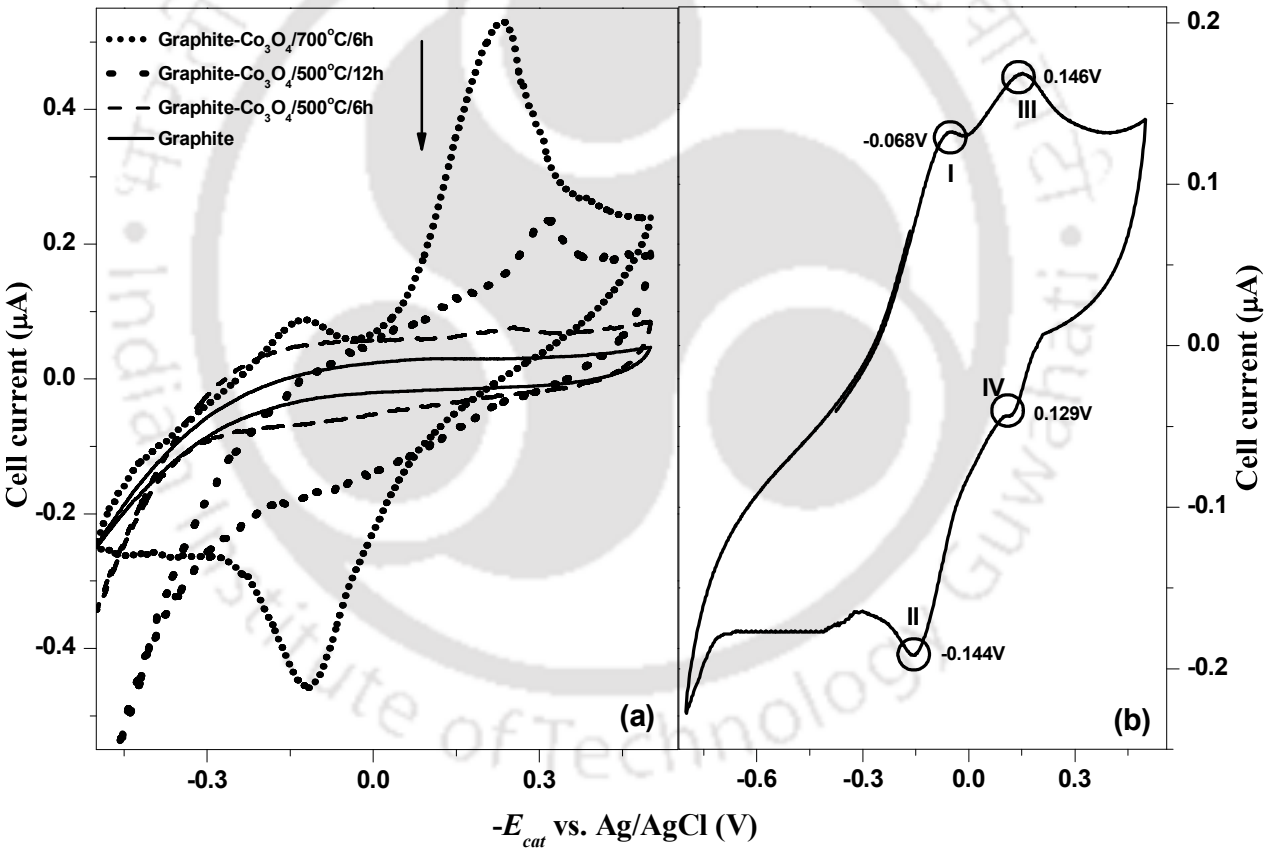

Figure 5.1: Cyclic voltammograms using graphite-Co_3O_4/700°C/6h, graphite-Co_3O_4/500°C/12h, graphite-Co_3O_4/500°C/6h electrode and bare graphite electrode with a scan rate of 50 mV/s, 0.1 M PBS, pH 7.2, N_2 flow rate 1.2 LPM, and electrolyte 190 mL: (a) in the presence of 1 mM H_2O_2, and (b) in the absence of H_2O_2.

scan rate of 50 mV/s. No redox peak was observed with the bare graphite and graphite-Co_3O_4/500°C/6h NPs electrodes. The graphite-Co_3O_4/500°C/12h electrode also didn't show any H_2O_2 reduction peak, but an oxidation peak at $-E_{cat}$= 0.30 V, and the cell current was also more compared to the graphite and graphite-Co_3O_4/500°C/6h NPs electrodes.

In contrast, a sharp H_2O_2 reduction peak appeared at $-E_{cat}$= –0.117 V with graphite-Co_3O_4/700°C/6h NPs electrode. The H_2O_2 oxidation peak was found at $-E_{cat}$=0.217 V with the evolution of tiny oxygen bubbles. Therefore, the further studies on of H_2O_2 sensing was carried out with the graphite-Co_3O_4/700^{o}C/6h NPs electrode.

Furthermore, the CV using the graphite-Co_3O_4/700°C/6h electrode was performed in 0.1 M PBS with a scan rate of 50 mV/s in the absence of H_2O_2 following the same procedure. The CV is shown in Figure 5.1b. In this case, two pairs of redox peaks were observed.

The anodic peaks, I and III imply the oxidation of $Co(OH)_2$ to Co_3O_4 and Co_3O_4 to CoOOH. The cathodic peaks, II and IV show the reduction of Co_3O_4 to $Co(OH)_2$ and CoOOH to Co_3O_4 (Eqs. 5.1 and 5.2). The oxidation or reduction peaks were recorded at −0.068 and −0.144 V vs. Ag/AgCl for the redox reaction 5.1. It was found at 0.146 V and 0.129 V vs. Ag/AgCl for the redox reaction 5.2 (Helia and Pishahang, 2014).

$$Co_3O_4 + 4H_2O + 2e^- \leftrightarrow 3Co(OH)_2 + 2OH^- \quad (5.1)$$

$$3CoOOH + e^- \leftrightarrow Co_3O_4 + OH^- + H_2O \quad (5.2)$$

The CVs with the graphite-Co_3O_4/700°C/6h electrode with different scan rates in the absence of H_2O_2 are recorded as shown in Figure 5.2. At a lower scan rate (< 200 mV/s), both the anodic peak current (I_{pa}) and cathodic peak current (I_{pc}) were increased gradually with the increase in scan rate, and a fairly linear relationship was observed for both the redox couple reactions (Figures 5.3a and 5.3b). The mean value of surface concentration of cobalt redox species were estimated as 5.92×10^{-13} mol/cm^2 taking the average values of the slopes from the linear fit (Figures 5.3a and 5.3b) using the Brown-Anson equation (Eq. 5.3) (Nenkova et al., 2017).

$$I_p = \frac{n^2F^2\nu A\Gamma}{4RT} \quad (5.3)$$

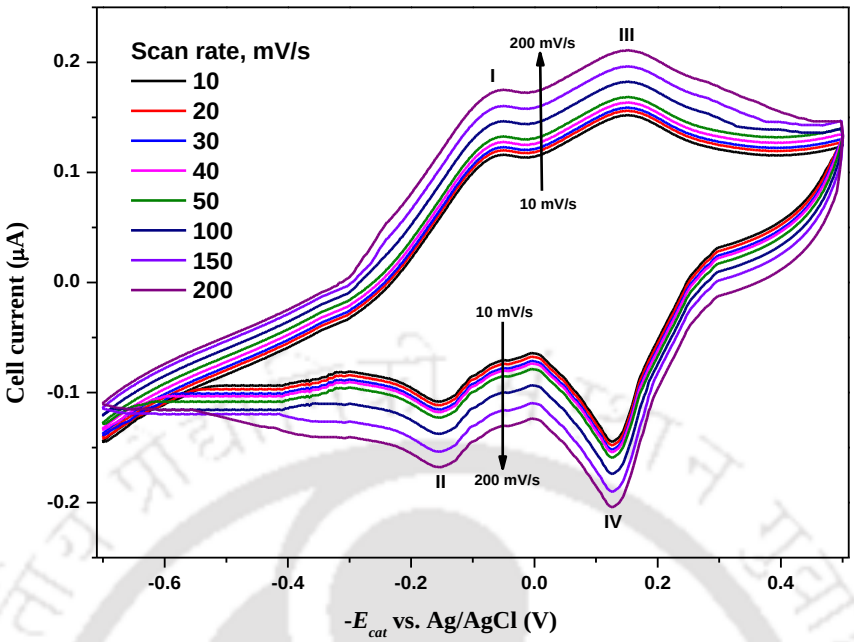

Figure 5.2: Cyclic voltammograms of graphite-Co_3O_4/700°C/6h electrode with different scan rates by sweeping from $-E_{cat}$= 0.5 to −0.7 V vs. Ag/AgCl, 0.1 M PBS, N_2 flow rate 1.2 LPM, and electrolyte 190 mL in the absence of H_2O_2.

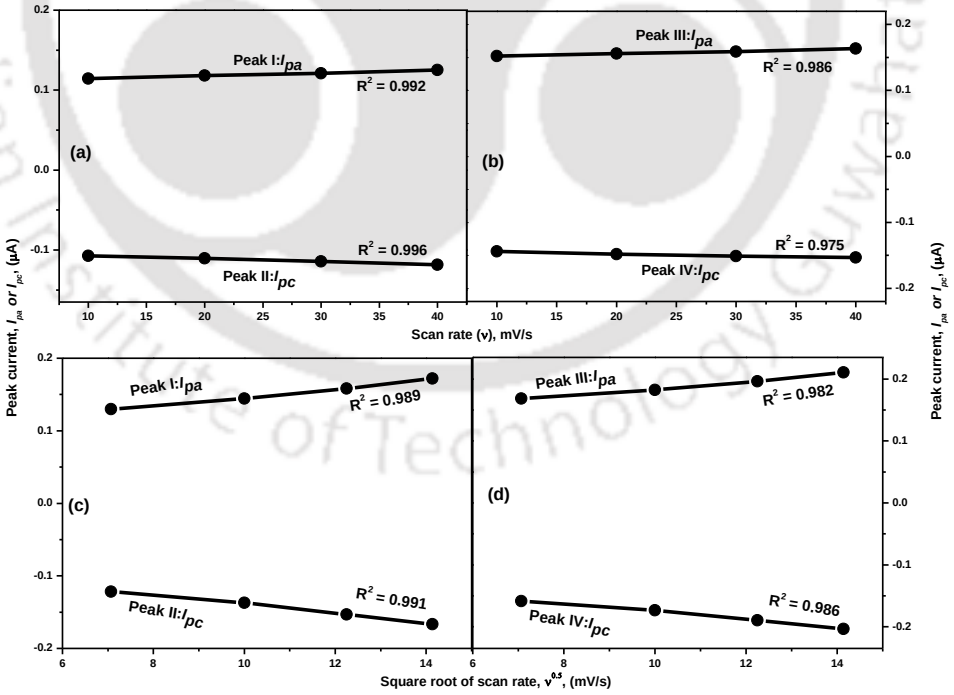

Figure 5.3: Variation of redox peak current with scan rate (ν) (a and b), and square root of scan rate ($\nu^{0.5}$) (c and d) for graphite-Co_3O_4/700°C/6h electrode in the absence of H_2O_2.

Where, I_p is the peak current (A), n is the number of electrons transferred per ion, F is Faraday's constant (96485 C/mol), v is the scan rate (V/s), A is the electrode surface area (cm^2), Γ is the surface concentration of the redox species (mol/cm^2), R is the universal gas constant (8.314 J/K/mol), and T is the reaction temperature (K). For the scan rates between 50 and 100 mV/s, both the anodic and cathodic peak currents were increased linearly with the square root of v which was on the basis of the Randles–Sevcik equation (Eq. 5.4) (Bard and Faulkner, 2001). It implies that the redox reactions were controlled by OH^- ion diffusion from the bulk to cobalt oxide/electrode surface (Figures 5.3c and 5.3d). Furthermore, both redox reactions were found to be quasi-reversible as the ratio of I_{pa}/I_{pc} ranged between 1.03 and 1.07.

$$I_p = 0.44nFAD^{1/2}(\frac{vF}{RT})^{1/2}C_s \qquad (5.4)$$

Where, D and C_s are the diffusion coefficient (cm^2/s) and the bulk concentration of substrate (H_2O_2, mol/cm^3), respectively, and other symbols have their usual meanings.

The peak current was increased with the increase in H_2O_2 concentration from 1 to 1000 µM (Figure 5.4a) as the redox reactions are diffusional controlled even at a higher H_2O_2 concentration, and the current recorded was not linear. However, the peak potential was independent of the concentration of H_2O_2. The CV curves at scan rates of 1, 10, 30, 50 and 100 mV/s are presented in Figure 5.4b. Both I_{pa} and I_{pc} were gradually increased with the increase in the scan rate. I_{pa} and I_{pc} was also increased linearly with the square root of the scan rate ($v^{0.5}$) in the range of 1-100 mV/s (Figure 5.5a). It supports that the redox reaction is controlled by the diffusion of H_2O_2 from bulk to the electrode/solution interface in PBS (Salimi et al., 2007). Furthermore, the peak currents were also increased with the increase in scan rate due to surface controlled reaction (Figure 5.5b). The ratio of I_{pa}/I_{pc} lied between 1.03 and 1.10 for different scan rates which is indicative of a quasi-reversible electrochemical system catalysed by Co_3O_4 NPs (Haque et al., 2013; Helia and Pishahang, 2014). With the increase in the scan rate, I_{pa} peak position was shifted slightly towards the positive potential and, I_{pc} peak was shifted slightly towards the negative potential due to sluggish electron movement and there is a perceptible time lag between the potential at the voltage source (here potentiostat) and that at the electrode-solution interface (Monk, 2010).

The enhancement of H_2O_2 reduction and oxidation reactions was resulted from a better electron transport process at H_2O_2/electrode interface due to the electrocatalytic activity of Co_3O_4

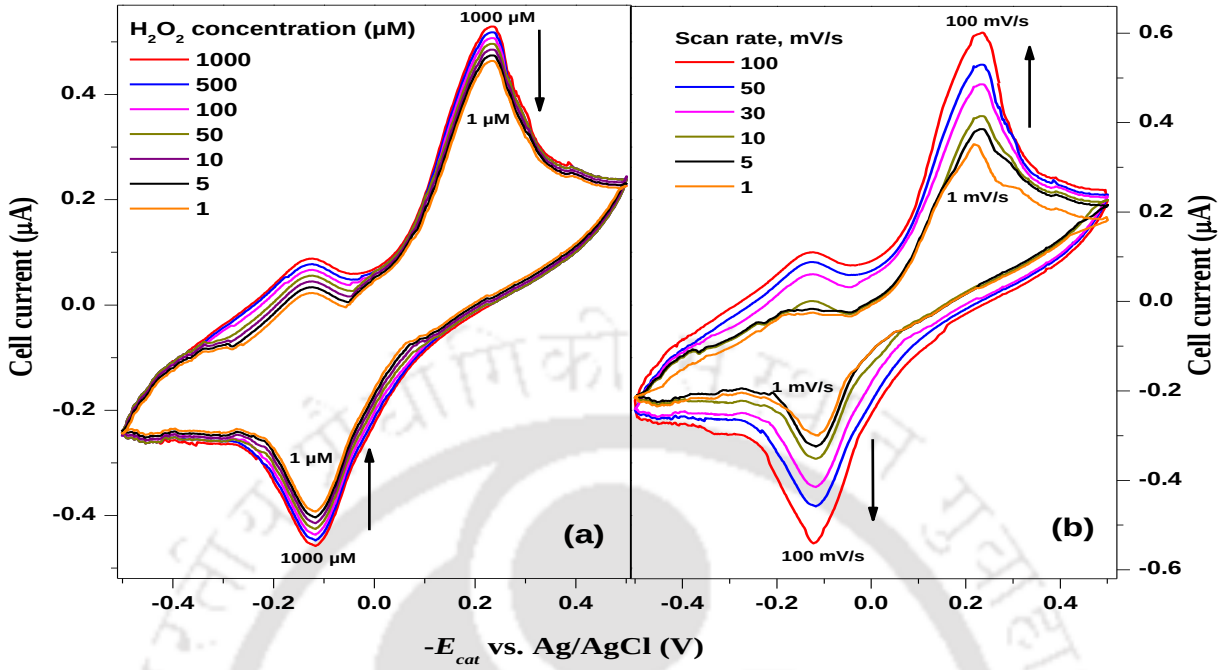

Figure 5.4: Cyclic voltammograms at (a) different H_2O_2 concentrations with a scan rate of 50 mV/s and (b) different scan rates in 1 mM H_2O_2, using graphite-Co_3O_4/700°C/6h electrode by sweeping from 0.5 to −0.5 V vs. Ag/AgCl, 0.1 M PBS, pH 7.2, N_2 flow rate 1.2 LPM, and electrolyte 190 mL.

NPs synthesized using a bio-mediated process. H_2O_2 could be reduced to water by Co_3O_4, and it is oxidized to CoOOH (Eq. 5.5) (Salimi et al., 2007; Helia and Pishahang, 2014). On the other hand, CoOOH further could oxidize H_2O_2 to oxygen (Eq. 5.6).

$$2Co_3O_4 + 4H_2O + H_2O_2 \rightarrow 6CoOOH + 2H_2O \quad (5.5)$$

$$6CoOOH + H_2O_2 \leftrightarrow 2Co_3O_4 + 4H_2O + O_2 \quad (5.6)$$

Like the graphite/Co_3O_4 NPs electrode, the CVs of the graphite/NiO NPs electrode was recorded by sweeping from $-E_{cat}$ = 0.32 to 0.48 V vs. Ag/AgCl in 0.1 M PBS in the absence of H_2O_2 (Figure 5.6) and also in the presence of H_2O_2 (Figure 5.7). The distinct redox peaks were observed in the absence of H_2O_2 (Figure 5.6a). The anodic peak was found at 0.195 V (Eq. 4.11), and the cathodic peak was at $-E_{cat}$ = –0.08 V (Eq. 4.12). The CVs was then recorded at different scan rates (10-200 mV/s) in the absence H_2O_2 (Figure 5.6a). In fact, the peak currents (I_{pa} and I_{pc}) were gradually increased with the increase in scan rate (Figure 5.6a). At a lower scan rate (< 50 mV/s), both I_{pa} and I_{pc} (I_{pa}/I_{pc}= 1.00 to 1.03) were increased linearly with the scan rate (v),

suggesting that the redox reactions were controlled by the surface reaction (surface confined redox reaction) (Figure 5.6b). The peak currents were also increased linearly with the square root of scan rate ($\nu^{0.5}$) at a higher scan rate (> 50 mV/s, I_{pa}/I_{pc}= 1.01 to 1.05). It indicates that the redox reactions were controlled by OH^- ions diffusion (Figure 5.6c) (Section 4.2.2.1, Chapter 4).

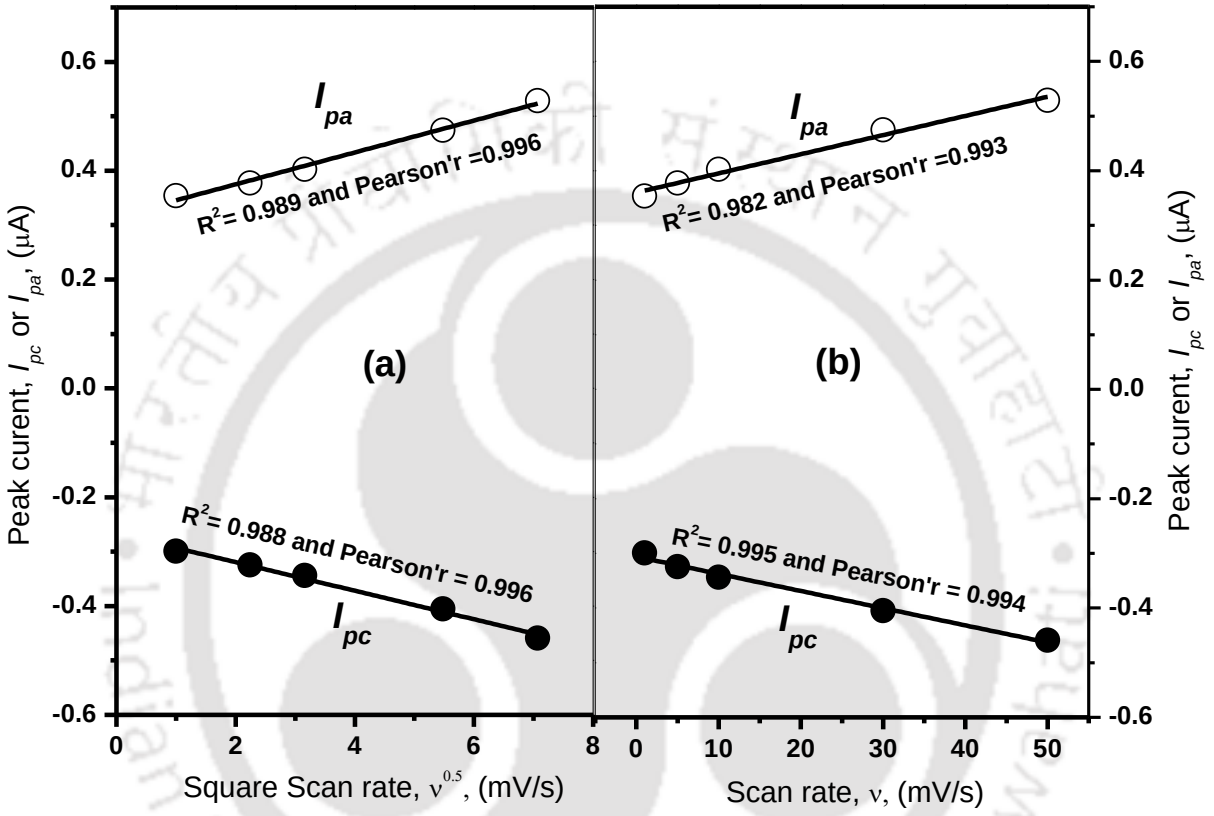

Figure 5.5: Variation of redox peak current with (a) square scan rate ($\nu^{0.5}$) and (b) scan rate for graphite-Co_3O_4/700°C/6h electrode in the presence of 1 mM H_2O_2.

When H_2O_2 was present in the PBS, the H_2O_2 reduction peak appeared at $-E_{cat}$ =– 0.129 V and oxidation peak at 0.220 V at a scan rate of 50 mV/s (Figure 5.7a). Therefore, there is a clear peak separation between the redox couple reactions of Ni-species and H_2O_2 in the case of the graphite/NiO NPs electrode. I_{pa} and I_{pc} were increased linearly with $\nu^{0.5}$. So, H_2O_2 reduction took place under the diffusion control from the bulk solution to the electrode/solution interface. Like Co_3O_4 NPs catalysed H_2O_2 sensing (Eqs. 5.5 and 5.6), H_2O_2 was reduced to water by NiO (Eq. 5.7) and was oxidized to oxygen (Eq. 5.8). The ratio I_{pa} to I_{pc} with different scan rates was found between 1.02 and 1.05 which indicates a quasi-reversible H_2O_2 redox system (Helia and

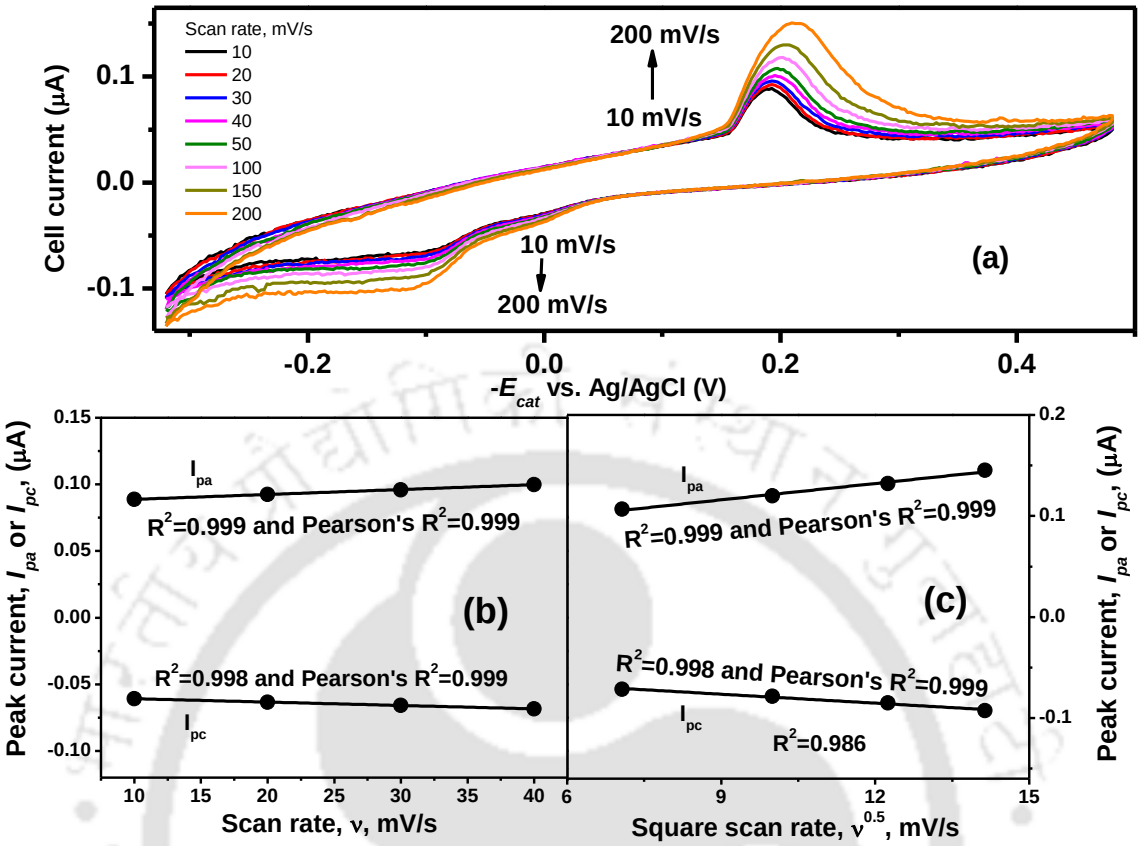

Figure 5.6: (a) Cyclic voltammograms with different scan rates in the absence of H_2O_2, (b) variation of redox peak current with scan rates (ν) without H_2O_2, and (c) variation of redox peak current with square root of scan rates ($\nu^{0.5}$) without H_2O_2 in the case of graphite/NiO NPs electrode by sweeping from 0.32 to −0.48 V vs. Ag/AgCl, 0.1 M PBS, pH 7.2, N_2 flow rate 1.2 LPM, and electrolyte 190 mL.

Pishahang, 2014). The concentration of the analyte was varied from 1 to 1000 µM, and the results are shown in Figure 5.7d. At a higher H_2O_2 concentration, Ni(II) oxidation to Ni(III) (Eq. 5.7) was faster in the cathodic cycle, and a higher reduction peak current was observed (Kamyabi and Hajari, 2017). On the other hand during the anodic scan, Ni(III) was reduced to Ni(II) by H_2O_2 (Eq. 5.8) giving a higher oxidation peak current (Helia and Pishahang, 2014).

$$2NiO + 2H_2O + H_2O_2 \rightarrow 2NiOOH + 2H_2O \quad (5.7)$$

$$2NiOOH + H_2O_2 \rightarrow 2NiO + 2H_2O + O_2 \quad (5.8)$$

The overpotential of H_2O_2 oxidation was found to be 0.675 V with the graphite-Co_3O_4/700°C/6h electrode. On the other hand, the overpotential of H_2O_2 reduction was found to

be 1.843 V which was close to the earlier reports (Table 5.1). In the case of NiO catalysed electrode, the overpotential of H_2O_2 reduction and oxidation were obtained as 1.831 and 0.672 V, respectively (Table 5.1).

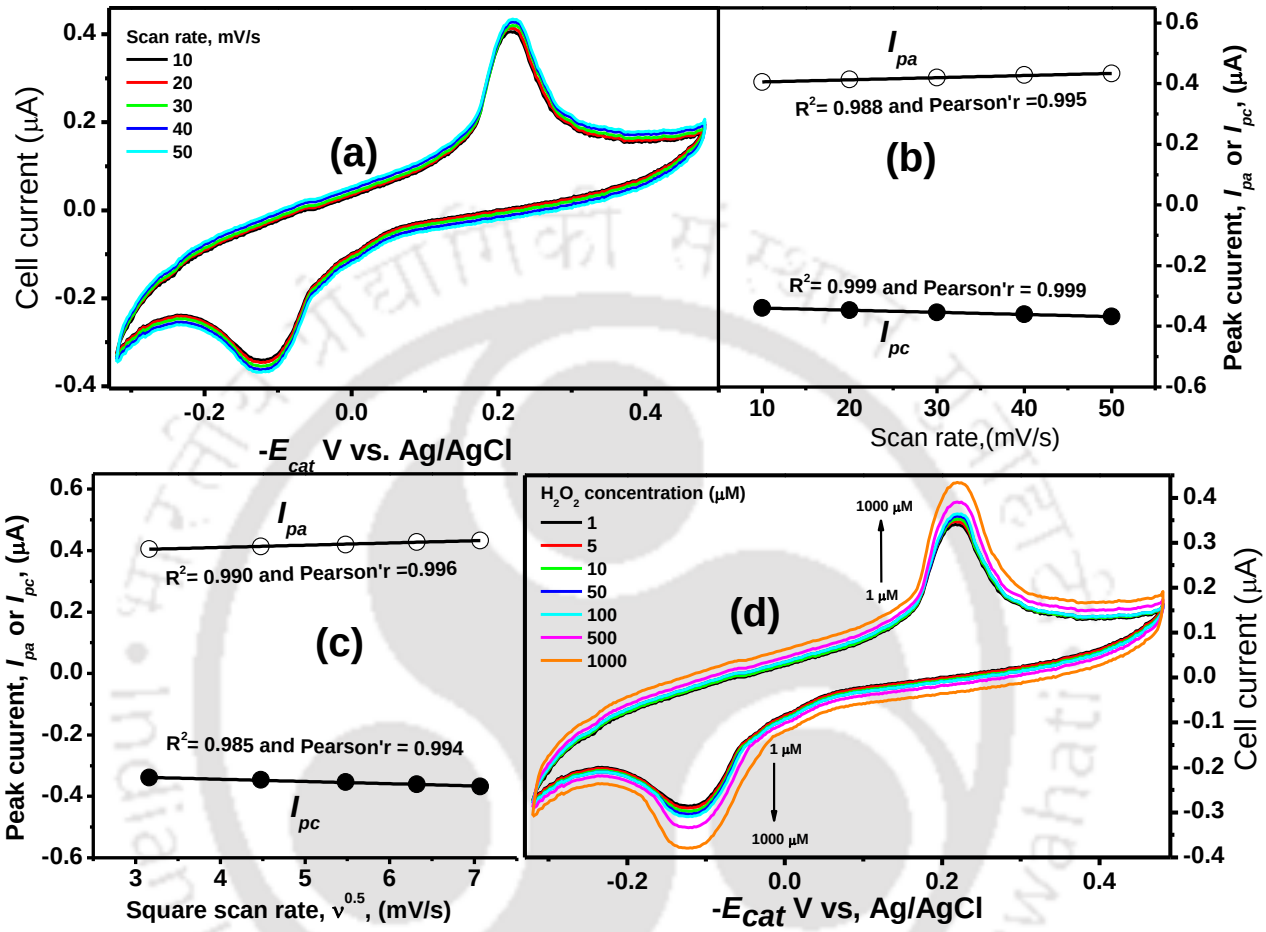

Figure 5.7: (a) Cyclic voltammograms with different scan rates in the presence of 1 mM H_2O_2, (b) variation of redox peak current with scan rates (ν) with 1 mM H_2O_2 and (c) variation of redox peak current with square root of scan rates ($\nu^{0.5}$) with 1 mM H_2O_2, and (d) cyclic voltammograms with different H_2O_2 concentration in the case of graphite/NiO NPs electrode by sweeping from 0.32 to −0.48 V vs. Ag/AgCl, 0.1 M PBS, pH 7.2, N_2 flow rate 1.2 LPM, and electrolyte 190 mL.

Table 5.1: Comparison of overpotential of H_2O_2 redox system using Co_3O_4 modified graphite electrodes.

H_2O_2 redox system	**Peak potential, V vs. Ag/AgCl**	**Overpotential, V**	**Catalyst used**	**Source**
Reduction	– 0.2	1.76	Co_3O_4 nanowalls	Jia et al., 2009
Oxidation	+ 0.8	0.092		
Reduction	– 0.3	1.66	Nano-NiO_x	Noorbakhsh and Salimi, 2009
Oxidation	--	--		
Reduction	– 0.35	1.61	NiO NPs	Qiu et al., 2010
Oxidation	– 0.29	0.602		
Reduction	+0.8	1.16	NiO NPs	Jandai et al., 2011
Oxidation	--	--		
Reduction	--	--	Co_3O_4 NPs	Hou et al., 2012
Oxidation	+ 0.373	0.618		
Reduction	– 0.19	1.77	Multiwalled carbon nanotubes	Helia and Pishahhang, 2014
Oxidation	+ 0.19	0.702		
Reduction	– 0.7	1.26	Co_3O_4 NPs	Su et al., 2016
Oxidation	+ 0.5	0.392		
Reduction	**– 0.117**	**1.843**	**Co_3O_4 NPs**	**Present study**
Oxidation	**+ 0.217**	**0.675**		
Reduction	**– 0.129**	**1.831**	**NiO NPs**	
Oxidation	**+ 0.220**	**0.672**		

5.2.1.2 Real H_2O_2 sample analysis and interference in H_2O_2 sensitivity

The performance of the graphite-Co_3O_4/700°C/6h electrode for the determination of H_2O_2 was studied by the amperometric method. Figure 5.8 shows the amperometric responses on the successive addition of H_2O_2 in an interval of 50 s at $-E_{cat}$=–0.117 V with a scan rate of 50 mV/s. H_2O_2 concentration of 1 μM was used for the successive addition. The addition of H_2O_2 resulted in an apparent increase of the cell currents (magnitude), and reached to steady-state signals within 5 s owing to a faster transport of H_2O_2 from the bulk solution to the active sites of the

electrode (Cheng et al., 2014; Haque et al., 2013). The calibration curve is presented in Figure 5.9 and the cell current was found to very linearly (R^2=0.99) even up to 3500 s (Figure 5.9).

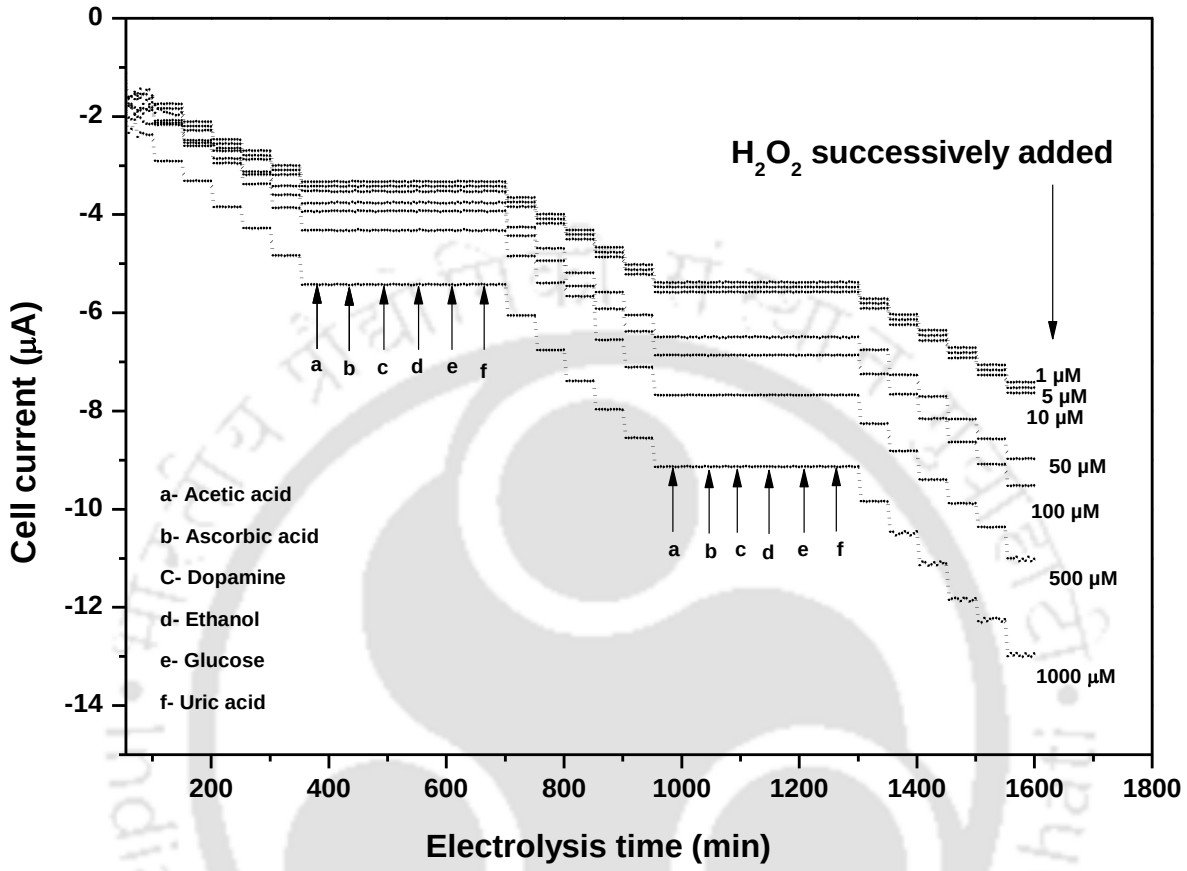

Figure 5.8: Amperometric response of graphite-Co_3O_4/700°C/6h electrode on successive addition of different concentration of H_2O_2 along with the effect of different interfering compounds added at the same concentration of H_2O_2 in 0.1 M PBS at $-E_{cat}$= -0.117 V vs. Ag/AgCl.

The limit of detection (LOD) and the limit of quantification (LOQ) were determined using Eqs. 5.8 and 5.9 (Marimuthu et al., 2014). Where, S_b is the standard deviation determined with 10 blank solutions, and b is the slope of the analytical curve. LOD and LOQ were found to be 0.0217 and 0.065 μM. H_2O_2 decomposition was found to be insignificant (~0.19 %) after 3500 s of electrolysis. The electrode sensitivity refers to the concentration range of analyte in which the sensor signal is linearly proportional to the concentration, and it was found to be 65.32 nA/μM/cm^2.

$$LOD = \frac{3S_b}{b} \quad (5.9)$$

$$LOQ = \frac{10S_b}{b} \quad (5.10)$$

The selectivity of the graphite-Co_3O_4/700°C/6h electrode towards H_2O_2 detection was tested by adding acetic acid, ascorbic acid, dopamine, glucose, and uric acid with a concentration of 0.1 mM to cause an interference effect. The experiment was started following a typical amperometric procedure with the successive addition of 1 mM H_2O_2 in 0.1 M PBS at $-E_{cat}$=-0.117 V, and then the interfering compounds were added in between 400 and 700 s, and 1000 and 1300 s (Figure 5.8). The results show that these compounds were unable to alter the response current of the graphite-Co_3O_4/700°C/6h electrode. It signifies a great selectivity of the electrode for H_2O_2 determination because of a lower overpotential of 1.843 V.

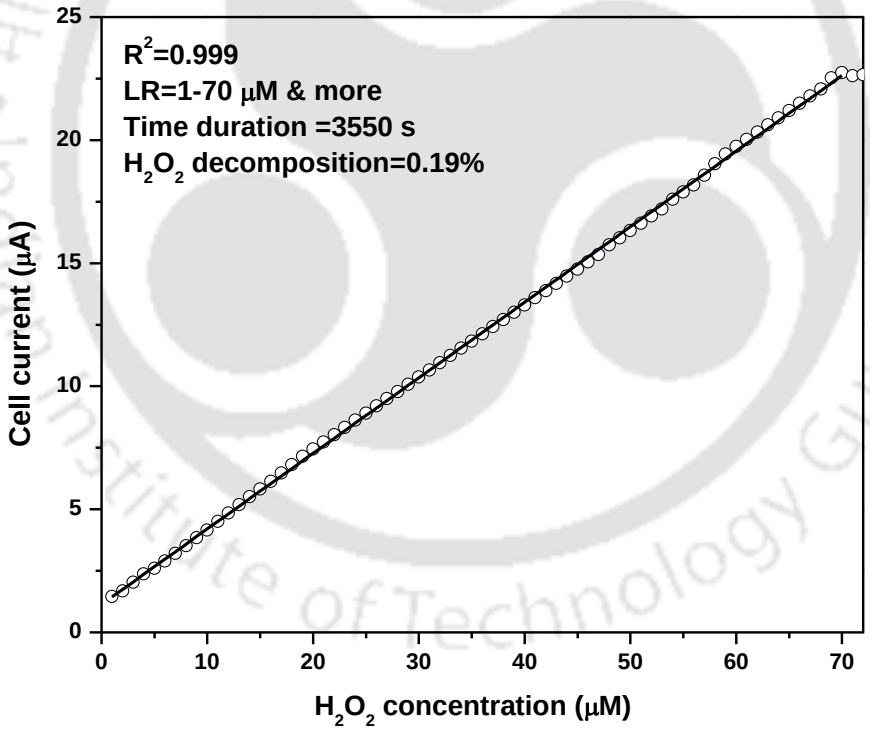

Figure 5.9: Calibration curve of current versus H_2O_2 concentration with successive addition of 1 μM H_2O_2 in 0.1 M PBS at $-E_{cat}$=-0.117 V vs. Ag/AgCl electrode in the case of graphite/Co_3O_4 NPs electrode.

The reproducibility and repeatability of the graphite-Co_3O_4/700°C/6h electrode were also studied (Figures 5.10a and 5.10b). The cell current obtained with five fresh graphite-Co_3O_4/700°C/6h electrodes at $-E_{cat}$=-0.117 V vs. Ag/AgCl was highly reproducible (relative standard deviation, rsd, 3.06 %) (Figure 5.10a). The repeatability experiment of the same electrode was carried out for the detection of 1000 µM H_2O_2 with five consecutive runs, and the electrode response was well within rsd of 1.72 % (Figure 5.10b).

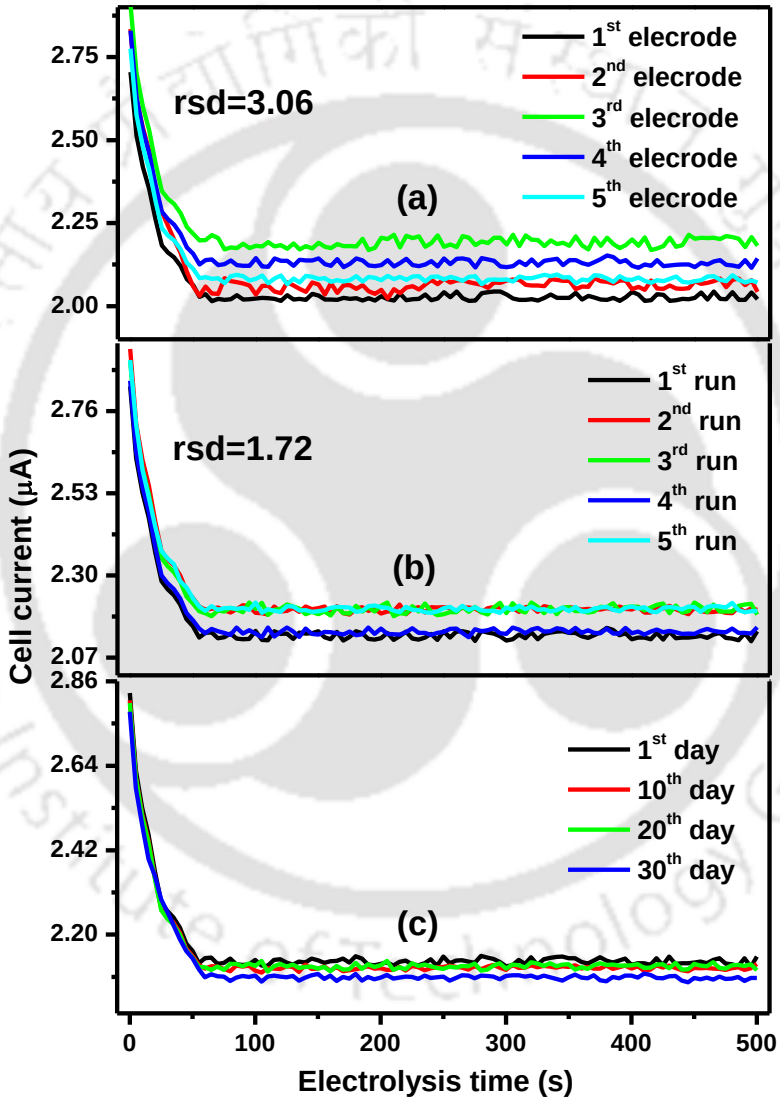

Figure 5.10: (a) Stability test of graphite/Co_3O_4 electrode in an interval of 10 days up to 1 month, (b) cell current variation time with five fresh graphite/Co_3O_4 electrodes, and (c) five consecutive runs with 1000 µM H_2O_2 with the same electrode at $-E_{cat}$=-0.117 V vs. Ag/AgCl.

The graphite-Co_3O_4/700°C/6h electrode was stored at room temperature for 4 weeks, and then this electrode was used to record the CV with 1000 µM H_2O_2 keeping other experimental condition same as in Figure 5.10c. The result shows that the electrode could supply 94 % of its initial cell current at $-E_{cat}$=-0.117 V implying its excellent electro-stability (Zhang et al., 2013).

For the amperometric experiment in the case of NiO NPs catalysed H_2O_2 sensing, an amount of 1 µM H_2O_2 was added successively in the PBS in an interval of 50 s at $-E_{cat}$ = –0.129 V with a scan rate of 50 mV/s. There was a quick step-wise increase (magnitude) in response current with the successive addition of H_2O_2, and the cell current reached a steady valley within 5 s (Figure 5.11a), because of a rapid transport of H_2O_2 from the bulk solution to the electrode surface. The response current varied linearly with the increase in H_2O_2 concentration up to 58 µM with a good correlation efficient (R^2 = 0.99) (Figure 5.11b). The graphite/NiO NPs electrode exhibited the LOD (Eq. 5.8) of about 0.0271 µM and LOQ (Eq. 5.9) of 0.0819 µM with a sensitivity of 62 nA/µM/cm^2.

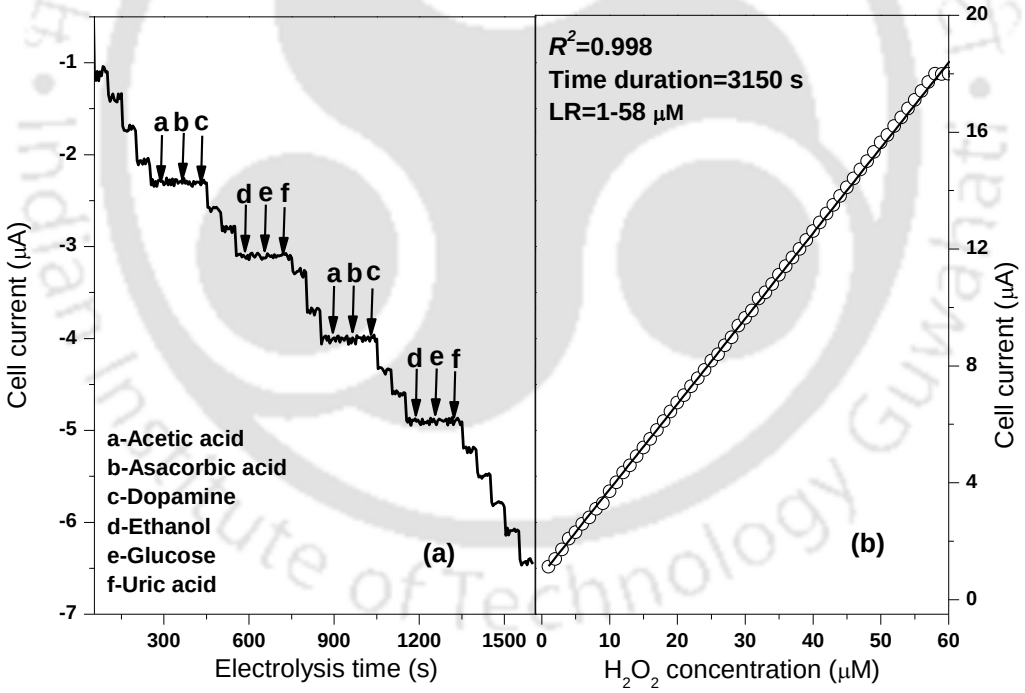

Figure 5.11: (a) Amperometric response of graphite/NiO NPs electrode on successive addition of 1 µM H_2O_2 along with the effect of different interfering compounds added at 0.1 mM concentration of H_2O_2 in 0.1 M PBS solution at $-E_{cat}$ = –0.129 V, and (b) calibration curve of current versus H_2O_2 concentration with successive addition of 1 µM H_2O_2 at $-E_{cat}$ = –0.129 V in the case of graphite/NiO NPs electrode.

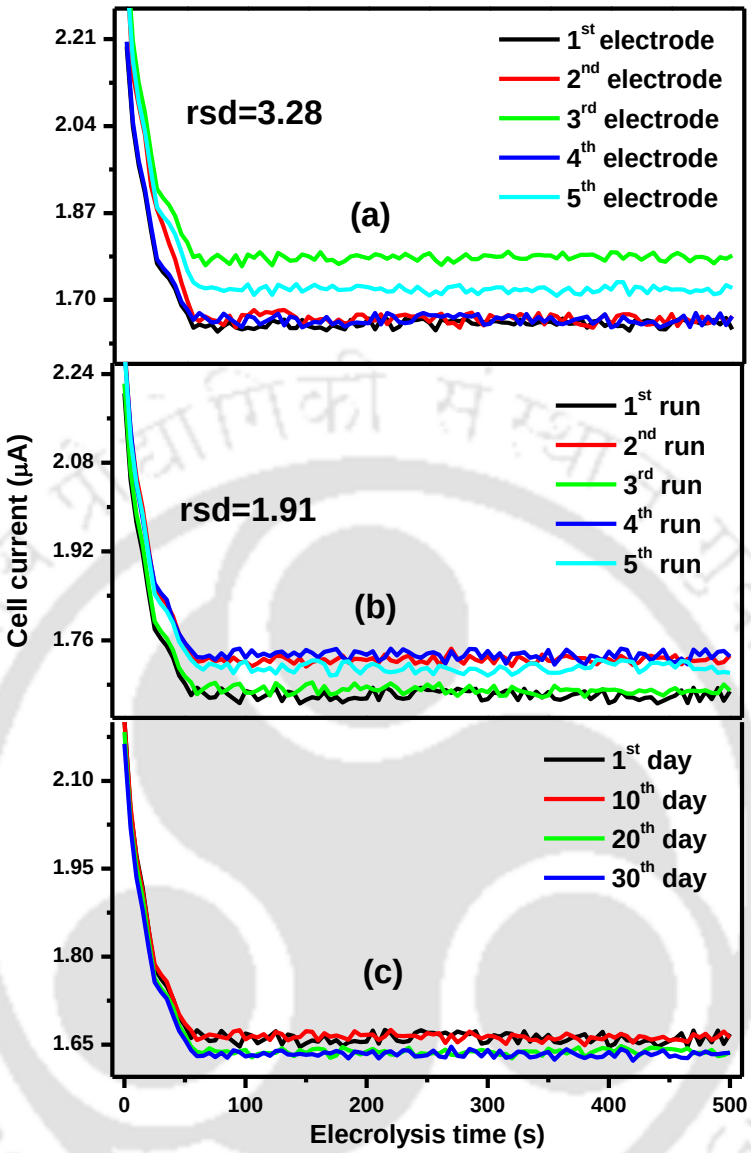

Figure 5.12: (a) Stability test of graphite/NiO electrode in an interval of 10 days up to 1 month, (b) cell current variation time with five fresh graphite/NiO electrodes, and (c) five consecutive runs with 1000 μM H_2O_2 with the same electrode at $-E_{cat}$= –0.129 V vs. Ag/AgCl

To investigate the selectivity of the graphite/NiO NPs electrode, an amount of 0.1 mM close electro-active species, namely, acetic acid, ascorbic acid, dopamine, ethanol, glucose and uric acid (Salazar et al., 2017) added at different time intervals as shown in Figure 5.11a. Successive addition of 1.0 mM H_2O_2 was examined with 0.1 mM concentration of each of the interfering compounds in 0.1 PBS solution. The graphite/NiO NPs electrode also exhibited an

excellent selectivity towards the analytes, H_2O_2, like the graphite/NiO NPs electrode (Kamyabi and Hajari, 2017).

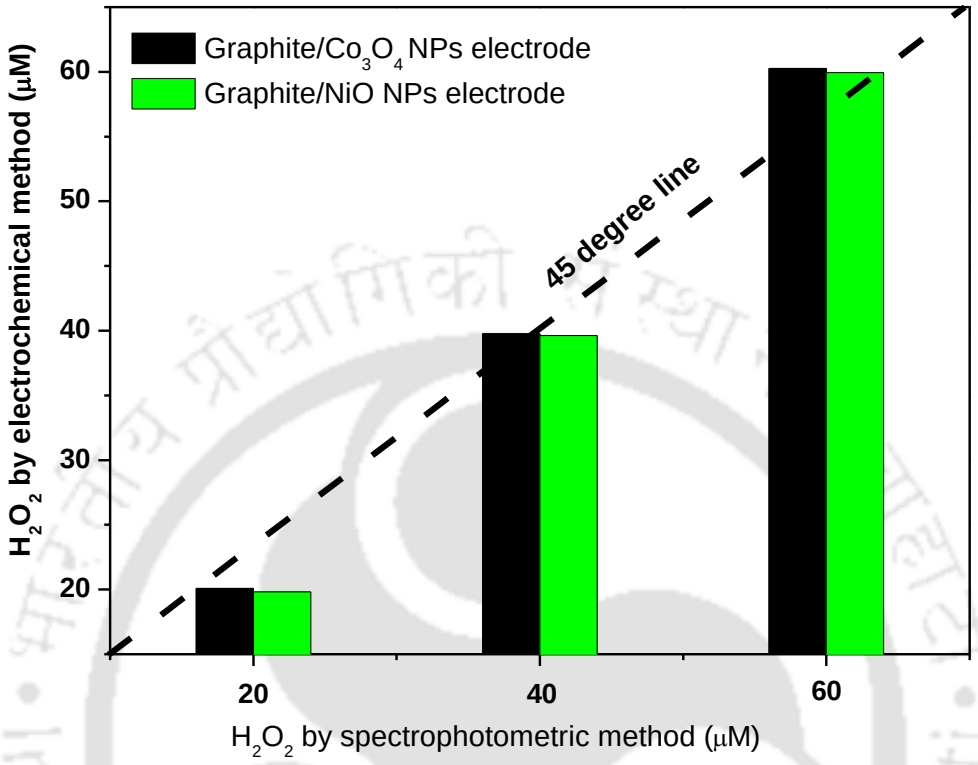

Figure 5.13: Parity plot of H_2O_2 concentration measured by electrochemical method vs. H_2O_2 measured by the spectrophotometric method (electrochemical determination at graphite/Co_3O_4 NPs electrode ($-E_{cat}$=-0.117 V vs. Ag/AgCl electrode) and graphite/NiO NPs electrode ($-E_{cat}$=-0.129 V vs. Ag/AgCl electrode) in 0.1 M PBS.

Furthermore, the reproducibility and repeatability of the graphite/NiO NPs electrode were tested following the similar procedure as with the graphite/Co_3O_4 NPs electrode (Figures 5.12a and 5.12b). We find that the performance of the graphite/NiO NPs electrode was also reproducible with a rsd of 3.28 % (Figure 5.12a). H_2O_2 sensing was repeatable with rsd of 1.91 % from 5 successive runs using 1000 μM H_2O_2 for every run (Figure 5.12b). The long-term stability of NiO NPs catalysed systems was also evaluated through H_2O_2 sensing (1000 μM H_2O_2 sensed in 55 cycles in each interval) at an interval of 10 days for a period of one month (total 220 cylces) under the same experimental conditions (Figure 5.12c). The electrode was rinsed in distilled water and stored at room temperature when it was not used during the stability test.

There was a reduction of 6 % in the response current after one month compared to the fresh electrode (Qiu et al., 2010). .

The concentration of H_2O_2 in three different samples containing the same concentration was determined using this calibration curve and the results are shown in Figure 5.13. The corresponding variations of cell currents with H_2O_2 concentration are shown in Figure 5.14. The highest deviation of 0.4 % was observed with the graphite/Co_3O_4 NPs electrode in comparison to the concentration measured by the spectrophotometric method. It was 0.46 % with the graphite/NiO NPs electrode.

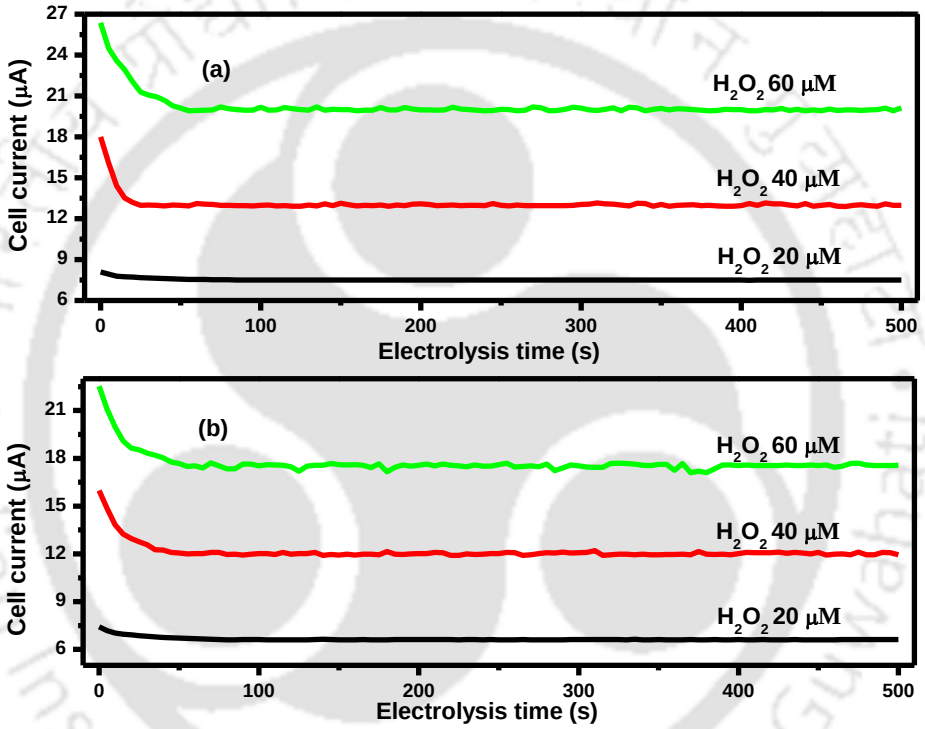

Figure 5.14: Cell current variation with (a) graphite/Co_3O_4 NPs ($-E_{cat}$=-0.117 V vs. Ag/AgCl electrode) and (b) graphite/NiO NPs ($-E_{cat}$=-0.129 V vs. Ag/AgCl electrode) electrodes for three different H_2O_2 samples measured by electrochemical method in 0.1 M PBS.

Table 5.2 summarizes the performance of the graphite-Co_3O_4/700°C/6h electrode and its comparison with electrochemical sensors modified with the Co_3O_4 spinel structures synthesized in various processes for H_2O_2 detection. The bio-mediated synthesized Co_3O_4 NPs exhibited a low detection limit, broad linear range, fast response time, and good selectivity and stability for H_2O_2 sensing due to having the excellent electrocatalytic ability even without using specialized Co_3O_4 NPs structures and carbonaceous materials. In fact, the LOD and sensitivity of graphite-

Co_3O_4/700°C/6h electrode were much lower than the electrodes modified using other type of nanomaterials for the same or for a lower amperometric response time (Table 5.3). It also can be seen that graphite-Co_3O_4/700°C/6h electrode exhibited a reasonably lower reduction potential for H_2O_2 sensing. A comparison of H_2O_2 sensing catalysed by NiO NPs in the present work with the earlier reports is provided in Table 5.4. The bio-inspired NiO NPs catalysed H_2O_2 sensing at a lower potential and limit of detection with a high sensitivity compared to the most of the earlier reports.

Table 5.2: Performance comparison with graphite-Co_3O_4/700℃/6h electrode (present study) with earlier reports using Co_3O_4.

Modified graphite substrate	**-E_{cat} (V)**	**LOD (μM)**	**LR (mM)**	**Sensitivity (nA/μM/cm^2)**	**AR (s)**	**Co_3O_4 synthesized process**	**Source**
Co_3O_4/CF-0.5	–4.8	85	0.02-1.15	-	~ 10	Hydrothermal and annealing	Liu et al., 2014
Co_3O_4/CF-1	–4.8	1.4	0.01-1.05	-	≤ 3		
Co_3O_4/CF-2	–4.8	4.5	0.01-0.4	230	≤ 3		
Co_3O_4 NPs/GC	–0.2	10	0-5.35	80.74	~ 10	Direct heating of Co foil on a hot-plate	Jia et al., 2009
Co_3O_4 thin film/ITO	–1.0	0.2 mM	0-1.2	1.357×10^3	~ 2	Electrodeposition method	Cao et al. 2014
Co_3O_4 /FTO	0.50	0.36	0-2	66.29	-	Chemical bath deposition	Kung et al., 2011
Co_3O_4 /GC	0.75	0.4 nM	-	4860	<2	Electrodeposition method	Salimi et al., 2007
Co_3O_4 NPs	–0.7	4.4	0.01–4	-	~ 10	Chemical reaction method	Mu et al., 2013
Co_3O_4/CoTRP (GC)	+0.3	0.2	-	-	-	Electrochemical oxidation	Quintino et al., 2005
Co_3O_4/MWCNTs	–0.19	2.46	0.02–0.43	1002.8	-	Microwave decomposition	Helia and Pishahang, 2014
Co_3O_4 cube	+0.453	1.208	0.04–2.88	211.5	~2	Hydrothermal method	Xia et al., 2014
Co_3O_4 /GC	-0.7	0.7	0.005-0.35	6.4 mA/mM	-	Photochemical	Su et al., 2016
Co_3O_4 NPs/graphite	**–0.117**	**0.0217**	**0.001-0.07**	**65.32**	**<5**	**Bio-mediated**	**Present work**

-E_{cat} vs. Ag/AgCl, LOD: Limit of detection, LR: Linear range, AR: Amperometric response, CF: Carbon fiber, NPs: Nanoparticles, ITO: Indium tin oxide, FTO: Fluorine doped tin oxide, GC: Glassy carbon, CNTs: Carbon nanotubes, CoTRP: tetraruthenated cobalt-porphyrin

Table 5.3: Performance comparison with graphite-Co_3O_4/700℃/6h electrode (present study) with earlier reports using other type of nanomaterial–modified electrode for H_2O_2 sensing.

Modified graphite substrate	-E_{cat} (V)	LOD (μM)	LR (mM)	Sensitivity (nA/μM/cm^2)	AR (s)	Nanoparticles synthesized process	Source
G-Fe_2O_3-CS/GCE	–0.30	1.1	0.001-6.0	84.32 μA/mM	~2	Solid-phase method in SLS	Hao et al., 2016
PDDA-G/Fe_3O_4	–0.4	2.5	0.02–6.25	61.2 ×10^3	--	Massart's method	Liu et al., 2011
ZnO nanorods	1.1	42	1-15	--	--	Chemical reaction method	Salih et al., 2016
CuO NFS/Nafion-Au	0.35	5	0.05-0.75	116.1 μA/mM	~3	Chemical reaction method	Gu et al., 2010
SPE/GS@CeO_2-Pt	–0.3	0.43	0.001-10	--	2	Solvothermal process	Yang et al., 2016
NiO nanosheets on graphite	0.33	0.4	0.5- 4	1077	5	Surfactant-templated method	Liu et al., 2015
SPE/GS-Nafion/Fe_3O_4-Au-HRP	–0.3	12	0.02–2.5	--	~3	Chemical reaction method	Xin et al., 2013
MnO_2/Ag nanowire modified GCE	–0.45	0.24	0.00024-4	--	~3	Chemical reaction method	Han et al., 2014
Mn_2O_3/Au	0.25	0.34	0.01-0.5	39.2 ×10^3	--	Electrodeposition method	Saha et al., 2015
Graphite/Co_3O_4 NPs	**–0.117**	**0.0217**	**0.001-0.07**	**65.32**	**<5**	**Bio-mediated**	**Present work**

-E_{cat} vs. Ag/AgCl, LOD: Limit of detection, LR: Linear range, AR: Amperometric response, G: Graphene, CS: Chitosan, GCE: Glassy carbon electrode, SLS: Sodium lignosulfonate, PDDA: Poly(diallydimethylammonium chloride), NFS: Nanoflowers, GS: Graphene sheets, SPE: Screen printed electrode, HRP: Horseradish peroxidase

Table 5.4: Performance comparison with graphite/NiO electrode (present study) with earlier reports using NiO.

Modified graphite substrate	-E_{cat} (V)	LOD (μM)	LR (mM)	Sensitivity (nA/μM/cm^2)	AR (s)	Nanoparticles synthesized process	Source
CB/nano-NiOx/GC	–0.3	1.67	0.005-20	7.62 nA μM^{-1}		Chemical method	Noorbakhsh and Salimi, 2009
TH/nano-NiOx/GC	–0.3	0.36	0.001-10	4.14 nA μM^{-1}	~ 3		
Mb/NiO/ MWCNTs/GC	–0.35	390	0.0008–0.0128	--	~ 7	Hydrothermal method	Qiu et al. 2010
NiO/MWCNTs/FTO	+0.8	32.84	0.0004-.004	--	-	Hydrothermal and annealing	Jandai et al., 2011
NiO/cMWCNT/PANI	+0.28	0.2	0.003-0.7	3.3×10^6	-	Chemical method	Lata et al., 2012
NiO/MWCNTs/GC	+0.3	19	0.2-2.53	--	-	Hydrothermal method	Shamsipur et al., 2012
NiO/RF/GC	–0.32	0.085	0.001-4	24 nA/μM	<2	Chemical method	Roushani et al., 2013
NiO-MnO/Au/GC	+0.7	62.5	0.0318 -0.5	--	-	Hydrothermal method	Ibrahim et al., 2016
ITO/NiO/$Ni(OH)_2$	+0.5	3.22	0.011-2.4	807×10^3	<2	PVD/OAD	Salazar et

HRP/NiO/ MWCNTs/PANI/GC	–0.2	0.43	0.003-0.43	--	-	Chemical method	al., 2017 Zhang et al., 2017
Graphite/NiO NPs	**–0.129**	**0.0271**	**0.001-0.058**	**65.32**	**<5**	**Bio-mediated**	**Present work**

-E_{cat} vs. Ag/AgCl, LOD: Limit of detection, LR: Linear range, AR: Amperometric response, CB: Celestine blue, TH: Thionine, Mb: Myoglobin, GC: Glassy carbon, MWCNTs: Multiwalled carbon nanotubes, FTO: Fluorine doped tin oxide, cMWCNTs: Carboxylated multiwalled carbon nanotubes, PANI: Polyaniline, RF: Riboflavin, ITO: Indium tin oxide, PVD: Physical Vapor Deposition, OAD: Oblique angle configuration, HRP: Horseradish peroxidase

5.3 Major findings

This work achieved that both the graphite/Co_3O_4 NPs and graphite/NiO NPs electrodes exhibited strong electrocatalytic activities for H_2O_2 sensing in a phosphate buffer solution in comparison to different electro-catalysts including the transition metal oxides. The following are the key conclusions from the present chapter.

The mean concentration of Co_3O_4 and NiO NPs immobilized on the carbon paste electrode was found to be 5.92×10^{-13} and 5.19×10^{-13} mol/cm^2 from the couple redox reactions between $Co(OH)_2/Co_3O_4$ and Co_3O_4/CoOOH, and NiO/NiOOH in the absence of H_2O_2.

The H_2O_2 reduction peak was only identified with the graphite-Co_3O_4/700 °C/6 h electrode at $-E_{cat} = -0.117$ V vs. Ag/AgCl. H_2O_2 reduction (sensing) was controlled by its diffusion in a quasi-reversible electrochemical system catalysed by Co_3O_4 NPs with the peak current ratio between 1.03 and 1.10. The limit of H_2O_2 detection was found as low as 0.0217 μM, and the sensitivity of the electrode was as high 65.32 nA/μM/cm^2. The electrode response for H_2O_2 detection was highly reproducibility and invariant in the presence of close electro-active species due to a lower overpotential.

In the case of the graphite/NiO NPs electrode, the H_2O_2 reduction (sensing) peak was found at $-E_{cat} = -0.129$ V vs. Ag/AgCl. The ratio of the peak current was varied from 1.00 to 1.05 also suggesting a quasi-reversible H_2O_2 sensing system catalysed by NiO NPs. The limit of H_2O_2 detection was obtained as 0.0271 μM, and the sensitivity of the electrode was found to be 62 nA/μM/cm^2.

The response currents of both Co_3O_4 and NiO NPs catalysed H_2O_2 sensing were unaltered by the presence of close electro-active species, and the current responses were also highly repeatable (rsd 1.72 to 191) and reproducible (rsd 3.06 to 3.28).

Electrochemical H_2O_2 determination (20-60 mg/L) catalysed by Co_3O_4 and NiO NPs synthesized by the proposed bio-inspired method well matched with the spectrophotometric method using titanic sulphate which could be applied at a higher concentration of H_2O_2.

References

Bard A.J., Faulkner L.R. Electrochemical Methods, 2nd ed., John Wiley and Sons, New York, **2001**.

Cao G.S., Wang R., Wang P., Li X., Wang Y., Wang G., Li J. Electrochemical Co_3O_4 nanoporous thin films sensor for hydrogen peroxide detection, *NANO: Brief Reports and Reviews* **2014**, 9, 1450047.

Chen W., Cai S., Ren Q., Wen W., Zhao Y. Recent advances in electrochemical sensing for hydrogen peroxide: a review, *Analyst* **2012**, 137, 49-58.

Cheng K., Cao D., Yang F., Xu Y., Sun G., Ye K., J Yin., Wang G. Facile synthesis of morphology-controlled Co_3O_4 nanostructures through solvothermal method with enhanced catalytic activity for H_2O_2 electroreduction, *J. Power Sources* **2014**, 253, 214-223.

Gu A., Wang G., Zhang X., Fang B. Synthesis of CuO nanoflower and its application as a H_2O_2 sensor, *Bull. Mater. Sci*. **2010**, 33, 17-20.

Han Q., Ni P., Liu Z., Dong X., Wang Y., Li Z., Liu Z. Enhanced hydrogen peroxide sensing by incorporating manganese dioxide nanowire with silver nanoparticles, *Electrochem. Commun.* **2014**, 38, 110-113.

Hao C., Shen Y., Wang Z., Wang X., Feng F., Ge C., Zhao Y., Wang K. Preparation and characterization of Fe_2O_3 nnoparticles by solid-phase method and its hydrogen peroxide sensing properties, *ACS Sustain. Chem. Eng.* **2016**, 4, 1069-1077.

Haque F., Rahman M.S., Ahmed E., Bakshi P.K., Shaikh A.A. A Cyclic Voltammetric Study of the Redox Reaction of Cu(II) in Presence of Ascorbic Acid in Different pH Media, *Dhaka Univ. J. Sci*. **2013**, 61, 161-166.

Helia H., Pishahang J. Cobalt oxide nanoparticles anchored to : Synthesis and application for enhanced electrocatalytic reaction and highly sensitive nonenzymatic detection of hydrogen peroxide, *Electrochim. Acta* **2014**, 123, 518-526.

Haque F., Rahman M.S., Ahmed E., Bakshi P.K., Shaikh A.A. A Cyclic Voltammetric Study of the Redox Reaction of Cu(II) in Presence of Ascorbic Acid in Different pH Media, *Dhaka Univ. J. Sci*. **2013**, 61 (2), 161-166,

Hou C., Xu Q., Yin L., Hu X. Metal–organic framework templated synthesis of Co_3O_4 nanoparticles for direct glucose and H_2O_2 detection, *Analyst* **2012**, 137, 5803-5808.

Ibrahim S., Charinpanitkul T., Kobatake E., Sriyudthsak M. Nanowires nickel oxide and nanospherical manganese oxide synthesized via low temperature hydrothermal technique for hydrogen peroxide sensor, *J. Chem.* **2016**, 1-6.

Jandai B., Woointranontb P., Chaiyasithc S., Pecharapa W. NiO/MWCNTs coated F-doped Tin oxide working electrode for hydrogen peroxide detection, *Energy Procedia* **2011**, 9, 575 - 580.

Jia W., Guo M., Zheng Z., Yu T., Rodriguez E.G., Wang Y., Lei Y. Electrocatalytic oxidation and reduction of H_2O_2 on vertically aligned Co_3O_4 nanowalls electrode: Toward H_2O_2 detection, *J. Electroanal. Chem.* **2009**, 625, 27-32.

Kamyabi M.A., Hajari N. Low potential and non-enzymatic hydrogen peroxide sensor based on copper oxide nanoparticle on activated pencil graphite electrode, *J. Braz. Chem. Soc*. **2017**, 28 (5), 808-818.

Kung C.W., Lin C.Y., Li T.J., Vittal R., Ho K.C. Synthesis of Co_3O_4 thin films by chemical bath deposition in the presence of different anions and application to H_2O_2 sensing, *Procedia Eng*. **2011**, 25, 847-850.

Lata S., Batra B., Karwasra N., Pundir C.S. An amperometric H_2O_2 biosensor based on cytochrome c immobilized onto nickel oxide nanoparticles/carboxylated multiwalled carbon nanotubes/polyaniline modified gold electrode, *Process Biochem*. **2012**, 47 (6), 992-998.

Liu M., He S., Chen W. Co_3O_4 nanowires supported on 3D N-doped carbon foam as an electrochemical sensing platform for efficient H_2O_2 detection, *Nanoscale* **2014**, 6, 11769-11776.

Liu X., Zhu H., Yang X. An amperometric hydrogen peroxide chemical sensor based on graphene-Fe_3O_4 multilayer films modified ITO electrode, *Talanta* **2011**, 87,243-248.

Liu W., Zhang H., Yang B., Li Z., Lei L., Zhang X. A non-enzymatic hydrogen peroxide sensor based on vertical NiO nanosheets supported on the graphite sheet, *J. Electroanal. Chem*. **2015**, 749,62-67.

Long J.S., Silvester D.S., Wildgoose G.G., Surkus A., Flechsig G., Compton R.G. Direct electrochemistry of horseradish peroxidase immobilized in a chitosan–$[C_4mim][BF_4]$ film: Determination of electrode kinetic parameters, *Bioelectrochem*. **2008**, 74, 183-187.

Mahmoudiana M.R., Alias Y., Basirun W.J., Woi P.M., Sookhakian M. Facile preparation of MnO_2 nanotubes/reduced graphene oxide nanocomposite for electrochemical sensing of hydrogen peroxide, *Sens. Actuators B* **2014**, 201, 526-534.

Marimuthu T., Mahmoudian M.R., Mohamad S., Alias Y. Synthesis and characterization of non-enzymatic hydrogen peroxide sensor of polypyrrole coated cobalt nanocomposites, *Sens. Actuators, B* **2014**, 202, 1037-1043.

Miao X., Yuan R., Chai Y., Shi Y., Yuan Y. Direct electrocatalytic reduction of hydrogen peroxide based on Nafion and copper oxide nanoparticles modified Pt electrode, *J. Electroanal. Chem*. **2008**, 612, 157-163.

Monk P.M.S. Fundamental of electroanalytical chemistry, Wiley India Pvt. Ltd., 2010, pp. 167.

Mu J., Zhang L., Zhao M., Wang Y. Co_3O_4 nanoparticles as an efficient catalase mimic: Properties, mechanism and its electrocatalytic sensing application for hydrogen peroxide, *J. Mol. Catal. A: Chem*. **2013**, 378, 30-37.

Neal C.J., Gupta A., Barkam S., Saraf S., Das S., Cho H.J., Seal S. Picomolar detection of hydrogen peroxide using enzyme-free inorganic nanoparticle-based Sensor, *Sci. Rep*. **2017**, 7, 1324.

Nenkova R.D., Ivanov Y.L., Godjevargova T.I. Influence of different nanoparticles on electrochemical behavior of glucose biosensor, *AIP Conf. Proc*. **2017**, 1809, 1-10.

Noorbakhsh A., Salimi A. Amperometric detection of hydrogen peroxide at nano-nickel oxide/thionine and celestine blue nanocomposite-modified glassy carbon electrodes, *Electrochim. Acta* **2009**, 54, 6312-6321.

Qiu J.D., Cui S.G., Deng M.Q., Liang R.P. Direct electrochemistry of myoglobin immobilized in NiO/MWNTs hybrid nanocomposite for electrocatalytic detection of hydrogen peroxide, *J. Appl. Electrochem*. **2010**, 40 (9), 1651-1657.

Quintino M.S.M., Winnischofer H., Araki K., Toma H.E., Angnes L. Cobalt oxide/tetraruthenated cobalt-porphyrin composite for hydrogen peroxide amperometric sensors, *Analyst* **2005**,130, 221-226.

Roushani M., Abdi Z., Daneshfar A., Salimi A. Hydrogen peroxide sensor based on riboflavin immobilized at the nickel oxide nanoparticle-modified glassy carbon electrode, *J. Appl. Electrochem.* **2013**, 43, 1175-1183.

Saha B., Jana S.K. , Majumder S. , Satpati B. , Banerjee S. Selective growth of co-electrodeposited Mn_2O_3-Au spherical composite network towards enhanced non enzymatic hydrogen peroxide sensing, *Electrochim. Acta* **2015**, 174, 853-863.

Salazar P., Rico V., Gonzalez-Elipe A.R. Non-enzymatic hydrogen peroxide detection at NiO nanoporous thin film-electrodes prepared by physical vapor deposition at oblique angles, *Electrochim. Acta* **2017**, 235, 534-542.

Salih E., Mekawy M., Hassan R.Y.A., El-Sherbiny I.M. Synthesis, characterization and electrochemical-sensor applications of zinc oxide/graphene oxide nanocomposite, *J. Nanostruct. Chem*. **2016**, 6, 137-144.

Salimi A., Hallaj R., Soltanian S., Mamkhezri H. Nanomolar detection of hydrogen peroxide on glassy carbon electrode modified with electrodeposited cobalt oxide nanoparticles, *Anal. Chim. Acta* **2007**, 594, 24-31.

Shamsipur M., Asgari M., Mousavi M.F., Davarkhah R. A novel hydrogen peroxide sensor based on the direct electron transfer of catalase immobilized on nano-sized NiO/MWCNTs composite film, *Electroanal.* **2012**, 24 (2), 357- 367.

Su C.-Y., Lan W.-J., Chu C.-Y., Liu X.-J., Kao W.-Y., Chen C.-H. Photochemical green synthesis of nanostructured cobalt oxides as hydrogen peroxide redox for bifunctional sensing application, *Electrochim. Acta* **2016**, 190, 588-595.

Temocin Z., Yigitoglu M. Studies on the activity and stability of immobilized horseradish peroxidase on poly(ethylene terephthalate) grafted acrylamide fiber, *Bioprocess Biosyst. Eng*. **2008**, 32, 467-474.

Xia S., Yua M., Hu J., Feng J., Chen J., Shi M., Weng X. A model of interface-related enhancement based on the contrast between Co_3O_4 sphere and cube for electrochemical detection of hydrogen peroxide, *Electrochem. Commun*. **2014**, 40, 67-70.

Xin Y., Fu-Bing X., Hong-Wei L., Feng W., Di-Zhao C., Zhao-yang W. A novel H_2O_2 biosensor based on Fe_3O_4–Au magnetic nanoparticles coated horseradish peroxidase and graphene sheets–Nafion film modified screen-printed carbon electrode, *Electrochim. Acta* **2013**, 109, 750-755.

Yang X., Ouyang Y., Wu F., Hu Y., Zhang H., Wu Z. In situ & controlled preparation of platinum nanoparticles dopping into graphene sheets@cerium oxide nanocomposites sensitized screen printed electrode for nonenzymatic electrochemical sensing of hydrogen peroxide, *J. Electroanal. Chem*. **2016**, 777, 85-91.

Zhang J., Yang B., Guo Z., Song Q., Ye X., Zheng S. Nickel Oxide Nanoparticles Immobilized on MWCNTs/PANI Composite Film as an Electron Transfer Facilitator for Horseradish Peroxidase: Direct Electron Transfer and H_2O_2 Determination, *J. Electrochem. Soc*. **2017**, 164 (5) B3001-B3007.

Zhang Z., Gu S., Ding Y., Zhang F., Jin J. Determination of hydrogen peroxide and glucose using a novel sensor platform based on $Co_{0.4}Fe_{0.6}LaO_3$ nanoparticles, *Microchim. Acta* **2013**, 180, 1043-1049.

Chapter -6

Conclusions and Recommendations for Future Work

In this chapter, remarkable accomplishments, major conclusions of the entire doctoral work, and limitations of the present work are summarized. The directions for the further extension of the present work are also provided.

6.1 Conclusions

The conclusions from the present study are outlined as follows:

- H_2O_2 decomposition was significant at elevated pH (> 8) and temperature (> 50 °C), and traces of Cu^{2+} and Mn^{2+} ions catalytically decomposed H_2O_2 even in an acidic electrolyte media, however, Co^{2+} and Ni^{2+} ions exhibited insignificant catalytic effect of H_2O_2 decomposition.
- In the case of H_2O_2 generation at the bare graphite electrode (commercial), the yield of H_2O_2 formation was the highest in the NaCl supporting electrolyte media followed by Na_2SO_4 and $NaNO_3$, but $NaClO_4$ suppressed the generation of H_2O_2, in particular, at the later stage of the reaction (> 80 min) with the graphite/TiO_2-Ti electrode system. Therefore, the use of $NaClO_4$ as a supporting electrolyte may be avoided as it could destroy the Fenton's reagent by forming reactive oxygen species at the TiO_2-Ti anode when the coupled EFP and AO processes are considered. For the graphite/graphite electrode system, the influence of the SEs on the increasing order of the current efficiency was found as Na_2SO_4 > NaCl > $NaClO_4$>> $NaNO_3$.
- The optimal conditions were determined as pH 2.5, $-E_{cat}$ =–0.6 V vs. Ag/AgCl, 0.08 M SE, and O_2 flow rate 4 LPM with the graphite/graphite system. The current efficiency of H_2O_2 formation was found ~36 % after 2 h of electrolysis with the graphite/graphite systems using $NaClO_4$ as the SE. But, the primary limitation of this system (non-catalyzed) was that the CE_f of H_2O_2 formation was decreased steadily with the progress of electrolysis.
- Analytes present in *S. edule* were as effective as the reductants employed in conventional chemical methods for the synthesis of NiO and Co_3O_4 NPs, and no external capping agents were needed to inhibit particles agglomeration in the proposed bio-inspired method, and

these NPs catalytically improved the rate of H_2O_2 formation and achieved a steady CE_f during electrolysis.

- Nickel hydroxide was formed through the ligand exchange between the analytes and OH^- ions which were calcined at 500 °C for 2 h for the formation NiO NPs as evidenced from the thermogravimetric analysis and X-ray diffraction studies, and the resulting particles were free from contaminants/other nickel species. Similarly, the analytes present in the bio-extract mediated CoOOH reduction to $Co(OH)_2$ for the formation of monocrystalline Co_3O_4 in the calcination process at 700 °C for 6 h.
- Nearly spherical NiO NPs (avg. 14.48 nm) were formed with a weak ferromagnetic property (coercive field 0.31 kOe with 0.03 emu/g remanent magnetization) and high microporosity (75 %). Co_3O_4 NPs (avg. 31.79 nm and 90 % microporosity) exhibited a very weak ferromagnetic property with 0.37 emu/g.
- CE_f of H_2O_2 generation was much higher (~30 % more) in the case of NiO and Co_3O_4 NPs catalysed systems than the non-catalysed systems (graphite/TiO_2-Ti and graphite/graphite systems). Both NiO and Co_3O_4 NPs exhibited a low catalytic activity for decomposition of H_2O_2, so, decrease in CE_f with the progress of H_2O_2 generation was significantly lower than the bare graphite cathode.
- Overpotential of O_2 reduction forming H_2O_2 was found to be 1.843 and 1.831 V at the graphite/Co_3O_4 and graphite/NiO NPs cathodes.
- Mass transfer coefficient ($0.955\text{-}1.13\times10^{-5}$ m/s) was about one order magnitude lower with the Co_3O_4 and NiO NPs catalysed system compared to the bare graphite (synthesized by the carbon paste method) system of H_2O_2 generation (0.280×10^{-5} m/s).
- NiO and Co_3O_4 NPs catalyzed H_2O_2 formative gave a CIP cleavage of 71-78 % in EFP

against the mineralization efficiency of 31-46 % as the quinolone structure of CIP molecule was resistant to •OH radical attack, and the degradation process followed the pseudo 1st order kinetic behavior.

- The CIP molecule was cleaved through piperazine moiety breaking, cyclopropyl-group cleavage, and decarboxylation reaction and the majority of the fragments were originated from the cleavage of piperazine ring moiety.
- Both the Co_3O_4 and NiO NPs exhibited strong electrocatalytic activities for the H_2O_2 sensing in a deaerated phosphate buffer solution (0.1 M) in a quasi-reversible redox system.
- There was a significant (peak) separation potentials between redox couple reactions of Co(II)/Co(III) and Ni(II)/Ni(III) species, and H_2O_2 sensing.
- The limit of H_2O_2 detection and electrode sensitivity were obtained as 0.0217 μM and 65.32 nA/μM/cm^2 found with the graphite/Co_3O_4 NPs electrode, it was 0.0271 μM and 62 nA/μM/cm^2 at the graphite/NiO NPs electrode.
- Close electro-active species, such ascorbic acid, dopamine, etc. couldn't affect the redox reactions and response current of the H_2O_2 sensing catalysed by Co_3O_4 and NiO NPs.
- H_2O_2 determination catalyzed by Co_3O_4 and NiO NPs well matched (20-60 mg/L) with the spectrophotometric method which is ONLY effective at a higher concentration of H_2O_2.

6.2 Limitations of present work

- The quality of biomass (hence, bio-analytes) depends on geographical location and cultivation condition. So, the repeatability and consistency of the experimental results for both the nanoparticles may be affected.

- The synthesis of metal nanoparticles was carried out in a small desktop reactor (500 mL volume). So, the quality and purity of NiO and Co_3O_4 NPs could be sacrificed in a scaled up process.
- This work was focused only on the generation and sensing of H_2O_2 catalyzed by NiO and Co_3O_4 NPs. There are potential transition metal oxides NPs such as CuO, MnO_2, SnO_2 etc. for such applications having a low catalytic activity of H_2O_2 decomposition.
- Fabricated electrodes were tested for the limited nos of cycles for both H_2O_2 generation and sensing for the duration of a month. Studies on the long term stability of the modified electrodes lack in the present work.
- The present study acted on a fixed concentration of a single drug. The concentration of CIP used was much higher than a PhAC commonly present in industrial and municipal wastewater. This is one of the limitations of the present work to check the applicability of H_2O_2 in the EFP.

6.3 Recommendations of future work

The present work could be improved and carried forward by exploring further scopes and taking care of the limitations of the present work as outlined in the above section. The recommendations are:

- ☑ Bio-inspired technique for the formation of NiO and Co_3O_4 NPs proposed in this work is at the initial stage of the development. So, the dedicated investigations are needed to bring this technique at the maturity level.
- ☑ An attempt was made for the elucidation of the mechanism of the NiO and Co_3O_4 NPs formation mediated by *S. edule* extract. Detail studies are imperative for a clear

understanding of the mechanism of NPs formation and its stabilization in a bio-inspired process.

- ☑ H_2O_2 generation studies were performed in an undivided cell. Investigations in a divided cell would further light on H_2O_2 decomposition, if any, even at a trace level.
- ☑ Applications of H_2O_2 generated in metal oxides catalysed systems needs through studies with a focus on the emerging contaminants in in-situ EFP.
- ☑ NiO and Co_3O_4 NPs have numerous catalytic applications such as in sensor development, electrochemical CO_2 reduction to value-added chemicals, etc. These are also the prudent areas of further researches.

Publications

Journal Publications

1. **R. K. Das** and A. K. Golder, Co_3O_4 spinel nanoparticles decorated graphite electrode: Bio-mediated synthesis and electrochemical H_2O_2 sensing, ***Electrochim. Acta, 2017,*** *251, 415-426* (Elsevier).
2. **R. K. Das** and A. K. Golder, Use of plant based analytes for the synthesis of NiO nanoparticles in catalyzing electrochemical H_2O_2 production, ***J. Electroanal. Chem.*** **2018,** 823, 9-19 (Elsevier)
3. **R. K. Das** and A. K. Golder, Impact of supporting electrolytes on the stability of Ti/TiO_2 counter electrode during H_2O_2 electrogeneration, ***Surf. Eng. Appl. Electrochem.*** **2017,** 53, 570-579 (Sringer).
4. **R. K. Das**, S. Saha, Ch.V. Rao and A. K. Golder, Bio-inspired AgNPs, multilayers reduced graphene oxide and graphite nanocomposite for electrochemical H_2O_2 sensing, ***Bull. Mater. Sci.*** **2018**, *41 (86) 1-11* (Sringer).
5. **R. K. Das**, A. S. Giri, and A. K. Golder, Role of supporting electrolytes for hydrogen peroxide generation on graphite cathode, ***Int. J. Cur. Eng. Sci. Res.*** **2014,** 1(4), 31-34 (TRO India).
6. V. Rani, **R. K. Das** and A. K. Golder, Fabrication of graphene-graphite paste electrode for H_2O_2 formation and its implication for ciprofloxacin degradation***, Surf. Interf.,*** **2017,** 7, 99-105 (Elsevier).
7. S. Chakraborty, Ch.V. Rao, **R.K. Das**, A.S. Giri, A.K. Golder, 2016, Bio-mediated silver nanoparticle synthesis: mechanism and microbial inactivation, ***Toxicol. Environ. Chem.,*** **2017,** 99, 434-447 (Taylor & Francis).
8. M. Malika, Ch V. Rao, **R.K. Das**, A.S. Giri and A.K. Golder, Evaluation of bimetal doped TiO_2 in dye fragmentation and its comparison to mono-metal doped and bare catalyst, ***Appl. Surf. Sci.,*** **2016**, 368, 316–324 (Elsevier).
9. A. K. Behera, Ch V. Rao, **R.K. Das**, A.S. Giri and A.K. Golder, Fabrication and characterization of ag-doped titania: Impact of dye-sensitization, phenol decomposition kinetics and biodegradability index, ***Desalin. Water Treat.,*** **2015**, 1-10 (Taylor & Francis).

International Conferences

1. **R. K. Das** and **A.** K. Golder, Hydrogen peroxide electro-generation at different supporting electrolytes using graphite both as working and counter electrodes with Ag/AgCl reference, CHEMCON-2015, December 27-30, **2015**, Indian Institute of Technology, Guwahati, India.
2. **R. K. Das**, V. Rani and **A.** K. Golder, Two electron transfer hydrogen peroxide generation using high purity (99.95%) isomolded graphite cathode, International Conference on Water:From Pollution to Purification (ICW-2015), January 23-26, **2015**, Centre for Environment Education and Technology (CEET), Kottayam, India.

3. **R. K. Das**, A. S. Giri, and A. K. Golder, Role of supporting electrolytes for hydrogen peroxide generation on graphite cathode, International Conference on Civil and Chemical Engineering (ICCCE-2014), 30 November, **2014**, Warangal, India.
4. **R. K. Das** and A. K. Golder, Stability of aqueous H_2O_2 at elevated temperature and pH in presence of common cations, CHEMCON-2013, December 27-30, **2013**, Institute of Chemical Technology, Matunga, Mumbai, India.

National Conferences

1. **R.K. Das** and A.K. Golder, Enhanced H_2O_2 electro-generation at metal catalyzed graphene-graphite cathode, March 25- March 27 (Reflux **2016**), Indian Institute of Technology Guwahati, India.
2. **R.K. Das** and A.K. Golder, Synergistic effect of formation of H_2O_2 at cathode and OH^o(ad) at anode on decontamination studies- A review, Annual Chemical Engineering Symposium, March 29- March 30 (Reflux **2014**), Indian Institute of Technology Guwahati, India.
3. **R.K. Das** and A.K. Golder, Synergistic effect of supporting electrolytes on H_2O_2 formation using graphite both as working and counter electrodes with Ag/AgCl reference electrode, June 4-6 June (National conference Challenges in Environmental Research, **2015**), Indian Institute of Technology Guwahati, India.

Institute conference

1. R.K. Das, V. Rani and **A. K. Golder**, Different type of the anode used affect hydrogen peroxide generation with various supporting electrolyte in undivided cell. March 23-26, 2015, **Students' Academic Board (SAB) PhD Council, IIT Guwahati, India**.

Workshop

1. National workshop on Technical writing conducted under the technical education quality improvement programme sponsored by the Ministry of Human Resource Development, Government of India, held on 6-7 December'2014.

Leadership quality

2013 **QIP Short Term Course volunteer**: Advanced Chemical Process Design, July 8-12, 2013, Department of Chemical Engineering, Indian Institute of Technology Guwahati, India (Coordinator: Dr. A. K. Golder and Prof. R.G. Uppaluri).

2015 **Coordinator for room accommodation:** CHEMCON 2015, 68th Annual session of Indian Institute of Chemical Engineers, December 27-30, 2015, IIT Guwahati, Assam.